

UNIVERSITY OF SHEFFIELD

DOCTORAL THESIS

**Line tracking applications for
Gravitational Wave data and searching for
long-duration burst signals**

Author:
Ross KENNEDY

Supervisor:
Dr. Ed DAW

*A thesis submitted in fulfillment of the requirements
for the degree of Doctor of Philosophy*

in the

LIGO Research Group
High Energy Physics

December 17, 2018

University of Sheffield

Abstract

High Energy Physics

Doctor of Philosophy

Line tracking applications for Gravitational Wave data and searching for long-duration burst signals

by Ross KENNEDY

The line-tracking filter iWave can be applied in several different contexts with gravitational wave data from the LIGO interferometers. In this thesis we explore several of these applications with regards to signal processing and hardware. The filter can be used to remove lines which pollute data from the detectors in a less aggressive method than the currently adopted LPEF filter. A technique for recursively removing these lines using iWave is described in this work.

We also discuss the topic of parametric instabilities which pose a limiting factor to the sensitivity of the LIGO detectors. Parametric instabilities are formed from an opto-mechanical feedback loop between the TEM modes of the laser in the 4km arm cavity and the cavity mirrors. A damping scheme to control these instabilities was developed at the LIGO Hanford detector. The results from implementing this scheme are presented in this thesis.

The analysis pipeline X-SphRad is discussed as a method for detecting long duration burst signals in the all-sky regime. This pipeline uses spherical harmonics as an efficient method for measuring correlation between detectors as well as providing statistics for rejecting detector glitches. The results from running separate analyses for 2-detector and 3-detector networks over the O2 observation run are presented.

Acknowledgements

It's been a privilege to work as part of the LIGO collaboration over the past few years. I still can't believe how lucky I have been to start my PhD in the same year that gravitational waves were first detected. LIGO is an amazing experiment and my journey to at least partially understand it has been hugely rewarding. During the PhD I was given the unique opportunity to visit the LIGO Hanford detector. My time there provided me with greater insight to how the detector works and also allowed me to meet a lot of people in the collaboration I wouldn't have met otherwise. Thanks to everyone I met at the site and made my time out there a great experience.

I want to thank my supervisor Ed who took me on board and taught me so much. You inspired me to learn and always explained things in an understanding way. Thanks for providing such a great opportunity and for helping me through every step of the way.

I'd like to thank all the friends I've met in Sheffield for their help and support. As well as all the stupid jokes, pub quizzes and great times we've shared together, I could always rely on my friends to help me through the tougher times. Cheers guys!

Thanks to my family back home in Scotland who have always supported me and at least tried to understand when I told them about my work. Especially to my parents who always knew how important it was for me. I hope you guys are proud and secretly relieved that I'm finished.

Lastly I want to thank my girlfriend Ellie who's been there for me through everything. Despite doing a PhD at the same time as me, you always helped me through when I was struggling. You've been my anchor throughout everything and I couldn't have done it without you.

Contents

Abstract	iii
Acknowledgements	v
1 Gravitational waves	1
1.1 Introduction	1
1.2 Gravitational wave theory	6
1.3 Sources of gravitational waves	9
1.3.1 Compact Binary Coalescence	9
1.3.2 Burst Signals	10
1.3.3 Continuous Sources	10
1.3.4 Stochastic Gravitational Wave Background	10
1.4 Interferometer Design	11
1.4.1 Interferometry using Fabry-Perot Cavities	11
1.4.2 Use of sidebands	12
1.4.3 Advanced LIGO	12
2 Signal processing with iWave	15
2.1 Introduction	15
2.2 Motivation and overview	15
2.3 Theory of the iWave filter	17
2.3.1 Open loop state	17
Rotation of iWave complex output	19
2.3.2 Closed loop state	23
2.3.3 Tracking glitches	32
2.3.4 Tracking wandering lines	34
2.3.5 Tracking examples with no noise	34
2.3.6 Tracking examples with added noise	37
2.3.7 Tracking examples with no input signal	39
2.3.8 Summary	42
2.4 Line removal from GW150914 event	42
2.4.1 Data from GW150914	42
2.4.2 Filtering with LPEF	43
2.4.3 Whitening filter	44
2.4.4 Peak finding	46
2.4.5 Static v.s. dynamic line removal	49
2.4.6 Recursive line removal	51
3 Parametric Instabilities	63
3.1 Introduction	63
3.2 PI theory	63
3.2.1 Gaussian beam mode	64
3.2.2 Higher order modes	66

3.2.3	Mechanical mode interaction	67
3.2.4	Three mode interaction	68
3.2.5	Parametric gain	69
3.2.6	Observations of PI at LIGO detectors	71
3.3	ESD Damping scheme	73
3.3.1	Description of ESD	73
3.3.2	QPD v.s. OMC signal chains	74
3.3.3	iWave model for tracking PI	76
3.4	Results from damping	79
3.4.1	Attempted damping of PI from two mechanical modes	79
3.4.2	15217 Hz mode	82
3.4.3	15009Hz mode	84
3.4.4	Controlling multiple modes during a lock	84
3.5	Discussion	86
4	X-SphRad line removal modification	87
4.1	Introduction	87
4.2	All-sky searches for transient GW using X-SphRad	88
4.2.1	Data conditioning	88
4.2.2	Background estimation and simulated injections	88
4.2.3	Spherical Harmonic correlation	89
4.2.4	Frequency domain clustering	90
4.2.5	Linear and alpha cuts	91
4.2.6	Null stream	91
4.3	Whitening data with line removal	92
4.3.1	O1 wandering line	92
4.3.2	Automated line removal process	95
4.3.3	O2 excited violin mode removal	99
5	Results from O2 analysis	105
5.1	3 detector analysis	105
5.2	2 detector analysis	109
5.2.1	Background and Foreground results	109
	Closed box	109
	Open box	110
5.2.2	Cuts	111
5.2.3	Injection recovery	113
	Astrophysical models	113
	Ad-hoc models	119
6	Conclusion	123
A	Injection efficiency plots from 2 detector analysis	125
B	Manual for X-SphRad analysis	135
	Bibliography	141

List of Figures

1.1	Orbital decay of binary pulsar system PSR1913+16. Measurements agree with decay predicted from general relativity [77].	3
1.2	Schematic of first interferometer used as a GW detector [35].	4
1.3	Gravitational wave signal from binary black-hole inspiral measured by aLIGO detectors [12]	6
1.4	Exaggerated effect of plus-polarised quadropolar gravitational wave on a circle of masses	8
1.5	Spectrogram of BNS event [10] from LIGO detectors. Chirp signal increases in frequency over time as the binary system coalesces.	9
1.6	Design of Advanced LIGO detector [8]. Several additions including input and output mode cleaners improves the detector sensitivity.	13
2.1	Orthogonal state outputs from static iWave tracking. Both states converge to the input signals amplitude but the Q-phase leads the I-phase by 90°	18
2.2	Amplitude output from static iWave tracking. Amplitude converges to the input signal value exponentially with response time equal to τ	18
2.3	Complex output from static iWave before rotations are applied. The black outline represents the steady state of the filter and the blue dashed line represents the data exponentially approaching this state.	19
2.4	Sequential matrix rotations of original iWave output using Equation 2.5. Dotted lines represent angle of rotation of the last data point in the data.	20
2.5	I and Q phase frequency response with varying τ . Larger τ relates to smaller bandwidth for both I and Q.	21
2.6	Results from amplitude tracking a sinusoid with constant frequency and added Gaussian noise using open loop iwave. Output amplitude is an exponential function over time with response time τ . Increasing τ over three examples with an average SNR of 26.71.	22
2.7	Variance of amplitude tracking after lock is acquired for increasing τ . Higher τ results in more accurate tracking for static frequency signals. Small error bars due to small difference between variance for each simulation.	23
2.8	Schematic for iWave in closed loop configuration. Changes in tracking frequency Δ controlled by measured departures in phase $\delta\Phi$	24
2.9	Scaled frequency output from iWave for varying τ with offset starting frequency. Signal frequency acquired faster for smaller τ values.	25
2.10	Frequency tracking response time for varying τ and constant $\eta = 1$. Response time is larger than τ value due to feedback filter $C(z)$	26
2.11	Amplitude output for closed loop iWave with offset starting frequency. Output resembles a sigmoid function due to initial change the filters central frequency followed by subsequent exponential averaging.	27

2.12	Fit of sigmoid function (red) compared to tracked amplitude output from closed loop iWave with offset starting frequency (blue).	27
2.13	Scaled frequency output from closed loop iWave tracking static frequency sinusoid with offset starting frequency. Frequency output overshoots signal frequency with larger η values.	28
2.14	Frequency tracking of a 60 Hz line with no noise ($\tau = 1$, gain= $(9 * ts/\tau)^2$). Frequency output is similar to a damped oscillator and locks on after 10 seconds.	29
2.15	Frequency tracking of a 60 Hz line with Gaussian noise ($\tau = 1$, gain= $(9 * ts/\tau)^2$). Added noise and large gain causes frequency tracking to also contain more noise.	29
2.16	Frequency tracking of a 60 Hz line with Gaussian noise ($\tau = 1$, gain= $(9/8 * ts/\tau)^2$). Reduction in gain compared to Figure 2.15 allows for more accurate frequency tracking.	30
2.17	χ^2 for frequency tracking for low tau and varying gain (Average SNR = 27.07, 100 seconds). Larger χ^2 values show less accurate frequency tracking. Frequency tracking becomes less accurate with lower τ and higher gain.	31
2.18	Fractional line reduction after filtering static 60Hz line using closed loop iWave with varying τ and η factor. Larger reduction in line magnitude (yellow) indicates better tracking/filtering of the input signal. Lower reduction (blue) indicates that the filter was not able to lock on or filter the signal effectively.	32
2.19	Frequency tracking line with Gaussian background noise and SNR of -10 with $\eta=10$ and $\tau=1$. Glitch occurs after 25 seconds due to large background noise causing frequency tracking to fail.	33
2.20	Tracking output of iWave with applied to data containing wandering line at 60 Hz without added background noise. Filter parameters set to $\tau = 1$ $\eta = 1$. iWave loses lock on frequency due to small gain resulting in non-zero phase error. Larger difference between signal and tracked frequency causes larger variance in phase error and lower output amplitude.	35
2.21	Tracking output of iWave with applied to data containing wandering line at 60 Hz with no added background noise. Filter parameters set to $\tau = 1$ $\eta = 10$. With no background noise, iWave is able to achieve and maintain lock onto the line after 4 seconds due to higher gain compared to Figure 2.20	36
2.22	Tracking output of iWave with applied to data containing wandering line at 60 Hz with no added background noise. Filter parameters set to $\tau = 0.1$ $\eta = 2$. With no background noise, iWave is able to lock onto signal faster than in Figure 2.21 due to higher gain and reduced τ	36
2.23	Tracking output of iWave with applied to data containing wandering line at 60 Hz with added background noise. Filter parameters set to $\tau = 1$ $\eta = 1$. Additional noise in input data causes larger noise in error signal compared to Figure 2.20.	37
2.24	Tracking output of iWave with applied to data containing wandering line at 60 Hz with added background noise. Filter parameters set to $\tau = 1$ $\eta = 10$. Similar output to Figure 2.21 but with more noise in error signal due to noise in input signal.	38

2.25	Tracking output of iWave with applied to data containing wandering line at 60 Hz with added background noise. Filter parameters set to $\tau = 0.1 \eta = 2$. Improved lock time compared to Figure 2.24 but output contains more noise due to the filter's larger bandwidth.	38
2.26	Tracking output of iWave with applied to data containing wandering line at 60 Hz with added background noise. Filter parameters set to $\tau = 0.1 \eta = 10$. Increasing gain when input contains background noise causes larger noise in frequency tracking as well as error signal.	39
2.27	Tracking output of iWave with applied to data containing wandering line at 60 Hz with added background noise. Line is only present over first half of the data. Filter parameters set to $\tau = 1 \eta = 1$. Higher noise in error signal when there is no input signal and amplitude output tends to zero.	40
2.28	Tracking output of iWave with applied to data containing wandering line at 60 Hz with added background noise. Line is only present over first half of the data. Filter parameters set to $\tau = 0.1 \eta = 2$. Higher noise in error signal when there is no input signal and amplitude output tends to zero. Frequency tracking reaches unphysical values due to increased gain and τ	41
2.29	Tracking output of iWave with applied to data containing wandering line at 60 Hz with added background noise. Line is only present over first half of the data. Filter parameters set to $\tau = 0.1 \eta = 10$. With higher gain and lower τ the output frequency reaches unphysical values, the error signal noise increases and there are glitches in the output amplitude tracking not present in the input data.	41
2.30	Spectrum of DARM data from both interferometers during GW150914 event. strain data is dominated by seismic noise at lower frequencies and shot noise at higher frequencies. Line features come from violin modes and power lines.	43
2.31	Spectrum of LPEF filtered data from H1 during GW150914 event. Waveforms crossing frequency regions where lines existed will not be observed over those frequencies using this filtering technique.	44
2.32	Whitening filter frequency response for normalising spectra seen in Figure 2.30.	45
2.33	Spectrum of DARM data from both interferometers during GW150914 event after whitening filter.	46
2.34	Lower frequency mechanical modes of test masses. Orange stars represent the output of the peakfinding algorithm used to set iWave's input frequency during recursive line removal.	47
2.35	500Hz violin mode region. Orange stars represent the output of the peakfinding algorithm used to set iWave's input frequency during recursive line removal.	48
2.36	1000 Hz violin mode region. Orange stars represent the output of the peakfinding algorithm used to set iWave's input frequency during recursive line removal.	49
2.37	Static iWave line removal of largest line in H1 spectrum over varying τ	50
2.38	Dynamic iWave line removal of largest line in H1 spectrum over varying τ . Dynamic line removal is more successful than the static line removal from Figure 2.37.	51
2.39	Whitened H1 data after iterative line removal using $\tau = \Gamma^{-1}/2$	52

2.40	Whitened H1 data after iterative line removal using $\tau = \Gamma^{-1}/4$	52
2.41	Whitened H1 data after iterative line removal using $\tau = \Gamma^{-1}/8$	53
2.42	Whitened L1 data after iterative line removal using $\tau = \Gamma^{-1}/2$	53
2.43	Whitened L1 data after iterative line removal using $\tau = \Gamma^{-1}/4$	54
2.44	Whitened L1 data after iterative line removal using $\tau = \Gamma^{-1}/8$	54
2.45	H1 spectrum comparison before and after recursive iWave line removal. All line regions are reduced in magnitude by iwave while leaving the structure of the background the same.	55
2.46	L1 spectrum comparison before and after recursive iWave line removal. All line regions are reduced in magnitude by iwave while leaving the structure of the background the same. Due to the larger amount of resonant violin modes the 500 Hz region is not as reduced compared to Figure 2.45	56
2.47	H1 cumulative spectrum comparison before and after recursive iWave line removal. Line removal reduces the total cumulative sum from $5.1924e-20$ to $2.8586e-21$ increasing the total sensitivity by a factor of 18.2.	57
2.48	L1 spectrum comparison before and after recursive iWave line removal. Line removal reduces the total cumulative sum from $2.3872e-19$ to $2.9521e-21$ increasing the total sensitivity by a factor of 80.9.	57
2.49	Lower frequency mechanical modes of test masses after line removal process. There is a significant reduction in the line amplitude compared to Figure 2.34.	58
2.50	500Hz violin mode region after line removal process. There is a significant reduction in the line amplitude compared to Figure 2.35.	58
2.51	1000 Hz violin mode region. after line removal process. There is a significant reduction in the line amplitude compared to Figure 2.36.	59
2.52	Spectrogram data from Hanford detector before iterative line removal is applied. GW150914 signal can be seen in at lower frequencies between 0 to 0.5 seconds.	59
2.53	Spectrogram data from Hanford detector after iterative line removal is applied. GW150914 signal can be seen in at lower frequencies between 0 to 0.5 seconds.	60
2.54	Spectrogram data from Livingston detector before iterative line removal is applied. GW150914 signal can be seen in at lower frequencies between 0 to 0.5 seconds.	60
2.55	Spectrogram data from Livingston detector after iterative line removal is applied. GW150914 signal can be seen in at lower frequencies between 0 to 0.5 seconds.	61
2.56	Overlaid H1 and L1 time-series of GW150914 event after iWave line-removal processing. Similar to the whitened time-series shown in Figure 1.3 but achieved through iWave line removal method.	62
3.1	Properties of a Gaussian beam with wavelength 1064nm and waist size $100 \mu\text{m}$. Top plot: Beam waist as a function of z position. Bottom plot: Gouy phase as a function of z position	65
3.2	Beam profiles for low order Hermite-Gaussian and Laguerre-Gaussian modes [16].	67

3.3	Stokes and anti-Stokes scattering [44]. For Stokes scattering (left) a photon from the fundamental laser mode is absorbed by the mirror adding energy into the mechanical mode and Higher order mode. Anti-Stokes scattering is where energy from the mechanical mode is transferred to the Higher order mode through interaction with a photon from the fundamental laser mode.	68
3.4	Three mode interaction [16]. PI are induced due to feedback from the interaction between the mirror mechanical mode, the laser's fundamental Gaussian mode and the laser's Higher-order mode.	69
3.5	HOM spacing in Hz over the period of two interferometer locks. Increased cavity power during lock states results in changes in RoC of the cavity optics which increases the higher order mode spacing. . . .	70
3.6	First observation of PI at LIGO Livingston [32]. Direct correlation between cavity power and PI amplitude shown as decreasing power causes the PI to ring down.	71
3.7	Spectrogram of first PI seen at LIGO Hanford. PI rings up to critical levels after 25 minutes and then decreases as the laser power is reduced.	72
3.8	iWave tracking of PI at LIGO Hanford. Exponential increase in PI mode can be seen in iWave's amplitude output.	72
3.9	ESD electrodes deposite on reaction mass. Adapted from [55]	73
3.10	PI damping scheme using QPD signal chain. Bandpassed mechanical mode signal from QPD is used to drive ESD quadrants and actuate the ETM.	74
3.11	PI damping scheme using OMC signal chain. Bandpassed mechanical mode signal from OMCPD is used to drive ESD quadrants and actuate the ETM.	75
3.12	Spectra of output signals from QPD transmission (red) and OMCPD (black). Mechanical mode at 1510 Hz appears in both spectra however signal-to-noise ratio from OMCPD data is much greater.	76
3.13	Medm for control of filters for damping of mechanical mode using QPD damping scheme.	77
3.14	Medm screen used for filter control for QPD damping scheme	77
3.15	Medm screen used for damping filter control for adjusting output gain and phase.	77
3.16	Overview medm screen for OMC damping scheme. Damping signal to ESD for each mode is controlled by input matrices.	78
3.17	iWave tracking of 15kHz mechanical mode. Input signal (red), bandpassed signal (blue) and iWave tracked signal (green).	79
3.18	Spectrum of PI seen simultaneously from 15520Hz and 15540Hz mechanical modes. OMC output (black) shows 20 Hz comb from beat between the two modes. Both modes seen in X-arm QPD output (red) at a lower amplitude but with no comb effect. iWave tracking output (pink) reduces 15520Hz mode in relation to the 15540 Hz mode when it is locked on to the higher frequency mode.	80
3.19	Spectrogram of PI from 15520 Hz and 15540 Hz mechanical modes. Damping was not effective in this case causing lock loss.	81
3.20	Amplitude tracking output of 15540 Hz mode. Damping was attempted at 450 seconds but the mode continued to ring up after iWave lost the ability to track the line.	81

3.21	Frequency tracking of 15540 Hz mode. Tracking switches to lower frequency line after the original mode is damped. Frequency the switches back as the mode rings up again. A linearly increasing artifact can also be seen here which is also present in Figure 3.19.	82
3.22	Spectrum of 15217 Hz mechanical mode region. Two modes exist within the 10 Hz range of the bandpass filter.	83
3.23	Damping of 15217 Hz mechanical mode using iWave. After the damping gain is increased to 1000 the amplitude begins to decrease until the frequency tracking locks onto the mechanical mode 1 Hz higher. . . .	83
3.24	Actuating on 15009Hz mechanical mode using bandpassed OMC signal.	84
3.25	RMS outputs for damping multiple mode during extended lock. (a) 14980 Hz ITMY (b) 15009 Hz ETMY (c) 18040 Hz ETMY (QPD) (d) 18040 Hz ETMY (OMC)	85
4.1	Spectrogram of wandering line at 655Hz present during O1 after the data is whitened using LPEF. The LPEF whitening filter is not able to remove the wandering line due to the non-static frequency of the signal. When this data is analysed by pipelines such as X-Sphrad large amounts of candidate events are detected from this frequency band which are mostly from this instrumental noise. This reduces the likelihood of detecting an astrophysical signal from sets of data where the wandering line is present.	93
4.2	Spectrogram of tracked I-phase output from iWave linetracking of 655Hz wandering line. This data is subtracted from the LPEF filtered data in Figure 4.1 to filter out the wandering line.	94
4.3	Spectrogram of O1 data after LPEF filtering and iWave line subtraction of 655Hz wandering line. With the line removed from the data candidate events at lower energies are able to be detected by analysis pipelines such as X-Sphrad. This is discussed further in Section 4.3.2.	95
4.5	Thresholded tf-map of correlated HL data. Excess power from the wandering line is clustered and detected as events.	96
4.4	Flow chart for automated line removal process with X-SphRad.	97
4.6	Thresholded tf-map of correlated HL data after line removal. Events at lower energies are now detected in the absence of the wandering particularly at lower frequencies.	98
4.7	Thresholded tf-map of correlated HL data after line removal without bandpassing. Line tracker loses lock on the wandering line in the presence of the injection.	98
4.8	Energy of clustered events against central frequency. Red and black data points indicate events before and after line removal respectively. Injection scale is increased for each plot downwards. Increasing injection scale causes increasing events above wandering line frequency particularly after line removal.	99
4.9	Incoherent v.s. coherent energies for offsource background without line removal. The colour axis is the base-10 logarithm of the cluster's coherent energy (circenergy).	101
4.10	Incoherent v.s. coherent energies for off-source background with line removal. Events seen at much higher energies than without line removal indicating glitches have been introduced by the line removal process. The colour axis is the base-10 logarithm of the cluster's coherent energy (circenergy).	102

4.11	Followup tf-map of segment of injection analysis containing a glitch due to line removal after 150 seconds.	103
4.12	Time-series data from frequency tracking and filtered output with bandpassed line tracking process. Glitch appears at same time as large change in frequency	104
4.13	Time-series data from frequency tracking and filtered output from line tracking process without bandpassing. Glitch is no longer seen in time series data indicating the bandpassing was the cause of the glitch. . . .	104
5.1	Incoherent v.s. coherent energy for 3 detector dummy on-source. Event can be seen passing the cut with $E_{SH} > I_{SH}$. The colour axis is the base-10 logarithm of the cluster's coherent energy (circenergy).	106
5.2	Incoherent v.s. coherent energy for 3 detector dummy on-source. Loudest event from previous figure observed here with $I_{null} > E_{null}$. The colour axis is the base-10 logarithm of the cluster's coherent energy (circenergy).	106
5.3	Thresholded tf-map from followup of highest significant event from the dummy on-source. Event can be seen as a glitch centred around 250 seconds. Other glitches can be seen with similar frequency distributions coming from Virgo detector noise.	107
5.4	Average spectrum over analysis time for each detector. Higher noise floor and numerous lines can be seen for Virgo in comparison to the two LIGO detectors.	108
5.5	Event rates for off-source and dummy on-source before and after cuts for 3 detector analysis. Events at higher significance after cuts can be attributed to autocorrelated glitches from Virgo data.	108
5.6	Event rates for off-source and dummy on-source before and after cuts for 2 detector analysis. Events before cuts will be dominated by glitches. Events after cuts show a sharper decrease in rate with increasing significance seen compared to the 3 detector closed box results in Figure 5.5	109
5.7	Event rates for off-source and on-source before and after cuts for 2 detector analysis. There are no on-source events after cuts emerging from the background at higher significance. This indicates that the on-source is comprised of only background events.	110
5.8	Coherent energies from on-source events (red) and off-source events (blue). Events with lower frequency tend to the diagonal of equal coherent and incoherent energies.	111
5.9	Distribution of alpha cut value with frequency. Events above red line indicate those which passed the cut. Higher frequency events more likely to survive the alpha cut.	112
5.10	Histogram of events surviving different cuts over central frequency. Alpha cut reduces the amount of events significantly more than the linear cut.	112
5.11	ADI-D injection waveform spectrogram. The profile of this waveform is an anti-chirp with a small bandwidth of 54 Hz and long duration of 142 seconds.	113
5.12	ADI-E injection waveform spectrogram. The profile of this waveform is an anti-chirp with a larger bandwidth of 149 Hz and a duration of 76 seconds.	114

5.13	Duration v.s. bandwidth for all recovered ADI-D injections. Duration has a linear relationship with bandwidth for this waveform.	115
5.14	Duration v.s. bandwidth for all recovered ADI-E injections. The distribution of recovered waveforms is split into two trends due to larger injection bandwidth.	115
5.15	Recovered duration with increasing distance to source for ADI-B injections.	116
5.16	Recovered duration with increasing distance to source for ADI-C injections.	116
5.17	Magnetar-F injection waveform spectrogram	117
5.18	Magnetar-G injection waveform spectrogram	117
5.19	Duration v.s. bandwidth for all Magnetar-F injections. The distribution of recovered waveforms is split into two trends due to the large bandwidth of the Magnetar-F injections.	118
5.20	Averaged duration per distance from source for Magnetar-F injections.	118
5.21	Sensitivity distances for recovery of astrophysical waveforms using X-SphRad. Larger bandwidth and duration of a waveform results in sensitivity at greater distances. Magnetar waveforms have lower intrinsic amplitudes than ADI waveforms meaning X-SphRad is only sensitive to them at shorter distances.	119
5.22	Bandwidth with increasing distance to source for Mono-A injections. Overestimate in bandwidth is associated with Fourier leakage.	120
5.23	Number of pixels with increasing injection scale for Quad-A waveforms. Due to Fourier leakage, the recovered pixels continue to increase when they should reach a plateau.	121
5.24	Sensitivity distance for ad-hoc waveforms at 50% and 90% detection efficiency. Although distance is not based on an astrophysical model, it still indicates how well waveforms are recovered in comparison with each other.	122
A.1	ADI-A: Fraction of recovered injections with higher significance than the loudest dummy on-source event.	125
A.2	ADI-B: Fraction of recovered injections with higher significance than the loudest dummy on-source event.	126
A.3	ADI-C: Fraction of recovered injections with higher significance than the loudest dummy on-source event.	126
A.4	ADI-D: Fraction of recovered injections with higher significance than the loudest dummy on-source event.	127
A.5	ADI-E: Fraction of recovered injections with higher significance than the loudest dummy on-source event.	127
A.6	Magnetar F: Fraction of recovered injections with higher significance than the loudest dummy on-source event.	128
A.7	Magnetar G: Fraction of recovered injections with higher significance than the loudest dummy on-source event.	128
A.8	Mono A: Fraction of recovered injections with higher significance than the loudest dummy on-source event.	129
A.9	Mono C: Fraction of recovered injections with higher significance than the loudest dummy on-source event.	129
A.10	Quad A: Fraction of recovered injections with higher significance than the loudest dummy on-source event.	130

A.11 Quad B : Fraction of recovered injections with higher significance than the loudest dummy on-source event.	130
A.12 SGA : Fraction of recovered injections with higher significance than the loudest dummy on-source event.	131
A.13 SGC : Fraction of recovered injections with higher significance than the loudest dummy on-source event.	131
A.14 WNBA : Fraction of recovered injections with higher significance than the loudest dummy on-source event.	132
A.15 WNBB : Fraction of recovered injections with higher significance than the loudest dummy on-source event.	132
A.16 WNBC : Fraction of recovered injections with higher significance than the loudest dummy on-source event.	133

List of Tables

2.1	Fraction of simulations that included a glitch (Average SNR = -10.3556 Noise = 50 fstart = 60Hz duration = 10s Nsims = 100). Glitches are much more likely to occur at lower τ and higher gain values.	34
2.2	Whitening cascade filter parameters	45
4.1	Top 10 dummy on-source events without line removal. Top four events are long duration events from excited violin mode.	100
4.2	Top 10 dummy on-source events with line removal. Fewer events seen with longer duration indicating line removal was successful.	101
5.1	Top 10 highest significance events from on-source surviving cuts. GPS time is with respect to the Hanford detector. From Figure 5.7 these can be attributed to background events.	111
5.2	Properties of injected astrophysical waveforms	113
5.3	Properties of injected ad-hoc waveforms	119

List of Abbreviations

ADI	Accretion Disk Instability
CBC	Compact Binary Coalescence
DFT	Discrete Fourier Transform
ESD	Electrostatic Static Drive
ETM	End Test Mass
FWHM	Full Width Half Maximum
GRB	Gamma Ray Burst
HOM	Higher Order Mode
IIR	Infinite Impulse Response
ITM	Input Test Mass
LPEF	Linear Predictive Error Filter
OMC	Output Mode Cleaner
PI	Parametric Instability
QPD	Quadrant Photo Diode
RMS	Root Mean Square
ROC	Radius Of Curvature
VCO	Voltage Controlled Oscillator

Chapter 1

Gravitational waves

The detection of gravitational waves (GW) has been a challenging concept since their prediction over 100 years ago. Detectors sensitive enough to measure these extremely weak signals were not developed until very recently and the proposal to to begin development on them was met with scepticism. The development effort and conviction to the theory have been justified with the recent GW events detected by the LIGO interferometers.

In this chapter we describe the events leading to the first GW detection starting with their initial prediction by Einstein. We then outline the theory of GW as an outcome from General Relativity as well as a summary of the LIGO interferometers used to detect them. The historical review of gravitational wave science is taken from [22].

1.1 Introduction

The theory of general relativity describes the interaction between mass and space time. Spacetime is the medium that allows anything with mass to interact with each other. This is described well by paraphrasing John Wheeler, "Spacetime tells matter how to move, and matter tells spacetime how to curve". The theory has been backed up by some landmark experimental results including the observation of the bending of starlight by the Sun during the eclipse [28] and the observation of a time delay between radar pulses to the inner terrestrial planets caused by again the mass of the Sun [66]. Observations like these definitively prove that mass and energy are bound by the laws governed by general relativity.

A more subtle outcome from general relativity is the existence of gravitational waves. These are ripples in space-time caused by the interaction of massive objects. A good analogy for this is that of the surface of a vast ocean. In the same way that waves in the ocean distort it's surface, space-time is deformed by gravitational waves. Predominantly this perturbation of the ocean's surface is made up of background noise from sources either too weak or too far away to be isolated to a single source. However if we have an extremely violent event which is close enough to the observer on the ocean surface it can rise above this noise.

The theory of gravitational waves was originally described by Einstein in 1916 a year after the General Theory of Relativity was published. The paper [6] shows how gravitational waves can be derived from the field equations from general relativity. It is also shown in that the source for such waves would be from a time dependent quadrupole moment and that they would travel at the speed of light. Although three forms of the waves were discussed, it was argued that they would only carry energy

in their transverse-transverse form. This original paper did have some problems so it wasn't until 1918 when the corrected version "On Gravitational waves" [7] was published.

Another 18 years later Einstein contradicted himself again on the subject of gravitational waves. This time he claimed that they could not exist and he submitted a paper to Physical Review with Nathan Rosen arguing against his previous theory. A referee report was then sent to Einstein which contained crucial criticism of the work in the paper. After receiving the report Einstein reacted in a rather extreme fashion. Previously the journals that he had submitted to in the past had not reviewed his work before publishing. He replied to the U.S.-based journal saying how he had not authorized the paper to be seen by any other specialists in the field. He then withdrew the paper from Physical Review and never published with them again. The paper was then submitted and subsequently published in the Journal of the Franklin Institute.

The reviewer has more recently been discovered to be H. P. Robertson subsequently went to visit Einstein's new assistant Leopold Infeld. Robertson expressed his criticisms of the paper with Infeld and agreement was met between the two about its outcomes. The thoughts were then passed onto Einstein who had also discovered similar problems. A revised version of the paper was written which proved how gravitational waves could exist within a cylindrical coordinate system known as the Einstein-Rosen metric. Despite this Rosen who had since moved to Russia still had doubts about this revision. He had not been aware of the revised publication until he saw it in a newspaper clipping. He continued to argue for the case that they did not exist in several papers after this.

This skepticism of the existence of GWs continued for several years but was brought back into focus during the Berne and Chapel Hill conferences in the mid 1950s. During the Berne conference in 1955, Felix Pirani introduced the geodesic deviation equation which is the gravitational version of the Lorentz force from electromagnetism. This provided a new way of describing how a GW would affect the way that particles moved with respect to each other. At the Chapel Hill conference in 1957, the way in which gravitational waves could transfer energy was described in an idea which was simple to understand. This was described by Herman Bondi and Richard Feynman as the "sticky bead argument". The argument concerned two masses one being the stick A and the other being a bead B which was threaded through A. If a gravitational wave is subject to this structure the bead would rub against the stick due to their relative motion. This motion is due to the quadrupole moment of the GW and that the stick would have a greater reaction force compared to the beads. In turn this would cause heat and hence the gravitational wave has introduced energy to the system that would not have existed otherwise.

The first method of detecting gravitational waves was introduced by Weber in 1966. His experiment was a so-called bar detector which could be used to measure gravitational waves from astrophysical sources. A 1.5 ton bar was suspended in vacuum was the centre of the experiment. Quartz transducers were used to convert the mechanical strain of the bar into a voltage readout. The bar was particularly sensitive to signals of frequency close to the resonant frequency of its compressional mode. By experimenting with how the detector's noise varied with thermal fluctuations indicated that its strain sensitivity was a few parts in 10^{16} [76]. This sensitivity had never been achieved before and made the task of detecting a gravitational wave signal more realistic than previously thought. Weber claimed to observe a coincident

signal from two of these detectors separated over 1000km in 1970 [75]. In the paper Weber optimistically stated that a large anisotropy "exceeding 6 standard deviations" from the detector and that the location of the peaks indicated that it was coming from the galactic centre. Due to this surprising result many other groups took to building their own bar detectors. Many of these groups ended up publishing null results for their experiments [38, 74, 27, 13] which put Weber's original detection into doubt. It seemed that the idea of detecting gravitational waves had become more tangible but the sensitivity needed to detect them was still far off.

Indirect evidence of gravitational waves was observed by Hulse and Taylor in the binary pulsar PSR1913+16. After discovering the binary system in 1974, they produced a paper in 1978 where they observed a decrease in the orbital period of the binary system [69, 70]. The rate of change of the orbital period was shown to decrease corresponding to the model from general relativity. Specifically this indicated that the system had been radiating energy in the form of gravitational waves. This was very exciting at the time as this was the first real indication that gravitational waves had energy and could be observed from astrophysical events. After observing the system for 30 years this gave even more promising results in favour of gravitational waves. In the paper in 2010 they observed the orbital period as " 0.997 ± 0.002 times that predicted as a result of gravitational radiation damping in general relativity" [77].

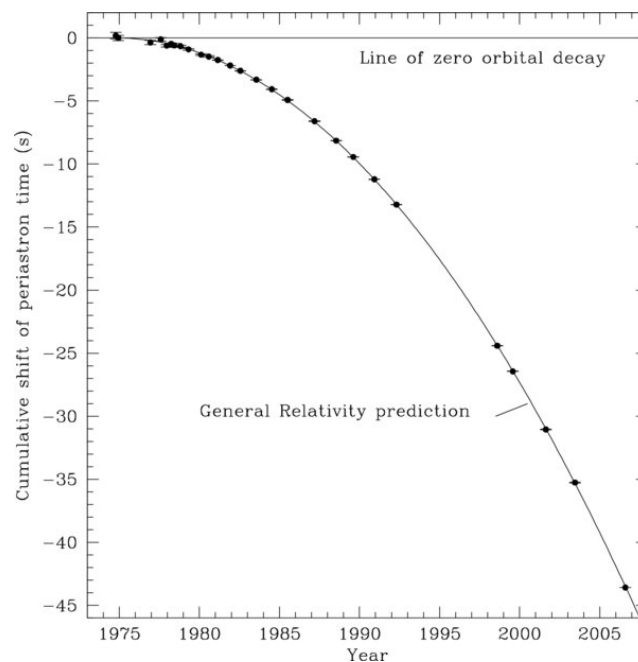


FIGURE 1.1: Orbital decay of binary pulsar system PSR1913+16. Measurements agree with decay predicted from general relativity [77].

Due to the null results of the Weber bar experiments the GW community needed to pursue more sensitive detectors. One such idea was that of a cryogenic resonator, where the original bar detector was reduced in temperature to effectively increase the quality factor of the resonator. Another detector discussed was the laser interferometer developed from the Michelson-Morley interferometer. Although the idea had been discussed previously, the first laser interferometer built for the purposes of GW detection was built by one of Weber's colleagues Robert Forward in 1972 [57].

This California-based detector collected data in collaboration with several bar detectors from Maryland, Glasgow and Frascati for a period of 150 hours and found no coincident events [34]. Despite the fact that Forward built this first detector the credit for inventing what are now known as the LIGO detectors is now credited to Rainer Weiss. Weiss wrote a document in 1972 commonly known as the Weiss RLE report [79] which describes the proposed antennae design as well as a thorough discussion of the possible noise sources such a detector would have. The report also contained a detailed comparison between laser interferometers and Weber bars concluding that the laser interferometers would have a SNR 10^4 greater than that of the Weber bars.

Weiss managed to convince the group at Caltech via Kipp Thorne that interferometers were the new future of gravitational wave detection. A big contribution to this was due to Ronald Drever from Glasgow University. He had been working on a 10 m interferometer in Glasgow during the 1970s but came over to Caltech during the 1980s to work on the 40 m interferometer. This became the prototype for what are now known as the LIGO detectors and was used to develop the technology required. The NSF funded the construction of the Caltech 40 m prototype as well as the 1.5 m prototype at MIT. Funding for these experiments came due to a successful proposal by Weiss in 1983 [78] which also allowed Weiss to continue studying the requirements for a 10 km interferometer.

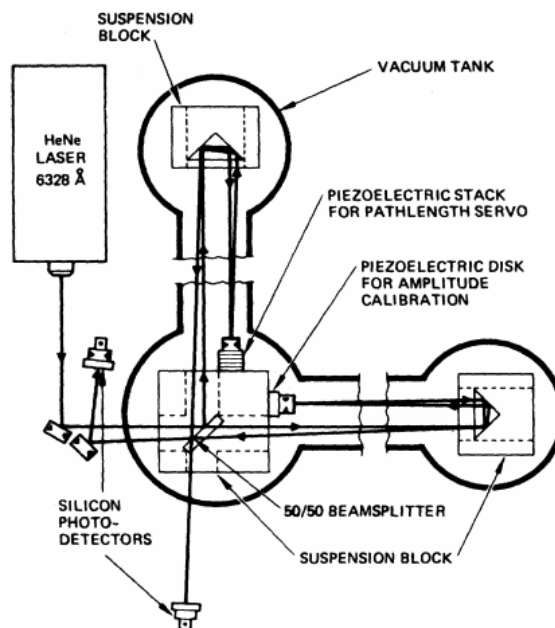


FIGURE 1.2: Schematic of first interferometer used as a GW detector [35].

This was the beginning of MIT and Caltech's endeavour to get the larger scale interferometers (LIGO) funded. LIGO was met by fierce opposition from scientists who received funding from the NSF. LIGO would be the most the NSF ever invested in one single experiment and NSF funded scientists were concerned that they would have their funding reduced due to this. The astronomical community were also opposed to LIGO since it was a self proclaimed observatory. Although GW had been indicated from theory and indirectly observed by from PSR1913+16, astronomers

believed that this was not enough to call it an observatory. By using this term they were claiming they would definitely observe an event, when the best predictions of its capability of observing were very small. This would not be enough to justify its huge budget which could have been spent on telescopes which were more justifiable in what they could observe.

Despite this opposition LIGO began its construction in the mid 1990s supported by the NSF and led by Barry Barish [4]. Barish also led the effort to organise the LIGO Scientific collaboration (LSC) which employed the efforts of institutions outside of Caltech and MIT. The LSC is now a worldwide collaboration with around 1000 scientists involved in 15 institutions. During the early 2000s the initial LIGO detectors became operational and began improving their sensitivity. In 2009 initial-LIGO had improved their strain sensitivity to smaller than one part in 10^{21} [11]. Sensitivity was again improved by enhanced-LIGO to 2×10^{-22} which upgraded the laser sources and readout systems [8, 37]. LIGO in collaboration with Virgo the Italian based interferometer, collected observational data from 2002 to 2011. Although no observations were made during this period, upper limits to various astrophysical sources were made [11, 23]. Advanced LIGO came online in 2015 with a sensitivity a factor of 10 better than Initial LIGO. "Higher laser power, larger test masses and improved mirror coatings lead to the improved sensitivity at mid and high frequencies." [8] aLIGO was now the most sensitive gravitational wave detector ever built and predicted to detect 40 binary-neutron star events per year.

The first gravitational wave signal was detected in 2015 from a binary black hole inspiral. The signal strength was much larger than the sensitivity of the aLIGO detectors with a peak strain of 1×10^{-21} . This incredibly loud signal produced a false alarm rate of 1 in 203,000 years which is equivalent to a significance greater than 5.1σ [12]. Undeniably very obvious detection marked the first direct observation of a gravitational signal wave signal. As well as this it was the first observation of a binary black hole merger. This would not have been possible to be seen in the electromagnetic spectrum making it a unique method of detecting these astrophysical events.

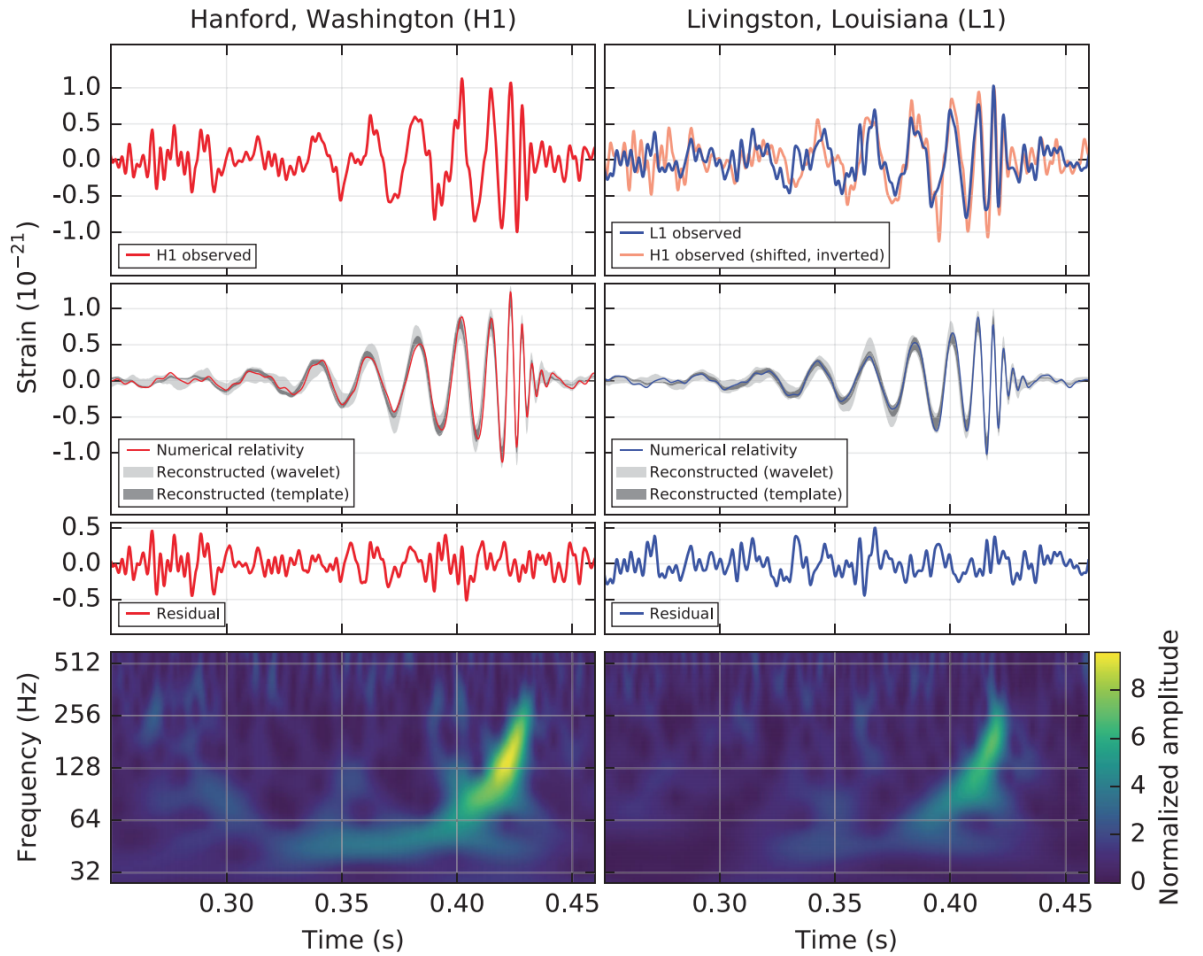


FIGURE 1.3: Gravitational wave signal from binary black-hole inspiral measured by aLIGO detectors [12]

1.2 Gravitational wave theory

Gravitational wave sources are an outcome from the theory of general relativity. Spacetime in this theory can be described as a four-dimensional manifold which defines the interaction between mass and energy. In this section we derive the solution for gravitational waves as a perturbation from flat spacetime following the treatment given in Schutz [65].

The curvature of space-time is defined by the symmetric 4 dimensional tensor known as the metric. The metric acts as a rotation matrix which dictates the trajectory of matter and energy contained within a region of space-time. Massive objects contained within a space-time region distort the local metric creating curvature. The motion of any freely moving particle within a space-time region follows a geodesic which is dependent on the curvature of that region. For a flat space-time the Minkowski metric is used to predict the motion of massive objects.

$$(g_{\mu\nu}) = (\eta_{\mu\nu}) = \begin{bmatrix} -1 & 0 & 0 & 0 \\ 0 & 1 & 0 & 0 \\ 0 & 0 & 1 & 0 \\ 0 & 0 & 0 & 1 \end{bmatrix} \quad (1.1)$$

This flat metric is the metric for space-time in the absence of other massive objects. Waves in this medium can be explained by a perturbation of this metric.

$$g_{\mu\nu} = \eta_{\mu\nu} + h_{\mu\nu} \quad (1.2)$$

The last component in this equation is the perturbation of the metric and $|h_{\mu\nu}| \ll 1$. For small changes in coordinates we can express the coordinate transform as,

$$x^{\alpha'} = x^\alpha + \xi^\alpha(x^\beta) \quad (1.3)$$

This expression introduces a transformation that doesn't alter Equation (1.2). From the Einstein field equations it is possible to alter the gauge while remaining in the Lorentz class of gauges if the vector satisfies,

$$\left(-\frac{\partial^2}{\partial t^2} + \nabla^2 \right) \xi_\alpha = 0 \quad (1.4)$$

This can be expressed in terms of a plane wave solution.

$$\xi_\alpha = B_\alpha \exp(ik_\mu x^\mu) \quad (1.5)$$

The metric perturbation term in equation (1.2) can now be expressed in terms of this transformation vector,

$$h_{\alpha\beta}^{(\text{NEW})} = h_{\alpha\beta}^{(\text{OLD})} + \xi_{\alpha,\beta} + \xi_{\beta,\alpha} \quad (1.6)$$

This is usually expressed in terms of the trace-reversed metric so as to reduce the number of terms in the Einstein equation. The trace-reversed metric is defined as,

$$\bar{h}_{\alpha\beta} = h_{\alpha\beta} - \frac{1}{2}\eta_{\alpha\beta}h \quad (1.7)$$

Again this can be expressed in terms of the transformation vector,

$$\bar{h}_{\alpha\beta}^{(\text{NEW})} = \bar{h}_{\alpha\beta}^{(\text{OLD})} - \xi_{\alpha,\beta} - \xi_{\beta,\alpha} + \eta_{\alpha\beta}\xi_{,\mu}^\mu \quad (1.8)$$

Equation (1.5) can be inserted into the previous equation. The exponentials are then divided throughout to give the expression,

$$A_{\alpha\beta}^{(\text{NEW})} = A_{\alpha\beta}^{(\text{OLD})} - iB_\alpha k_\beta - iB_\beta k_\alpha + i\eta_{\alpha\beta}B^\mu k_\mu \quad (1.9)$$

Another choice of gauge is applied here known as the transverse-traceless gauge. Transverse refers to the fact that the waves are predicted to follow a single spatial

direction i.e. $A_{\alpha\beta}$ only has non-zero terms in the two orthogonal components to the direction of propagation. i.e.

$$A_{\alpha z} = 0 \quad \text{for all } \alpha \quad (1.10)$$

The traceless part refers to,

$$\eta^{\alpha\beta} A_{\alpha\beta} = 0 \quad (1.11)$$

$$A_{\alpha t} = 0 \quad \text{for all } \alpha \quad (1.12)$$

From this a matrix can be constructed with significantly fewer elements than if we had not applied this choice of gauge.

$$A_{\alpha\beta}^{\text{TT}} = \begin{bmatrix} 0 & 0 & 0 & 0 \\ 0 & A_{xx} & A_{xy} & 0 \\ 0 & A_{xy} & A_{yy} & 0 \\ 0 & 0 & 0 & 0 \end{bmatrix} \quad (1.13)$$

As can be seen from this, there are only four elements that are then attributed to the motion of the gravitational wave. This results in quadrupole type distortions to the local metric. The effect of this can be considered through the motion of two test particles separated by a distance $x = l, y = z = 0$.

$$D_{\text{proper}} = \int |g_{\mu\nu} dx^\mu dx^\nu|^{\frac{1}{2}} = \int_0^l |g_{xx}|^{\frac{1}{2}} dx \quad (1.14)$$

Taking the metric component at $x = 0$ and then expanding via a first order Taylor series gives,

$$g_{xx}|_{x=0} = \eta_{xx} + h_{xx}^{\text{TT}}|_{x=0} \quad (1.15)$$

$$D_{\text{proper}} \approx l \cdot \left[1 + \frac{1}{2} h_{xx}(x=0) \right] \quad (1.16)$$

So the proper distance between the two particles is altered by the perturbation h_{xx}^{TT} . This motion can be characterised by the strain equation.

$$\frac{\delta l}{l} = \frac{1}{2} h_{xx} \quad (1.17)$$

Strain is what is predominantly used as the measure of the gravitational wave. It measures the variation in the distance between two objects compared to it's original length.

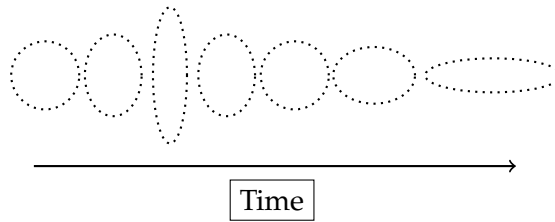


FIGURE 1.4: Exaggerated effect of plus-polarised quadrupolar gravitational wave on a circle of masses

The character of the metric perturbation is that of a quadrupole. There are two polarisations of this known as the plus (+) and cross (\times). If there is for example a circular ring of particles, the effect of either of these polarisations would be to distort the ring into an ellipse with the same area as the circle. This distortion oscillates with time as the perturbation has a plane wave solution. For example, a plus-polarised wave travelling in the z -direction would have oscillations in the x and y directions. As the x -direction diameter increases the y -direction length decreases and vice versa. This 90° distortion in length makes a Michelson type interferometer an obvious method for the measurement of this type of signal.

1.3 Sources of gravitational waves

Gravitational waves are predicted to have very weak signal strength compared to the background. For this reason sources of gravitational waves are astrophysical events from high density objects in order to be detected by LIGO.

1.3.1 Compact Binary Coalescence

Compact Binary Coalescence (CBC) are one of the more notable sources of gravitational radiation as they have distinct signal waveform. Examples of these compact objects include neutron star, stellar mass black hole, and white dwarf binary systems. As the two compact objects orbit each other they are predicted to be constantly emitting gravitational radiation. This in turn causes the system to inspiral where the orbital period of the system decreases as the semi-major-axis of the orbit also decreases. Eventually the two objects coalesce releasing a distinct signal known as a "chirp". CBC events have been detected by the LIGO interferometers during the O1 and O2 observation run. Several Binary Black Hole (BBH) events have been observed [12],[9] as well as a Binary Neutron Star (BNS) coalescence [10]. The BNS event is particularly of note since it was also observed by Virgo interferometer and an Electromagnetic (EM) counterpart signal was detected by the Fermi-GBM telescope.

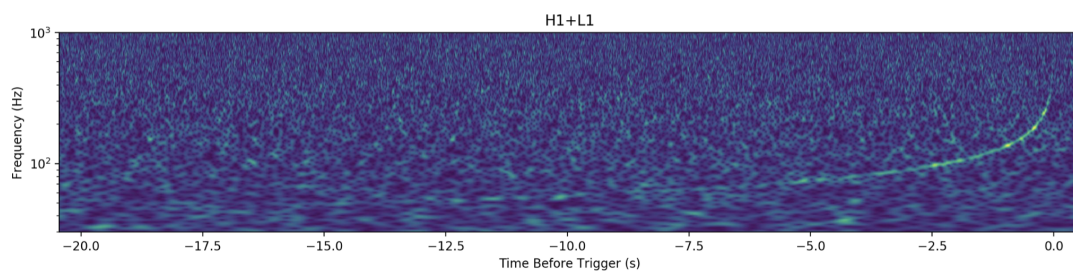


FIGURE 1.5: Spectrogram of BNS event [10] from LIGO detectors. Chirp signal increases in frequency over time as the binary system coalesces.

1.3.2 Burst Signals

Contrary to CBC waveforms, burst type signals are not accurately modelled. There are many different possible sources of these events which again require high energy mechanisms in order to produce a signal high enough for detection. Shorter duration events may come from gamma ray bursts from the gravitational collapse of highly evolved stars or from core collapse supernovae from an accreting white dwarf [64]. Longer duration burst signals may come from core collapse supernovae or long gamma-ray bursts (GRB) [5].

Modelled long duration sources also exist which are used for injections discussed in Chapter 5 however they are not as accurately constrained as the CBC waveforms. Accretion disk instabilities (ADI) are theorised to produce GW emission [61]. GW signals from ADI are created by accretion disks around Kerr black holes with an asymmetric torus of mass. This produces an anti-chirp waveform characterised by the parameters of the system such as the mass of the black hole. GW emission may also be produced by post merger neutron stars with toroidal magnetic fields [25]. These sources produce an anti-chirp waveform although at a much lower intrinsic amplitude compared to ADI.

1.3.3 Continuous Sources

Continuous wave sources (CW) produce a long lasting signal at a fixed frequency. This means that they have a far more well defined signal (i.e. a sinusoid) however analysis of them becomes more difficult when corrections due to Doppler modulation from the source and the Earth's motion become involved [64]. One proposed source of continuous signals is thought to be rapidly rotating neutron stars in our own galaxy [73]. Sources like this should supply long term signals lasting from months to years [29]. The price for this longevity is that the signal strength is very weak compared with burst signals. A measurement of the gravitational wave signal of these combined with the electromagnetic counterpart would provide abundant possibilities for further astrophysical research. For this reason combined with the fact that it would be unlikely to find such sources through interferometric methods alone means that the search for them at LIGO has been focused on known pulsars with well defined timings and other known sources [73].

1.3.4 Stochastic Gravitational Wave Background

The background gravitational wave signal is thought to come from sources that are too weak to be resolved individually. In a similar way to the cosmic microwave background, a component of the gravitational wave background may come from cosmological sources such as inflation. A significant contribution may also come from compact binary coalescences, neutron stars and supernovae. This search will look at very long signals in the time domain lasting between hours and weeks [73]. The detection of a gravitational wave background would provide a significant opportunity for testing models of cosmology. Since normal matter has a very low gravitational opacity, gravitational waves are not scattered in the same way as electromagnetic light [39]. This means that the stochastic gravitational wave background could be measured even further back in time than the cosmic microwave background (CMBR).

However this requires the detector to be sensitive enough to detect it which poses a significant challenge.

1.4 Interferometer Design

The LIGO experiment is designed to measure quadrupolar gravitational perturbations as described in the previous section. Currently there are two detectors built in the US and another planned for construction in India. The design of the detector is similar to that of a Michelson interferometer but significantly more enhanced. To begin with the arms of the interferometer are each 4 km in length. In order to keep this huge system in resonance multiple mirrors with various different outputs are required. This requires even more effort to stabilize each of the subsystems in the detector. Each arm also contains a resonant cavity which is used to improve the chances of detection. In the newest generation (aLIGO) the strain sensitivity is estimated to increase by a factor of 10 compared to Initial LIGO [8] which should increase the volume of the universe visible to the detector by 3 orders of magnitude. This has been achieved by the quantum physics of both the light and mirror motion being coupled to one another [36]. Other improvements like this have made the current LIGO interferometers the most sensitive gravitational wave detectors to date.

1.4.1 Interferometry using Fabry-Perot Cavities

The design of the LIGO detectors is that of a Michelson interferometer. In this system light is produced from the pre-stabilized laser source (PSL) at 1064 nm and is normally incident on the 50:50 beam splitter. This splits the beam in half producing one transmitting and one reflecting beam. The orthogonal beams are then passed through the inner mirrors (ITM) and then reflected off the end mirrors (ETM). At this point the beams have entered the Fabry-Perot cavities where they continue to bounce back and forth between the ITM and ETM. By doing this the effective power of the laser is increased. These are also used to increase the interaction time with the gravitational wave signal. When light enters the cavity it is reflected back and forth several times before it again passes through the central beam splitter. If the storage time of the light in the arm cavity is half the period of the gravitational wave signal it would supply all the information necessary to make a detection [47] The two beams then recombine at the beamsplitter and are reflected towards the output photodiode. At this point if there has been no changes in the phase of either of the beams, the two should be completely out of phase with each other so no signal should be measured hence why the output is referred to as the darkport. Signal oscillations at the dark port can come from noise sources such as seismic, thermal and shot noise. More importantly this is where a gravitational wave signal is measured as the phase shift in the arms is altered in the same way as described in Figure 1.4. This is measured as a differential arm length (DARM) i.e. the difference in the length of the two interferometer arms.

1.4.2 Use of sidebands

Sidebands are an essential feature in the signal used in the interferometer and are used for two reasons. Firstly radio frequency (RF) sidebands are used for controlling the interferometer and signal sidebands as a carrier of the gravitational wave signal and noise in the detector. Sidebands are created by phase modulating the input signal. For example [36] if we have an input field with frequency ω_0 it can be represented by,

$$E_{\text{in}} = E_0 \exp(i\omega_0 t) \quad (1.18)$$

If this signal is then modulated by some frequency Ω then it is described by,

$$E = E_0 \exp(i(\omega_0 t + m \cos(\Omega t))) \quad (1.19)$$

The modulation index m is a reference to how much power is distributed to the signal sidebands compared to the carrier frequency. This can be reexpressed in terms of a Bessel function J_k ,

$$E = E_0 \exp(i\omega_0 t) \sum_{k=-\infty}^{\infty} i^k J_k(m) \exp(ik\Omega t) \quad (1.20)$$

By doing a first order approximation of this we arrive at,

$$E = E_0 \exp(i\omega_0 t) \left(1 + i \frac{m}{2} (\exp(-i\Omega t) + \exp(i\Omega t)) \right) \quad (1.21)$$

Clearly from this expression it can be seen that with phase modulation, sidebands are created above and below the frequency of the input field ω_0 . Sidebands are controlled by an electro-optical modulators (EOM) which are positioned before the beam is incident on the beamsplitter.

1.4.3 Advanced LIGO

The newest generation of the LIGO experiment is Advanced LIGO which has made several additions in order to improve strain sensitivity. Improvements include better seismic isolation and test mass suspensions which reduce the noise at lower frequencies and higher laser power which improves sensitivity at mid to high frequencies. One feature in the design of the Advanced LIGO detector is the addition of power and signal recycling mirrors. The power recycling mirror introduced during initial LIGO [11] PRM increases the effective power of the laser input before the beam reaches the beamsplitter. Light that is normally wasted by reflection back towards the laser source is now recycled back into the interferometer. This essentially turns the interferometer into a resonant cavity and can be tuned by adjusting the positions of the optics [8]. By increasing the effective laser power the signal to noise ratio in the detector is also increased.

The more recent inclusion of signal recycling mirrors. These are positioned at the output from the beamsplitter. As mentioned before if the interferometer is set up correctly and there are no changes to the arm length, there should be no signal measured at the output. The central laser frequency is resonant in the power recycling cavity but the sidebands are resonant in the signal recycling mirrors. Resonant sideband signals are then reflected back into the interferometer and are tuned by the

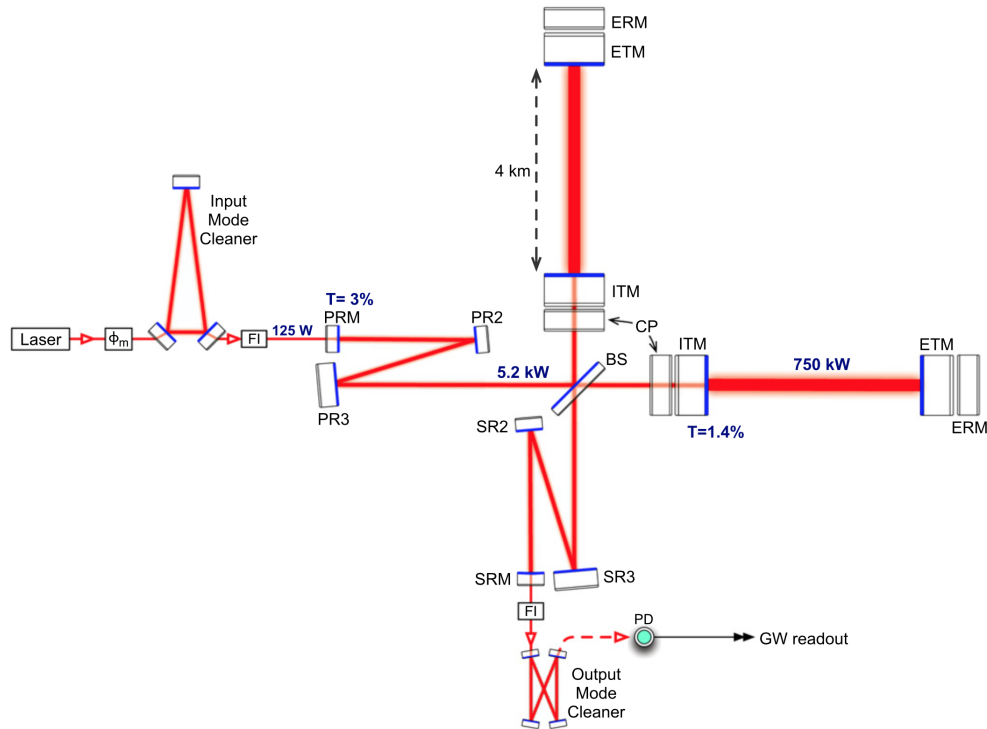


FIGURE 1.6: Design of Advanced LIGO detector [8]. Several additions including input and output mode cleaners improves the detector sensitivity.

positions of the mirrors in the signal recycling cavity. By doing this the sidebands induced by a gravitational wave signal can be added coherently to the recycled sidebands from the laser signal [53]. This increases the signal strength by the number of bounces the beam makes in the cavity.

The new detector also includes the input mode cleaner (IMC) and the output mode cleaner (OMC). The input mode cleaner is used for a few reasons. Firstly it spatially filters the laser before it enters the interferometer which allows the fundamental Gaussian mode and higher order spatial modes to be simultaneously resonant in the cavity. It also filters the polarisation of the beam and provides an in-vacuum, suspended, frequency reference for the laser at higher frequencies [58]. The OMC is used to filter out all RF sideband and higher order spatial mode light by the time the beam reaches the darkport. This means that only signals induced by a gravitational wave should be measured by the main photodetectors. [8].

One of the main focuses on with the new detector is being able to get into into a locked state. A lock is where all of the cavities in the detector are simultaneously resonant and the interferometer is at it's operating point. An initial lock is achieved using the third-harmonic technique [15] but is also controlled using the arm length stabilization (ALS) system [8]. Using ALS each of the arm cavities are individually locked by separate lasers positioned behind each ETM. Both of these lasers operate at a wavelength of 532 nm (half the wavelength of the PSL) which enables them to be distinguished from the main laser. The ALS beams are interfered with each other and also the main laser at the beamsplitter. By interfering with each other they produce a differential mode signal which is used to stabilize the the DARM signal. Interference with the main laser produces a common mode signal which is used to

control the main laser frequency.

The detection of the actual gravitational wave signal is done by a method known as DC readout. This method involves using a local oscillator to slightly offset the arm cavities from resonance [14]. This allows for a detection of a gravitational wave carrier signal to be made directly, while allowing the detector to remain almost in resonance at the dark fringe. Using the DC offset method is much simpler than the previous method known as Pound-Drever-Hall. In this method a local oscillator is used to create an RF signal by interfering with the sidebands induced by the gravitational wave signal. The signal from the output photodiode is then demodulated at the RF frequency. DC readout also allows for the future improvement of using squeezed light in the signal readout. Squeezed light can be used to reduce quantum noise without having to increase the laser power [52][51].

Chapter 2

Signal processing with iWave

2.1 Introduction

One of the main characteristics of the strain data from LIGO detectors are the numerous lines can be seen in it's spectrum. Most of these come from known sources in the detector and are problematic to remove when searching the data for GW signals. It can be difficult to identify a signal if it sweeps through the frequency bands of these lines. The data that is used for searches is usually cleaned using filtering of some kind which whitens the data, removing the lines and leaving behind only normalized background noise [21]. Filtering in this way can often be quite aggressive with the data leaving sections of the spectrum which used to contain lines with 'holes' or gaps in the spectrum. An alternative method is to remove lines using the line-tracking filter iWave. As this suggests the filter can be used to track the properties of a line using a feedback loop and then subtract it from the data. iWave can be applied not only to sinusoids with static frequency, but also to sinusoids that have frequency which wanders unpredictably over time. This is often the case with the lines in LIGO detectors as they come from sources such as resonances in the fibre suspensions known as violin modes.

In this chapter the iWave filter will be discussed as a method for tracking lines. Firstly the theory of the filter will be introduced with examples of how it can be applied to data. We will then discuss a method for using this filter to remove lines from a set of data from the GW150914 event.

The work in this chapter is developed from the work of my supervisor Ed Daw on the line tracking filter iWave. I contributed to the development of this filter by testing and modelling the filter properties on simulated data and data from the LIGO detectors. I was also responsible for developing and implementing the recursive line removal algorithm used to filter data from the LIGO detectors.

2.2 Motivation and overview

iWave is an IIR filter which can return attributes such as frequency and amplitude information from a sinusoidal line in a given input set of broadband data. This is an alternative method of identifying these parameters from the more dominantly used Fourier analysis. For a digital set of data $x[j]$ a Discrete Fourier Transform or DFT can be used to return the amplitude as a function of frequency.

$$X[k] = \sum_{j=0}^{N-1} x[j] \exp^{-2\pi i k j / N} \quad (2.1)$$

$X[k]$ defines the amplitude at a given $k2\pi$ frequency of the set of data $x[j]$ with N samples.

The number of samples and the sampling rate have a direct correlation to our resolution in the frequency domain. The Nyquist limit $f_{Nq} = f_{SR}/2$ is the maximum frequency that can be measured from a data set. To calculate a Fourier transform requires a length of the time used is given by $dt = N/f_{SR}$. By the uncertainty principle the frequency resolution of the Fourier series is given by $df = 1/dt$. For shorter sets of data (smaller N) our frequency resolution decreases, whereas for longer data sets (larger N) the frequency resolution increases.

For a signal with a static frequency using a DFT is an obvious way to measure it's frequency. However this may not always be the case for other signals that do not remain at a constant frequency. By taking a Fourier transform the amplitude is averaged over the frequency band it is contained in.

Fourier analysis can however be used to create a spectrogram or time-frequency map. This is a series of Fourier transforms taken over the duration of the data, dividing it into chunks. This array of chunks together forms a 3 dimensional array with time in the x -axis, frequency in the y -axis and amplitude in the z -axis. While this gives a representation of a given set of data, information about frequency and amplitude evolution is limited by our choice of chunk length. Information about the signal will only be available for those periods represented in these chunks.

This leads us to the main advantage of the iWave filter which is that it works purely in the time domain. For a given set of input broadband data, iWave filters the data around the line and outputs information about the signal such as frequency and amplitude at the the same sampling rate as the input data. Rather than the average distribution in frequency of the data over a chunk of time, we have a sample by sample measurement of a signals attributes.

The filter is still limited in how well it can track a signal by the properties of the signal. Firstly if the signal is weak compared to background noise the tracker may not be able to lock onto it. Similarly if there is more than one signal in the data the filter can only lock onto the one which is closest in frequency to it's starting frequency. Lastly if a signal varies too quickly in frequency (i.e. if df/dt is too large) the tracker may not be able to remain locked onto it. Some of these drawbacks can be mitigated by using a bandpass filter around the range of the targeted signal. This limits the influence of the rest of the spectrum on the filter and focuses it on a particular frequency band.

Usually signals will vary in SNR and df/dt for different cases so the parameters of the filter require tuning. The main parameters used for tuning are the response time τ and the gain. The parameter τ can be tuned higher if the signal is fairly static. This in turn decreases the frequency band of the filter which then reduces the amount of background noise in the filtered signal. However for the case where the frequency of a signal is more time dependent, decreasing τ allows the tracker to measure the signal's frequency over time to a greater accuracy. Consequently this will increase the bandwidth of the filter, increasing the amount of background noise in the output signal.

2.3 Theory of the iWave filter

There are two states which iWave can be used to filter data. Firstly the open loop state in which the filter maintains a constant frequency band and secondly the closed loop state where the frequency band is servoed to follow the frequency of a signal. Both of these states are discussed in the following sections. The theory described here is taken from work by Ed Daw which is yet to be published [26].

2.3.1 Open loop state

To describe the iwave filter we must first look at its open loop arrangement. In this case only the amplitude is estimated and with a single resonant filter on a constant frequency band. Consider the half range Z-transform of a set of discrete data sampled at a period of τ_s .

$$z_0(\Sigma) = \sum_{n=-\infty}^0 x_n e^{n\Sigma} \quad (2.2)$$

This is similar to the expression for the DFT expressed in Equation 2.1 however this expression sums the previous values of the series and includes some extra terms. The term Σ here is related to the complex phase of the signal $\Sigma = w - j\Delta$. The phase shift per sample is taken from the imaginary part of Σ which is $\Delta = 2\pi f\tau_s$. The real part of w corresponds to the weighting factor of the transform which is related to the response time τ of the filter by $w = \tau_s/\tau$. Samples which occurred $\tau = \tau_s/w$ previously to the present sample will be weighted $1/e$ compared to the most recent sample. This transform will have a bandwidth with full width half maximum of $\Gamma = w/\pi\tau_s$ at $f = \Delta/2\pi\tau_s$.

The Z-transform can be considered as a filter by looking at it in terms of a recursion relation.

$$y_n = x_n + e^{-\Sigma} y_{n-1} \quad (2.3)$$

In Equation 2.3 the output term y_n is related to the input term x_n and the previous output term y_{n-1} . To avoid this equation diverging with increasing n the input term is scaled by $(1 - e^{-w})$.

$$y_n = (1 - e^{-w})x_n + e^{-w} e^{j\Delta} y_{n-1} \quad (2.4)$$

The I and Q phase outputs are the real and complex outputs from Equation 2.4. These correspond to the in phase (I-phase) and quadrature phase (Q-phase) oscillator signals where Q-phase leads the I-phase by 90° . Figure 2.1 shows the two orthogonal state outputs from iWave after tracking a 60Hz static sinusoid with unit amplitude using a τ value of 1.

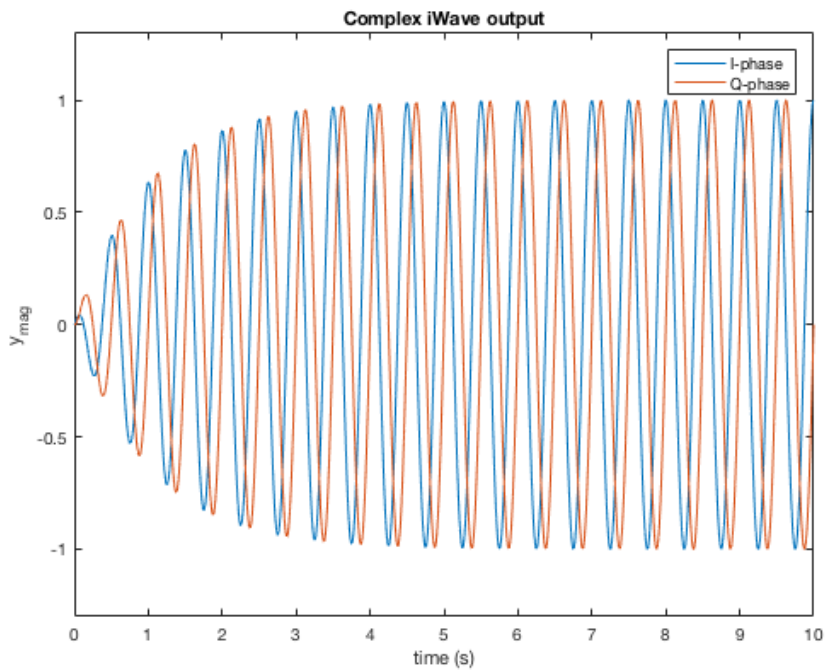


FIGURE 2.1: Orthogonal state outputs from static iWave tracking. Both states converge to the input signals amplitude but the Q-phase leads the I-phase by 90° .

Figure 2.2 shows how these I and Q phase outputs can be used to calculate the magnitude of this complex output i.e. $A = \sqrt{I^2 + Q^2}$.

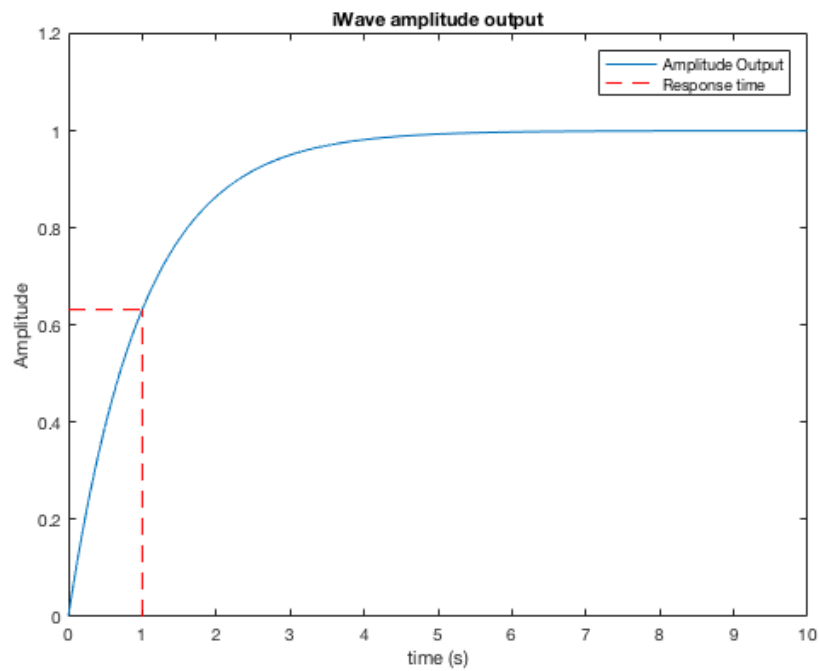


FIGURE 2.2: Amplitude output from static iWave tracking. Amplitude converges to the input signal value exponentially with response time equal to τ .

The trend of this data is expectedly an exponential average where the output from the filter converges on the amplitude of the line. From this plot it can be seen that the response time τ is the time it would take the output signal to reach $A(1 - 1/e)$ where A is the amplitude of the input signal.

Rotation of iWave complex output

Plotting the complex output y from Equation 2.4 it can be seen that once the filter reaches a steady state it has an elliptical shape in the complex plane. The eccentricity of this ellipse is more distinct for cases where the input frequency is smaller. This is shown in Figure 2.3 where the input frequency is 1 Hz. This ellipse indicates that there is an imbalance in the phase of the real and complex outputs from the recursion relation. In order to correct this a rotation must be applied to y in order for it to be a circle in the complex plane.

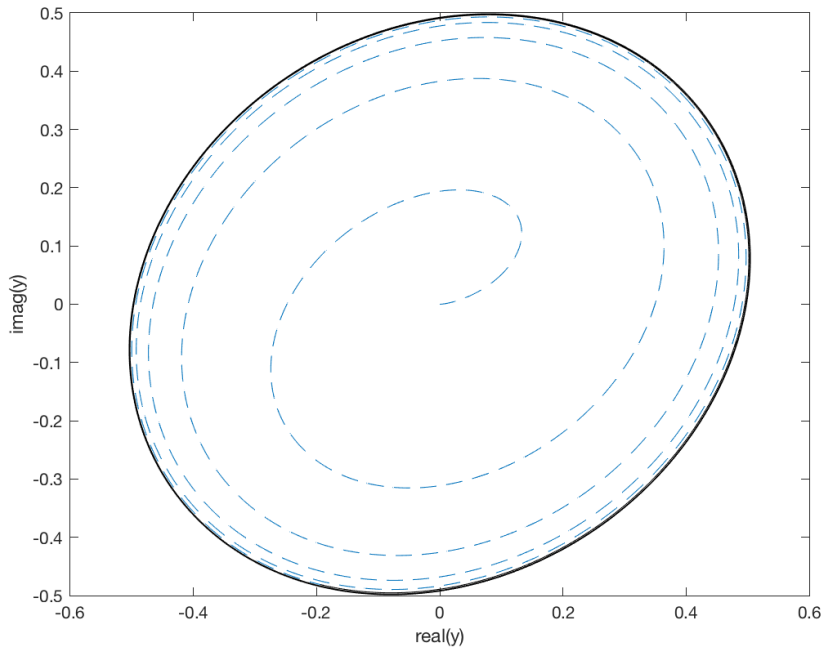


FIGURE 2.3: Complex output from static iWave before rotations are applied. The black outline represents the steady state of the filter and the blue dashed line represents the data exponentially approaching this state.

For an input signal containing a sine wave with 0° phase the transformation matrix for this will be.

$$\begin{pmatrix} \mathbb{R}(y_{rot}) \\ \mathbb{I}(y_{rot}) \end{pmatrix} = \begin{pmatrix} \cos \alpha & \sin \alpha \\ -\sin \alpha & \cos \alpha \end{pmatrix} \begin{pmatrix} \frac{2}{a_f + a_b} & 0 \\ 0 & \frac{2}{a_f - a_b} \end{pmatrix} \begin{pmatrix} \cos \beta & \sin \beta \\ -\sin \beta & \cos \beta \end{pmatrix} \begin{pmatrix} \mathbb{R}(y) \\ \mathbb{I}(y) \end{pmatrix} \quad (2.5)$$

The values of α , β , a_f and a_b are explained in [26]. This rotation can be decomposed into the three matrix components of 2.5.

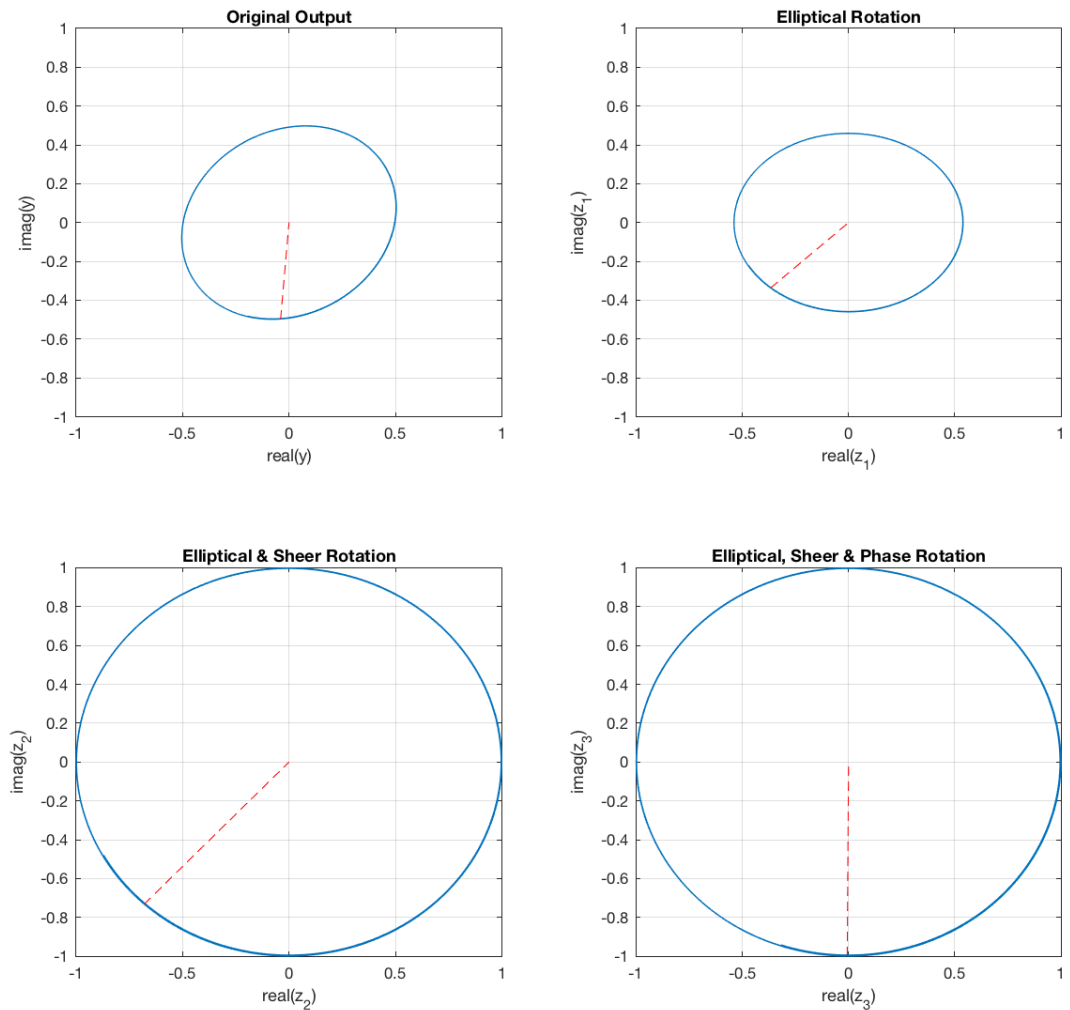


FIGURE 2.4: Sequential matrix rotations of original iWave output using Equation 2.5. Dotted lines represent angle of rotation of the last data point in the data.

Figure 2.4 displays the effect of the three matrix rotations have on the original complex output of the recursion relation in Equation 2.3. In this figure only the data after the filter has reached a steady state has been plotted. To interpret Equation 2.5 each of the rotation terms have been applied to the original output in succession. Firstly the ellipse is rotated using the third rotation matrix from Equation 2.5, such that the semi-major axis is now aligned with the complex plane axis. Subsequently the shear matrix (i.e the second matrix component) is applied after the elliptical transform. The shear matrix transforms the ellipse into a circle in the complex plane and increases the amplitude by a factor of two to retrain it to the same amplitude as the input data. Finally this output is rotated again in order to correct for the phase lag introduced by the recursion relation. After these three matrices are applied and the filter has reached a steady state, the complex output represents a synthesised in phase version of the input signal.

After this rotation the transfer function for the I and Q phase outputs is given by the following in the z -plane.

$$\begin{aligned}\Re(H(z)) &= \frac{w \cos \Delta - (1-w)wz^{-1}}{1 - 2(1-w) \cos \Delta z^{-1} + (1-w)^2 z^{-2}} \\ \Im(H(z)) &= \frac{w \sin \Delta}{1 - 2(1-w) \cos \Delta z^{-1} + (1-w)^2 z^{-2}}\end{aligned}\tag{2.6}$$

The frequency response of this transfer function reveals the effect of τ on the frequency band of the filter.

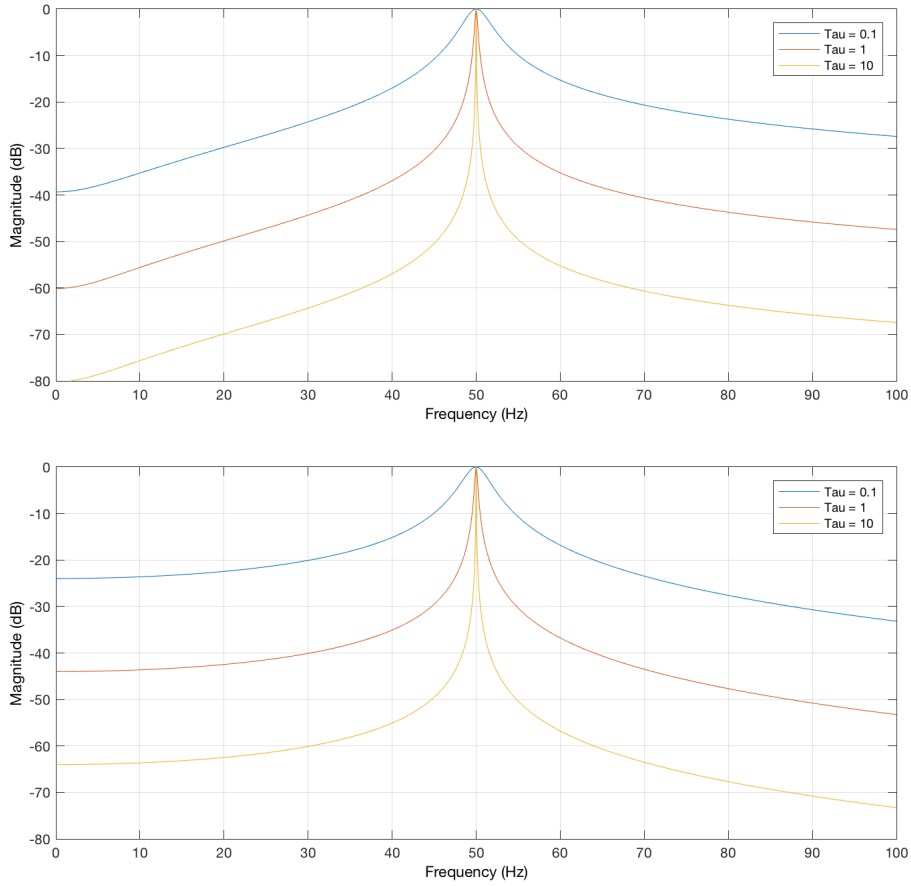


FIGURE 2.5: I and Q phase frequency response with varying τ . Larger τ relates to smaller bandwidth for both I and Q.

It can be seen in Figure 2.5 that the frequency sensitivity band of iWave increases as τ decreases in value. This is due to the full width half at half maximum Γ being related to τ by $\Gamma = 1/\pi\tau$.

When noise is included to the data it makes it more difficult for iWave to track a given signal. Similarly to Figure 2.2 the amplitude of a 60Hz line with added Gaussian background noise is measured using static line tracking in the following example.

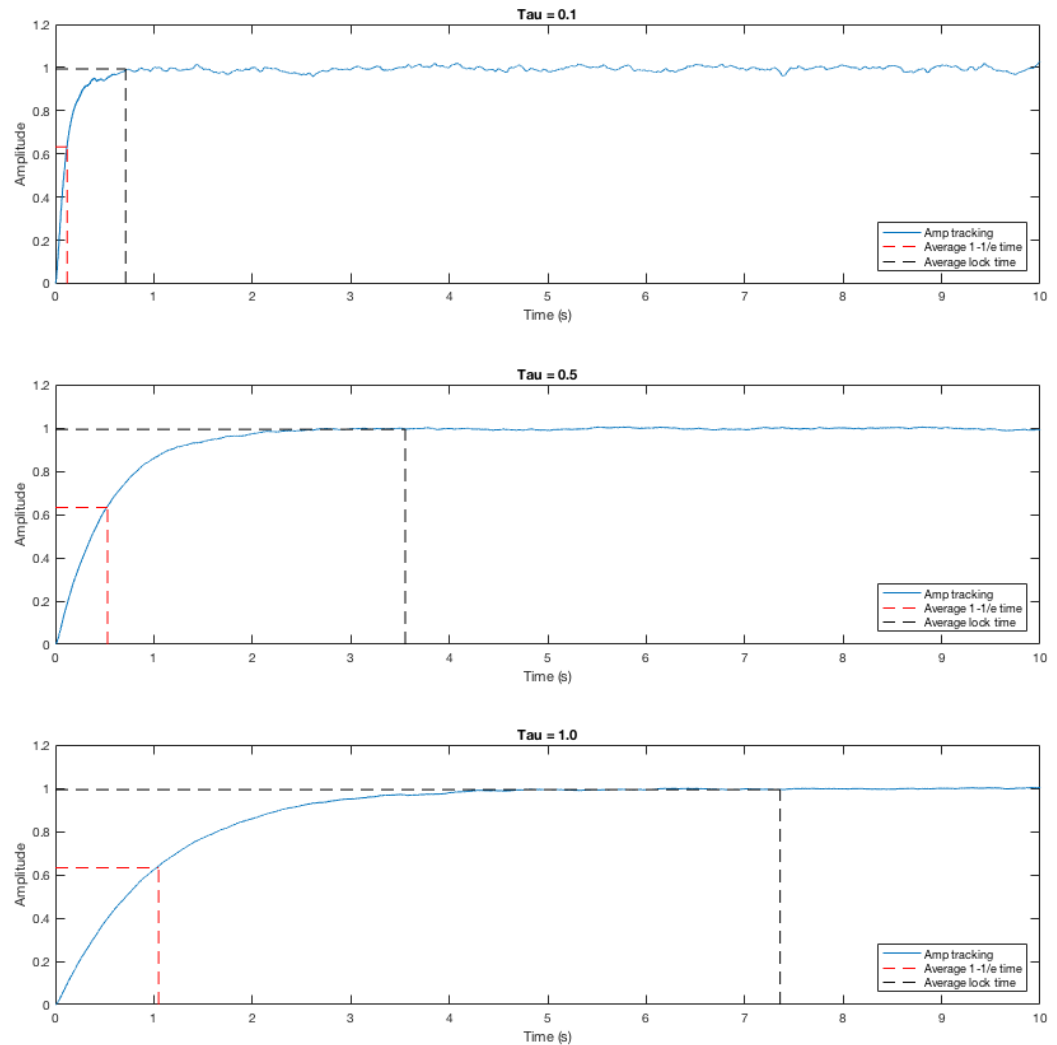


FIGURE 2.6: Results from amplitude tracking a sinusoid with constant frequency and added Gaussian noise using open loop iwave. Output amplitude is an exponential function over time with response time τ . Increasing τ over three examples with an average SNR of 26.71.

Figure 2.6 shows the effect of varying τ while tracking the amplitude of a line with background noise. With smaller values of τ the bandwidth of the filter increases as seen in Figure 2.5. With this larger bandwidth the amplitude output contains more of the background noise. As the value of τ is increased the amount of noise in the output is decreased as the bandwidth of the filter decreases. Consequently as τ is increased the filter also takes longer to converge at the amplitude of the line. The exponential profile of the output can be characterised by Equation 2.7.

$$A(t) = A_{signal} \left(1 - e^{(-t/\tau)} \right) \quad (2.7)$$

The variance after locking was also tested during this analysis. The time for which the filter can be described as locked was estimated to be when the amplitude reached the value $1 - e^{-5}$. The tracking amplitude after this point was used to calculate the variance. In Figure 2.7 the profile of this variance for increasing τ is again exponential. Ten simulations for each value of τ were used to calculate the average variance.

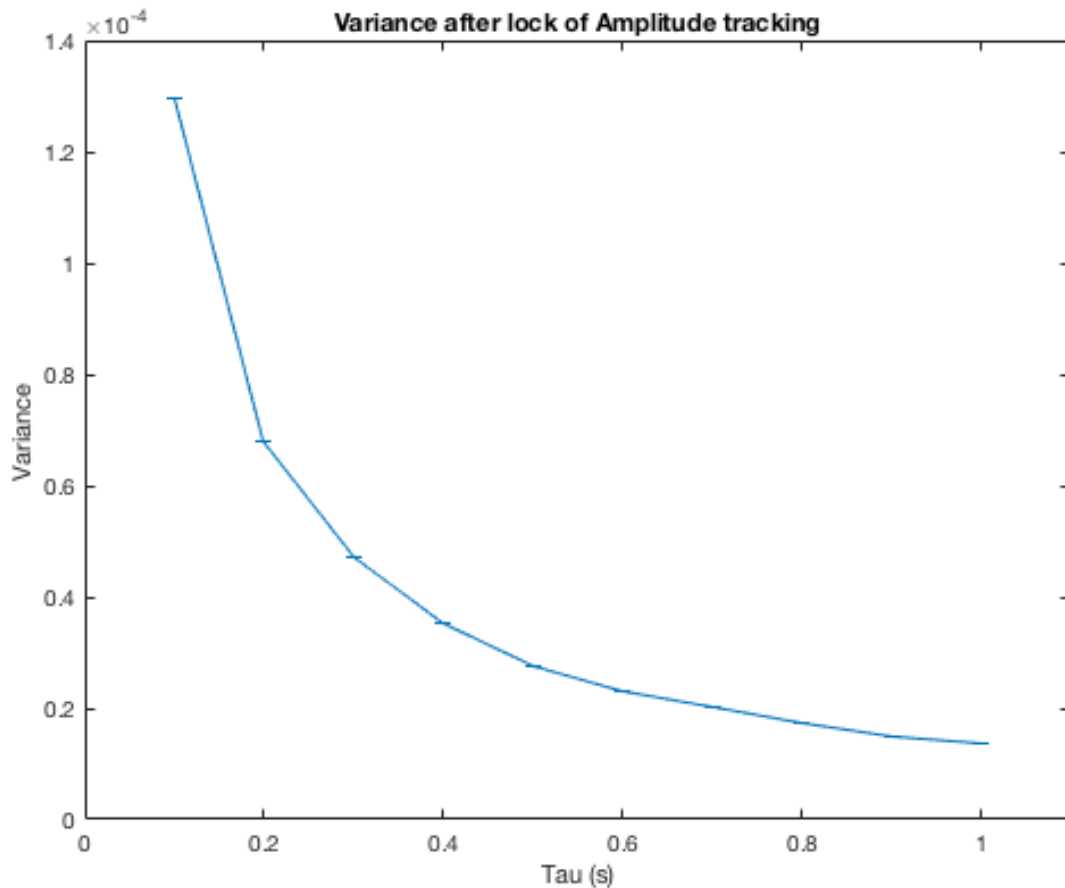


FIGURE 2.7: Variance of amplitude tracking after lock is acquired for increasing τ . Higher τ results in more accurate tracking for static frequency signals. Small error bars due to small difference between variance for each simulation.

2.3.2 Closed loop state

Using the two orthogonal I and Q states the departure in phase between the input and output can be measured. The schematic for how this is acquired is indicated in Figure 2.8.

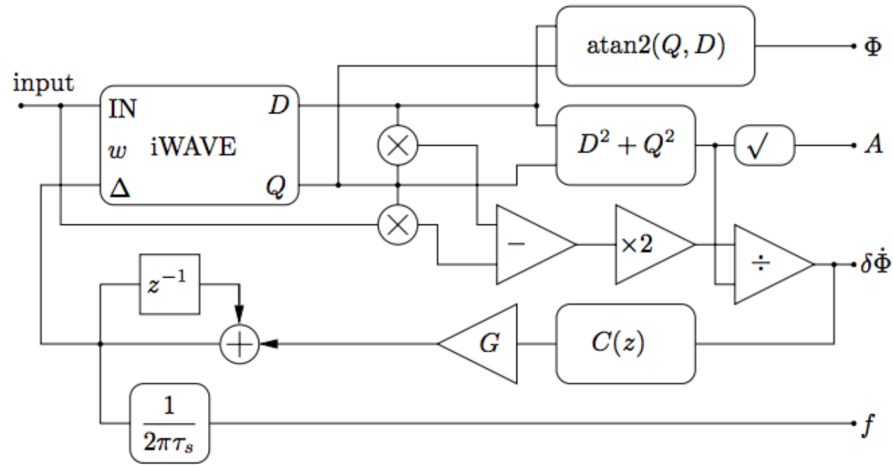


FIGURE 2.8: Schematic for iWave in closed loop configuration. Changes in tracking frequency Δ controlled by measured departures in phase $\delta\dot{\Phi}$.

Figure 2.8 demonstrates iWave's function as a phase locked loop (PLL) where both the amplitude and the frequency of a signal can be tracked. The central frequency of the filter is controlled by summing the departures in phase $\delta\dot{\Phi}$ between the complex output and the input. As an example consider an input equivalent to $x_n = \cos(n\Delta + \Phi)$ where n is the n th value and Φ is its phase. From this the rotated I and Q phase output will then be $I_n = \cos(n\Delta)$ and $Q_n = \sin(n\Delta)$ respectively. When the input and Q-phase output are multiplied will be as follows:

$$\begin{aligned} x_n Q_n &= \cos(n\Delta + \Phi) \sin(n\Delta) \\ &= (\cos(n\Delta) \cos \Phi - \sin(n\Delta) \sin \Phi) \sin n\Delta \end{aligned} \quad (2.8)$$

In the limit where $\Phi \approx 0$, Equation 2.8 can be reduced to,

$$\begin{aligned} x_n Q_n &= \cos(n\Delta) \sin(n\Delta) - \Phi \sin^2(n\Delta) \\ &= \sin(2n\Delta) - \frac{\Phi}{2} + \frac{\Phi}{2} \cos(2n\Delta) \end{aligned} \quad (2.9)$$

By then subtracting the $\sin(2n\Delta)$ term using the product of I_n and Q_n we are left with an approximation of half of the input phase.

$$I_n Q_n - x_n Q_n = \frac{\Phi}{2} - \frac{\Phi}{2} \cos(2n\Delta) \quad (2.10)$$

When this output is multiplied by two this gives the approximate value of the input phase with an additional $\cos(2n\Delta)$ component. This additional value can be partially removed by applying an extra iWave filter in series.

The frequency of the input signal is then estimated using a feedback loop. Departures in phase are iteratively summed which leads to the filter converging on the line frequency. The frequency tracking reaches a steady state when $\delta\dot{\Phi}$ approaches 0. The value of $\delta\dot{\Phi}$ then becomes the error signal where the filter tracks the signals frequency more closely as it approaches 0. The recursion relation of the frequency tracking can then be expressed by Equation 2.11.

$$f_n = G * \frac{\delta\dot{\Phi}_n}{2\pi\tau_s} + f_{n-1} \quad (2.11)$$

The gain term here G is used to scale the amount each sample of the departure in phase influences the output frequency. Higher gain leads to the filter converging on the input frequency faster but also adds more noise to the frequency tracking. This is due to higher gain causing the filter to overshoot the frequency causing it to oscillate around the line frequency. When there is already noise in the data this effect is particularly noticeable. Lower gain then leads to the filter taking a longer time to converge on the input signals frequency but adds less noise to the feedback loop. This gain is characterised by Equation 2.12

$$G = \frac{\eta * \tau}{\tau_s} \quad (2.12)$$

This gain must be added to the feedback loop otherwise it cannot lock onto the input frequency. The term η here is a more controlled method of tuning the response of the filter. Starting the filter with an offset frequency from the input signal and $\eta \approx 1$ the frequency tracking output behaves similarly to the amplitude tracking i.e. an exponential.

To demonstrate this frequency tracking capability input data containing a 60Hz sine wave with no background noise is tracked using iWave with the initial frequency of the filter is set to 55Hz using varying τ values. The scaled frequency output is given by $f_{sc} = (f_{norm} - f_{start}) / (f_{sig} - f_{start})$.

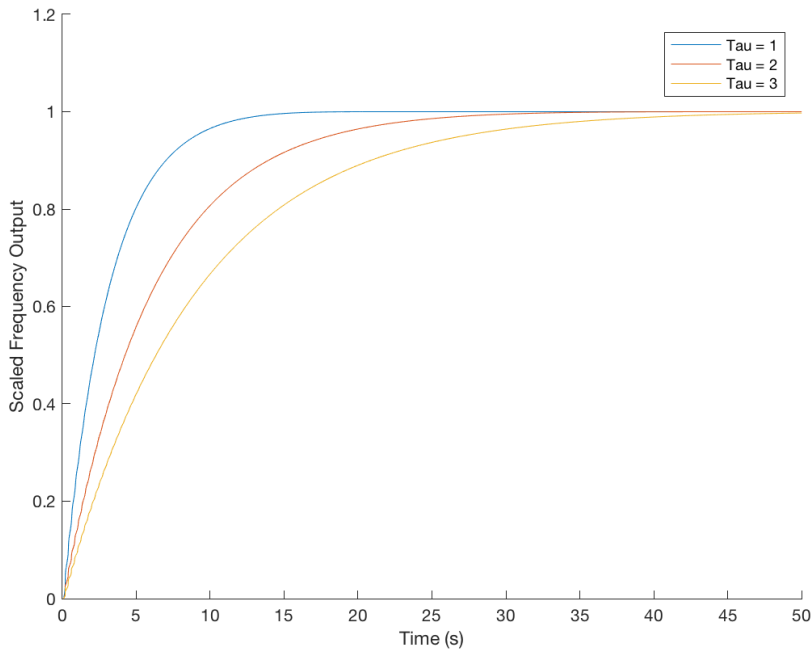


FIGURE 2.9: Scaled frequency output from iWave for varying τ with offset starting frequency. Signal frequency acquired faster for smaller τ values.

From Figure 2.9 it can be seen that the response time for frequency tracking in this lower gain configuration is dependent on τ in a similar way to the static amplitude tracking. However the e-folding time here is longer than τ in this case since the frequency tracking is governed by the feedback filter $C(z)$ and the gain. Using the same method for measuring the amplitude response time we can measure the response time for the frequency tracking. Results from this are indicated in Figure 2.10.

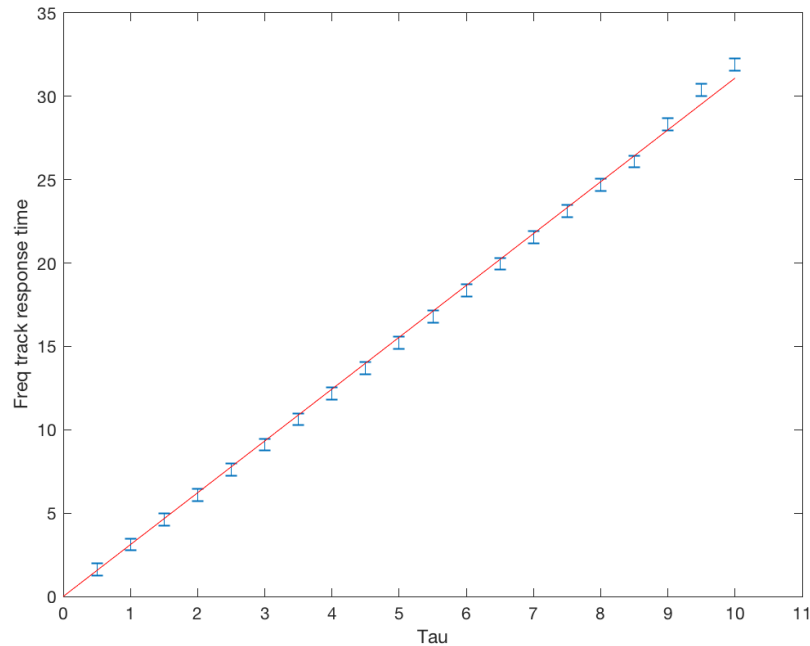


FIGURE 2.10: Frequency tracking response time for varying τ and constant $\eta = 1$. Response time is larger than τ value due to feedback filter $C(z)$.

It is also interesting to look at the amplitude output in the closed loop case starting from an offset frequency. Instead of an exponential the output comes in the form of a sigmoid function.

The equation for this output fits with the model of the sigmoid function

$$A(t) = \frac{A_{signal}}{1 + e^{-b(t-c)}} \quad (2.13)$$

The coefficient c is the midpoint of the output amplitude and b controls the steepness of the amplitude output. An example of this sigmoid function fit is shown in Figure 2.12.

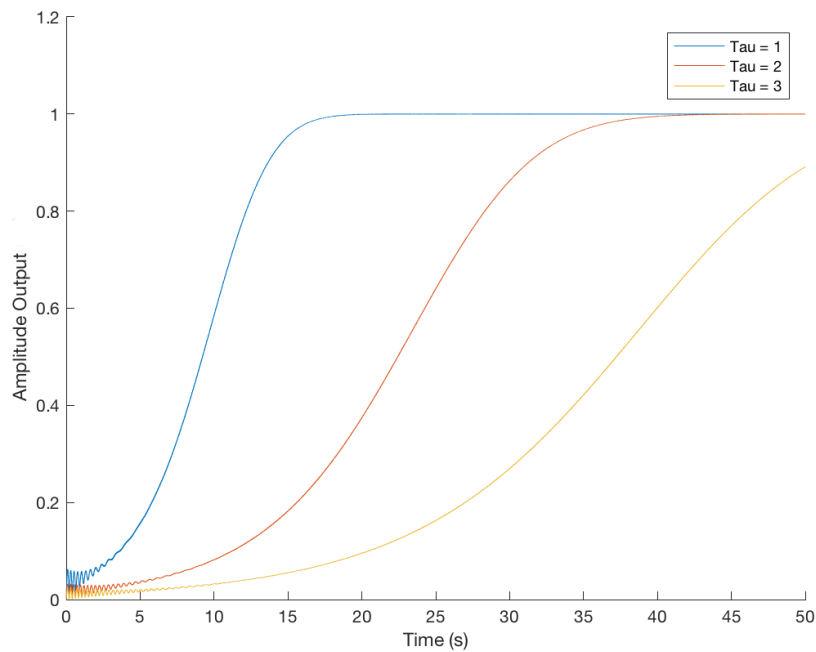


FIGURE 2.11: Amplitude output for closed loop iWave with offset starting frequency. Output resembles a sigmoid function due to initial change the filters central frequency followed by subsequent exponential averaging.

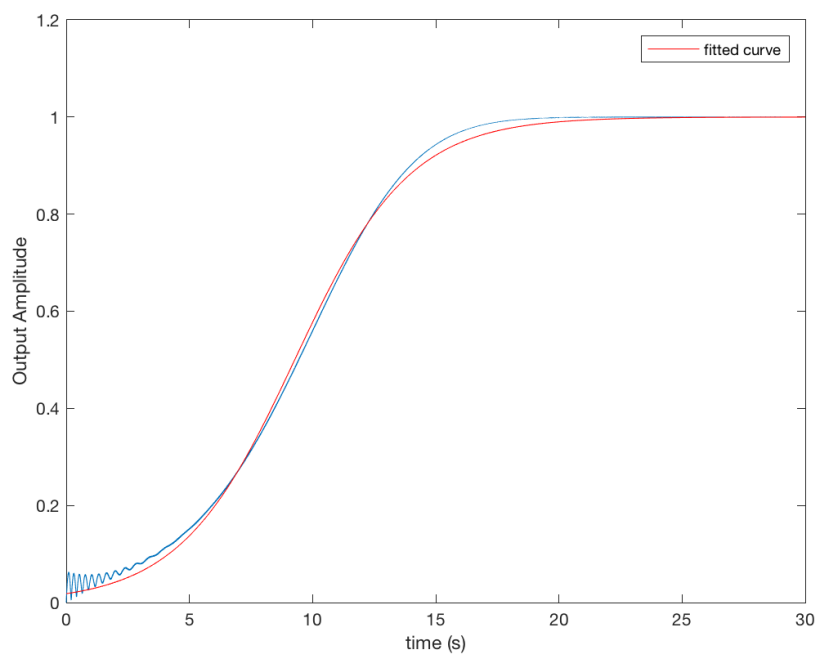


FIGURE 2.12: Fit of sigmoid function (red) compared to tracked amplitude output from closed loop iWave with offset starting frequency (blue).

To demonstrate the effect of increasing gain has on frequency tracking the output frequency of tracking a 60Hz signal is measured while τ is kept constant and the gain is varied. As η is increased the frequency tracking output becomes more like a damped oscillator. The frequency output will overshoot the frequency of the signal but will eventually reach a steady state at the signal frequency.

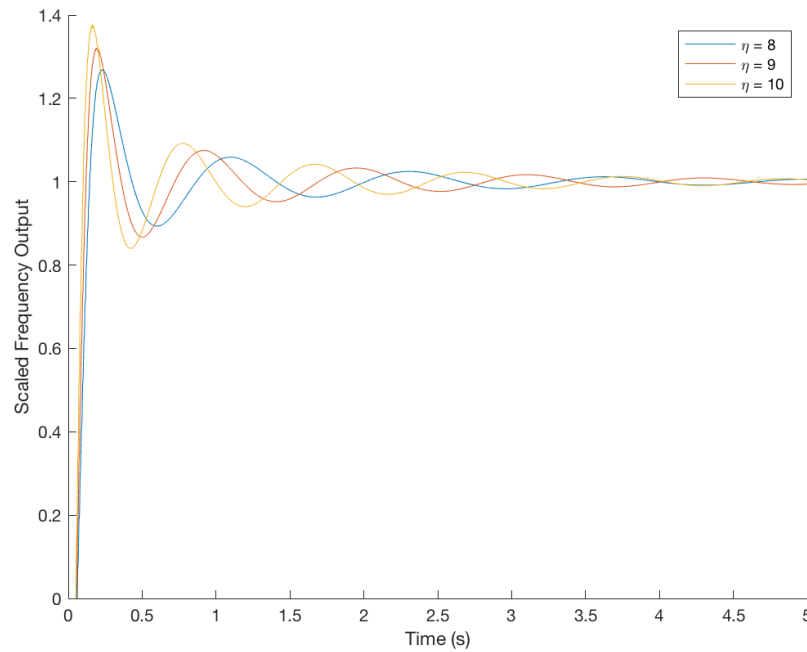


FIGURE 2.13: Scaled frequency output from closed loop iWave tracking static frequency sinusoid with offset starting frequency. Frequency output overshoots signal frequency with larger η values.

The frequency tracking output from iWave acts similarly to the amplitude tracking when Gaussian noise is added to the signal. In Figure 2.14 a 60Hz signal was tracked using iWave with parameters $\tau = 1$ and $\text{gain} = (9 * t_s / \tau)^2$. With no background noise the tracker converges on the signal frequency with limited variance. It oscillates for the first 10 seconds before settling on the frequency which contains the most signal.

However when Gaussian noise in Figure 2.15 is added to the signal iWave's ability to track the frequency is decreased. Using the same parameters as Figure 2.14 to track the noisy signal the frequency tracking becomes less accurate.

Using the same data we find that signal tracking can be improved when the data contains Gaussian noise by decreasing the gain. In Figure 2.16 the gain factor is set to $\eta = 9/8$ resulting in more accurate frequency tracking.

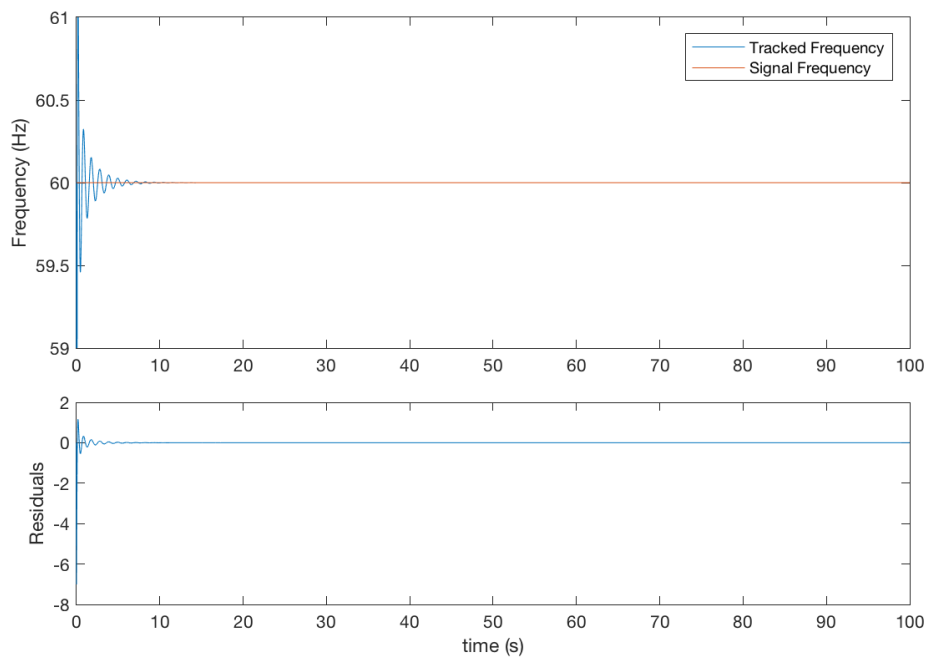


FIGURE 2.14: Frequency tracking of a 60 Hz line with no noise ($\tau = 1$, $\text{gain}=(9 * ts/\tau)^2$). Frequency output is similar to a damped oscillator and locks on after 10 seconds.

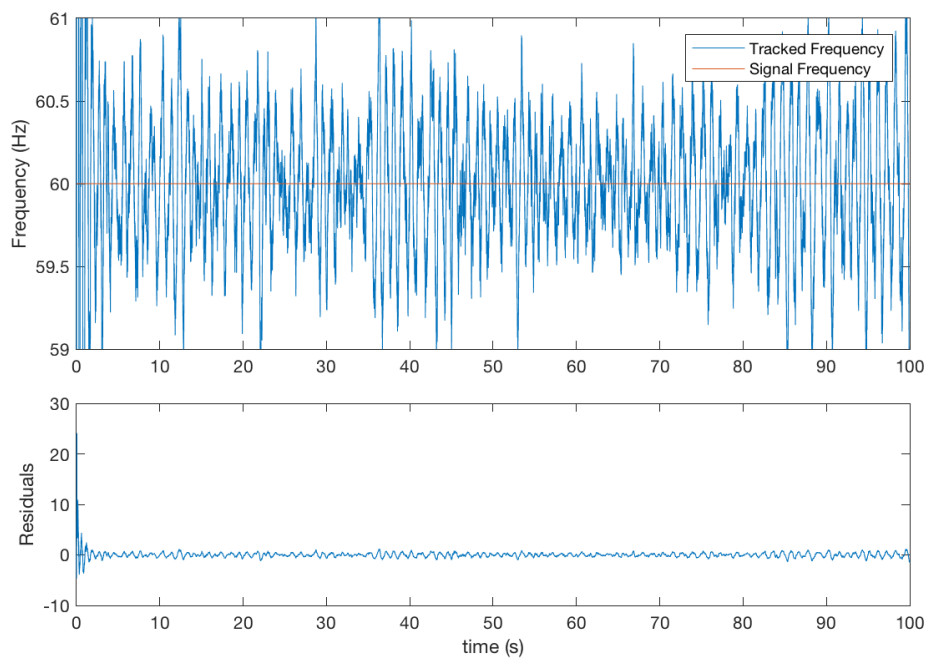


FIGURE 2.15: Frequency tracking of a 60 Hz line with Gaussian noise ($\tau = 1$, $\text{gain}=(9*ts/\tau)^2$). Added noise and large gain causes frequency tracking to also contain more noise.

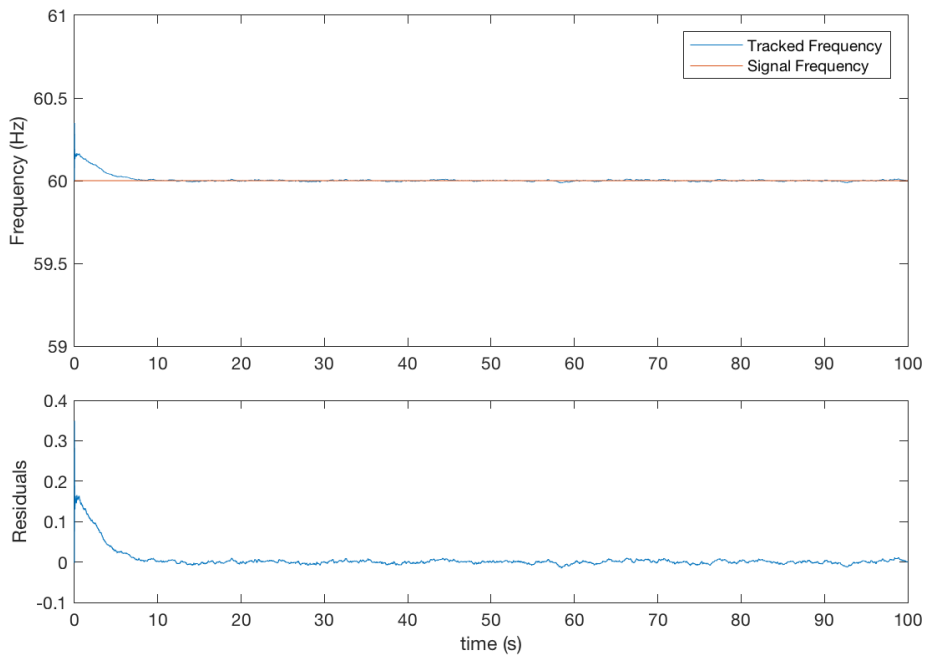


FIGURE 2.16: Frequency tracking of a 60 Hz line with Gaussian noise ($\tau = 1$, $\text{gain}=(9/8*ts/\tau)^2$). Reduction in gain compared to Figure 2.15 allows for more accurate frequency tracking.

This reduction in gain allows for better frequency tracking particularly when we have a static line. We can test this hypothesis by measuring the least squares fit i.e. χ^2 of each combination the parameters used. The χ^2 probability is defined as,

$$\chi^2 = \sum_i^N \frac{(y_i^{obs} - y_i^{pred})^2}{y_i^{pred}} \quad (2.14)$$

In following example y_{obs} and y_{pred} are the tracked frequency and the real frequency of the line respectively.

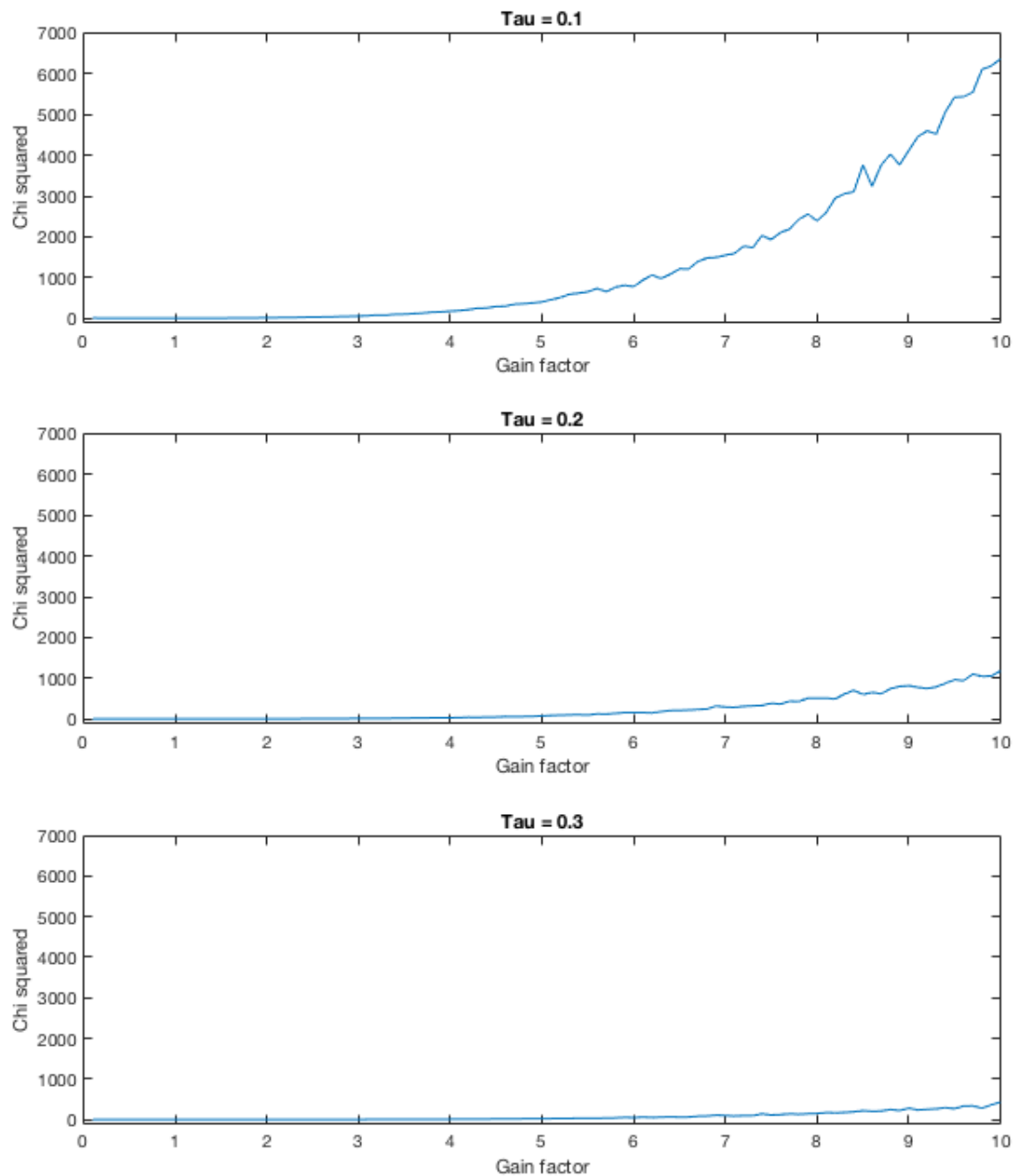


FIGURE 2.17: χ^2 for frequency tracking for low tau and varying gain (Average SNR = 27.07, 100 seconds). Larger χ^2 values show less accurate frequency tracking. Frequency tracking becomes less accurate with lower τ and higher gain.

In Figure 2.17 very low tau parameters are used and a high SNR. It can be seen that as tau is lowered and gain is increased the frequency tracking becomes significantly more erratic. In terms of modelling the frequency of a static line, this result shows that larger tau and smaller gain are more effective parameters. This is especially the case when tracking particularly long signal in the time domain. Larger values of τ

means that it takes longer for the tracker to lock onto the signal but is also varies less in frequency once locked on.

To test how well iWave can remove a line from data over it's parameter space, iWave is applied to data containing a 60Hz line with varying τ and gain factor. In the following example the fractional difference between the peaks of the original data and the line subtracted data are measured over a set of gain and tau parameters.

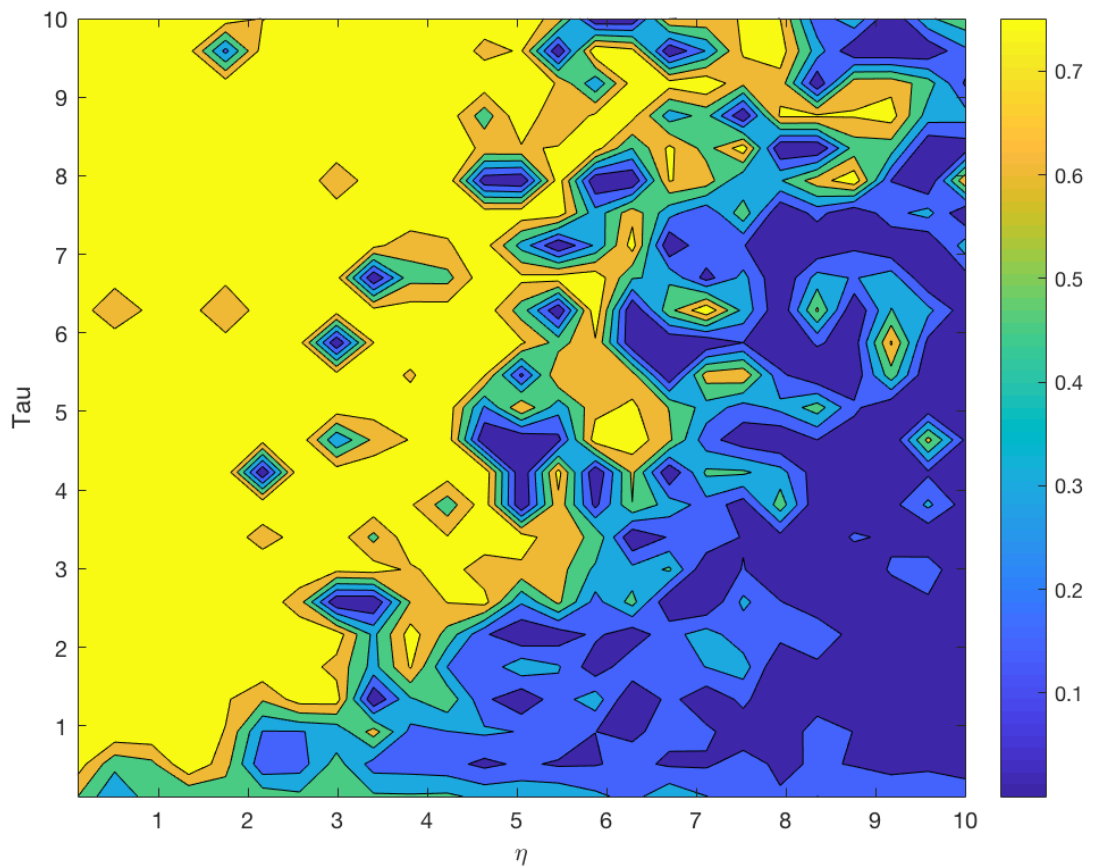


FIGURE 2.18: Fractional line reduction after filtering static 60Hz line using closed loop iWave with varying τ and η factor. Larger reduction in line magnitude (yellow) indicates better tracking/filtering of the input signal. Lower reduction (blue) indicates that the filter was not able to lock on or filter the signal effectively.

2.3.3 Tracking glitches

The results from above are only for lower data which includes low noise. When higher noise is added incidences of glitches in the tracking occur. This is especially the case when a high gain and low tau parameters are used. Usually some fluctuation causes the tracker to change in frequency quickly which in turn causes an instability in the feedback loop. Since the tracker relies on averaging the previous values of frequency, large fluctuations over short periods of time can cause a runaway effect especially when the response time is small. Larger tau values typically don't have this same problem as they average over a longer set of previous values.

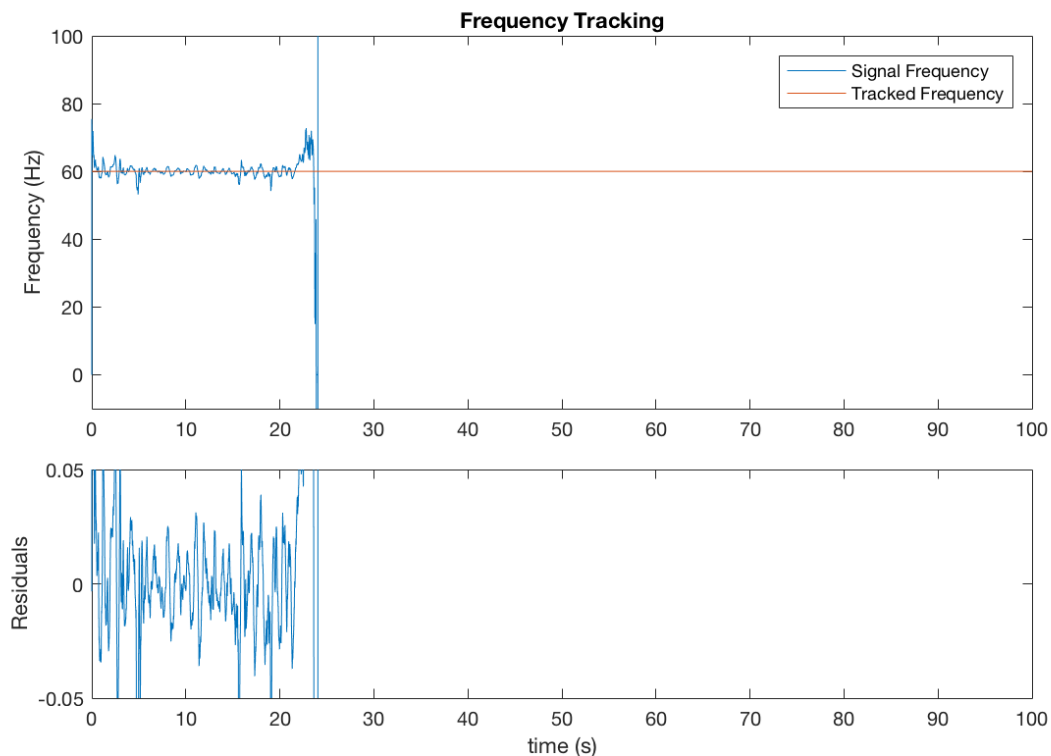


FIGURE 2.19: Frequency tracking line with Gaussian background noise and SNR of -10 with $\eta=10$ and $\tau=1$. Glitch occurs after 25 seconds due to large background noise causing frequency tracking to fail.

In the figure above a discontinuity can be seen at around 25 seconds. The frequency of the tracking changes to unphysical values at this point, going below zero and then above the Nyquist frequency of the data. Behaviour like this happens more frequently when we use a higher gain factor and lower tau. Glitches rarely occur when there is little or no noise present in the data. They are also more likely to happen with increasing length of data. To avoid this problem the data should be filtered to preserve the signal of interest while removing the broadband noise.

We can get an average of how often glitches occur by running the tracker on various instances of random noise with the static 60Hz signal. For each configuration of the parameters 100 simulations of random noise was added to the data. A glitch was identified if maximum of the tracking was above the Nyquist frequency or below zero i.e. an unphysical frequency. Tau values between 0.1 and 1 are used since glitches like this normally only occur in this range of tau values.

From table 2.1 it is obvious that larger tau values and smaller gain values result in a smaller percentage of glitches. The amount the percentage increases with gain also increases with decreasing tau. This effect is exaggerated since the signal is below the noise floor with the average SNR = -10.3556.

	GF = 1	GF = 2	GF = 3	GF = 4	GF = 5	GF = 6	GF = 7	GF = 8	GF = 9	GF = 10
Tau = 0.1	0.16	0.40	0.74	0.91	0.93	1.00	1.00	1.00	1.00	1.00
Tau = 0.2	0.02	0.19	0.40	0.58	0.58	0.77	0.83	0.88	0.96	0.99
Tau = 0.3	0.01	0.13	0.19	0.34	0.42	0.52	0.59	0.61	0.72	0.84
Tau = 0.4	0.00	0.09	0.08	0.24	0.27	0.33	0.45	0.43	0.65	0.65
Tau = 0.5	0.01	0.08	0.08	0.13	0.17	0.30	0.33	0.45	0.38	0.49
Tau = 0.6	0.00	0.03	0.10	0.06	0.11	0.20	0.21	0.34	0.33	0.36
Tau = 0.7	0.00	0.04	0.02	0.08	0.21	0.17	0.23	0.28	0.22	0.26
Tau = 0.8	0.01	0.03	0.03	0.05	0.04	0.09	0.24	0.14	0.28	0.19
Tau = 0.9	0.00	0.01	0.02	0.04	0.11	0.13	0.20	0.15	0.21	0.23
Tau = 1.0	0.00	0.00	0.02	0.05	0.02	0.08	0.20	0.14	0.23	0.18

TABLE 2.1: Fraction of simulations that included a glitch (Average SNR = -10.3556 Noise = 50 fstart = 60Hz duration = 10s Nsims = 100). Glitches are much more likely to occur at lower τ and higher gain values.

2.3.4 Tracking wandering lines

Wandering lines are signals which have a non-stationary or arbitrary drift in frequency over time. Tracking a line with a randomly varying frequency becomes a more complicated task for iWave compared to lines with a static frequency. To be able to track variations in frequency the closed loop version of iWave must be used.

For the following examples a randomly oscillating line was generated using the following method. A Gaussian distribution with unit mean was created and lowpassed using a butterworth filter with a cutoff frequency of 0.1 Hz. After this the data is then cumulatively summed and scaled such that the modulus of the data has a maximum value of 1. Adding a starting frequency of 60Hz to the summed data gives a slowly drifting line which can be used as the frequency of the signal. The signal was then generated using $D = \sin(2\pi f/f_s)$ where f is the wandering frequency and f_s is the sampling frequency which is set to 16384Hz.

2.3.5 Tracking examples with no noise

For the first example iWave is applied to the wandering line with $\tau = 1$ and $\eta = 1$. In this configuration the frequency tracking is not able to directly follow the signal frequency. With the gain at this low value the PLL cannot maintain lock when the rate of change of frequency is too high. The error signal here is the phase error between the input and output data represented by $\delta\Phi$ in Figure 2.8. This can be used as an indicator of how well the tracker is locked onto the the wandering line. It can be seen that as the tracked frequency approaches the signal frequency the value of the error also crosses zero. Also as the difference in the signal and tracked frequencies increases so does the variance in the the error. As the error signal deviates more from zero the amplitude of the tracked signal also decreases. This indicates that as the filter moves further away from the frequency of the line the magnitude of the

output also decreases. The advantage of this is that if there is no signal to lock onto then the output from iWave will stay at zero.

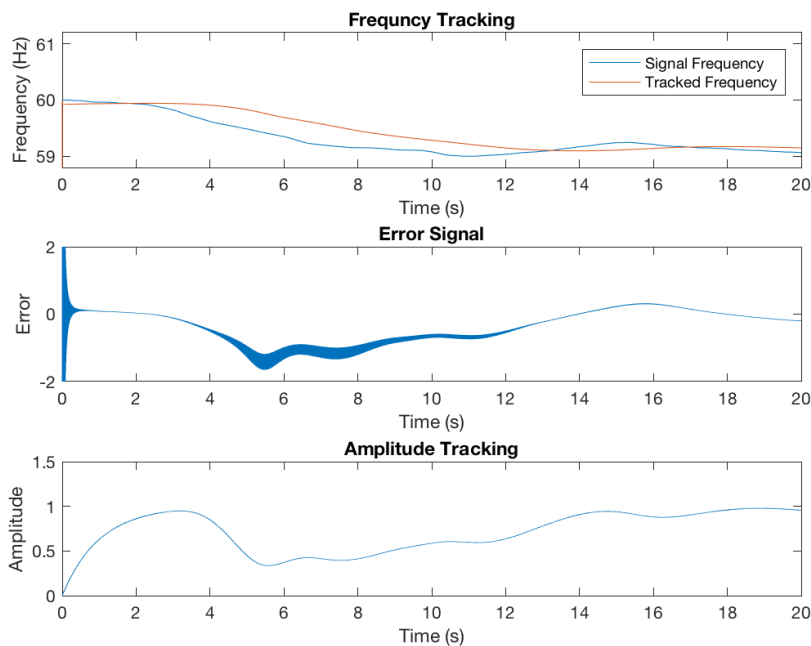


FIGURE 2.20: Tracking output of iWave with applied to data containing wandering line at 60 Hz without added background noise. Filter parameters set to $\tau = 1$ $\eta = 1$. iWave loses lock on frequency due to small gain resulting in non-zero phase error. Larger difference between signal and tracked frequency causes larger variance in phase error and lower output amplitude.

In order to more accurately track the line a higher gain value is used in Figure 2.21. For this example $\eta = 10$ which improves the frequency tracking by allowing iWave to make larger changes in frequency as described in Equation 2.11. The tracked frequency rings down until it locks onto the frequency of the line. This ring down can also be seen in the error signal where it again approaches zero as it locks onto the signal frequency. The tracked amplitude converges on the signal at around 4 seconds which is longer than the response time τ . Again this is due to the time needed for tracker to lock onto the frequency of the line.

Faster and more accurate frequency tracking can be achieved by setting the value of τ lower instead. In Figure 2.22 iWave tracks the wandering line with $\tau = 0.1$ and $\eta = 2$. Setting τ lower here increases the gain of the feedback loop from Equation 2.12 but also increases the width of the filter (Figure 2.5). Since there is no background noise here the tracker is able lock onto the line faster than the higher τ configuration with no additional noise to the output signal.

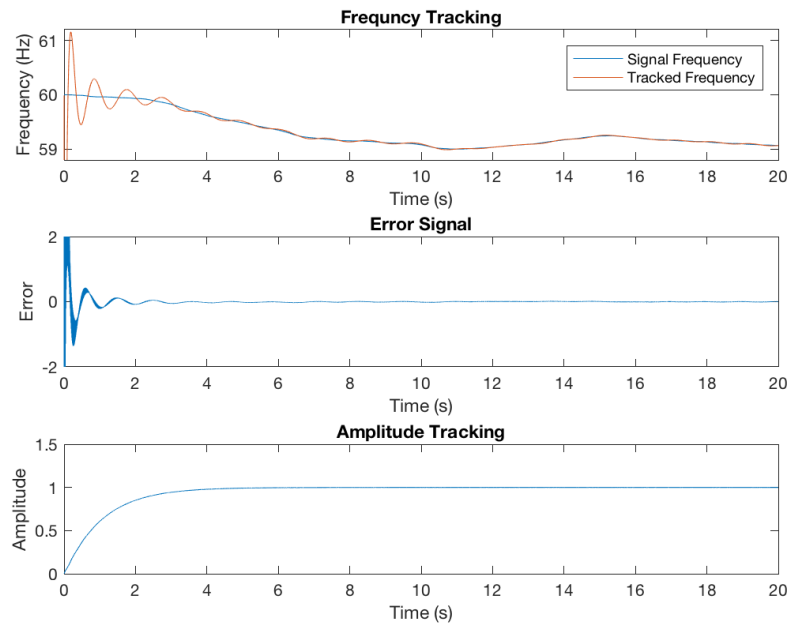


FIGURE 2.21: Tracking output of iWave with applied to data containing wandering line at 60 Hz with no added background noise. Filter parameters set to $\tau = 1$ $\eta = 10$. With no background noise, iWave is able to achieve and maintain lock onto the line after 4 seconds due to higher gain compared to Figure 2.20

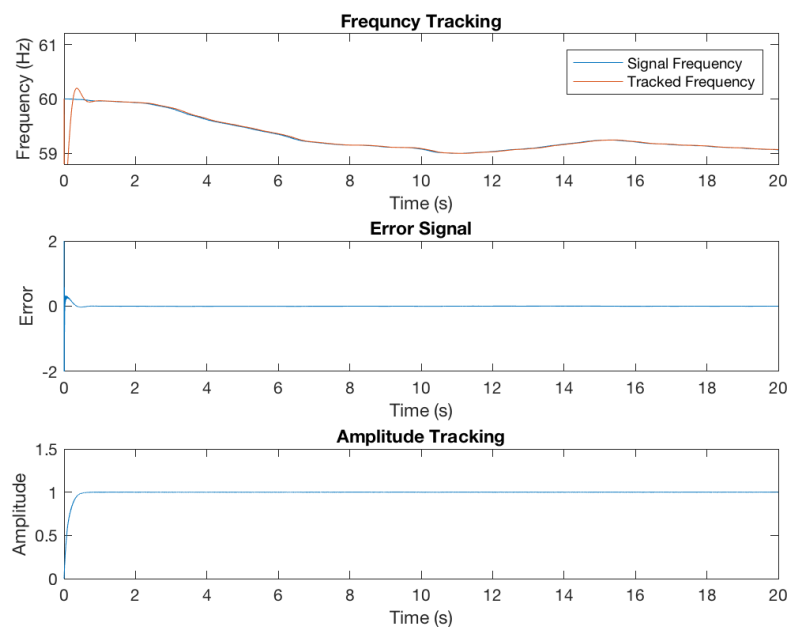


FIGURE 2.22: Tracking output of iWave with applied to data containing wandering line at 60 Hz with no added background noise. Filter parameters set to $\tau = 0.1$ $\eta = 2$. With no background noise, iWave is able to lock onto signal faster than in Figure 2.21 due to higher gain and reduced τ .

2.3.6 Tracking examples with added noise

For the following few examples the same process described previously to generate a wandering line was used but in this case white Gaussian noise was added to the data giving it a signal to noise ratio of 5. In Figure 2.23 the amplitude and error react to deviations from the signal frequency similarly to Figure 2.20. In this case the error signal has a significant amount of added noise which again increases the further the tracking frequency is from the signal frequency. The amount of noise on the amplitude output is limited here by the bandwidth of the filter.

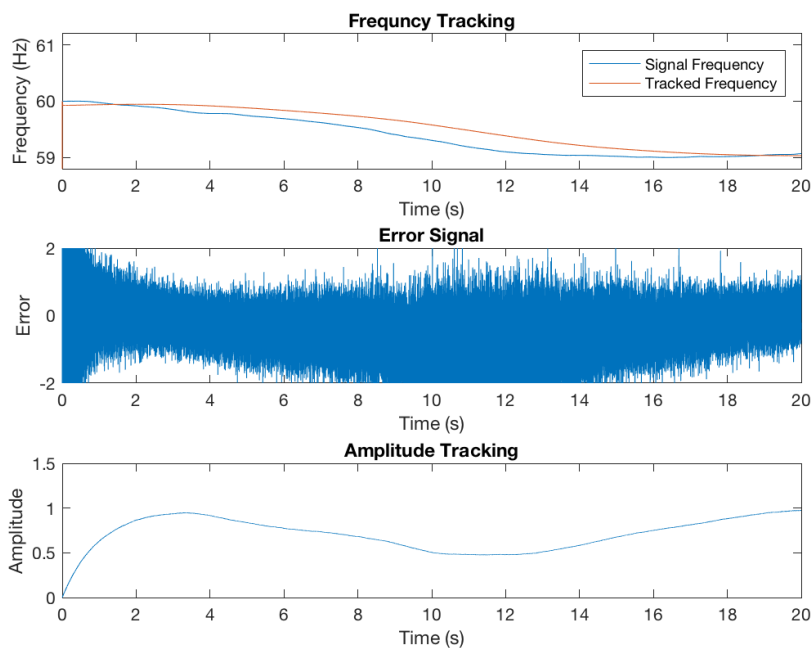


FIGURE 2.23: Tracking output of iWave with applied to data containing wandering line at 60 Hz with added background noise. Filter parameters set to $\tau = 1$ $\eta = 1$. Additional noise in input data causes larger noise in error signal compared to Figure 2.20.

In Figure 2.24 the gain is increased which allows the tracker to maintain locked on the signal. The phase error now reduces to a constant background noise once it has locked onto the line. Again the amount of noise on the amplitude is limited by the filter bandwidth and with increased gain it converges on the amplitude of the input signal after around 4 seconds. This is similar to the example in Figure 2.21 with the main difference being the added noise to the error signal and takes longer to achieve lock.

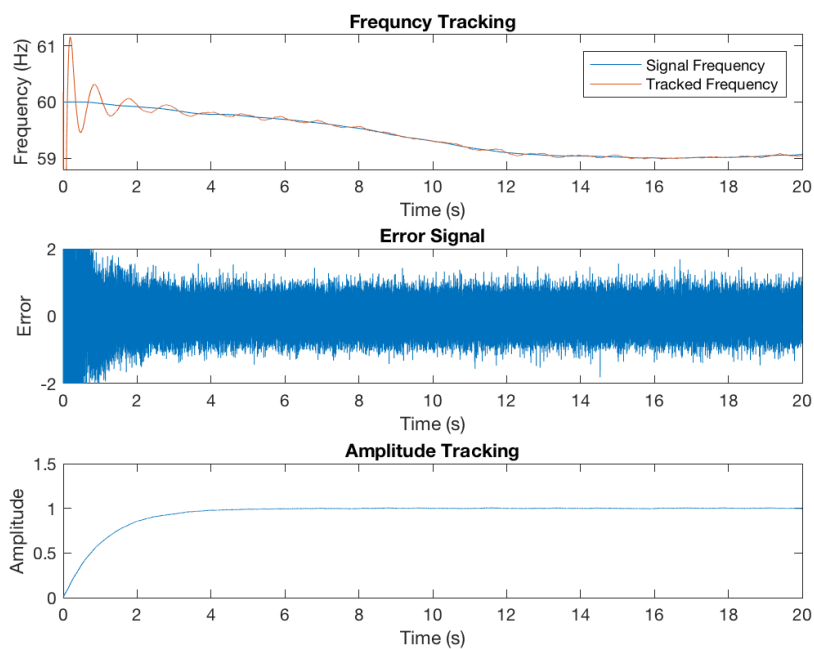


FIGURE 2.24: Tracking output of iWave with applied to data containing wandering line at 60 Hz with added background noise. Filter parameters set to $\tau = 1$ $\eta = 10$. Similar output to Figure 2.21 but with more noise in error signal due to noise in input signal.

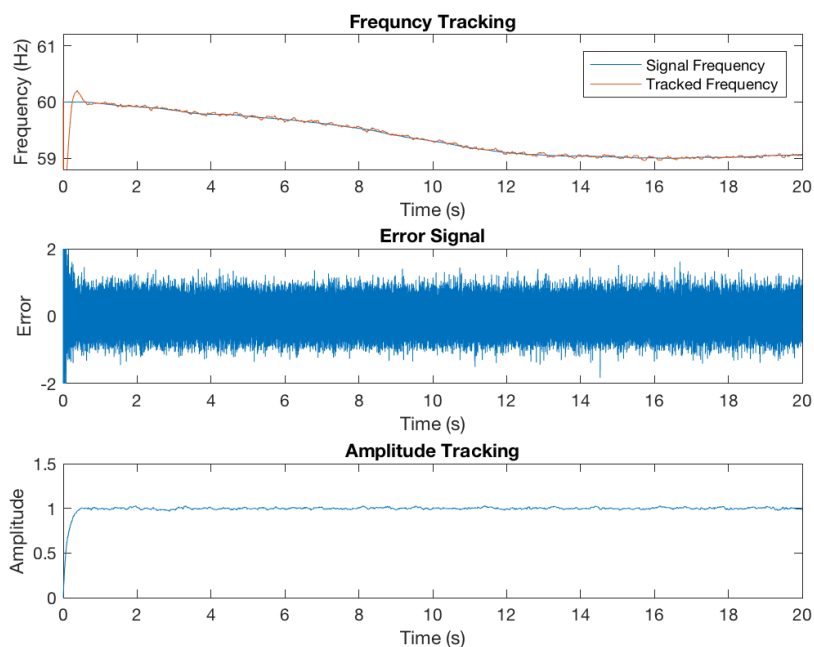


FIGURE 2.25: Tracking output of iWave with applied to data containing wandering line at 60 Hz with added background noise. Filter parameters set to $\tau = 0.1$ $\eta = 2$. Improved lock time compared to Figure 2.24 but output contains more noise due to the filter's larger bandwidth.

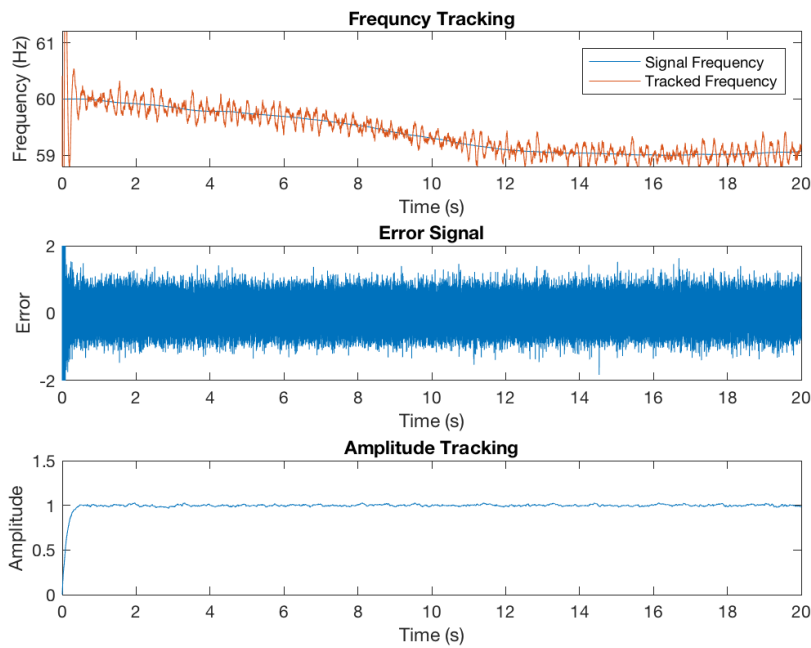


FIGURE 2.26: Tracking output of iWave with applied to data containing wandering line at 60 Hz with added background noise. Filter parameters set to $\tau = 0.1$ $\eta = 10$. Increasing gain when input contains background noise causes larger noise in frequency tracking as well as error signal.

Figure 2.25 shows the tracking of the noisy wandering line when the value of τ is decreased. Again the gain is increased by decreasing τ but also increases the bandwidth of the filter adding noise to the output amplitude. The result shows that when choosing the parameters for tracking the amount of background noise must also be considered. Although a smaller τ allows for the filter to react more quickly to changes in signal frequency it will also add more noise to the output data. Similarly in Figure 2.26 when η is increased as well as decreasing τ the frequency tracking does stay locked on the signal but also has added noise.

2.3.7 Tracking examples with no input signal

Another important result is how iWave reacts when the input data only contains background noise. For the following examples the first half of the data contains a wandering line with added white noise background and the second half only contains the white noise background. In the first example the τ and η parameters are both conservatively set to 1. The results from this in Figure 2.27 show that the phase error becomes significantly more noisy after 50 seconds as there is no longer a signal to lock onto. Despite this the frequency tracking remains around the same frequency band but also has some indications of glitchy behaviour. The amplitude output drops down to zero after 50 seconds as the filter is now only outputting the filtered background.

For the second example the value of τ is decreased to 0.1 which causes the frequency tracking to become unstable after the signal ends. In Figure 2.28 the frequency tracking displays more glitchy behaviour where it drops below zero at some points. This however does not have an effect on the output amplitude where it decreases to the filtered background noise level around zero after the signal stops.

In the third example Figure 2.29, the output from iWave exhibits glitchy behaviour both in the amplitude and frequency tracking. Similarly to Figure 2.28 the frequency tracking drops below zero after the signal stops but also the output amplitude contains short glitches which are not present in the input data. Glitches like this can exist in the data when the closed loop gain is set too high. As shown by Table 2.1, glitches become less common for higher τ and lower η . Also with higher background noise the likelihood of glitches also increases.

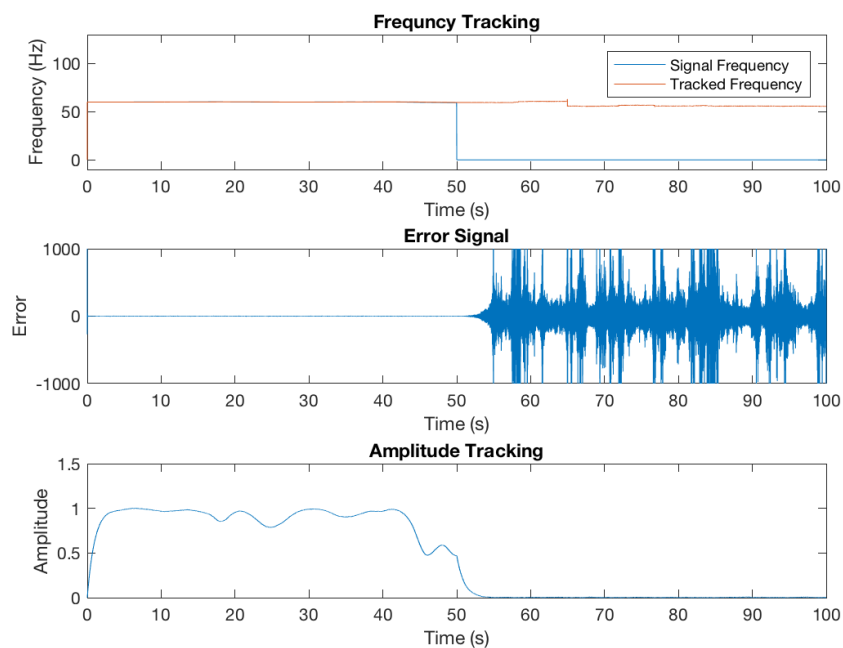


FIGURE 2.27: Tracking output of iWave with applied to data containing wandering line at 60 Hz with added background noise. Line is only present over first half of the data. Filter parameters set to $\tau = 1$ $\eta = 1$. Higher noise in error signal when there is no input signal and amplitude output tends to zero.

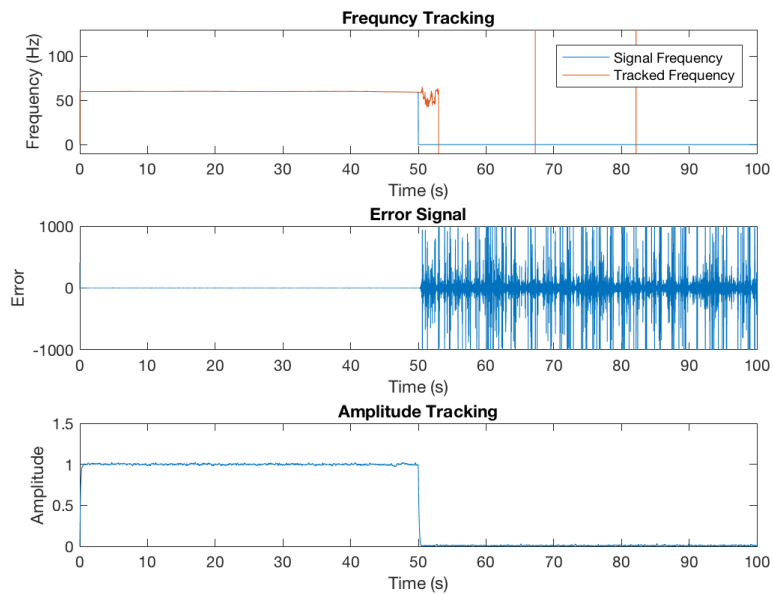


FIGURE 2.28: Tracking output of iWave with applied to data containing wandering line at 60 Hz with added background noise. Line is only present over first half of the data. Filter parameters set to $\tau = 0.1$ $\eta = 2$. Higher noise in error signal when there is no input signal and amplitude output tends to zero. Frequency tracking reaches unphysical values due to increased gain and τ .

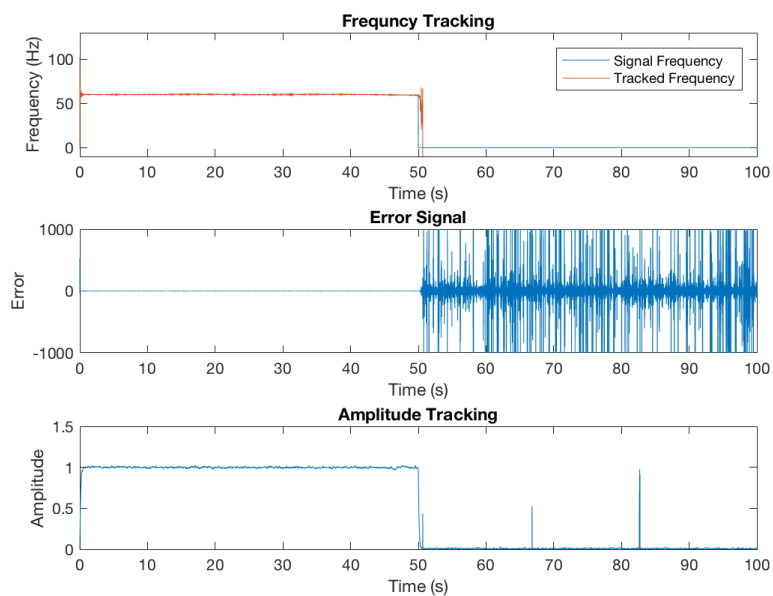


FIGURE 2.29: Tracking output of iWave with applied to data containing wandering line at 60 Hz with added background noise. Line is only present over first half of the data. Filter parameters set to $\tau = 0.1$ $\eta = 10$. With higher gain and lower τ the output frequency reaches unphysical values, the error signal noise increases and there are glitches in the output amplitude tracking not present in the input data.

2.3.8 Summary

The iWave filter's ability to track a continuous sinusoidal signal over the filter's parameter space has been demonstrated in this section. When the filter is in open loop it is a resonant filter which exponentially averages the input data over its bandwidth determined by its response time τ and the starting frequency. In its closed loop configuration iWave presents a useful method for tracking lines which wander in frequency even with background noise added to the data. The same exponential averaging occurs and the centre of the resonant filter is determined by a PLL. Errors in phase between the input and output data can be used to lock onto the signal by adjusting the frequency of the PLL until the error signal approaches zero. It is also shown that the filter can have glitchy behaviour when τ is below 1 and the gain of the PLL is set too high and when the data contains background noise. To be able to track wandering lines with added background noise accurately the τ and η parameters need to be tuned depending on the rate of change of the signals frequency.

2.4 Line removal from GW150914 event

As explained previously the iWave filter can be used to track and then subtract lines from a set of data. This becomes useful for cases where unwanted lines pollute a set of data where a signal exists. By removing these unwanted lines the signal can be more easily extracted from the data. Notch filters are more commonly used to remove lines from the data however this also means that any signal from the band that is being notched out is also not included in the data. Alternatively linear predictive error filtering (LPEF) [21] can be used to whiten a spectrum but again this turns regions where lines exist into holes in the spectrum. Line removal by iWave filtering provides a method of removing lines by tracking and subtracting the power from a particular line. In this section iWave is used to recursively filter out lines from data taken during the GW150914 event[12].

2.4.1 Data from GW150914

In order to test how line removal can be used to filter data containing a GW signal two sets of data from the LIGO interferometers were taken containing the GW150914 event. The sampling rate used is 4096 Hz compared to the faster sampling rate for DARM data which is 16384 Hz. Using a lower sampling rate makes the line removal process faster since there are significantly less lines to remove and less data to filter. Also since the chirp signal from GW150914 is between 35 Hz and 250 Hz [12] power from above 2 kHz isn't necessary to include for this example. Each of the data sets contains a 512 second block where the chirp signal is located towards the end of the block. Since the iWave filter exponentially averages the line signal it will have subtracted more of it towards the end of the block compared to the start.

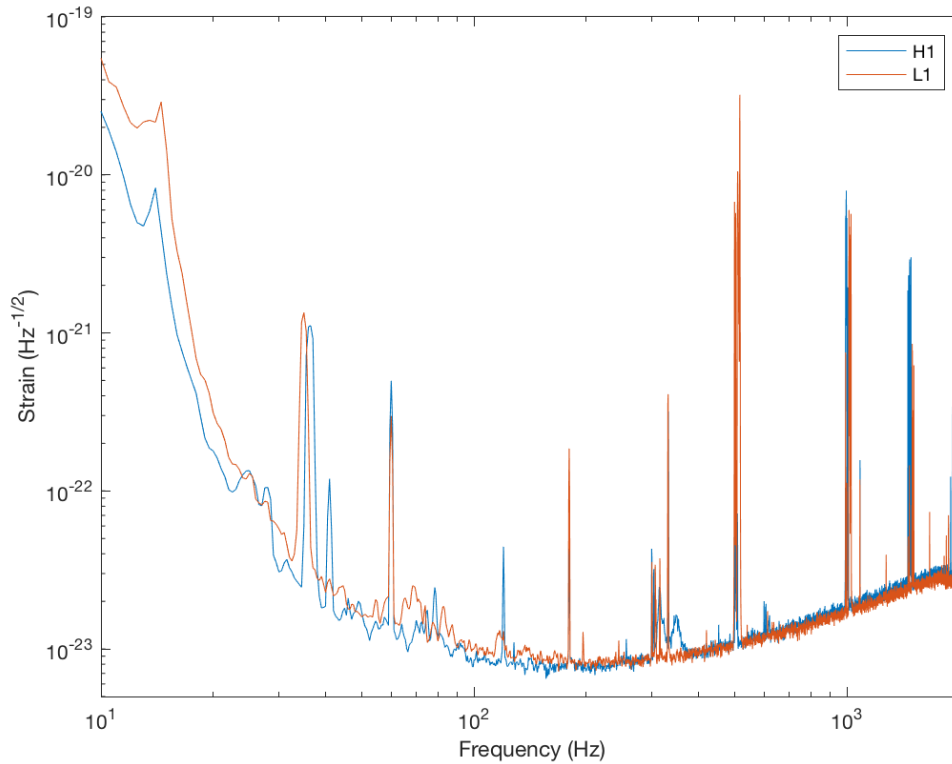


FIGURE 2.30: Spectrum of DARM data from both interferometers during GW150914 event. strain data is dominated by seismic noise at lower frequencies and shot noise at higher frequencies. Line features come from violin modes and power lines.

Figure 2.30 shows the spectrum of differential arm length (DARM) from the two 40 km cavities of each detector. This is also known as strain data and this data in particular contains the BBH event GW150914. It can be seen that the strain data is dominated by seismic noise at lower frequencies and shot noise at higher frequencies. As well as this lines exist at various regions in the spectrum coming from a variety of different sources. The loudest of these lines are the violin modes appearing at harmonics of 500 Hz in the DARM spectrum. Violin modes come from resonances in the suspension fibres of the 40 kg masses and have a very high Q. As well as this, mechanical modes of the mirrors resonate at lower frequencies, calibration lines exist around 30 Hz and the 60 Hz power line are always present in the spectrum [72].

2.4.2 Filtering with LPEF

For comparison we first whiten the data using the LPEF filter. The LPEF filter takes an average of the spectrum over the segment of data and uses this to construct a whitening filter [21].

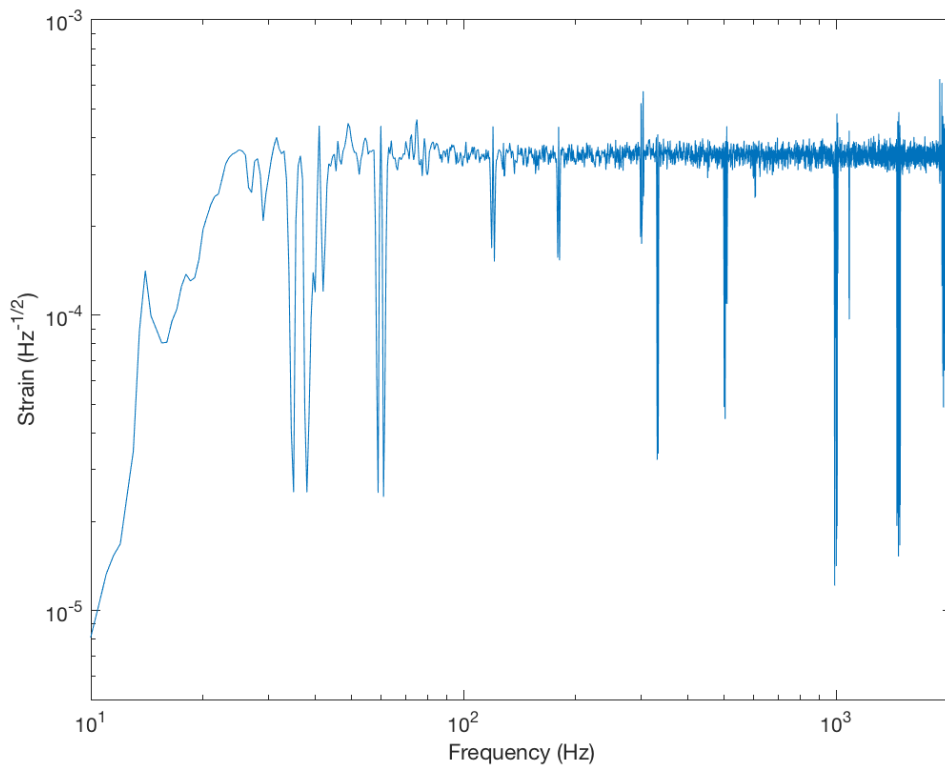


FIGURE 2.31: Spectrum of LPEF filtered data from H1 during GW150914 event. Waveforms crossing frequency regions where lines existed will not be observed over those frequencies using this filtering technique.

The spectrum output from the LPEF filtered data can be seen in Figure 2.31. While the overall spectrum is normalised over frequency, the LPEF filter has aggressively filtered the power lines in the spectrum. Regions where lines existed previously in the data are now much lower in amplitude compared to other their neighbouring frequency regions. While this means that the lines are no longer present in the data, this can have a negative impact when searching for GW signals. The LPEF filtered data will reduced sensitivity to a GW signal if it's waveform crosses the frequency band of the filtered lines.

2.4.3 Whitening filter

Before beginning the line removal process, the data is first whitened using a time domain filter. This filter only reshapes the spectrum to make it more uniform in the frequency domain so that the average power across frequency is more constant. This is important since without whitening line tracking with iWave becomes more difficult. If iWave is set at a starting frequency in the more sensitive region of the spectrum (15 Hz) it will not be able to maintain lock on a line there due to the significantly higher amount of noise at lower frequencies.

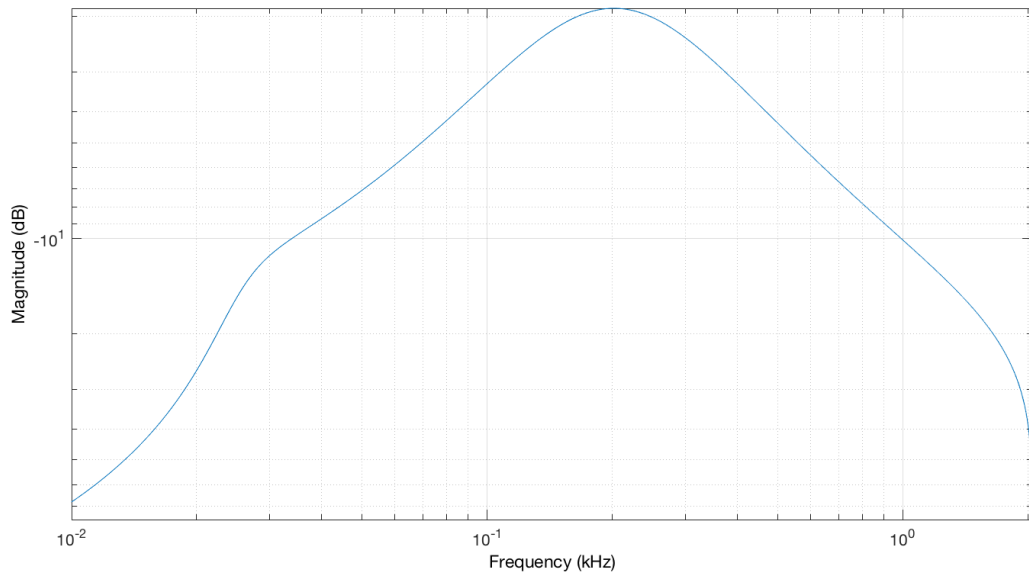


FIGURE 2.32: Whitening filter frequency response for normalising spectra seen in Figure 2.30.

The whitening filter is made up of a cascade of Butterworth low and high pass filters. Table 2.2 lists the three filters used to make up the whitening filter cascade.

Filter Type	Cutoff Frequency	Order
Highpass	25Hz	6
Highpass	100Hz	1
Lowpass	400Hz	1

TABLE 2.2: Whitening cascade filter parameters

By applying this filter to both the H1 and L1 data sets it can be seen in Figure 2.33 that the magnitude is now more normalised over frequency. Some frequency regions differ in magnitude between the two detectors. Particularly between 10 Hz and 30 Hz the L1 magnitude is larger than the H1 magnitude. To change this a more complicated set of filters could be applied to the L1 data however for this example the same whitening filter is applied to both.

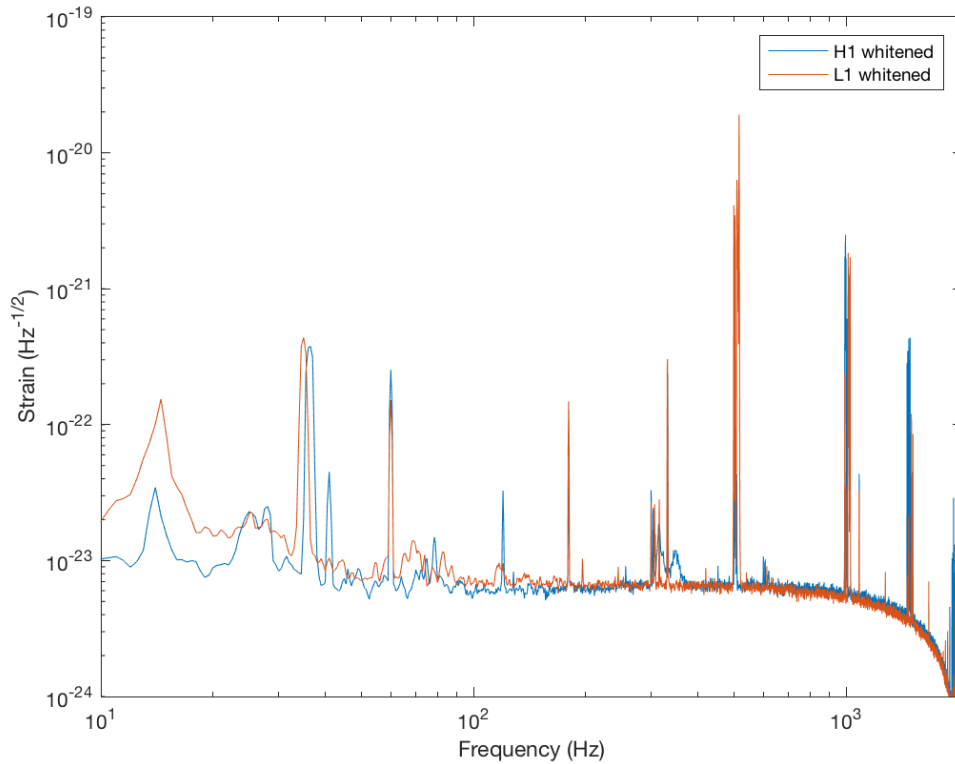


FIGURE 2.33: Spectrum of DARM data from both interferometers during GW150914 event after whitening filter.

2.4.4 Peak finding

After whitening the data the line removal process can then be applied to the whitened data. Firstly a function in MATLAB called `findpeaks` is applied to the spectrum data from each interferometer. As implied from its name this function finds the frequency and magnitude of the peaks in the spectrum. The spectrum data used for peak finding is made using a larger window of 100 seconds in order to resolve the narrow lines from one another. The function is set to find lines with a minimum peak prominence of 5×10^{-23} otherwise it picks up regions of background noise as peaks. The frequency locations of each of the lines in the spectrum are identified and sorted from highest to lowest in magnitude. Sorting the lines in this way means that iWave filters out the highest magnitude lines first which subsequently makes it easier for it to lock onto lower magnitude lines. This is particularly necessary for cases where neighbouring lines are within iWave's bandwidth from each other. Another output from the function is the approximate full width at half maximum Γ of each of the lines from the spectrum. This can then be used to set the τ parameter for each filter to be tailored to each peak taking $\tau = \Gamma^{-1}$.

Taking a closer look at some of frequency regions where lines exist it can be seen that these regions are made up of multiple lines. The magnitude and frequency from the lines located using the `findpeaks` function are also plotted here.

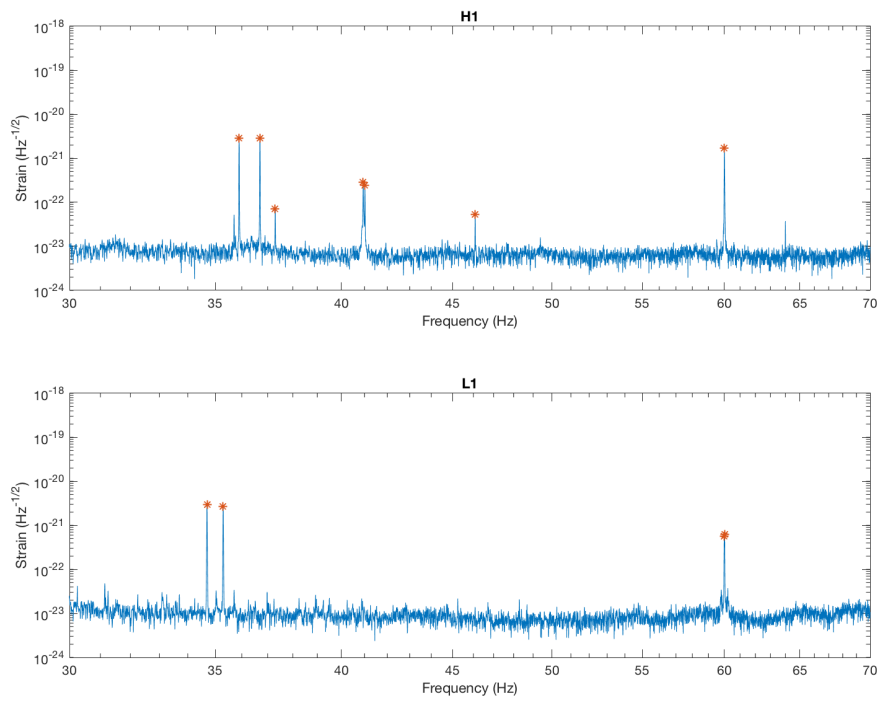


FIGURE 2.34: Lower frequency mechanical modes of test masses. Orange stars represent the output of the peakfinding algorithm used to set iWave's input frequency during recursive line removal.

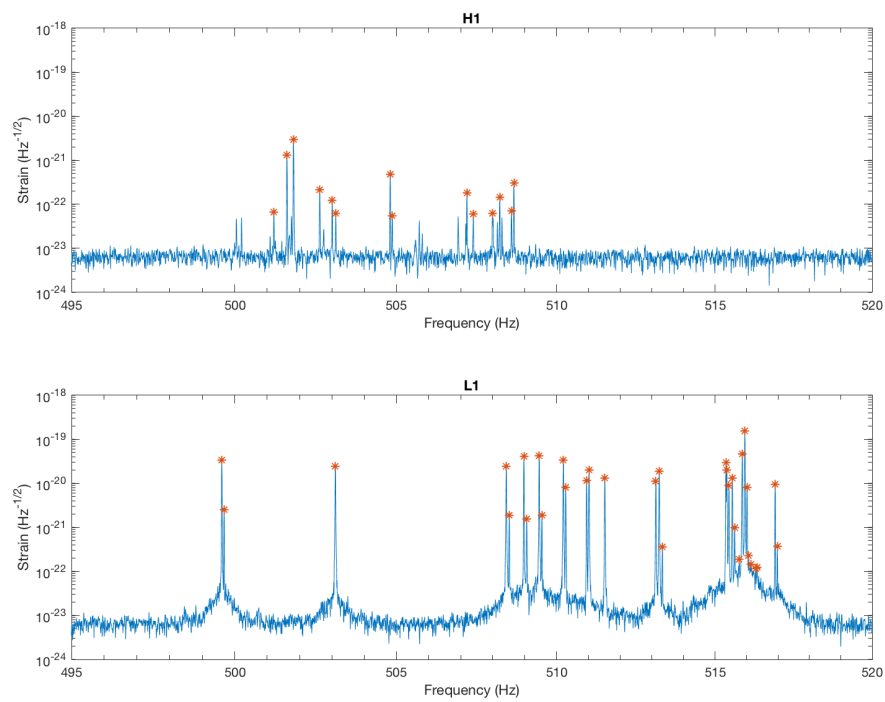


FIGURE 2.35: 500Hz violin mode region. Orange stars represent the output of the peakfinding algorithm used to set iWave's input frequency during recursive line removal.

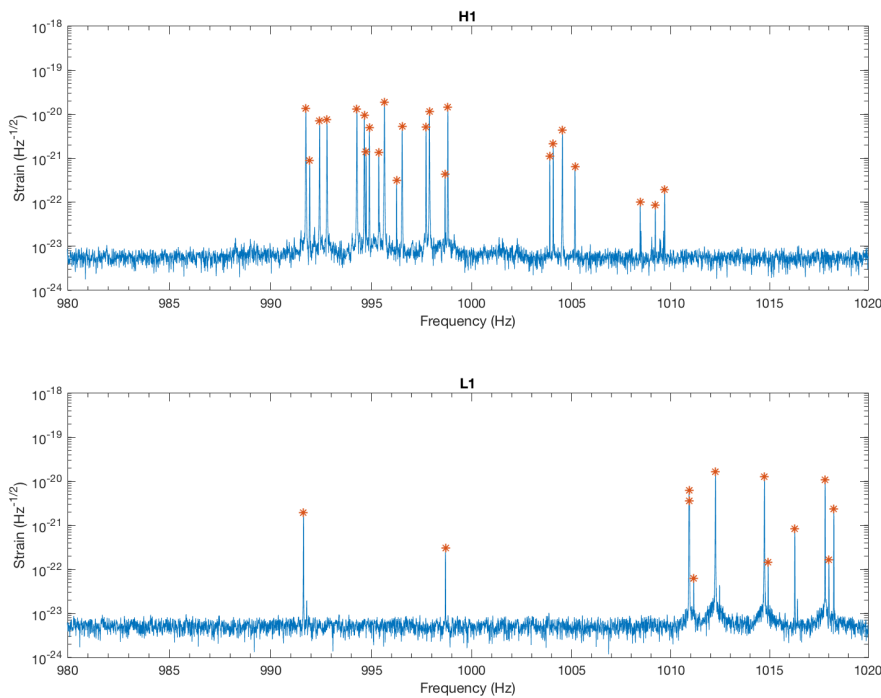


FIGURE 2.36: 1000 Hz violin mode region. Orange stars represent the output of the peakfinding algorithm used to set iWave’s input frequency during recursive line removal.

Figure 2.34 shows the low end frequency lines that were most dominant during the event. There are known lines here around 36 Hz which are calibration lines and the line at 60Hz is the power line from the mains voltage. However in the H1 spectrum there are pair of lines at 41 Hz which were unusual to this spectrum. After investigation these were discovered to have come from an excited roll mode from one of the triple suspensions [1]. Figures 2.35 and 2.36 show the violin mode forests at 500Hz and 1kHz respectively. These are the most predominant lines in the spectrum and also the most difficult to remove. Compared to the H1 spectrum the L1 violin modes are a lot more resonant particularly in the 500Hz region.

2.4.5 Static v.s. dynamic line removal

Before attempting to the full line removal process the differences between using the static and dynamic line tracking are investigated. To test this the largest line from the whitened H1 strain data is filtered using both static and dynamic iWave filtering. Figures 2.37 and 2.38 are generated using the last 200 seconds of the input and output data. The tracker requires a certain amount of time depending on τ to become reach the amplitude of the the line. This means that the line will be more removed at the end of the set of data compared to the beginning. The values of τ in the title of each plot come from the fractions of the width of the peak measured by the findpeaks function.

From Figure 2.37 it can be seen that static filtering does not seem to be able to remove the line completely. This may be due to a few factors for instance the starting

frequency may not be exactly at the frequency of the line as it is measured. The frequency of the peak is an estimate from the spectrum which is not an accurate enough to determine it's exact frequency. As well as this the peak may move in frequency over time to a certain degree. It can also be seen that as the bandwidth of the filter increases with decreasing τ the peak becomes more reduced. This is not surprising as the filter has a larger bandwidth when τ is decreased as well having being faster to reach the amplitude of the line.

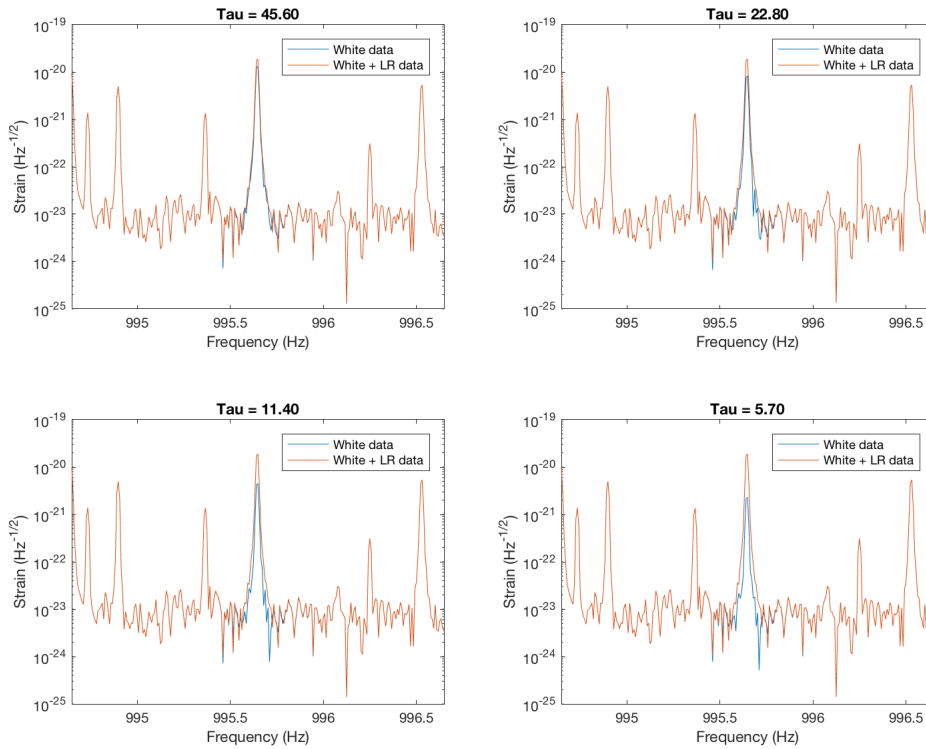


FIGURE 2.37: Static iWave line removal of largest line in H1 spectrum over varying τ .

From Figure 2.38 it is obvious that dynamic line tracking is more effective for this line. When the closed loop version of iWave is applied it can estimate the frequency of the line and adjust the filter accordingly. If the starting frequency of the tracker is exactly the frequency of the line then the dynamic line tracker will adjust its frequency to align with the region with the most signal. As well as this if there are any changes in the line's frequency over time the dynamic tracker will adjust the tracking frequency similarly. The three smaller values of τ ($\Gamma^{-1}/2$, $\Gamma^{-1}/4$ and $\Gamma^{-1}/8$) are able to remove the line by the last 200 seconds of the set of data.

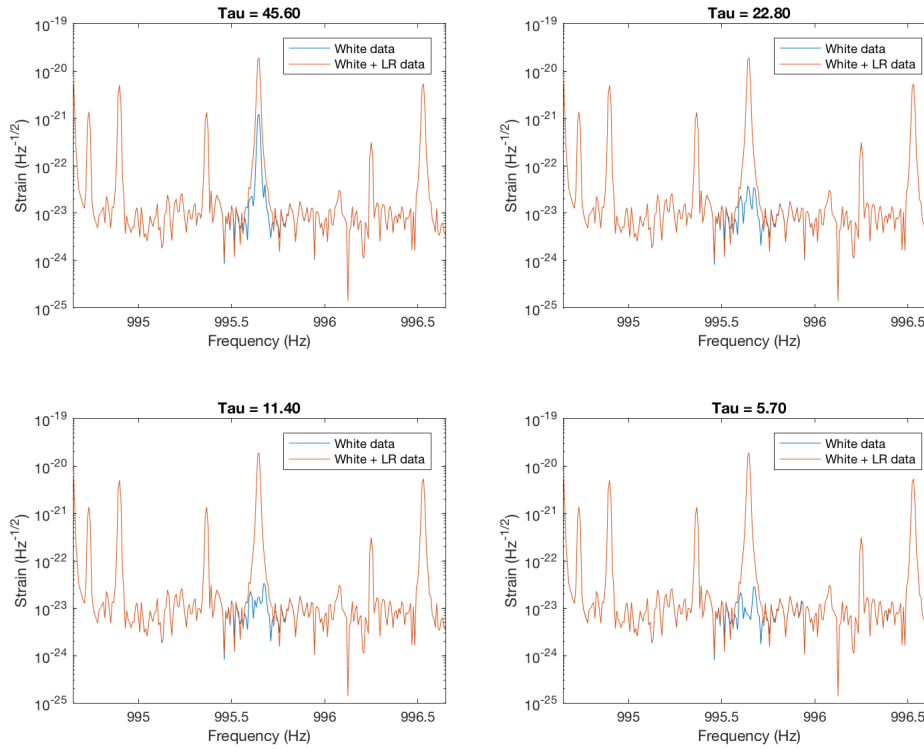


FIGURE 2.38: Dynamic iWave line removal of largest line in H1 spectrum over varying τ . Dynamic line removal is more successful than the static line removal from Figure 2.37.

2.4.6 Recursive line removal

After identifying where the lines are for each data set the iterative line removal can begin. Each of the lines in the spectrum found from the findpeaks function are iteratively filtered from both the H1 and L1 whitened data using iWave. This is done by filtering out the first highest magnitude line from the full data and then filtering out the next highest magnitude line from this filtered data and so on. Fractions of the line width $\Gamma^{-1}/2$, $\Gamma^{-1}/4$ and $\Gamma^{-1}/8$ are used in the following results.

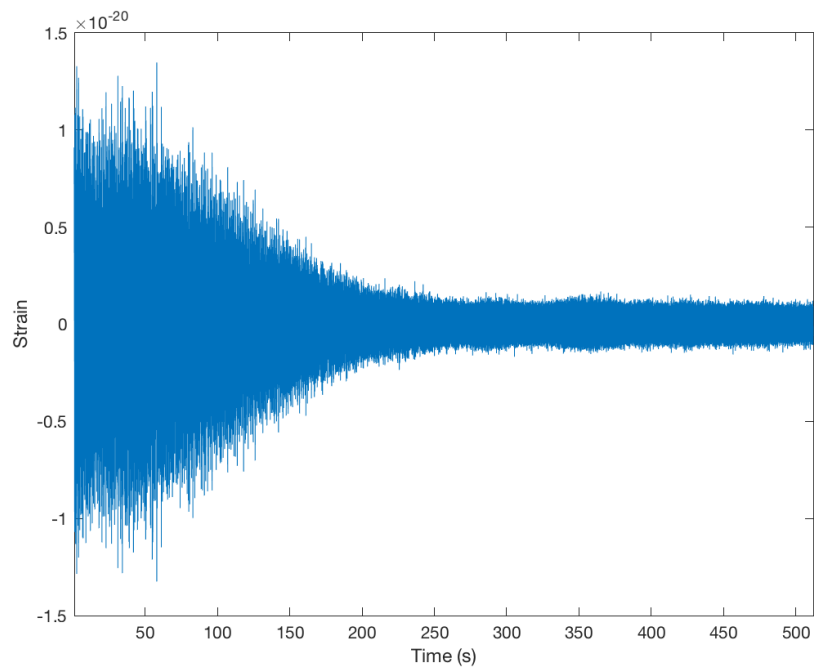


FIGURE 2.39: Whitened H1 data after iterative line removal using $\tau = \Gamma^{-1}/2$

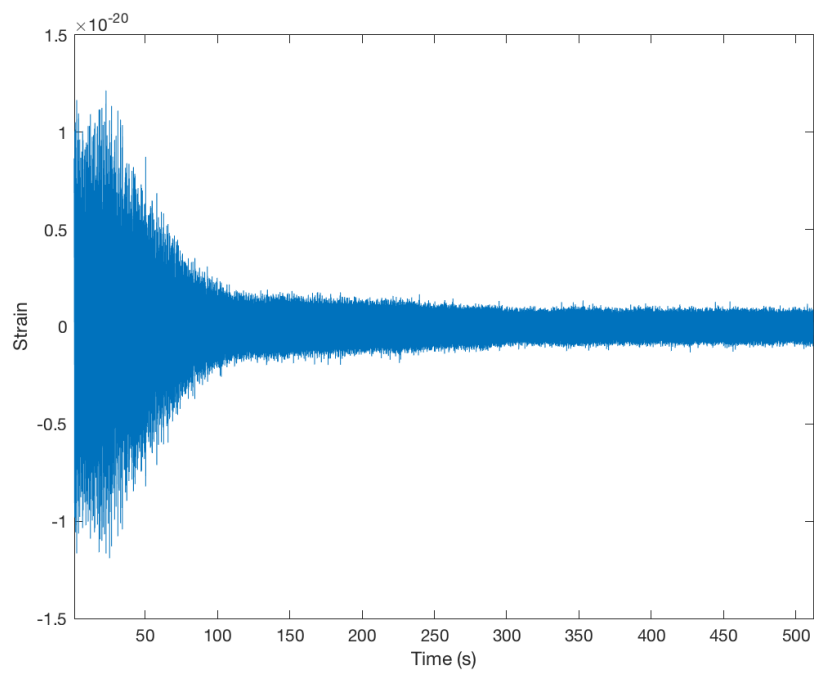


FIGURE 2.40: Whitened H1 data after iterative line removal using $\tau = \Gamma^{-1}/4$

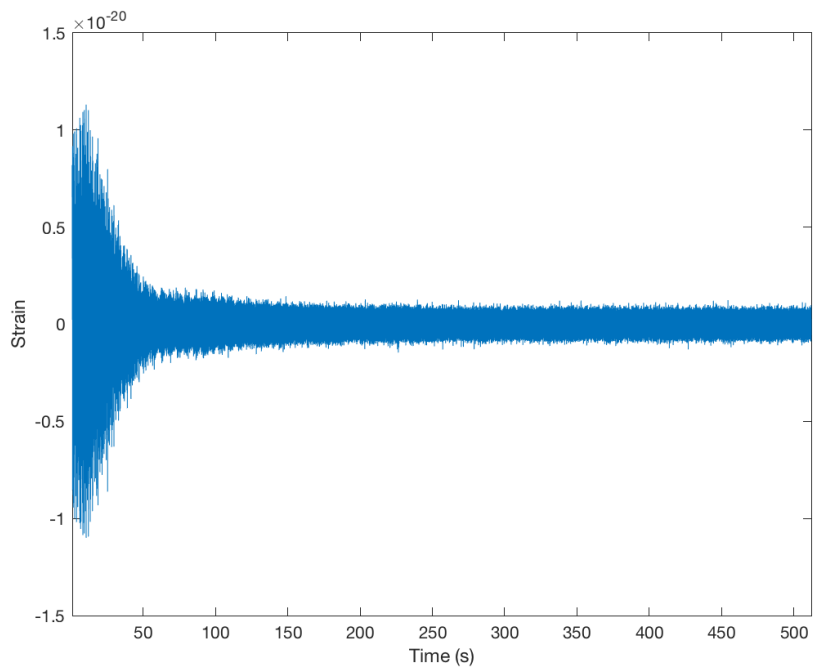


FIGURE 2.41: Whitened H1 data after iterative line removal using $\tau = \Gamma^{-1}/8$

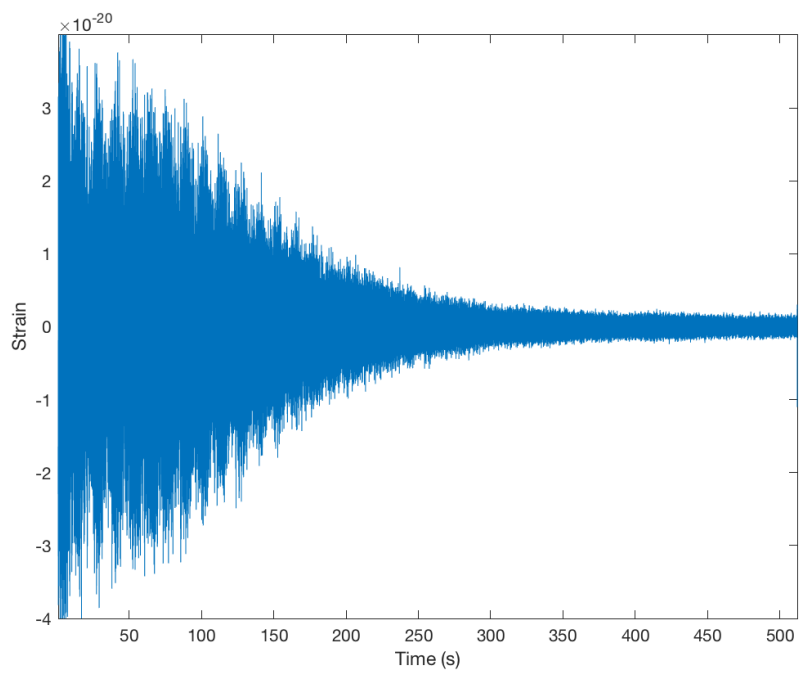


FIGURE 2.42: Whitened L1 data after iterative line removal using $\tau = \Gamma^{-1}/2$

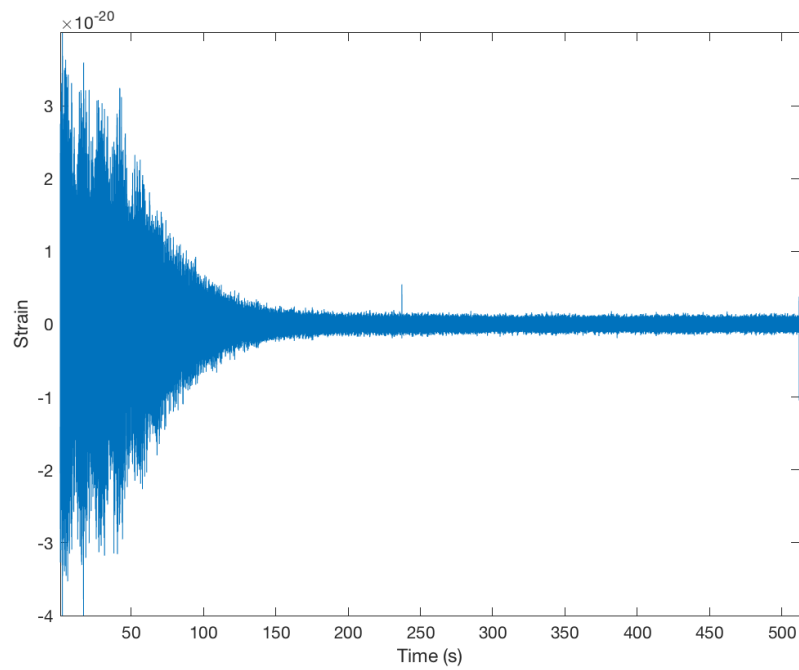


FIGURE 2.43: Whiten L1 data after iterative line removal using $\tau = \Gamma^{-1}/4$

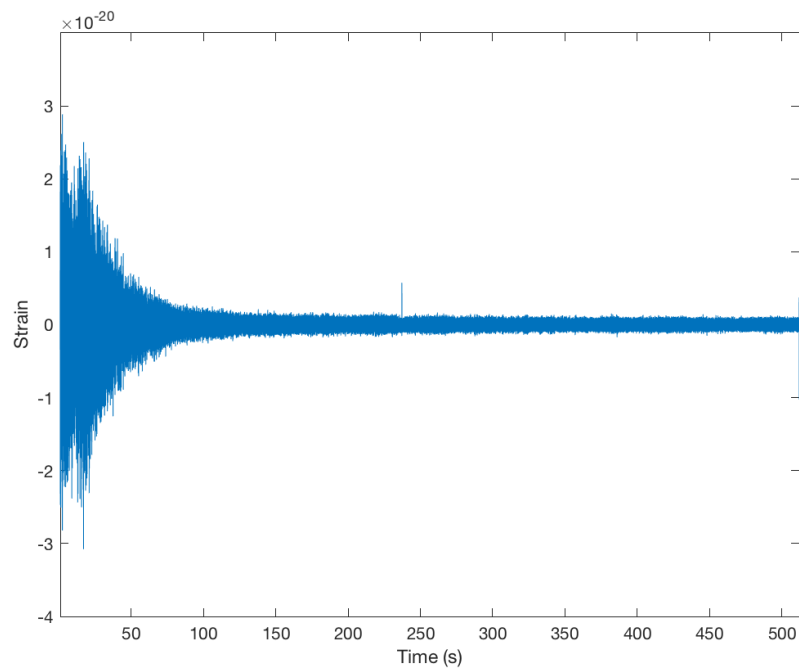


FIGURE 2.44: Whiten L1 data after iterative line removal using $\tau = \Gamma^{-1}/8$

From the time series figures above, it can be seen that most of the lines can be removed by 250 seconds. By this time most of the strain signal has reached a constant background noise level. Again for decreasing τ the time that it takes for these line

to be critically damped is also reduced. From these plots the most effective value of τ for the line removal was taken to be $\tau = \Gamma^{-1}/8$. This value reduces the time series data to the same background noise only faster indicating that even the broadest filter manages to track the lines to the same degree.

The performance of the iterative line removal can be seen to differ between H1 and L1. Looking at the spectrums from the last 200 seconds of the line removed data it seems that line removal is more successful for H1 than L1. This can especially be seen in the 500Hz region where most of the lines are removed from the H1 data and some remnants of the lines remain for the L1 data. From Figure 2.35 it can be see that this region contains a significant amount of higher noise around the L1 violin modes compared to the H1 violin modes indicating that this is the reason the lines are more difficult to track with iWave.

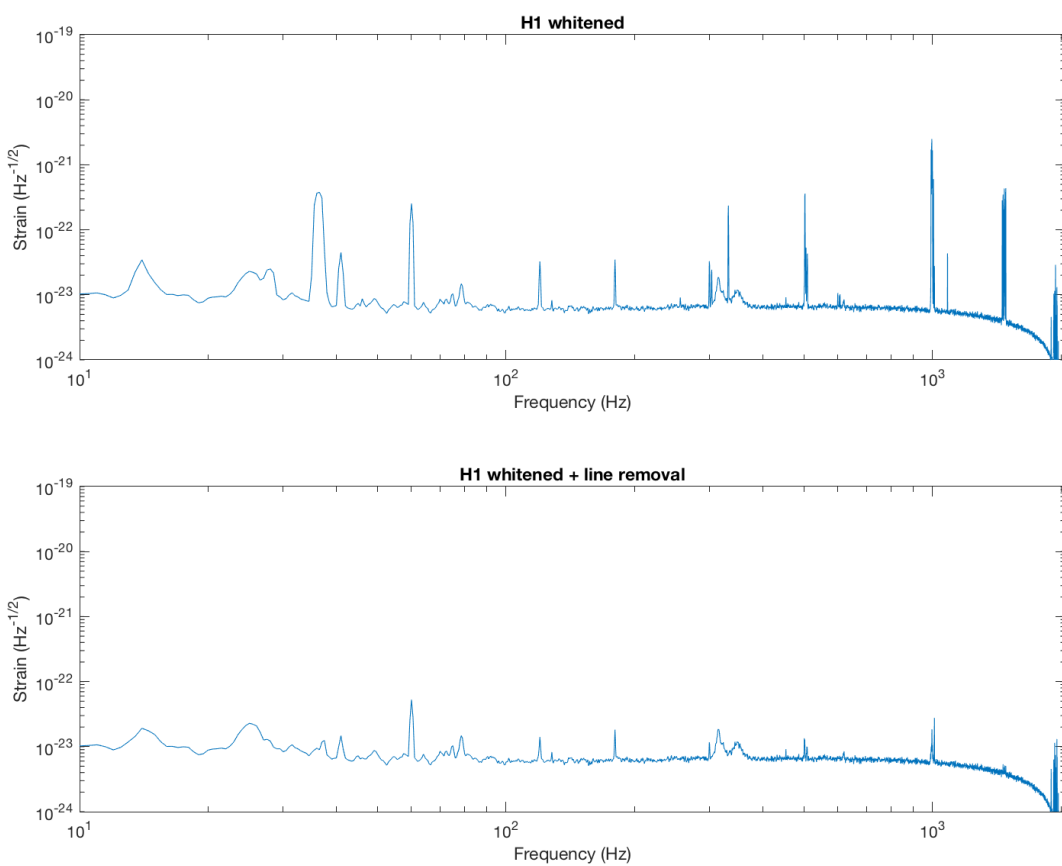


FIGURE 2.45: H1 spectrum comparison before and after recursive iWave line removal. All line regions are reduced in magnitude by iwave while leaving the structure of the background the same.

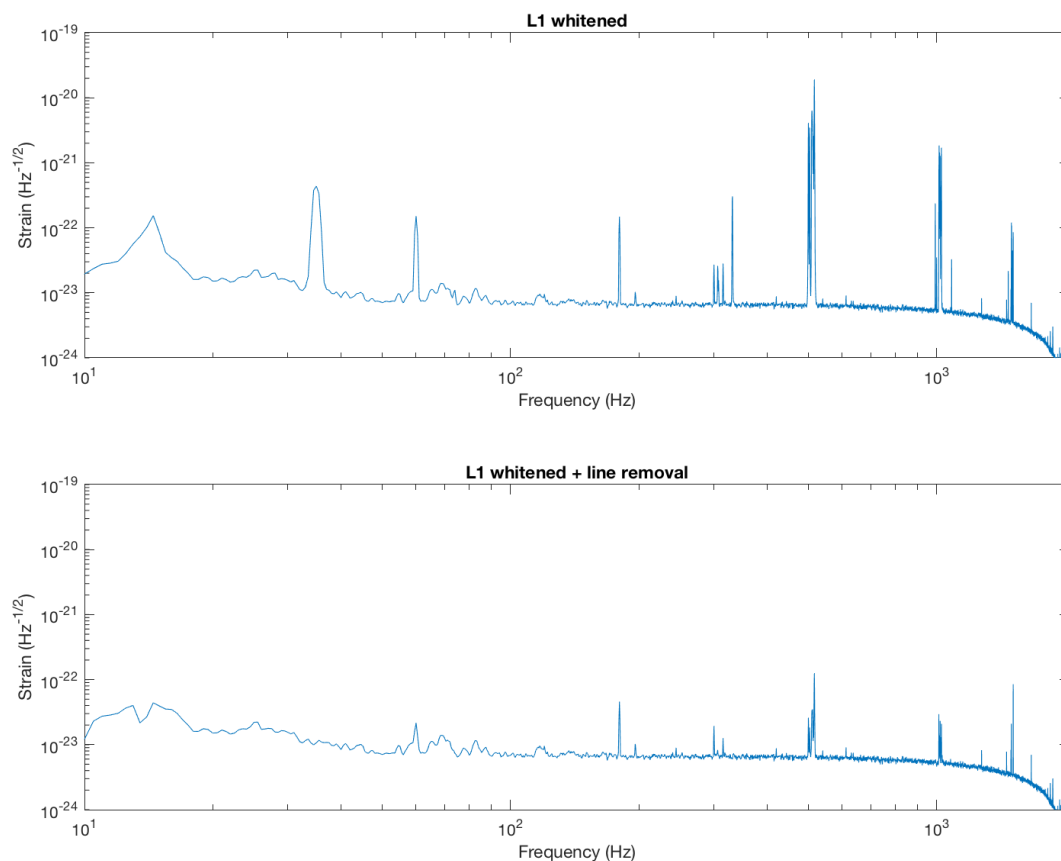


FIGURE 2.46: L1 spectrum comparison before and after recursive iWave line removal. All line regions are reduced in magnitude by iwave while leaving the structure of the background the same. Due to the larger amount of resonant violin modes the 500 Hz region is not as reduced compared to Figure 2.45

Despite applying line removal some lines still persist in the data. Applying another round of filtering can remove even more of these residual lines from the data. The same process of recursive line removal was applied to the data another two times in order to reduce the lines further.

Figures 2.47 and 2.48 show the cumulative sum of the spectrums with increasing frequency. In the whitened data without line removal, regions where lines exist cause large increases in the cumulative sum indicating that the sensitivity over this region has decreased. The cumulative sum for the line removed data show significantly less of an increase in comparison. Comparing the total sum of spectral density over all frequencies gives the increase in sensitivity given by iWave line removal for both the H1 and L1 data sets. For the H1 data the cumulative spectrum was decreased from $5.1924\text{e-}20$ to $2.8586\text{e-}21$ by iWave line removal. Similarly for the L1 data the cumulative spectrum was decreased from $2.3872\text{e-}19$ to $2.9521\text{e-}21$ by iWave line removal. Line removal by iWave increases the sensitivity of the H1 data by a factor of 18.2 and increases the sensitivity of the L1 data by a factor of 80.9. This increase in sensitivity is only limited to the regions where the lines were present in the data.

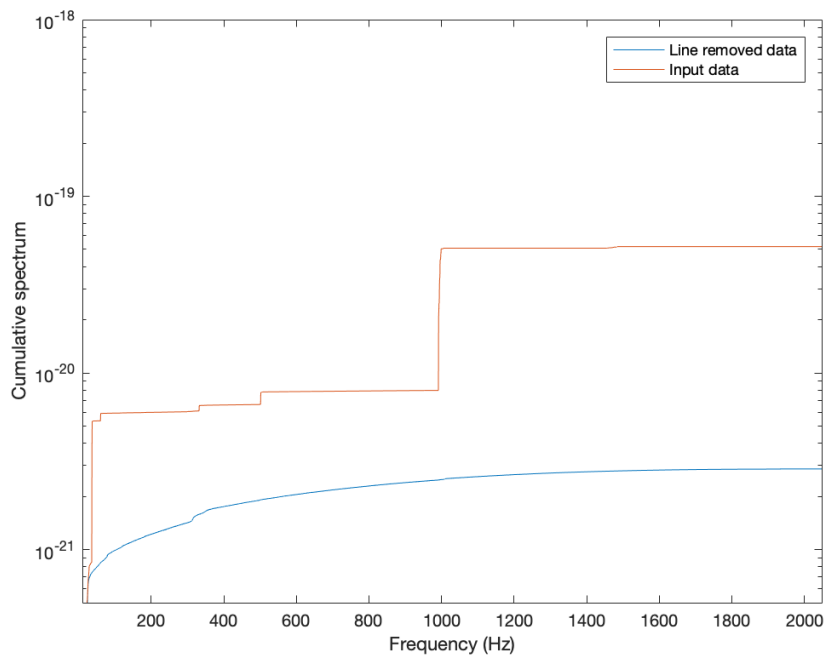


FIGURE 2.47: H1 cumulative spectrum comparison before and after recursive iWave line removal. Line removal reduces the total cumulative sum from $5.1924e-20$ to $2.8586e-21$ increasing the total sensitivity by a factor of 18.2.

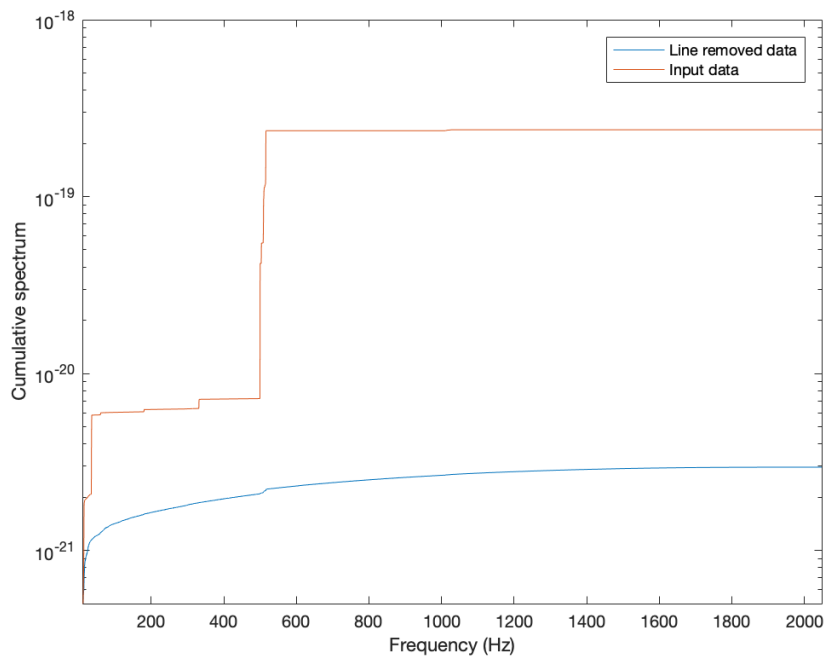


FIGURE 2.48: L1 spectrum comparison before and after recursive iWave line removal. Line removal reduces the total cumulative sum from $2.3872e-19$ to $2.9521e-21$ increasing the total sensitivity by a factor of 80.9.

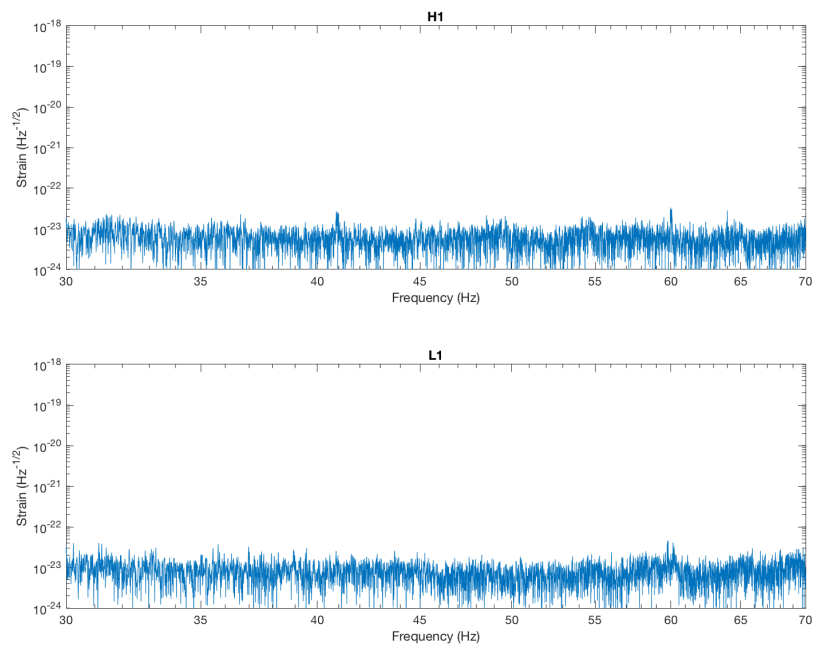


FIGURE 2.49: Lower frequency mechanical modes of test masses after line removal process. There is a significant reduction in the line amplitude compared to Figure 2.34.

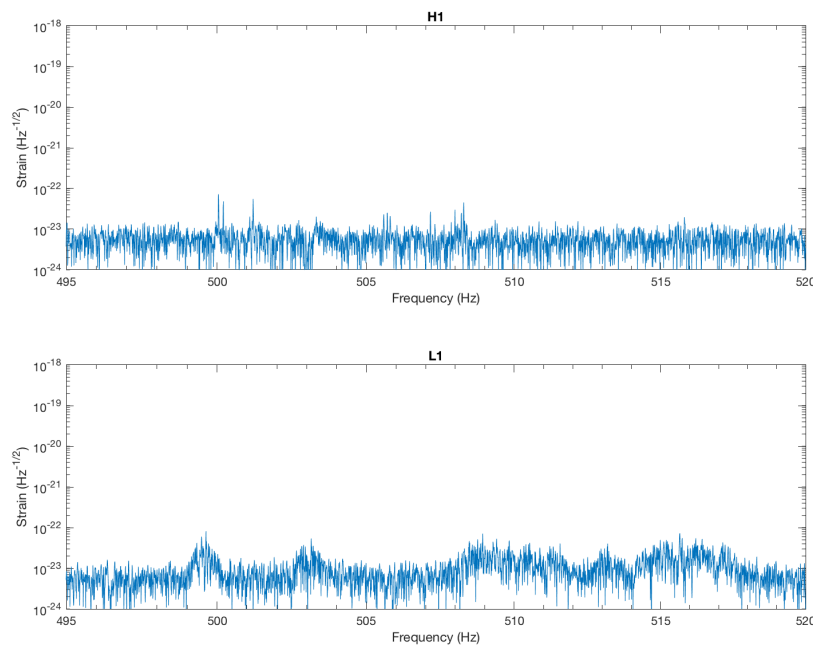


FIGURE 2.50: 500Hz violin mode region after line removal process. There is a significant reduction in the line amplitude compared to Figure 2.35.

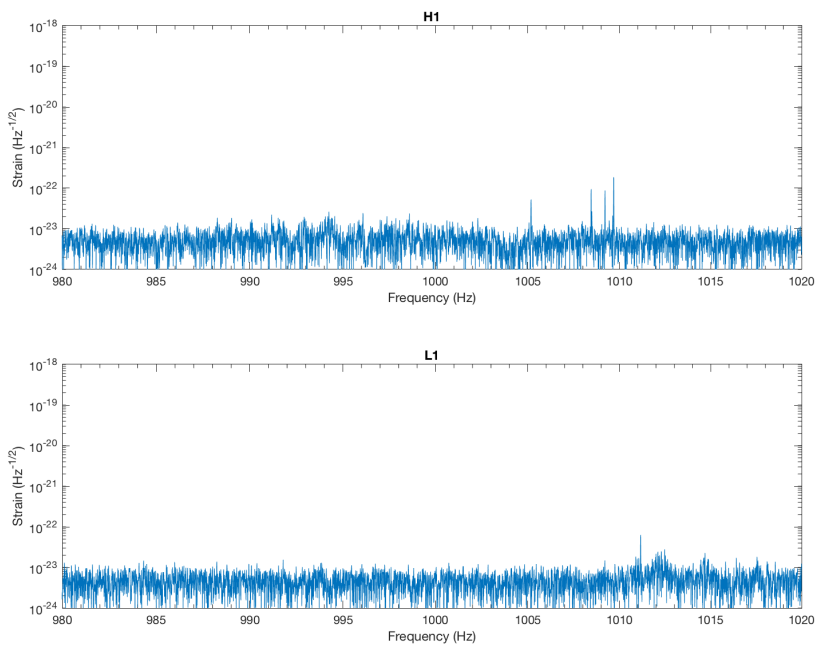


FIGURE 2.51: 1000 Hz violin mode region. after line removal process. There is a significant reduction in the line amplitude compared to Figure 2.36.

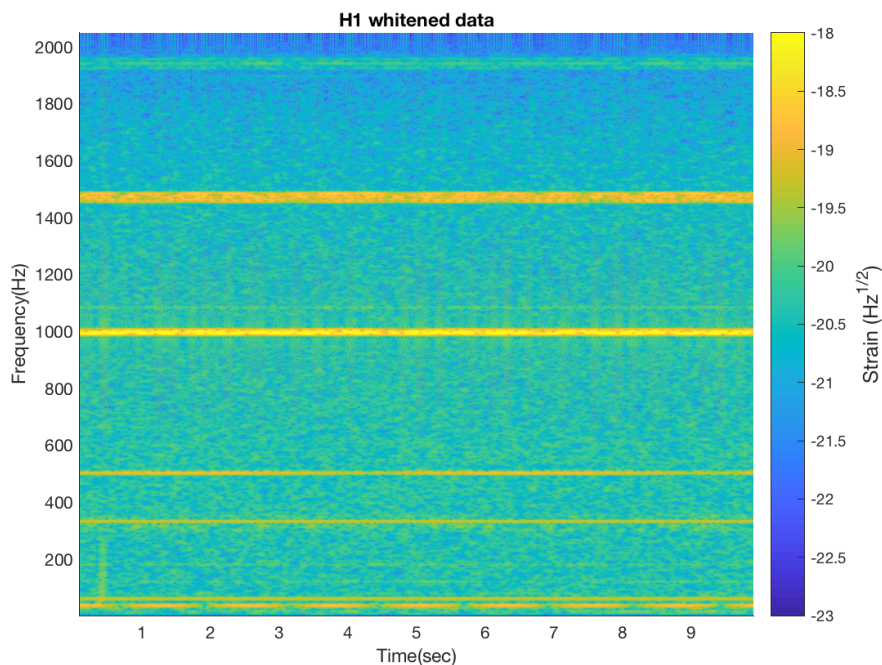


FIGURE 2.52: Spectrogram data from Hanford detector before iterative line removal is applied. GW150914 signal can be seen in at lower frequencies between 0 to 0.5 seconds.

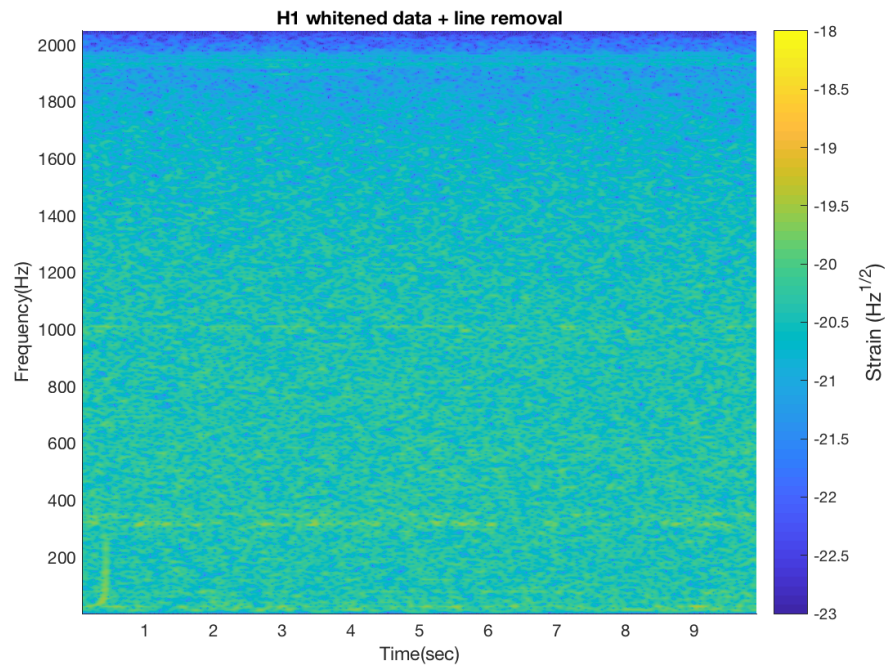


FIGURE 2.53: Spectrogram data from Hanford detector after iterative line removal is applied. GW150914 signal can be seen in at lower frequencies between 0 to 0.5 seconds.

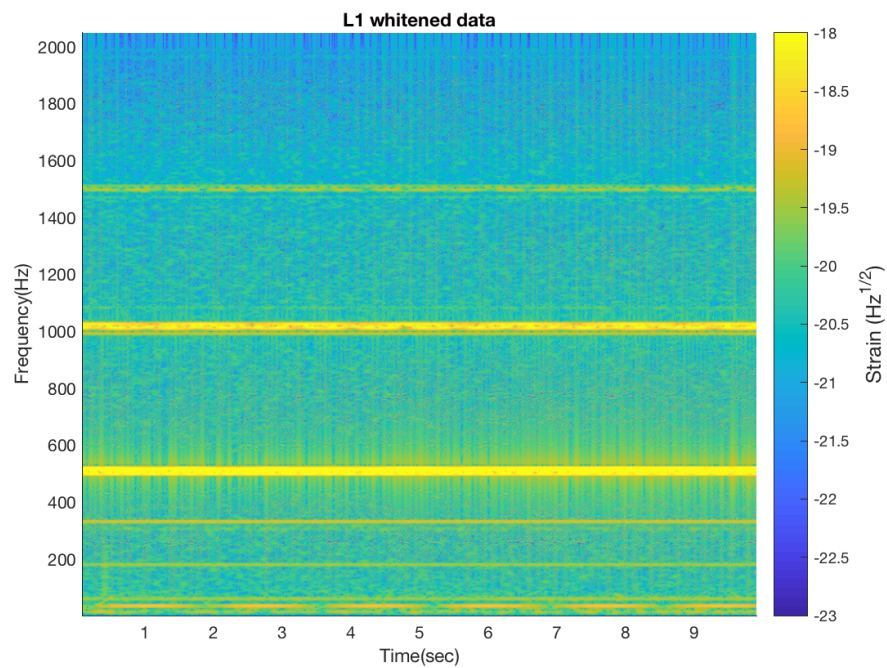


FIGURE 2.54: Spectrogram data from Livingston detector before iterative line removal is applied. GW150914 signal can be seen in at lower frequencies between 0 to 0.5 seconds.

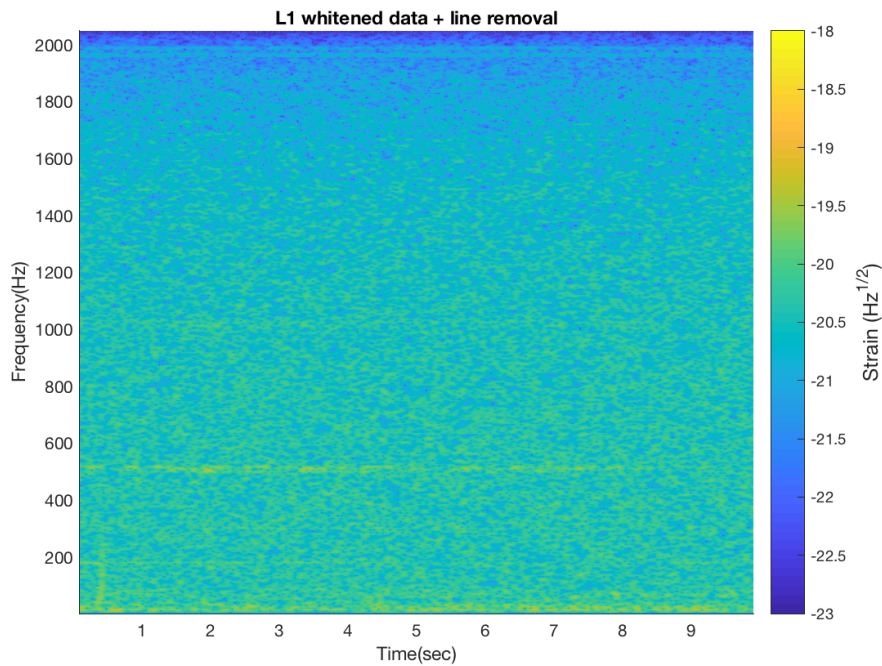


FIGURE 2.55: Spectrogram data from Livingston detector after iterative line removal is applied. GW150914 signal can be seen in at lower frequencies between 0 to 0.5 seconds.

Comparing the spectra between the Figures 2.34, 2.35, 2.36 and Figures 2.49, 2.50, 2.51 it is obvious that the lines have been reduced by a significant amount after iWave line removal. Spectrograms of the strain data before and after iterative line removal in Figures 2.52, 2.53, 2.54 and 2.55. In these spectrograms 10 seconds of data around the event's chirp signal are plotted where the event itself is in the first second of the data.

The time-series data of the line removed data around this event reveals the waveform itself. Figure 2.56 shows the overlaid time-series for the H1 and L1 data where the chirp signal is visible at around 0.1 seconds. The L1 data is delayed by 0.07 seconds to account for the time of flight between detectors and the H1 data is inverted to account for the relative orientation of the detectors. This result shows that the same filtered signal observed in the GW150914 event paper [12] can be acquired using iWave to whiten the data.

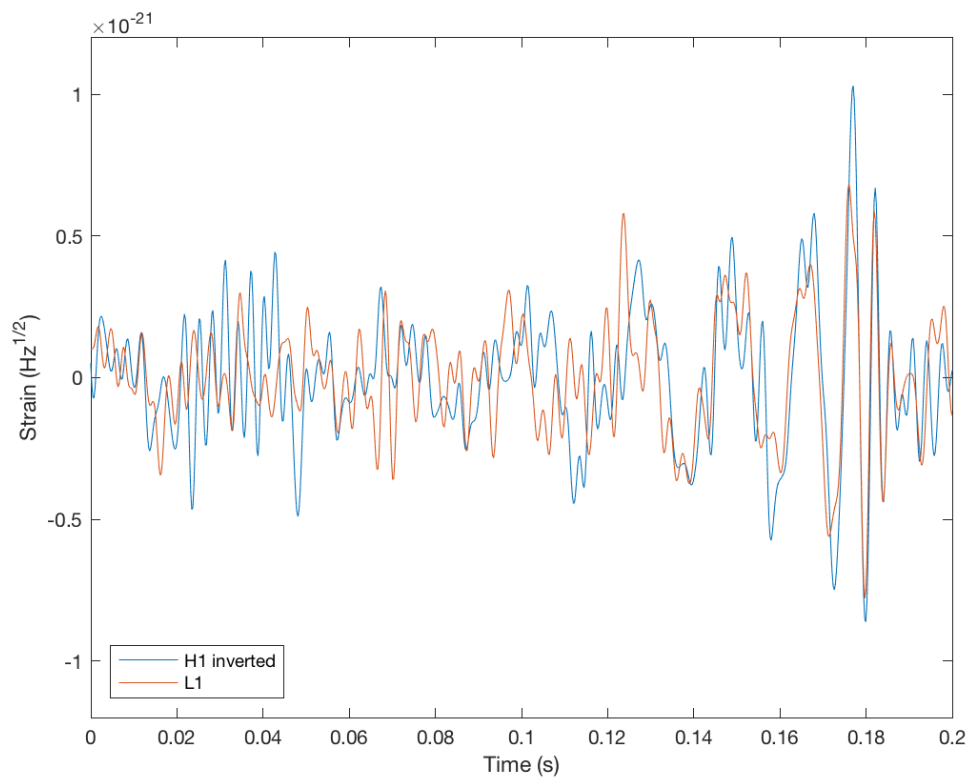


FIGURE 2.56: Overlaid H1 and L1 time-series of GW150914 event after iWave line-removal processing. Similar to the whitened time-series shown in Figure 1.3 but achieved through iWave line removal method.

Chapter 3

Parametric Instabilities

3.1 Introduction

Parametric instabilities (PI) pose a limiting factor to increasing the sensitivity of LIGO detectors. Higher power in the cavities yields a decrease in shot noise but also increases the likelihood of PI forming. They are created from an opto-mechanical feedback between radiation pressure and the mechanical mode of the test mass. Until recently they have been avoided by changing the temperature of the test masses using ring heaters [19] which moves mode spacing away from the frequency region where mechanical modes exist. However as the power in the cavity continues to increase this will no longer be a viable option. One alternative approach is to use electro-static drivers (ESD) to damp the test masses at the mechanical mode frequency excited the instability.

In this chapter we outline the theory of how these instabilities are formed. We then describe the development of the damping scheme used to mitigate PI at LIGO Hanford in 2016 as well as the results from implementing this scheme on several known mechanical modes.

This chapter is based on the work I completed as a fellow at the LIGO Hanford site. I worked in collaboration with Tega Edo, Carl Blair and Terra Hardwick to implement the damping scheme for parametric instabilities developed by Carl Blair at the LIGO livingston site. My contribution to this project comes from several aspects. I added and maintained parts of the simulink models to the site front end. I also developed a large portion of the user interfaces which allowed real time control of the damping scheme. I was also responsible for using the damping scheme during locked periods of the detector. All the results in Section 3.4 are from data I collected during these locked periods.

3.2 PI theory

The source of PI is from the interaction between TEM modes of the laser inside the Fabry-Perot cavity and the mechanical modes of a test mass. In this section the solutions for higher order TEM modes are derived from Maxwell's Equations. The feedback loop which causes the test mass mechanical modes to ring up will also be discussed.

3.2.1 Gaussian beam mode

For the following derivations we follow the theory described in Lasers by Siegmann [67]. The fundamental mode of a laser in a cavity is the Gaussian beam. Using Maxwell's Equations we can derive the Helmholtz equation also known as the time independent wave equation.

$$(\nabla^2 + k^2)\Psi(x, y, z) = 0 \quad (3.1)$$

Where $k = 2\pi/\lambda$ is the wave number and Ψ is the complex electric field. From now on we can consider the light source to be a beam propagating in the z direction with only slow variations in the transverse directions. If we assume that the electric field is perpendicular to the direction of propagation then we rewrite this equation as.

$$(\nabla^2 + k^2)\psi(x, y, z) \exp(-ikz) = 0 \quad (3.2)$$

Since we are not considering a pure plane wave solution, ψ here represents the directional dependence of a laser beam. The solution to this equation then becomes;

$$\frac{\partial^2 \psi}{\partial x^2} + \frac{\partial^2 \psi}{\partial y^2} + \frac{\partial^2 \psi}{\partial z^2} - 2ik \frac{\partial \psi}{\partial z} = 0 \quad (3.3)$$

If we assume paraxial behavior i.e. the variation of the field in the direction of propagation is small over the distance comparable to a wavelength then we can assume that $\frac{\partial^2 \psi}{\partial z^2} \approx 0$.

$$\nabla_T^2 \psi - 2ik \frac{\partial \psi}{\partial z} = 0 \quad (3.4)$$

Where $\nabla_T^2 = \frac{\partial^2}{\partial x^2} + \frac{\partial^2}{\partial y^2}$. This is what is known as the paraxial equation. In cylindrical coordinates this may also be written as

$$\frac{1}{r} \frac{\partial}{\partial r} \left(r \frac{\partial \psi}{\partial r} \right) - 2ik \frac{\partial \psi}{\partial z} = 0 \quad (3.5)$$

Where $r = \sqrt{(x^2 + y^2)}$ is the distance perpendicular to the axis of propagation.

The paraxial equation can support an infinite number of solutions. The most general of these solutions is that of a Gaussian Beam. This is because it stays Gaussian upon propagation through optical systems i.e. the Fourier transform of a Gaussian is a Gaussian. It is also the lowest order resonant mode in a cavity with spherical mirrors. The Gaussian solution is expressed by

$$\psi(x, y, z) = \sqrt{\frac{2}{\pi\omega^2(z)}} \exp \left[-\frac{r^2}{\omega^2(z)} - \frac{ikr^2}{2R(z)} - i(kz - G(z)) \right] \quad (3.6)$$

The main defining parameters of this equation are the spot size $\omega(z)$, the radius of curvature of the wave front $R(z)$ and the *Gouy phase* $G(z)$. The *spot size* is the distance from the axis of propagation at which the beam intensity drops by I_{max}/e^2 . This is

related to another parameter called the waist size which is the minimum value of $w(z)$.

$$w(z) = w_0 \sqrt{1 + \left(\frac{z}{z_R}\right)^2} \quad (3.7)$$

When at the focal point of the beam $z = 0$ the waist size is at it's minimum $w(z) = w_0$. Note that when $z = z_R$ the spot size has increased by a factor of $\sqrt{2}$. The value of z_R here is known as the Rayleigh length scale and is defined by

$$z_R = \frac{\pi w_0^2}{\lambda} \quad (3.8)$$

This parameter is also used to define the radius of curvature of the wavefront $R(z)$

$$R(z) = z \left(1 + \left(\frac{z_R}{z}\right)^2\right) \quad (3.9)$$

We can also see that when at the beam waist the radius of curvature of the wave front is flat i.e. $R_z = 0$. Where at a distance of z_R from the beam waist R_z has increased to $2z_R$.

The Gouy phase represents the phase shift of the beam compared to a plane wave [43].

$$G(z) = \arctan\left(\frac{z}{z_R}\right) \quad (3.10)$$

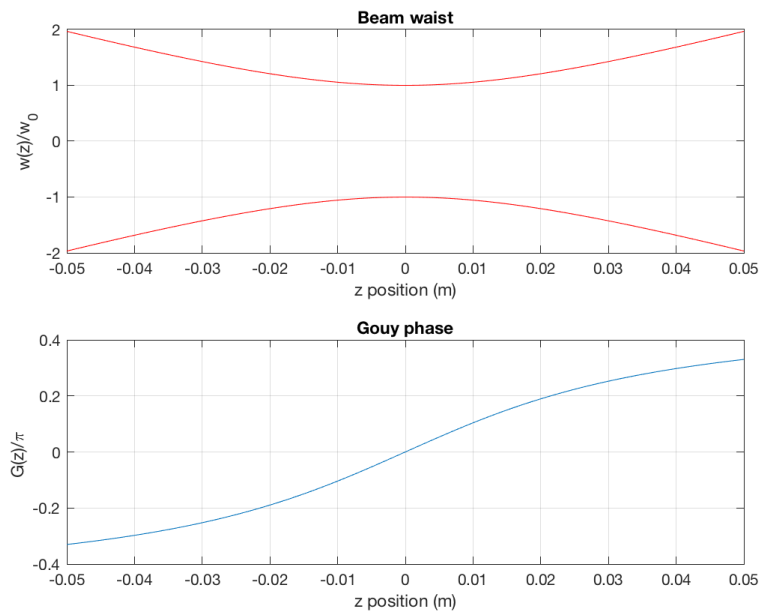


FIGURE 3.1: Properties of a Gaussian beam with wavelength 1064nm and waist size 100 μm . Top plot: Beam waist as a function of z position. Bottom plot: Gouy phase as a function of z position

3.2.2 Higher order modes

Although the predominant solution to Equation 3.5 is the Gaussian mode, other solutions exist in the form of higher order modes. Similarly to standing waves on a string, higher order modes can occur in an optical cavity where the beam is reflected between mirrors. Two of the mode groups discussed in this section are Hermite-Gaussian modes and Laguerre-Gaussian modes.

Hermite-Gaussian modes are a set of solutions to the Equation 3.5 in Cartesian coordinates.

$$\begin{aligned} \psi_{pq}(x, y, z) = & \sqrt{\frac{2}{2^{m+n} m! n! \pi w(z)^2}} H_p\left(\sqrt{2} \frac{x}{w(z)}\right) H_q\left(\sqrt{2} \frac{y}{w(z)}\right) \\ & \times \exp\left(\frac{r^2}{w^2(z)} - i \left[kz - (1 + p + q)G(z) + \frac{r^2}{2R(z)} \right]\right) \end{aligned} \quad (3.11)$$

The $H_p\left(\sqrt{2} \frac{x}{w(z)}\right)$ and $H_q\left(\sqrt{2} \frac{y}{w(z)}\right)$ terms here are Hermite polynomials of order p and q as a function of x and y .

Laguerre-Gaussian modes are also a solution to the paraxial equation but in polar coordinates.

$$\begin{aligned} \psi_{pq}(\rho, \phi, z) = & 2 \sqrt{\frac{p!}{(1 + \delta_{0q}) \pi (p + q)! w(z)}} \frac{1}{w(z)} (\cos q \phi) \\ & \times \left[\frac{\sqrt{2} \rho}{w(z)} \right]^2 L_p^q \left(\frac{2\rho^2}{w(z)^2} \right) \\ & \times \exp\left(\frac{-\rho^2}{w(z)^2} + i \left[\frac{k\rho^2}{2R(z)} - (p + q + 1)G(z) \right]\right) \end{aligned} \quad (3.12)$$

The $L_p^q\left(\frac{2\rho^2}{w(z)^2}\right)$ term is the Laguerre polynomial as a functions of ρ . Since both Hermite-Gaussian and Laguerre-Gaussian modes make up complete sets, any Laguerre-Gaussian mode can be represented in terms of Hermite-Gaussian modes and vice-versa [45]. When either sets of higher order mode are in their ψ_{00} they return to the fundamental Gaussian mode represented in Equation 3.6. Since any of the higher order modes are solutions to the paraxial equation, they are also always present in a laser beam. Various beam profiles for these modes are shown in Figure 3.2.

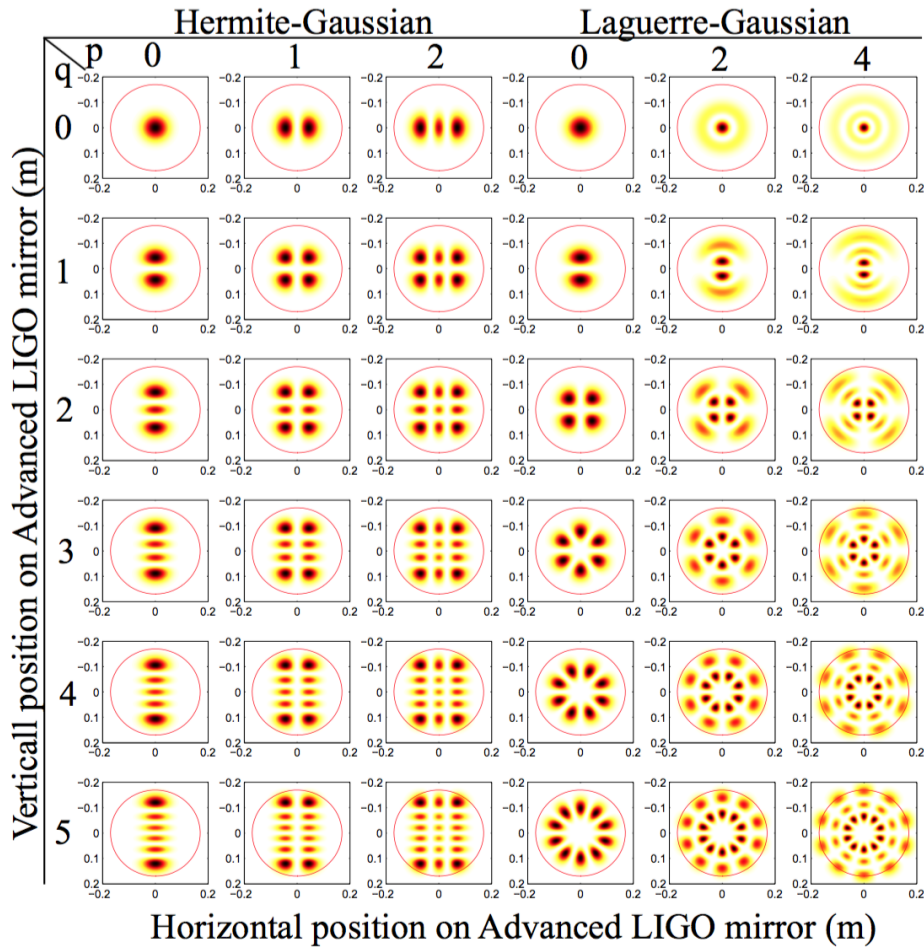


FIGURE 3.2: Beam profiles for low order Hermite-Gaussian and Laguerre-Gaussian modes [16].

The separation in frequency between the fundamental Gaussian mode and any higher order mode of order $n = p + q$ is given by,

$$\Delta\omega_n = \omega_0 - \omega_n = \frac{c}{L}(p + q) \arccos \left(\pm \sqrt{\left(1 - \frac{L}{R_1}\right)\left(1 - \frac{L}{R_2}\right)} \right) \quad (3.13)$$

Equation 3.13 gives the mode spacing in a cavity of length L and mirrors with radius of curvature (RoC) R_1 and R_2 .

3.2.3 Mechanical mode interaction

The fundamental Gaussian mode of a beam can lose energy via interaction with the mechanical modes of the mirrors in the cavity. Light is scattered by this interaction causing sidebands to appear at frequencies $\omega_0 \pm \omega_m$. This is known as Stokes process for the lower sideband and anti-Stokes process for the higher frequency sideband [44].

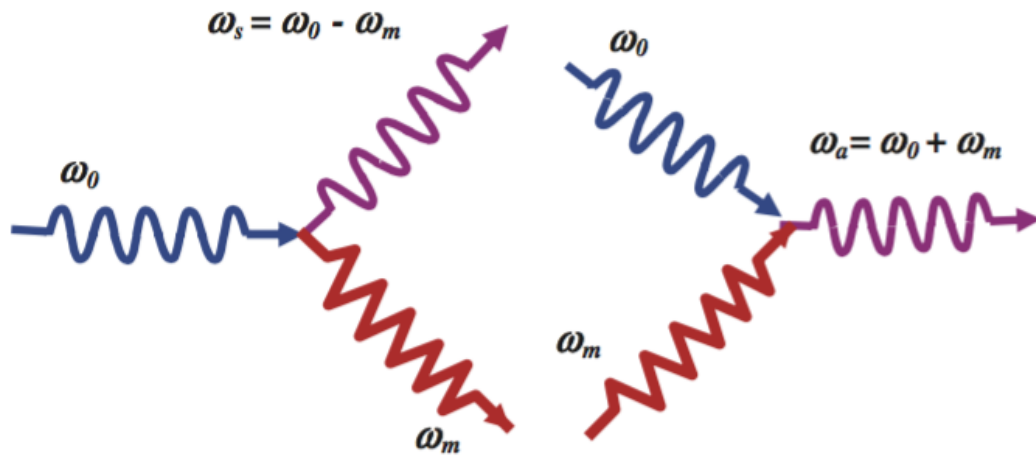


FIGURE 3.3: Stokes and anti-Stokes scattering [44]. For Stokes scattering (left) a photon from the fundamental laser mode is absorbed by the mirror adding energy into the mechanical mode and Higher order mode. Anti-Stokes scattering is where energy from the mechanical mode is transferred to the Higher order mode through interaction with a photon from the fundamental laser mode.

In the case of Stokes scattering, radiation pressure from the the fundamental mode of the laser is absorbed by the mirror creating a phonon at the mechanical mode frequency. From this process energy is transferred from the fundamental mode of the laser into the mechanical mode of the mirror and into the scattered photon at frequency $\omega_s = \omega_0 - \omega_m$. The opposite process occurs for Anti-Stokes scattering when the fundamental mode of the laser transfers energy from the mechanical mode of the mirror into a photon of frequency $\omega_a = \omega_0 + \omega_m$.

3.2.4 Three mode interaction

Parametric instabilities can be considered as a feedback loop between three modes i.e. the fundamental Gaussian mode (TEM_{00}), the mechanical mode of the mirror and the Higher-order mode of the laser (TEM_{01}). This begins with the Stokes process of scattering light from the fundamental mode ω_{00} into the lower sideband of frequency $\omega_{00} - \omega_m$ via the mechanical mode of the mirror. The TEM_{01} mode becomes resonant with the sideband when their frequencies roughly overlap $\omega_{01} \approx \omega_{00} - \omega_m$. As the TEM_{01} mode increases in magnitude, it begins to beat against the TEM_{00} mode at the frequency of the mechanical mode ω_m . This beating exerts radiation pressure on the surface of the mirror which in turn excites the mechanical mode. As the mechanical mode becomes more resonant more light gets scattered into the TEM_{01} closing the feedback loop.

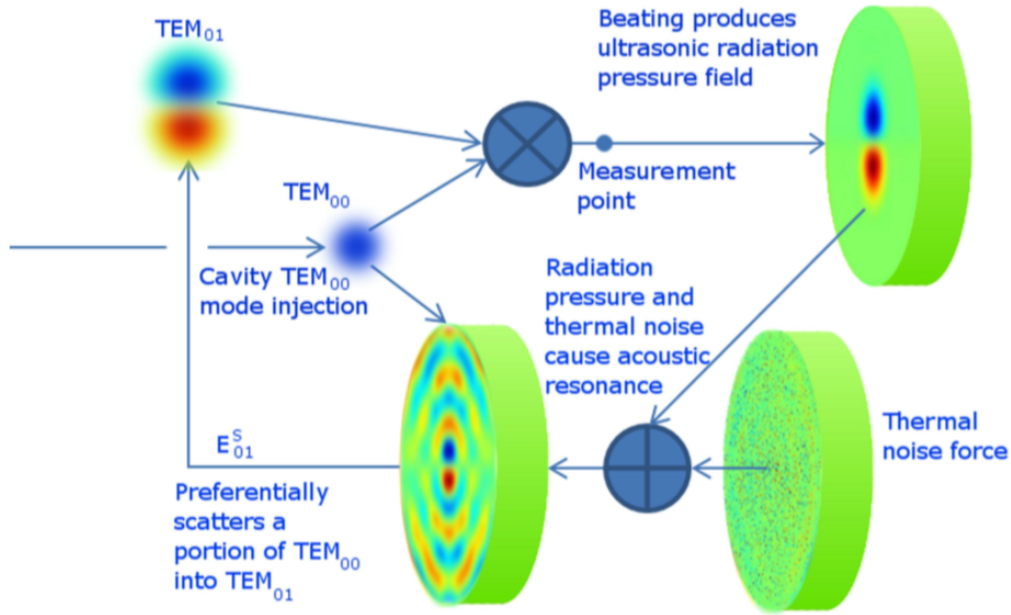


FIGURE 3.4: Three mode interaction [16]. PI are induced due to feedback from the interaction between the mirror mechanical mode, the laser's fundamental Gaussian mode and the laser's Higher-order mode.

3.2.5 Parametric gain

The parametric gain of a mechanical mode m is given by

$$R_m = \frac{4\pi Q_m P}{M\omega_m^2 c\lambda_0} \sum_{n=0}^{\infty} \Re[G_n] B_{m,n}^2, \quad (3.14)$$

where Q_m is the quality factor of the mechanical mode defined as $Q_m = \frac{\omega_m}{\gamma_m}$ where γ_m is the line width of the mechanical mode. The power stored in the arm cavity is given by P , the mass of the mirror is given by M and the wavelength of the laser is given by λ_0 . The optical gain given by G_n is the transfer function of the incident and reflected optical fields on the mirror. The term $B_{m,n}$ is the overlap factor between the mechanical mode m and the TEM mode $n = p + q$. This is the spatial overlap of the TEM mode's beam profile with the surface deformation of the mirror caused by the mechanical mode.

Parametric gain can be used to express the e -folding time of a mechanical modes exponential growth

$$\tau_m = \frac{2Q_m}{\omega_m(R_m - 1)}. \quad (3.15)$$

From Equation 3.15 it can be seen that when $R_m > 1$, the magnitude of the mechanical mode m will exponentially increase. If $R_m = 1$ the mechanical mode will remain

at the same magnitude and if $R_m < 1$ the mechanical mode exponentially decrease in magnitude.

Parametric gain has direct correlation to laser power P which means that as the power increases in the cavity more unstable modes are created. The second generation of LIGO detectors also increased the test mass quality factors Q_m in an effort to reduce thermal noise [42]. The increase of Q_m again increases the parametric gain creating more unstable modes.

From Equation 3.13 it can be seen that the HOM spacing is dependent on the RoC of the mirrors in the cavity. This mode spacing will also dictates the position of the beat note. Figure 3.5 shows the evolution of mode spacing of order $n = 1$ during locked periods of the interferometer measured using the thermal compensation system (TCS) [19]. This measurement is an estimate of the mode spacing made calculated from the RoC of the cavities optics using Equation 3.5 [2]. Once higher laser power of around 100kW begins to circulate in the cavity, radiation pressure heats the test masses. This self-heating changes the RoC of the test mass in the cavity which increases the HOM spacing. Mechanical mode groups sensitive to PI exist above 15 kHz where the beat note for the $n = 3$ HOM mode exists. It can be seen that if left in the present configuration the beat note will drift through these mechanical mode frequencies exciting them via the three mode interaction described previously.

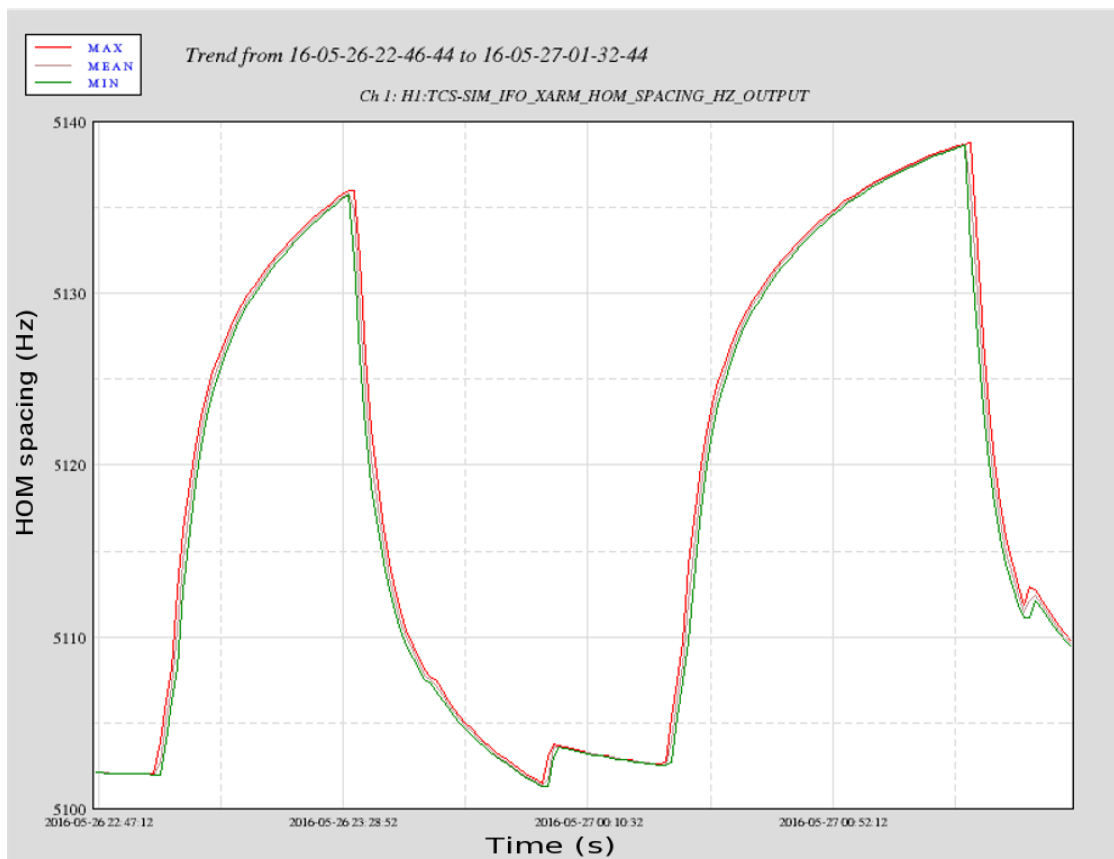


FIGURE 3.5: HOM spacing in Hz over the period of two interferometer locks. Increased cavity power during lock states results in changes in RoC of the cavity optics which increases the higher order mode spacing.

3.2.6 Observations of PI at LIGO detectors

The first parametric instability in a LIGO interferometer was observed at the LIGO Livingston detector [32]. The instability was formed when the cavity power was increased to $P_{arm} = 50\text{kW}$ bringing HOM spacing to $\Delta\omega_n = 5.1 \pm 0.3\text{kHz}$. In this case the mechanical mode at 15.54 kHz was downconverted to the detection band to 845 Hz. This change in frequency is caused by aliasing from the 16384 Hz sampling rate photodiode which measures the strain from the interferometer. The instability grows in amplitude when the cavity power is increased to 50 kW and the optical beat note begins to overlap with the mechanical mode. Eventually the mode amplitude begins to saturate the photodiode output. The laser power is then reduced decreasing the cavity power to 16 kW and the instability begins to decrease in amplitude. From this example a direct correlation between laser power and PI amplitude is observed indicating that similar instabilities will ring up if the laser power is increased to this level. During the O1 observation run this issue was avoided by using ring heaters to change the RoC of the test mass and hence the position of the optical beat note in relation to the 15kHz mechanical modes

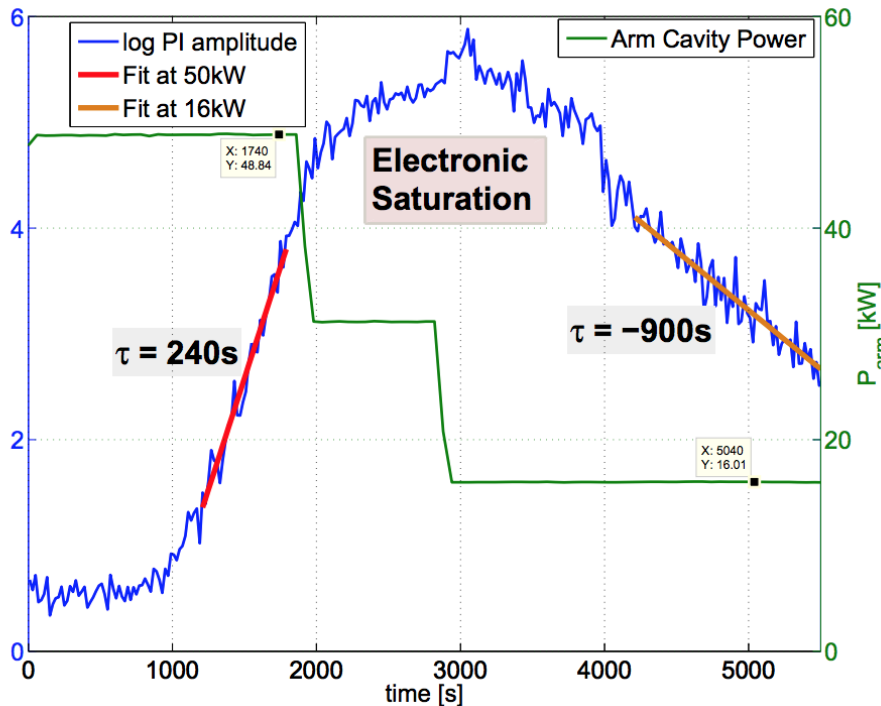


FIGURE 3.6: First observation of PI at LIGO Livingston [32]. Direct correlation between cavity power and PI amplitude shown as decreasing power causes the PI to ring down.

A similar PI was later observed at the LIGO Hanford detector [3]. Again the 15.54 Hz mechanical mode is excited by the input laser power of 15 W until the electronic readout begins to saturate. As the laser power is reduced to 10W the amplitude of the mode begins to decrease. After applying the ring heater method the instability does not reappear similarly to what was observed for the PI at Livingston. This second observation confirms that both instabilities are produced by PI in the arm cavities and that they have a direct correlation with laser power.

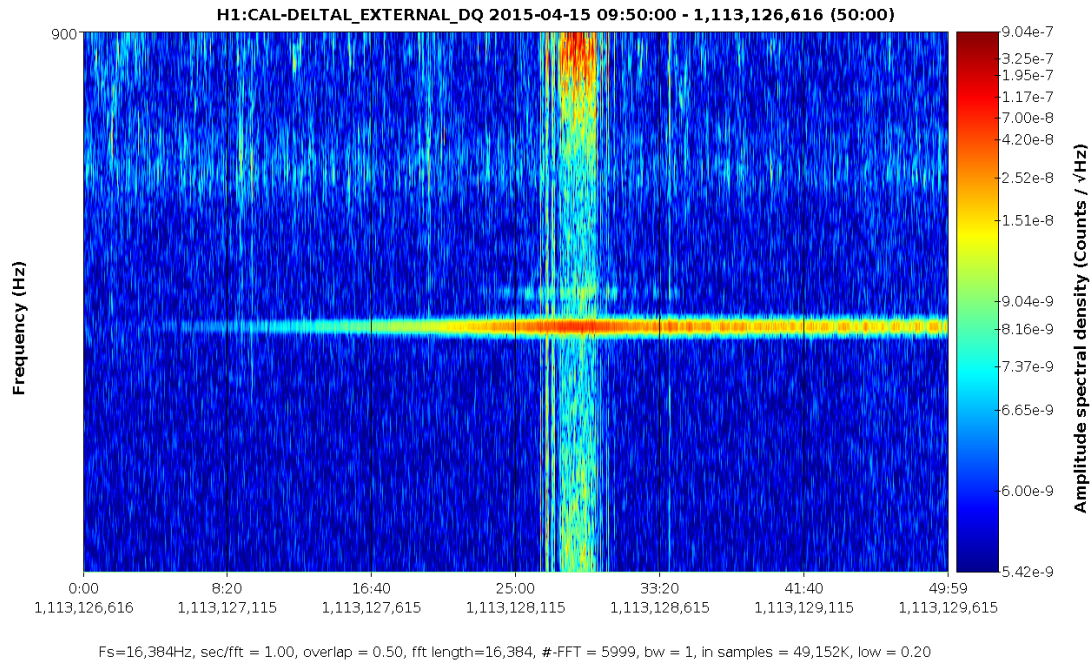


FIGURE 3.7: Spectrogram of first PI seen at LIGO Hanford. PI rings up to critical levels after 25 minutes and then decreases as the laser power is reduced.

This PI observed at the Hanford detector could also be tracked using the iWave filter described in Chapter 2. The tracking of the downconverted mechanical mode at 843 Hz is shown in Figure 3.8. A 10Hz bandpass filter was used in series with the iWave filter in order for the PLL to lock onto the line. Without bandpassing the filter would lock onto one of the violin mode harmonics at 1000 Hz. The filter locks onto the PI signal after it's SNR sufficiently increases. The exponential trend of the PI can be seen from the amplitude tracking output. This filtering method for extracting the PI signal becomes useful for damping instabilities described in subsection 3.3.3.

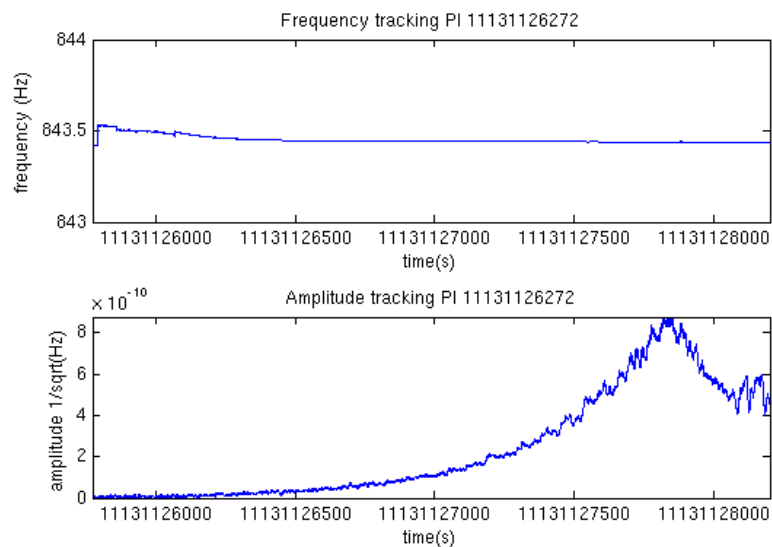


FIGURE 3.8: iWave tracking of PI at LIGO Hanford. Exponential increase in PI mode can be seen in iWave's amplitude output.

3.3 ESD Damping scheme

The inevitable increase in the number of unstable modes with increasing laser power means that a method of damping unstable modes is required. Previous methods of avoiding PI include using ring heaters [19] to actuate on the RoC of the test mass. However as cavity power increases this will not be a viable option as there will be too many unstable modes that moving the beat note position will lead to overlap with other mechanical modes [32]. Electro-static drivers (ESD) can be used to differentially actuate on a test mass in order to damp mechanical modes of the test mass. The ESD damping scheme was originally developed and effectively demonstrated at the LIGO Livingston detector [17]. In this section we describe how the ESD applies force to the test mass. The damping scheme developed for the Hanford detector in which the actuation signal is obtained to damp a particular mechanical mode is also discussed.

3.3.1 Description of ESD

Electrostatic drivers (ESD) are used in the LIGO interferometers to actuate on the test masses. They are primarily used while *locking* [56] the interferometer to control the length of the cavity in order to maintain resonance. Gold electrodes are deposited on the reaction mass located behind each test mass. Force is applied to the test mass via fringing electric fields created by the potential difference between electrodes [55]. The dielectric material of the test mass is attracted by the electric field with a force dependent on the potential difference between electrode pairs of the ESD

$$F_{ESD} = \alpha(\Delta V)^2. \quad (3.16)$$

The actuation force on the mirror F_{ESD} from Equation 3.16 is proportional to the square of the potential difference ΔV . The term α here is a constant dependent on the separation between the test mass and reaction mass.

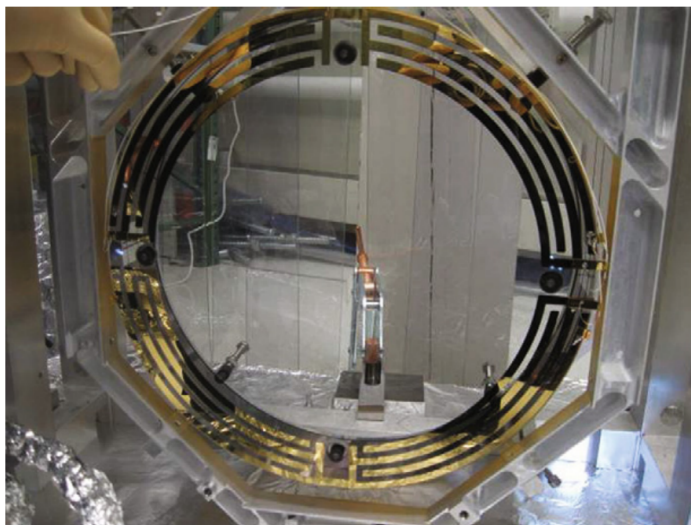


FIGURE 3.9: ESD electrodes deposited on reaction mass. Adapted from [55]

Applying differential voltages to the quadrants of the ESD seen in Figure 3.9 allows for angular control of the test mass. By using this technique the ESD can either excite or damp the mechanical modes of the test mass.

3.3.2 QPD v.s. OMC signal chains

Using the ESD to manipulate test mass mechanical modes requires the signal from the particular mode to be applied as a voltage to the ESD quadrants. Two methods used to extract this signal are using the quadrant photodiode (QPD) and the output mode cleaner photodiode (OMCPD). Both of these channels have a sampling rate 64 kHz in order to observe the mechanical modes at 15 kHz or higher.

Firstly the QPD method shown in Figure 3.10 uses the transmitted light from the cavity through the end test mass (ETM). Signals from the quadrants of the QPD are combined appropriately in order to observe the beat note between the fundamental TEM_{00} mode and the particular higher order mode TEM_{pq} . This signal is then band-passed using a Chebyshev filter with a 10 Hz band centred on the frequency of the particular mechanical mode. The gain and phase of the band-passed signal can then be adjusted in order to tune the amount of damping force applied. This signal is then differentially applied to the lower left and upper right quadrants of the ESD in order to actuate the test mass to either damp or excite the mechanical mode.

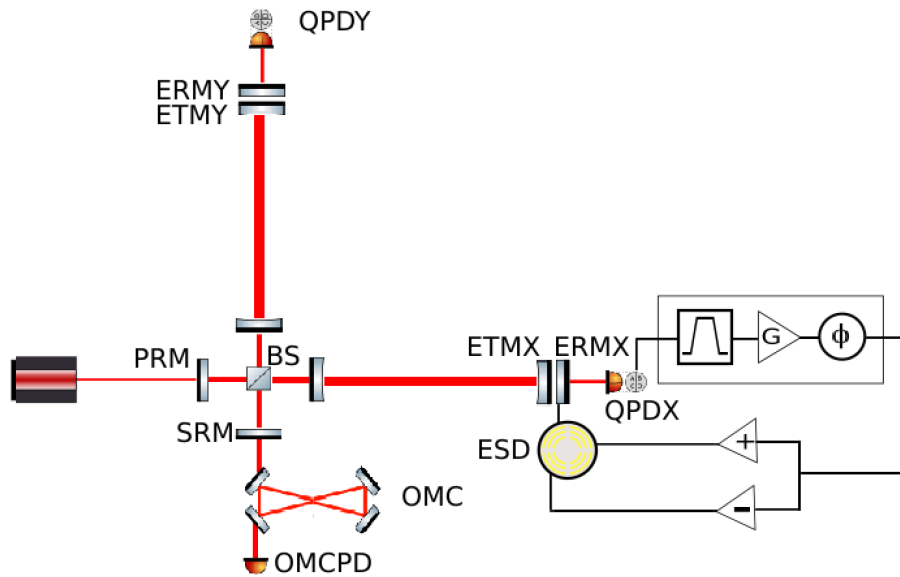


FIGURE 3.10: PI damping scheme using QPD signal chain. Band-passed mechanical mode signal from QPD is used to drive ESD quadrants and actuate the ETM.

The other method used to obtain the mechanical mode signal is from the OMCPD shown in Figure 3.11. The OMCPD only contains one signal compared to the QPD so restricting the output to observe one particular beat note is not possible. Instead the OMCPD observes the strain signal from the interferometer which includes all of the mechanical modes. Similarly to the QPD damping scheme the signal is bandpassed

over a 10 Hz region of the mechanical mode. Again this signal is differentially applied to the ESD which actuates the mirror.

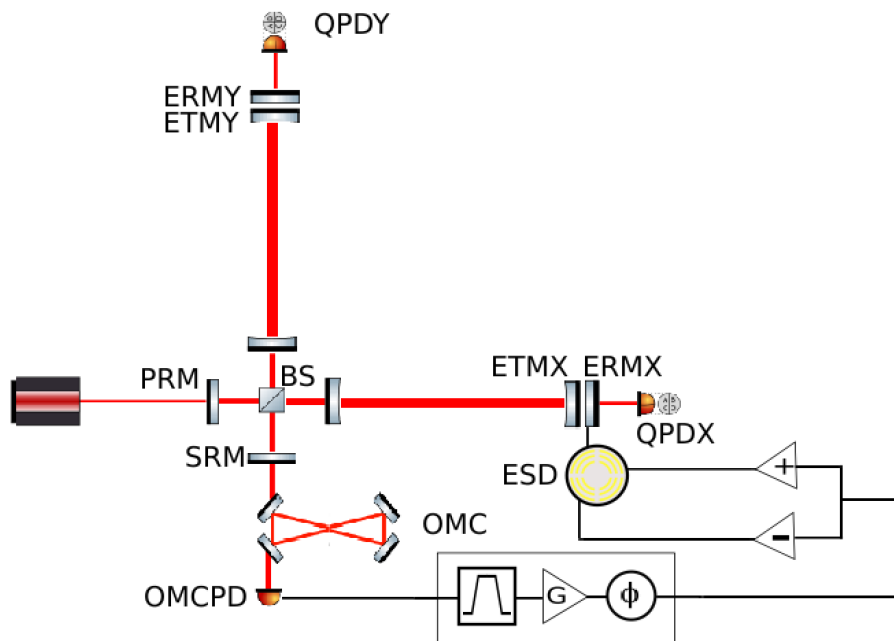


FIGURE 3.11: PI damping scheme using OMC signal chain. Band-passed mechanical mode signal from OMCPD is used to drive ESD quadrants and actuate the ETM.

While both of these methods are able to be used for the purposes of damping PI, the OMC damping scheme is more reliable. Figure 3.12 shows a comparison between the OMC and QPD output spectra. It is clear that the SNR of the OMC data is much greater than the QPD data. The OMC output clearly shows the excited mechanical mode from PI at 15009Hz as well as all the other modes around this region. The sources of these other modes are not limited to one test mass since the OMC is measuring the strain output from the interferometer. Any of the modes seen here could originate from any of the test masses. The QPD signal on the other hand measures the transmitted light from one cavity so it only observes mechanical modes from either the ITM or ETM of that cavity. This means that although a more sensitive measurement of the mechanical modes is possible using the OMC it is more difficult to identify which test mass to actuate on. Also the mechanism that produces the beat note signal used to damp the mode is simplified for the QPD signal. For the QPD the beat signal is derived from the fluctuation of beam position on the QPD. The OMC cannot observe this angular fluctuation so the mechanism for how it is coupled to the OMCPD signal is less understood.

Both the OMC and QPD damping scheme will use a feedback loop to drive the ESD similarly to the way PI ring up. As the bandpassed signal from the mechanical mode increases so will the driving signal to the ESD quadrants. While only driving the LL and UR quadrants of the ESD may not be the most desirable method for damping specific modes, this configuration allows for actuation on the most amount of mode shapes.

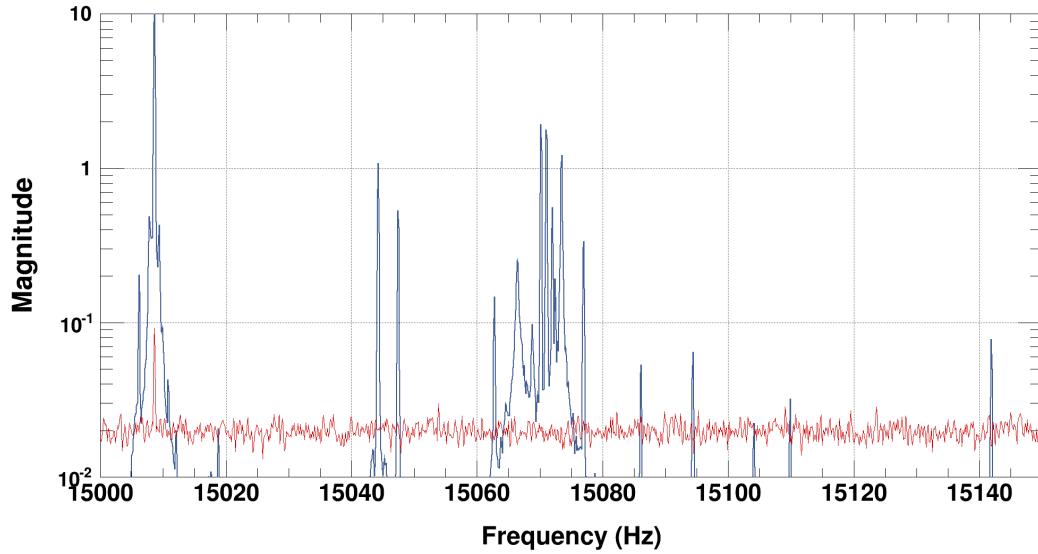


FIGURE 3.12: Spectra of output signals from QPD transmission (red) and OMCPD (black). Mechanical mode at 1510 Hz appears in both spectra however signal-to-noise ratio from OMCPD data is much greater.

3.3.3 iWave model for tracking PI

As described in Chapter 2, the iWave filter can be used to track continuous signals that wander in frequency. The mechanical modes of test masses present an opportunity to test iWave's ability to track signals in real time. A simulink model of iWave was adapted for the CDS system at the LIGO Hanford site for this purpose. This model was added to the signal chain described in Figures 3.10 and 3.11 after the bandpass filtering. If the mechanical mode signal appears within the bandpass region iWave is able to lock onto the signal.

Figures 3.16 and 3.14 show the medm screens used to control the filtering in real time. The iWave medm screen allowed for control of the response time τ and the starting frequency f_{start} . Setting τ lower allows for the filter to lock onto the signal faster but also introduces more noise into the output. By setting τ to around 1 second until it achieves lock and then ramping it up to a larger value compensates for this issue. Monitoring the output frequency, amplitude and error signal indicates if the signal is locked onto the mechanical mode. Also setting f_{start} as close to the particular mode frequency is necessary for locking on to that mode. The option of switching iWave from open to closed loop is possible by switching the feedback on. The whole filter can also be bypassed in order for the bandpassed signal to be used for damping. The I-phase output signal is then passed through the damping filter there the phase and gain of the damping output can be altered. The RMS output indicates how much driving voltage is being applied to the ESD.

Figure 3.17 shows the spectrum for the output from iWave tracking (green) against the bandpassed input (blue) and the OMDCPD signal (black) for a mechanical mode at 15 kHz. The bandpassed signal would normally be the signal that is used to drive the ESD as it focuses the output to a 10 Hz band around the mechanical mode. Other modes may exist within this band which means that the driving signal does

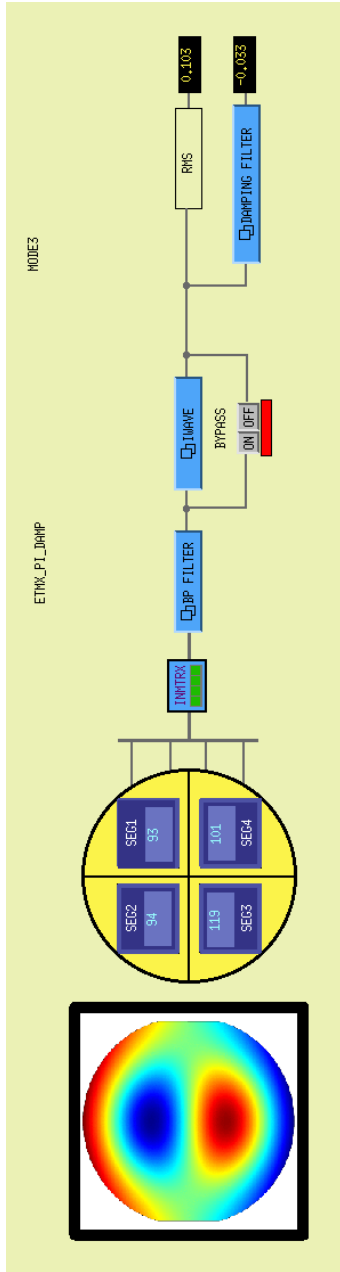


FIGURE 3.13: Medm for control of filters for damping of mechanical mode using QPD damping scheme.

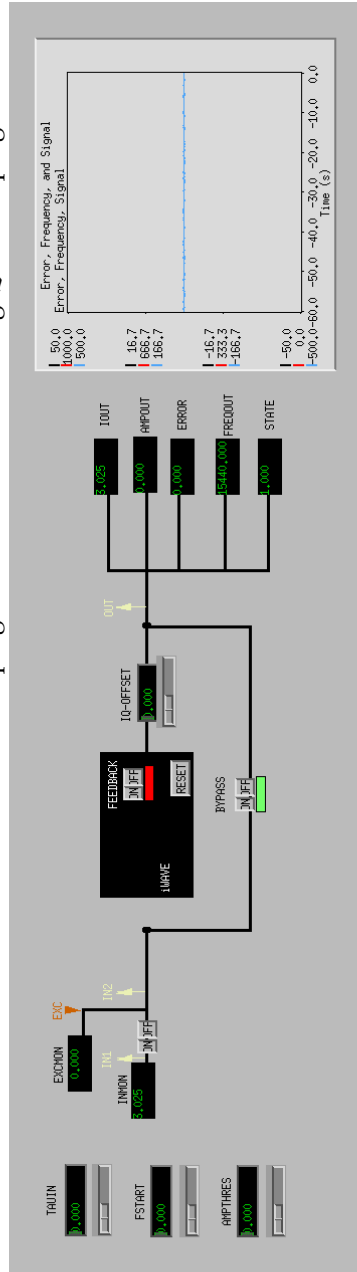


FIGURE 3.14: Medm screen used for filter control for QPD damping scheme

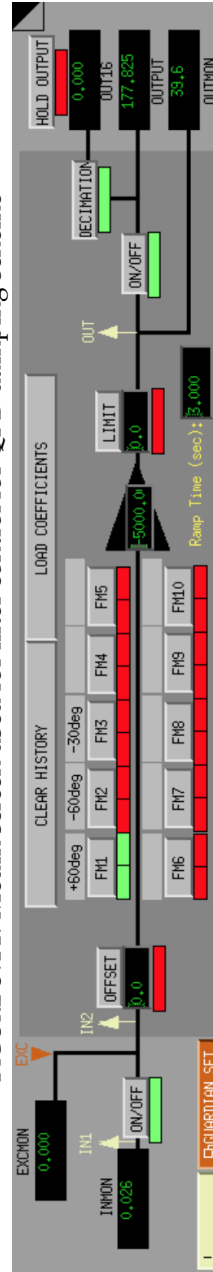


FIGURE 3.15: Medm screen used for damping filter control for adjusting output gain and phase.

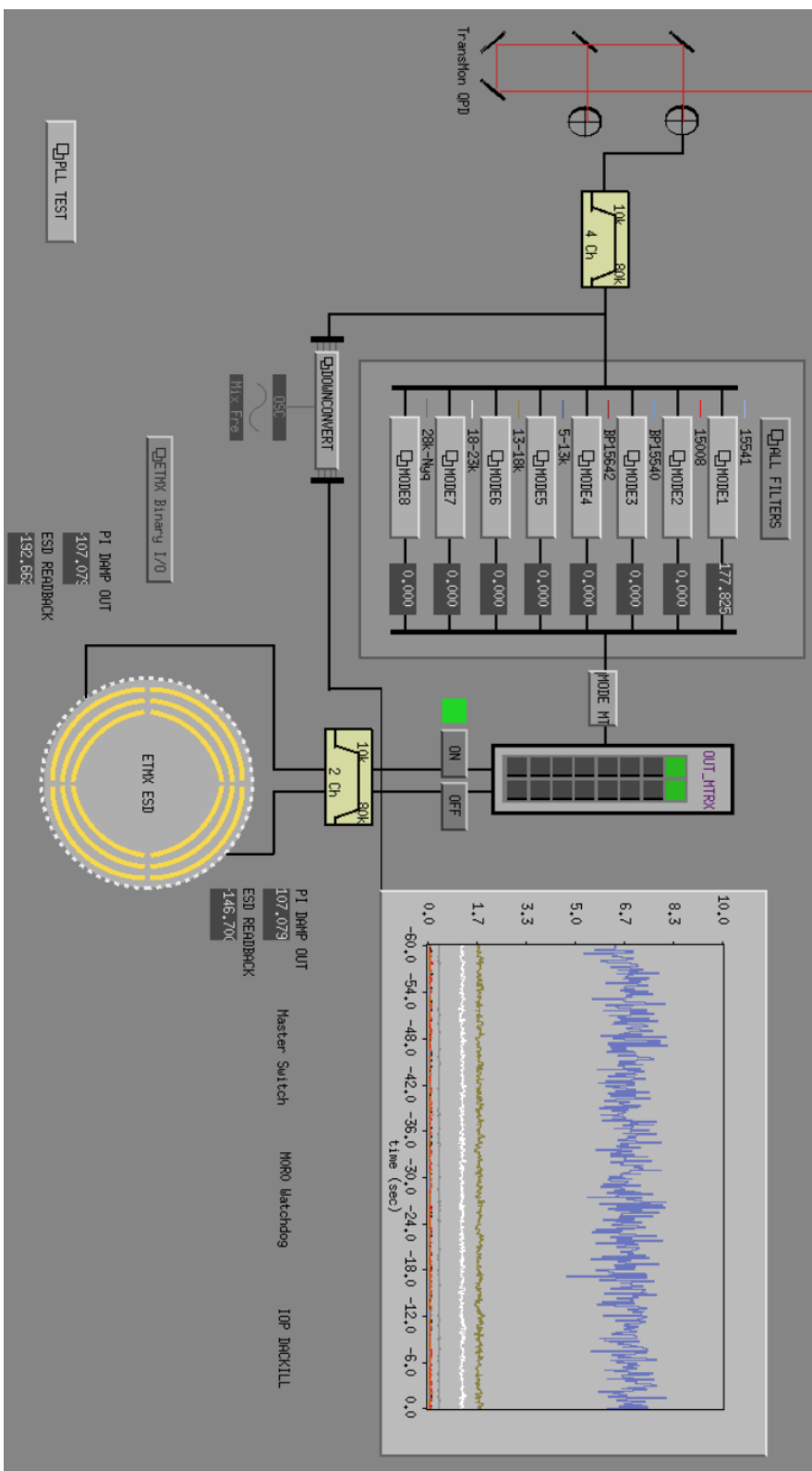


FIGURE 3.16: Overview medm screen for OMC damping scheme. Damping signal to ESD for each mode is controlled by input matrices.

not only contain the mechanical mode of interest. By applying iWave filtering the specific mode required for damping can be extracted from the bandpassed signal.

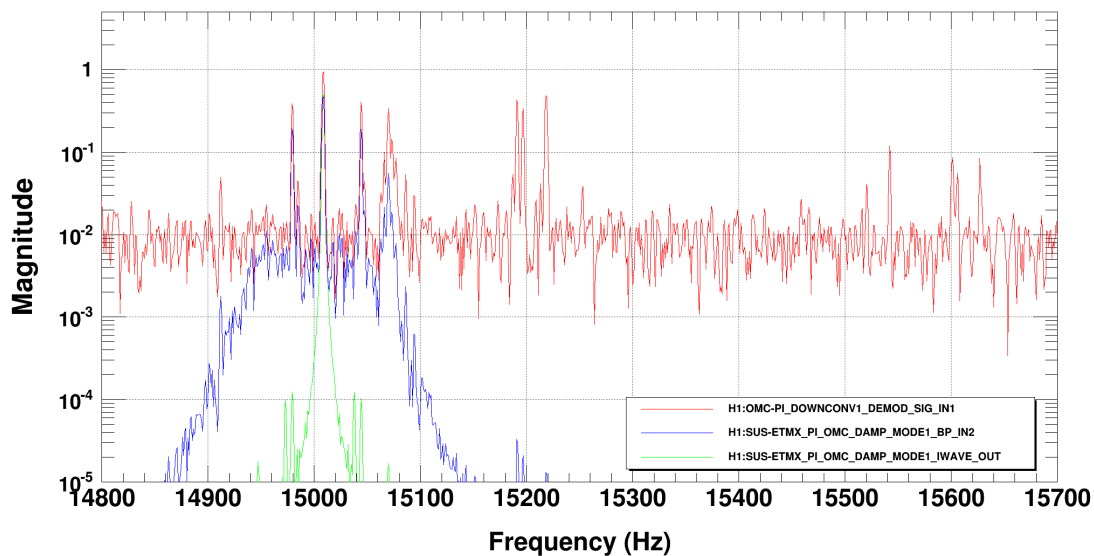


FIGURE 3.17: iWave tracking of 15kHz mechanical mode. Input signal (red), bandpassed signal (blue) and iWave tracked signal (green).

3.4 Results from damping

With damping scheme implemented at the site a method for actuation of the test masses was made possible. This allows for active control of PI as they ring up in real time. In order to experiment with damping PI the ring heater which moves the position of the beat note was turned off allowing PI to ring up in the detector as the power is increased. In this section the results from active damping of various test mass mechanical modes is discussed.

3.4.1 Attempted damping of PI from two mechanical modes

During a lock where the input laser power was 24 W PI were witnessed originating simultaneously from the ETMX 15540 Hz mode and ITMX 15520 Hz mode. As both of these modes exponentially ring up a 20 Hz comb was produced due to the interaction between the two modes. Eventually this instability caused the interferometer to lose lock demonstrating the need for damping them.

The spectrum around the region of the rung up mechanical modes is displayed in Figure 3.18. Sidebands around each of the mechanical modes can be seen from the OMC spectrum as well as the 20Hz comb which is not present in the QPD spectrum. Since the QPD is measuring angular changes in beam position it will not be able to observe the comb. The spectrum from the iWave line tracking can also be seen in this. When it is locked onto the 15540 Hz line the output amplitude is a factor of 2 smaller than the OMCD CPD signal. This may be due to the small τ value of 1 second used for the tracking. Decreasing τ gives the filter a larger FWHM where the line width of the mechanical modes are small due to their high Q . The lower 15520 Hz

mode can also be present in tracked iWave output spectrum however the amplitude of this line is greatly reduced.

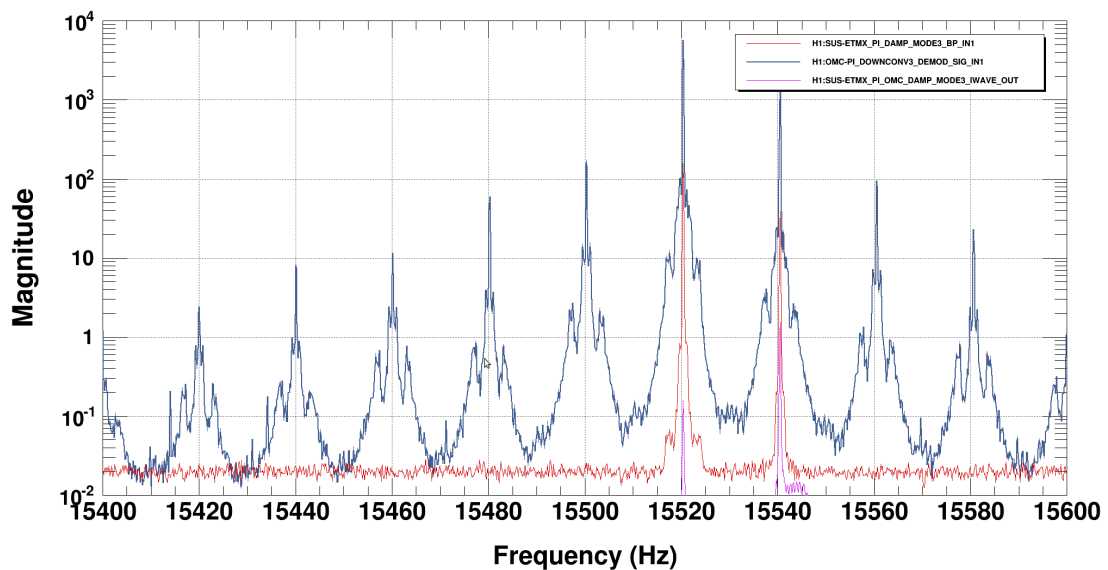


FIGURE 3.18: Spectrum of PI seen simultaneously from 15520Hz and 15540Hz mechanical modes. OMC output (black) shows 20 Hz comb from beat between the two modes. Both modes seen in X-arm QPD output (red) at a lower amplitude but with no comb effect. iWave tracking output (pink) reduces 15520Hz mode in relation to the 15540 Hz mode when it is locked on to the higher frequency mode.

Figure 3.19 displays a spectrogram of the two modes ringing up due to this instability. At approximately 500 seconds damping was attempted on 15540Hz mode using the OMC damping scheme with iWave filtering applied. The result from damping is more clearly shown in Figure 3.20 from the amplitude tracking of the 15540 Hz mode. After a gain of 1000 is applied to the output signal to the ESD the amplitude of the mechanical mode is drastically reduced in magnitude. However after the mode is damped iWave then locks onto the lower 15520Hz mode. This shift in frequency is displayed in Figure 3.21 which shows the iWave frequency tracking around this time. After this shift in frequency the magnitude of the mechanical mode again begins to increase due to PI. The linetracker then locks onto the 15540 Hz mode again however applying a damping gain is not successful in reducing the mode possibly due to a change in its phase. Both modes continue to ring up eventually breaking the locked state of the interferometer.

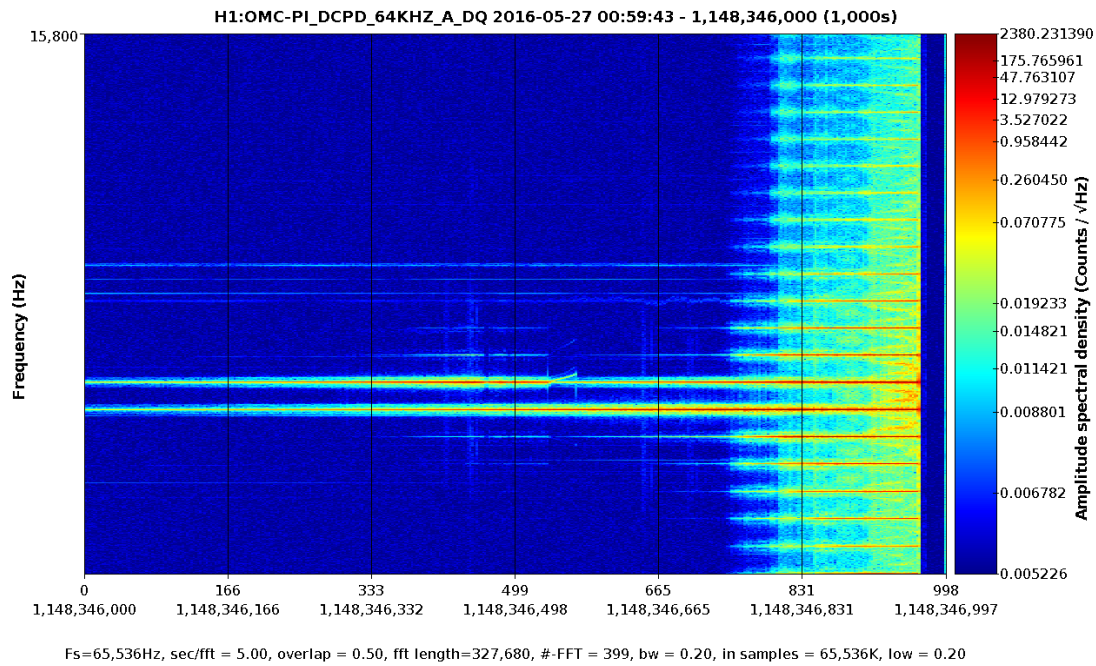


FIGURE 3.19: Spectrogram of PI from 15520 Hz and 15540 Hz mechanical modes. Damping was not effective in this case causing lock loss.

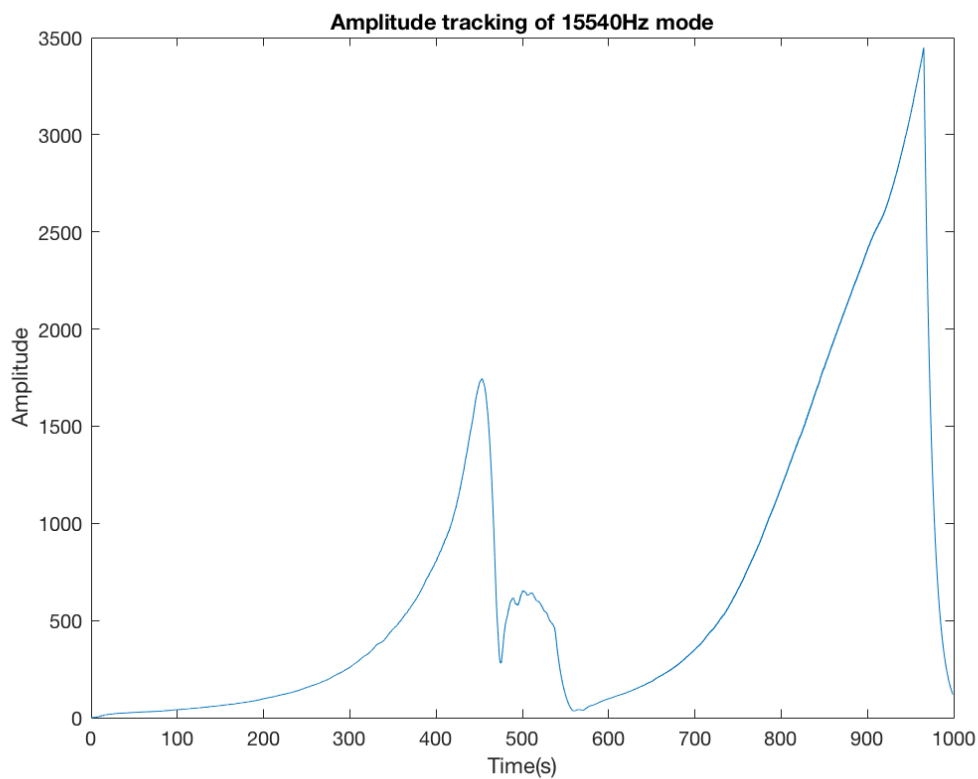


FIGURE 3.20: Amplitude tracking output of 15540 Hz mode. Damping was attempted at 450 seconds but the mode continued to ring up after iWave lost the ability to track the line.

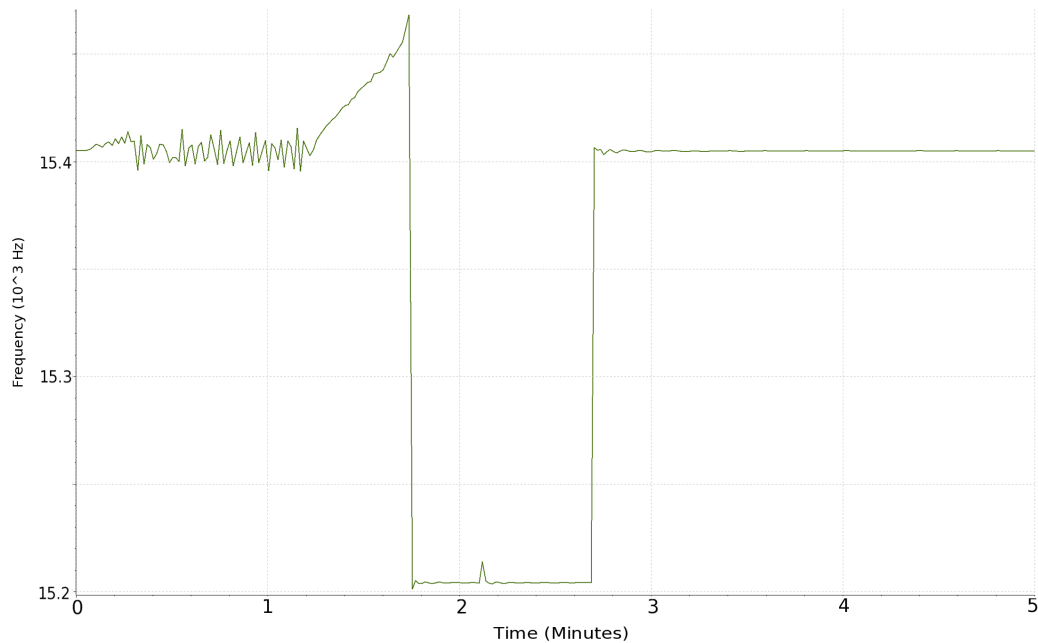


FIGURE 3.21: Frequency tracking of 15540 Hz mode. Tracking switches to lower frequency line after the original mode is damped. Frequency the switches back as the mode rings up again. A linearly increasing artifact can also be seen here which is also present in Figure 3.19.

3.4.2 15217 Hz mode

Rather than damping a mode which was ringing up due to PI the 155217 Hz mechanical mode was actuated on to excite and then damp the mode. This is a useful method for determining which line frequency belongs to which test mass especially when iWave line tracking is used. Figure 3.22 shows the spectrum of this frequency range where a slightly higher frequency mode is present at 15218 Hz. This mode is within the 10 Hz range of the bandpass filter which means that the damping signal would normally contain both modes. However when iWave is applied in series, the 15518 Hz mode can be reduced while it is locked on the 15517 Hz mode.

Figure 3.23 describes the results from actuating on the mechanical mode. The mode is first excited by increasing the gain of the damping filter to 1000. After the mode's amplitude is increased the gain is then set to -1000 which begins to damp the mode. The SNR of the 15217 Hz mode amplitude decreases until at around 275 seconds the filter can no longer maintain lock on the mode. This causes the filter to lock onto the higher frequency mode at 15218 Hz so the original test mass mode is no longer being directly actuated on. As well as this the amplitude output no longer represents the 15217 Hz mode amplitude.

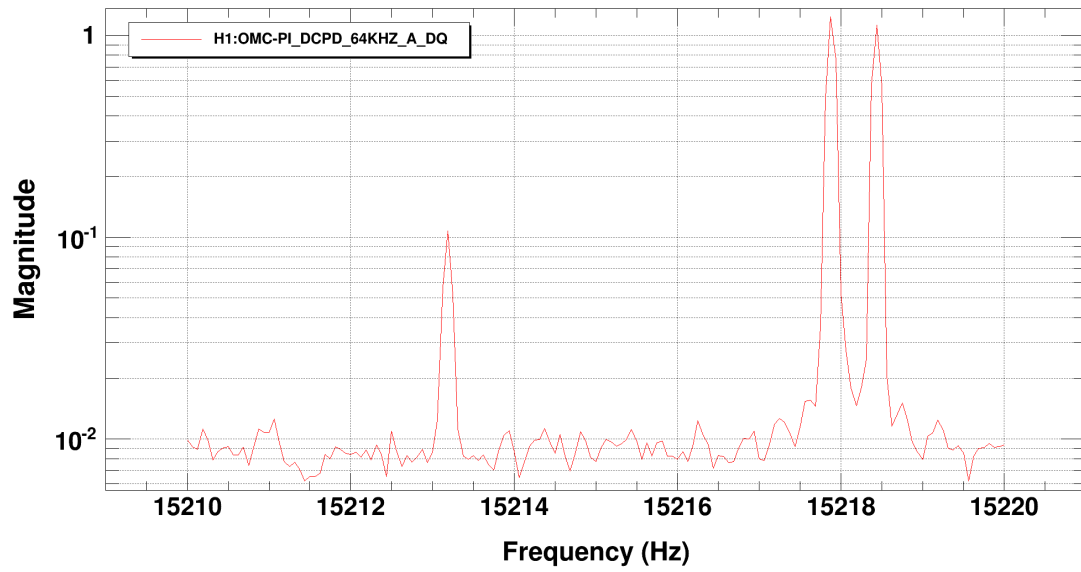


FIGURE 3.22: Spectrum of 15217 Hz mechanical mode region. Two modes exist within the 10 Hz range of the bandpass filter.

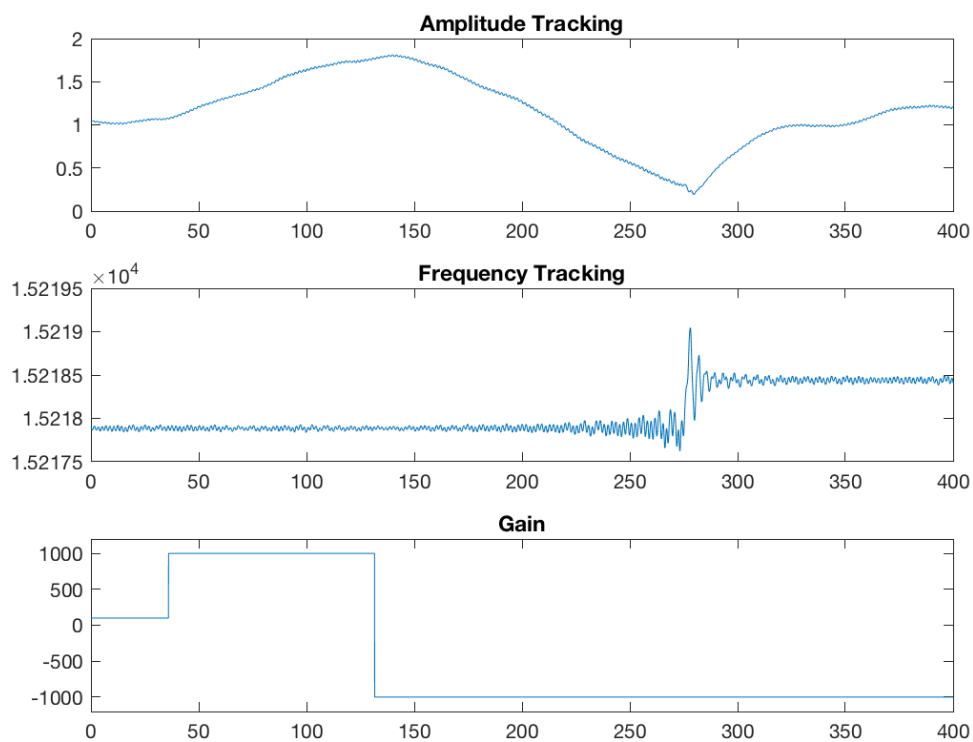


FIGURE 3.23: Damping of 15217 Hz mechanical mode using iWave. After the damping gain is increased to 1000 the amplitude begins to decrease until the frequency tracking locks onto the mechanical mode 1 Hz higher.

3.4.3 15009Hz mode

Testing actuation strength with regards to damping gain was also tested for the ETMY mechanical mode at 15009 Hz. In this case only the bandpass filter was used to drive the ESD. In Figure 3.24 the effect of changing the damping gain can clearly be seen. After 150 seconds the gain is set to -500 which excites the mechanical mode, exponentially increasing its output RMS from the bandpass filter. The RMS output here contains more noise compared to the iWave amplitude seen in Figure 3.23 due to the wider frequency band of the bandpass filter. The gain is then inverted to 500 which immediately begins to decrease the output RMS exponentially. The mode is eventually damped down to the background level seen before the damping magnitude was increased.

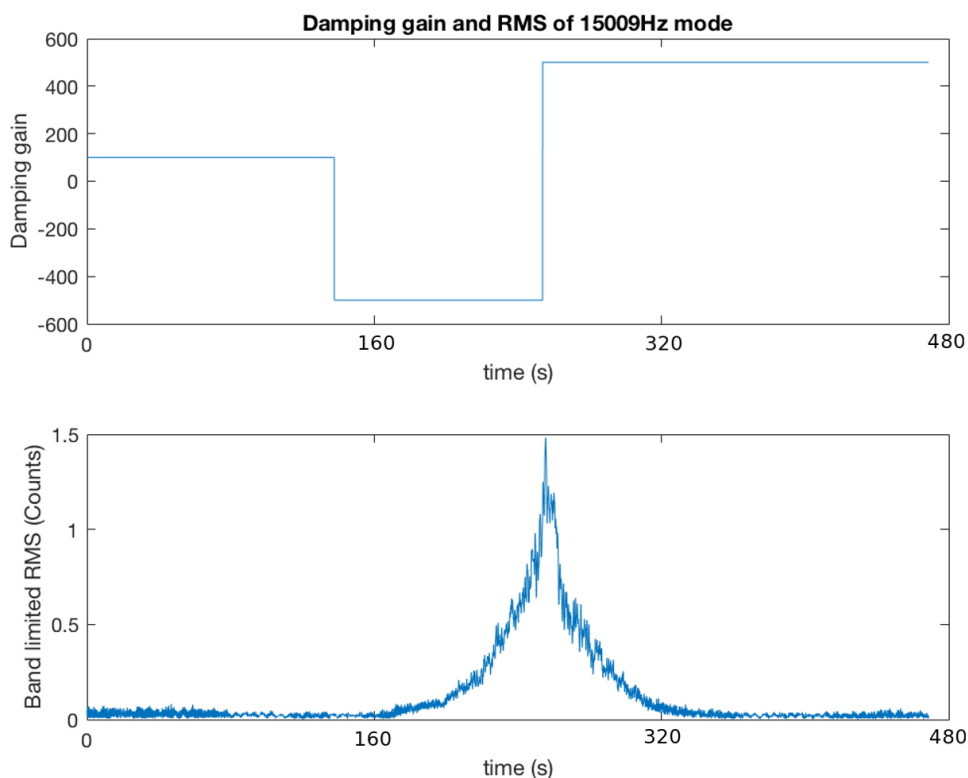


FIGURE 3.24: Actuating on 15009Hz mechanical mode using band-passed OMC signal.

3.4.4 Controlling multiple modes during a lock

Once the scheme for damping multiple modes simultaneously had been tested and implemented it was possible to damp known PI as they ring up during a lock. This became necessary when the interferometer acquired lock with input laser power of 34.6 W. Even with ring heaters turned on the optical beat note would still pass through the susceptible mechanical modes at 15 kHz. Figure 3.25 shows examples of how ESD damping was used to avoid lock loss as mechanical modes rang up. While the gain outputs were constant, the phase of the damping signal was altered

to control unstable modes. Most of the damping signals were acquired using band-passed OMC output except from the 15520 Hz mode where iWave filtering was also added to the signal chain.

The mode at 14980 Hz rang up three times during this lock and was corrected by applying changes in phase to the damping filter. The phase was originally set to -60° until it begins to ring up at which point the phase is changed back to 0° which damps the mode. The mode begins to ring up again after 5 minutes until the phase is again changed to 60° which damps it. This damped the mode for 13 minutes until it starts to ring up and the phase is changed to 30° which damps the mode and stays in this state for the rest of the lock.

Another mode at 15009 Hz rings up more slowly than the other modes but was still reaching high RMS values. Changing the phase from 0° to 60° caused the mode to ring down.

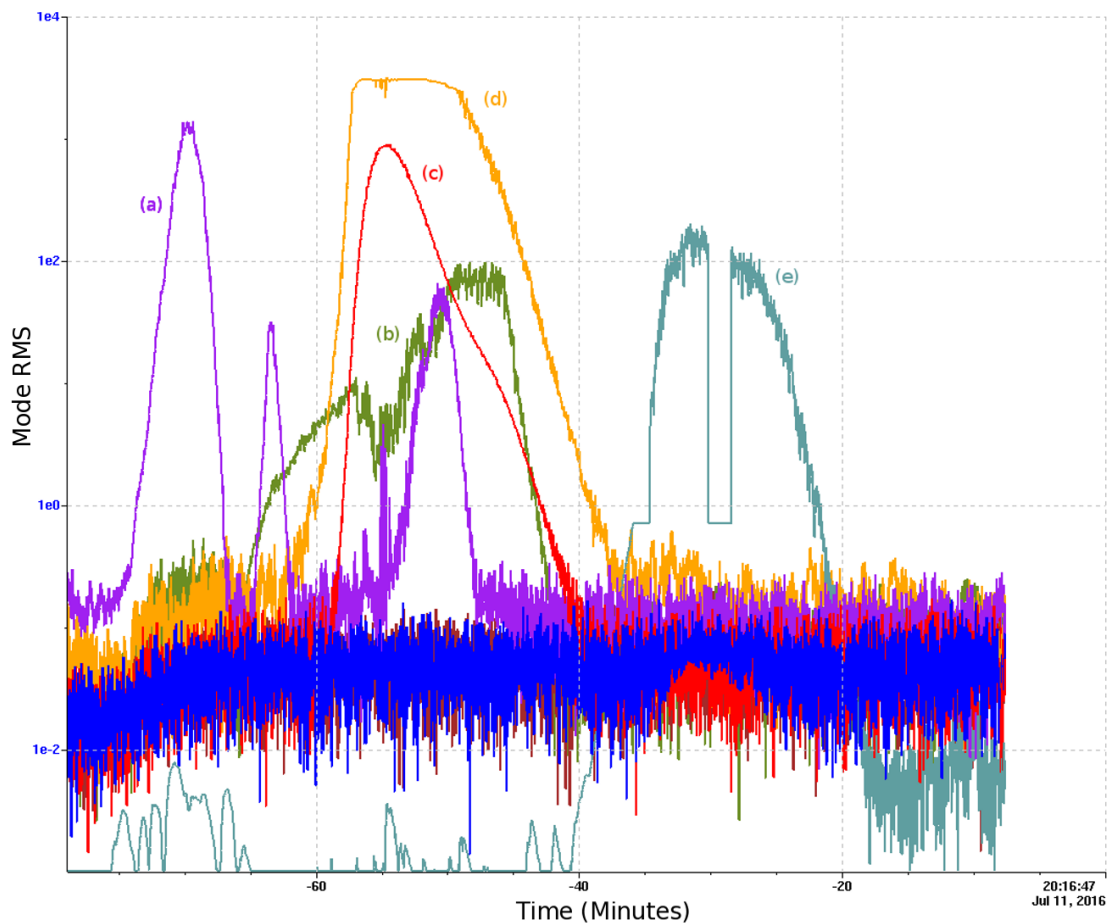


FIGURE 3.25: RMS outputs for damping multiple mode during extended lock. (a) 14980 Hz ITMY (b) 15009 Hz ETMY (c) 18040 Hz ETMY (QPD) (d) 18040 Hz ETMY (OMC) (e) 15520 Hz ITMX

In Figure 3.25 two trends describe the RMS values of the mode at 18040 Hz. The OMC RMS (yellow) is shown to exponentially increase until it reaches a steady value. Measuring the same RMS value using the QPD (red) shows that the instability

does not reach a steady value and is still in flux over this period. From this comparison it can be assumed that the OMCPD has become saturated at the mode frequency when it reaches this level of magnitude. Due to this the damping was switched to the QPD scheme. While in this configuration the phase was also changed from 0° to -30° which damped the mode. From this example it is apparent that the QPD signal is more reliable at damping mechanical modes when they reach levels of magnitude in the OMC signal above 10^3 .

As mentioned previously iWave tracking was applied to the damping of the 15520 Hz mode. Earlier in Figure 3.25 the RMS value increases and decreases arbitrarily as iWave locks onto the mode, begins damping it and then loses lock when it's SNR becomes too low. At one point the mode begins to ring up significantly until the output reaches a set threshold value ¹. At this point iWave filtering is bypassed and bandpass filtering is used to damp the mode. The damping phase is then changed from -30° to 30° which begins damping the mode.

3.5 Discussion

The implementation of ESD damping at the Hanford site is shown here to be necessary in order to maintain lock at higher laser power. After experimenting with the methods in which mode damping is achieved several observations became clear.

Firstly although iWave tracking is the most desirable approach to extracting the damping signal, it is not able to maintain lock on the mode after it is damped. This allows the mode to ring up again and can cause iWave to lock onto a neighbouring line which has a higher SNR value. Adaptations to the way in which iWave tracks the mode and applies the damping gain could solve these issues. An addition to iWave known as cross-subtraction could be used to simultaneously track multiple signals within a given frequency region. Subtracting the signals which are not related to the desired mechanical mode would mean that iWave would not be able to lock onto these other signals. Applying this would mean that the damping output from iWave would reliably contain the signal from the mechanical mode as it rings up.

Another technique to make iWave damping more robust is to servo the damping output to a constant value. By doing this the modes would not be able to become unstable and without dropping below a thresholded SNR value, iWave could maintain lock on them. This strategy relies on the output from iWave being able to track the phase of the signal correctly. As seen in 3.4.4 this can be an issue when only bandpass filtering is applied.

¹Thresholding the output from iWave was being tested at this point in order to maintain the damping value at a certain magnitude.

Chapter 4

X-SphRad line removal modification

4.1 Introduction

When searching for astrophysical GW signals the most likely events to be detected are those with modelled waveforms. These waveforms can be detected using techniques such as matched filtering [63] which allows signals to be detected below the noise floor. Several pipelines are dedicated to the search for these chirp like signals coming from binary inspirals and were used to detect the events seen from the observation runs so far [12], [9]. With this confirmation of the existence of GWs and the increasing sensitivity of the detectors the search for unmodelled GW sources has become more tangible. Pipelines such as X-pipeline [68] search for transient signals of duration 10-1000 seconds by detecting regions of excess power from the cross-correlated detector data. This can be used for targeted searches where the sky position and arrival time is known via an EM counterpart [50], [49] or using an all-sky search. In the latter case the data between detectors is time-shifted in order to observe over the full range of possible sky locations. Time delays of observed signals between detectors will relate to varying sky position if it is < 30 ms.

While searching for long duration GW candidates, detected as events are often sourced from the detectors themselves. At the moment notch filtering is used to remove frequency bands where these triggers come from. As well as this LPEF filtering is used to whiten the data before it is used for analysis. While both of these methods can be used to remove detector noise they leave bands of lower sensitivity in the frequency domain. LPEF filtering also does not remove lines which wander in the frequency domain which has been seen in previous searches [33].

In this chapter we describe the X-SphRad pipeline for detection transient GW signals in the all-sky regime. X-SphRad uses spherical radiometry as a method for rejecting glitches to improve search sensitivity [30]. We also discuss the modification to X-SphRad to remove detector noise from wandering lines and examples of running this modified pipeline over instances where these lines exist.

The work in this chapter is based on my contributions to the development of the established pipeline X-Sphrad. I added the line removal filter iWave to the pre-processing and tested it on a section of data containing a 600 Hz wandering line. I also ran two separate analyses including background estimation in order to compare the results using the original pipeline against the modified pipeline including iWave filtering. The results from this analysis and testing are given in Section 4.3.

4.2 All-sky searches for transient GW using X-SphRad

The X-SphRad pipeline is an adaptation of X-pipeline which uses spherical harmonics to measure correlation between detector pairs [29]. X-pipeline is used for the pre-processing and post processing steps in the analysis while the spherical radiometer module produces tf-maps, calculates detection statistics for each pixel and clusters pixels containing excess power.

4.2.1 Data conditioning

Data conditioning makes up the pre-processing step completed by X-pipeline which produces the input to X-SphRad. Firstly the data from each detector is segmented into periods where detectors are in observation mode simultaneously. Veto definers are also used to determine which sections of the remaining detector data contain a particularly large amount of glitches. These sections of data are defined as CAT1 vetoes and are removed in pre-processing in order to mitigate the amount of glitches considered as events. The remaining data which has passed this initial data quality check is segmented into 512 second blocks which contain coincident data.

These blocks are then whitened using a zero-phase linear predictive error filter LPEF [21]. The LPEF estimates the spectrum over the block time for a set of data and then uses this to construct a whitening filter which normalises the magnitude of the output spectrum over all frequencies. As well as normalising the overall noise curve of the spectrum, this process also removes power lines from the data. This assumes that the background noise in the data set remains fairly static, however it is shown in Section 4.3 that this is not always the case.

4.2.2 Background estimation and simulated injections

In order to determine the significance of the output events from X-SphRad the background events caused by detector noise must be measured. This is done by time shifting the data from one detector in relation to the other such that the output events are non-physical [48]. For a GW signal to be considered physical the offset in time between the two segments of data must be within the time required for a GW signal to travel between the detector pair. The analysis with physical time shifting is known as on-source whereas the non-physical background analysis is known as off-source. A higher amount of time-shifted segments results in a more accurate representation of the background and hence a higher confidence of detections made in the on-source. Both the on-source and off-source segments are analysed in the same way using X-SphRad. Off-source segments are also created from segments of data which pass data quality described in 4.2.1. Half of these off-source segments are used for tuning the cuts that are made to remove the remaining glitches during post-processing. The False Alarm Rate (FAR) is then calculated with other half of the off-source segments. This is the value used to determine the significance of the on-source events.

Simulated GW signals are also injected during the analysis to determine how well they are recovered by the pipeline. This is separate from the on-source and off-source analysis. Signals are injected into the detector data at evenly spaced intervals in time

with varying amplitude. The scale for each variation in amplitude is inversely proportional to the distance between the source of the modelled signal and the detector. This is defined as the h_{rss} for the simulated signal.

$$h_{rss} = \sqrt{\int_{-\infty}^{\infty} [h_{+}^2(t) + h_{\times}^2(t)] dt} \quad (4.1)$$

These injection scales are spaced logarithmically between 10 kpc and 1000 Mpc. The upper limits of detector sensitivity are determined by how well the injections are recovered compared to the background during post processing.

4.2.3 Spherical Harmonic correlation

The spherical harmonic transform is a method for efficiently computing correlation terms between detector pairs [20]. Measuring the data coming from a particular sky position can be estimated by using the order of spherical harmonic relating to it. This removes a significant amount of redundant calculations compared to using the grid search method. The spherical harmonic method is particular useful when analysing all-sky data as the time-delay due to source sky position can be isolated.

The correlation between detector pairs for a given sky position \hat{s} is originally expressed by Equation 4.2.

$$\xi_{a,b}(\hat{s}) = \int_{t-T/2}^{t+T/2} g_1(t' - \vec{r}_a \cdot \hat{s}) g_2(t' - \vec{r}_b \cdot \hat{s}) dt' \quad (4.2)$$

For efficiency this can be calculated using delay matrices in the spherical harmonic domain for each detector. This delay matrix $\mathbb{T}(\vec{r} \cdot \hat{s})$ retards the time series with relation to the sky position.

$$\vec{g}(\hat{s}) = \mathbb{T}(\vec{r} \cdot \hat{s}) \cdot \vec{g} \quad (4.3)$$

The j th delayed time series value from detector i relating to a particular sky position \hat{s} is given by Equation 4.4.

$$g_a[j; \hat{s}] = \sum_{k=0}^{N-1} \mathbb{T}_{j-k}(\vec{r}_i \cdot \hat{s}) g_a[k] \quad (4.4)$$

where $g_i[k]$ is the original time series from detector i . This delay matrix can be expressed in terms of spherical harmonics where the order (lm) refers to a particular solid angle Ω .

$$\mathbb{T}_{j-k}(\vec{r}_i \cdot \hat{s}) = \sum_{l=0}^{\infty} \sum_{m=-l}^l \mathbb{T}_{j-k}^{(lm)}(\vec{r}_i) Y_{lm}(\hat{s}) \quad (4.5)$$

$$\mathbb{T}_{j-k}^{(lm)}(\vec{r}_i) = \int \mathbb{T}_{j-k}^{(lm)}(\vec{r}_i \cdot \hat{s}) Y_{lm}^* d\Omega \quad (4.6)$$

In order to measure excess power in the frequency domain a discrete Fourier transform is applied to the time series data. From Parseval's theorem the total energy in the time domain is equivalent to the total energy in the frequency domain. This means that Equation 4.2 can be expressed in the Fourier domain using a DFT of both time-series data and their associated delay matrices.

$$\tilde{g}_a[q] = \sum_{k=0}^{N-1} g_a[k] e^{-2\pi i k q / N} \quad (4.7)$$

$$\tilde{\mathbb{T}}_q(\vec{r}_a \cdot \hat{s}) = \sum_{j-k=0}^{N-1} \mathbb{T}_{j-k}(\vec{r}_a \cdot \hat{s}) e^{-2\pi i (j-k) q / N} \quad (4.8)$$

Using the transformed expressions for the data and delay matrices for each detector, the correlation equation from Equation 4.2 can be expressed in terms of spherical harmonics.

$$\xi_{a,b}^{(lm)}(\hat{s}) = \frac{1}{N} \sum_{l=0}^{l_{max}} \sum_{m=-l}^l \sum_{q=0}^{N-1} \left[\tilde{g}_a[q] \left(\frac{1}{N} \tilde{\mathbb{T}}_q(\vec{r}_a \cdot \hat{s}) \tilde{\mathbb{T}}_q^*(\vec{r}_b \cdot \hat{s}) \right) \tilde{g}_b^*[q] \right] \quad (4.9)$$

4.2.4 Frequency domain clustering

After the spherical harmonic decomposition of the input data is calculated using Equation 4.9, time frequency maps can then be generated. For each pixel at time t and frequency f , the total power $P_{t,f}$ can be calculated by summing the correlation term for each detector pair over the spherical harmonic coefficients.

$$P_{t,f} = \sum_{a=b=1}^{N_{det}} \xi_{a,b}^{(lm)} = \sum_{l=0}^{l_{max}} |c_{lm}|^2 \quad (4.10)$$

In the case of up to 3 detectors the sum of correlation terms include the cross-correlation and auto-correlation terms for each detector pair. Note that the auto-correlation terms are not optimal for analysis as single detector glitches auto-correlate with themselves.

$$\sum_{a=b=1}^{N_{det}=3} \xi_{a,b}^{(lm)} = \xi_{1,2}^{(lm)} + \xi_{1,3}^{(lm)} + \xi_{2,3}^{(lm)} + \xi_{1,1}^{(lm)} + \xi_{2,2}^{(lm)} + \xi_{3,3}^{(lm)} \quad (4.11)$$

The summed pixel power is described as the coherent energy E_{SH} for that pixel. Region based thresholding is then applied to the pixels depending on their value of E_{SH} . The tf-map is divided into 10 regions and the 1% of pixels which contain the highest value of E_{SH} from each region are selected for clustering. These pixels are added to a cluster if they share an edge or a corner with another pixel [68]. Clusters with the highest cumulative energy are then considered as events i.e. possible GW signals. These events are ranked in terms of their significance which for X-SphRad is the summed coherent energy for all pixels in the cluster.

Another output term from X-SphRad is the incoherent energy $I_{SH} = |c_{00}|$ from the zeroth order spherical harmonic. I_{SH} can be described as the energy coming from all sky locations meaning it is not localised to one area in the sky.

4.2.5 Linear and alpha cuts

During post-processing cuts are made to the output events in order to remove glitches. The first of these cuts is the linear cut where the ratio $\frac{E_{SH}}{I_{SH}}$ is used [31]. Events which pass this cut will have coherent energy

$$E_{SH} > \kappa I_{SH} \quad (4.12)$$

where the constant κ is determined by tuning from background and injection trials.

At lower event energies the linear cut is not successful at removing events caused by glitches. To mitigate the amount of glitches further, another cut is used to filter out these events [71]. This is known as the alpha cut and is represented by,

$$\frac{2|E_{SH} - I_{SH}|}{(E_{SH} + I_{SH})^{0.8}} + 1 \geq \alpha \quad (4.13)$$

Again the constant α is determined by tuning from background and injection trials.

4.2.6 Null stream

The null stream is a linear combination of the data from each detector such that a GW signal will be cancelled out in a particular sky direction [46] [40]. For any detector i in the presence of a GW signal from sky position \hat{s} in an Earth centred coordinate system, the strain data can be represented as

$$h_i(t) = f_i^+(t, \hat{s})h_+(t) + f_i^\times(t, \hat{s})h_\times(t) + n_i(t), \quad (4.14)$$

where $f_i^+(t)$, $f_i^\times(t)$ are the antenna response to the plus and cross polarisation, $h_+(t)$, $h_\times(t)$ are the plus and cross polarised strain signals from a GW signal and $n_i(t)$ is the detector noise. For three detectors a set of linear equations can be written for the strain measured in the presence of the same GW signal.

$$h_1(t) = f_1^+(t, \hat{s})h_+(t) + f_1^\times(t, \hat{s})h_\times(t) + n_1(t) \quad (4.15)$$

$$h_2(t_2) = f_2^+(t_2, \hat{s})h_+(t) + f_2^\times(t_2, \hat{s})h_\times(t) + n_i(t_2) \quad (4.16)$$

$$h_3(t_3) = f_3^+(t_3, \hat{s})h_+(t) + f_3^\times(t_3, \hat{s})h_\times(t) + n_i(t_3), \quad (4.17)$$

The data measured at detectors 2 and 3 is time shifted with respect to detector 1 where $t_i = t + \tau_{1i}$. We define τ_{1i} as the geometrical arrival time delay for the GW signal in detector i with respect to detector 1. The null stream can then be defined as a linear combination of Equations 4.15, 4.16, 4.17 which cancel out the $h_+(t)$ and $h_\times(t)$ values associated with the GW signal.

$$N(\hat{s}, t) = A_{23}h_1(t) + A_{31}h_2(t + \tau_{12}) + A_{12}h_3(t + \tau_{13}), \quad (4.18)$$

where

$$A_{\alpha\beta}(\hat{s}, t) = f_{\alpha}^{+}(t_{\alpha}, \hat{s})f_{\beta}^{\times}(t_{\beta}, \hat{s}) - f_{\beta}^{+}(t_{\beta}, \hat{s})f_{\alpha}^{\times}(t_{\alpha}, \hat{s}). \quad (4.19)$$

Similarly to the correlated data described in Section 4.2.3, the null stream will have similar coherent and incoherent energies associated with the spherical harmonic order. In terms of the correlated data, an event is considered a candidate GW signal if it has significantly more coherent energy (E_{SH}) than incoherent energy (I_{SH}). The coherent energy from the GW signal should cancel out in the null stream, leaving the Gaussian background and incoherent energy. This means that the null stream would produce incoherent null energy (I_{null}) significantly greater than coherent null energy (E_{null}) for a strong GW signal.

4.3 Whitening data with line removal

As described previously, the LPEF filter used to whiten the data from each detector relies on the assumption that the background noise including the lines in the spectrum remain constant throughout the segment of data. There are cases where the LPEF filter fails to remove detector noise e.g. where wandering sinusoidal signals (wandering lines) exist in the data. When left in the data these regions of excess power are clustered and treated as events which in turn reduces the sensitivity of the whole analysis. The line tracking tool iWave described in Chapter 2 is an appropriate tool for removing these lines from the data. In this section we will discuss an example of a wandering line present during O1 and how iWave can be used to mitigate the amounts of events it creates. In addition to this is an analysis of applying this filtering technique during a period of O2 where the 500 Hz violin mode was ringing up.

4.3.1 O1 wandering line

During the analysis of O1 data an instrumental line wandering around 650Hz was observed to be present in H1 during the first half of the observation run. The source of this feature was identified as the beating between two VCO channels separated by <700 Hz in frequency [59]. In order to avoid the line affecting the output events from the analysis a notch filter was applied over it's frequency band during post processing to remove these events caused by the line [33]. While this removes the line it also removes the possibility of detecting any events from this frequency region. Previously to this post-processing, most of the events came from this line. Despite the notch filter there would also be a fraction normal amount of background events output by X-SphRad when the line was present. Due to it's non-static frequency, the line remains in the data after it is whitened using LPEF filtering. In Figure 4.1 this wandering line can be seen in a spectrogram of H1 data after LPEF filtering.

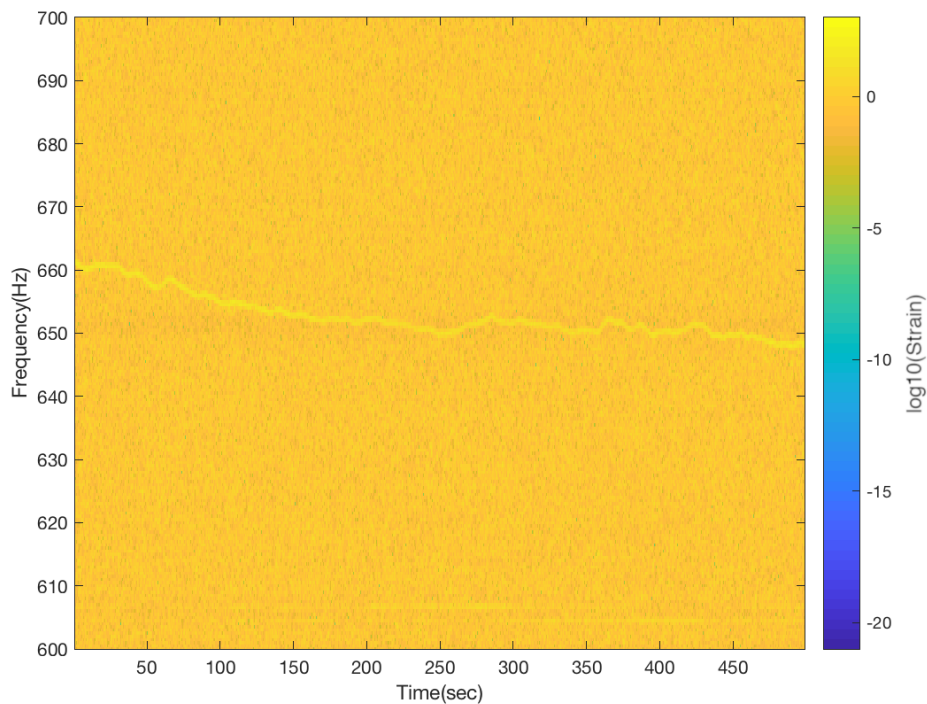


FIGURE 4.1: Spectrogram of wandering line at 655Hz present during O1 after the data is whitened using LPEF. The LPEF whitening filter is not able to remove the wandering line due to the non-static frequency of the signal. When this data is analysed by pipelines such as X-Sphrad large amounts of candidate events are detected from this frequency band which are mostly from this instrumental noise. This reduces the likelihood of detecting an astrophysical signal from sets of data where the wandering line is present.

In order to remove this example of the wandering line firstly a Type 2 Chebyshev band pass filter is applied to the data with a central frequency of 655 Hz with a buffer of 10 Hz either side. This makes it simpler for iWave to lock on to the line. The line tracker is then applied to this region with a starting frequency in the centre of the band, a response time τ of 2.2 s and gain factor η of 9. The filtered output from the line tracking is shown in Figure 4.2.

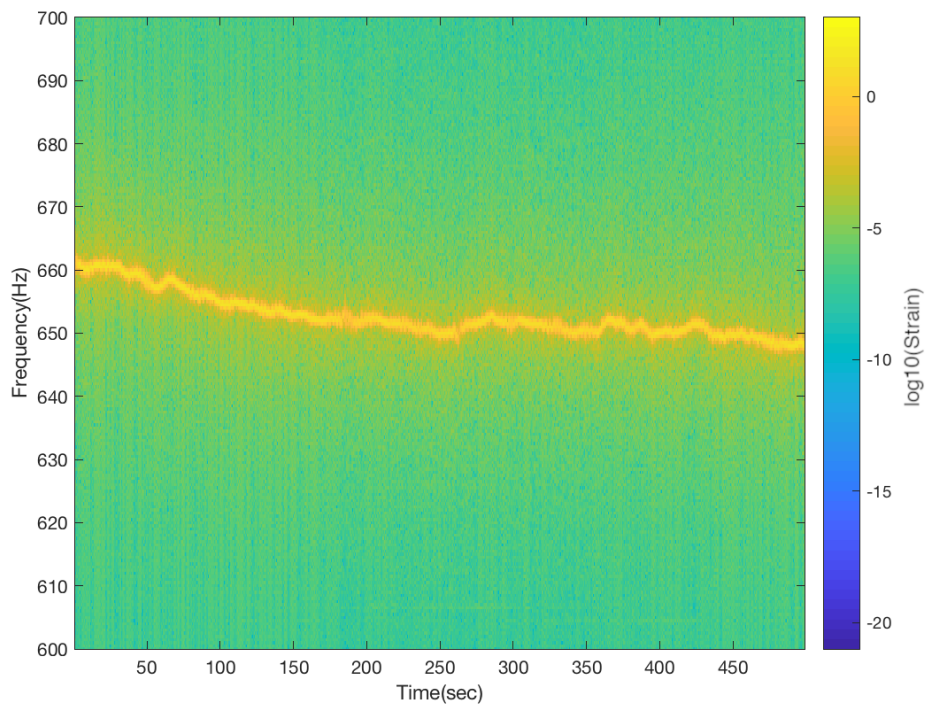


FIGURE 4.2: Spectrogram of tracked I-phase output from iWave line-tracking of 655Hz wandering line. This data is subtracted from the LPEF filtered data in Figure 4.1 to filter out the wandering line.

A part from the short periods where the filter loses lock, the tracked output from iWave adequately models the wandering sinusoid for most of the segment. Lock loss can be attributed to the servo in iWave not being able to keep up with variations in frequency. The wandering line is mostly removed from the data by subtracting the tracked signal from the LPEF filtered data. This line subtracted data can be seen in Figure 4.3. Again there is some remaining excess power after the subtraction over sections where iWave briefly loses lock. With the line removed from the data candidate events at lower energies are now more likely to be detected by X-Sphrad. This is addressed in more detail in Section 4.3.2.

While this technique for line removal is successful for this particular segment of data a more general approach would be needed for it to be applied to a full analysis run. The line is not present in every segment of the data so a method for identifying when the line is present and then applying the line removal would be an optimal solution.

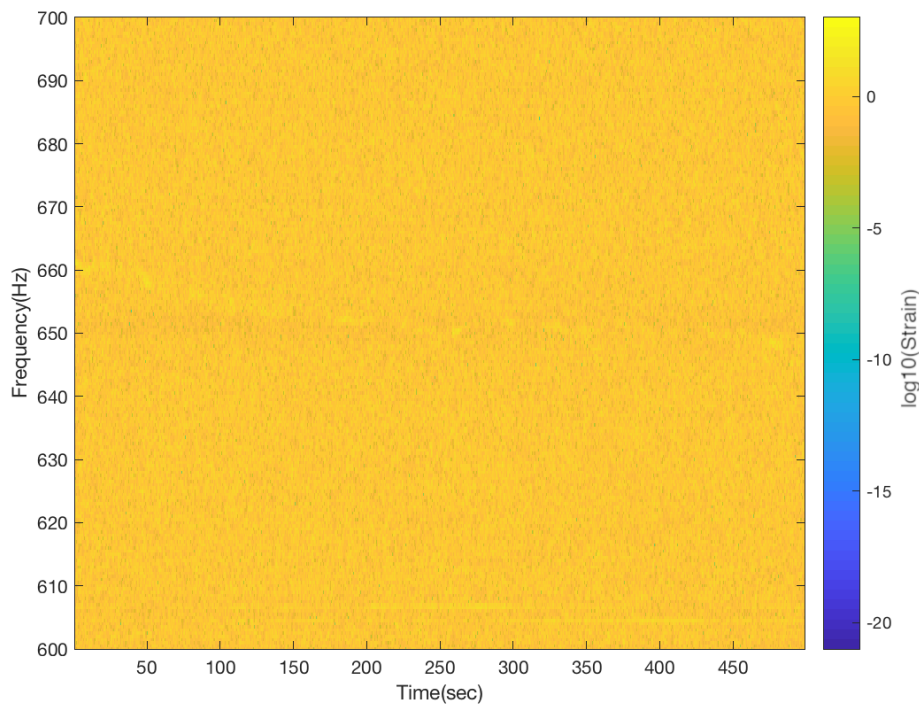


FIGURE 4.3: Spectrogram of O1 data after LPEF filtering and iWave line subtraction of 655Hz wandering line. With the line removed from the data candidate events at lower energies are able to be detected by analysis pipelines such as X-Sphrad. This is discussed further in Section 4.3.2.

4.3.2 Automated line removal process

The automated version of the line removal is a version that will only apply line removal if it is observed from the results of the clustering. This can be preferable if line removal isn't needed for each frame of data. This could also be adapted to indicate the frames in which these lines are present.

The adaptation for line removal in the pipeline is added after the clusters are detected. The clusters are saved to a file which contains information about their frequency range and trigger time. This file is then read by a script which determines how many triggers are within the same frequency range. Triggers with frequencies within 10 Hz of each other are grouped together. The group is then considered a line if the sum of the time separations for each trigger is over a quarter of the length of the whole segment.

If a group of triggers survives this then the lineremoval process is applied to this frequency range. A Type 2 Chebyshev band pass filter is applied to the data in the frequency range with a buffer of 10 Hz either side. This makes it simpler for the linetracking tool to lock on to the line. The line tracker is then applied to this region with a starting frequency in the centre of the band. After tracking the line it is then subtracted from the original data. While this has removed the wandering line from the data, the same cluster output file is still the same as before. This means that the

clustering algorithm needs to be applied to the newly filtered data to identify the clusters after line removal.

This automated line removal process was tested on the same data from Figure 4.1. Firstly for comparison the normal X-SphRad pipeline is applied to the data. When thresholding is applied to the tf-map, the pixels with the highest correlated power dominate the output. This means that the thresholding applied here does not represent the same thresholding for a segment of data which only contains background Gaussian noise. Pixels containing lower correlated power are not included due to the presence of the 600 Hz line. Excess power from this line appears in the thresholded tf-map as groups of pixels around 600 Hz. These pixels are then clustered together as events with above average significance. Since there is a limit to the amount of potential GW candidate follow-ups for one segment of data, events of lower significance are not contained within the output from the analysis.

Figure 4.5 shows the tf-map of the correlated data containing the line after thresholding. The red boxes seen here indicate the bounding boxes for the top 30 candidate events. An injection with $E_{SH} = 20$ (stamp line b) is also added here for comparison. When the injection scale is this high it can easily be detected as event. Most of the other events come from the line at 600 Hz spanning over the full time segment.

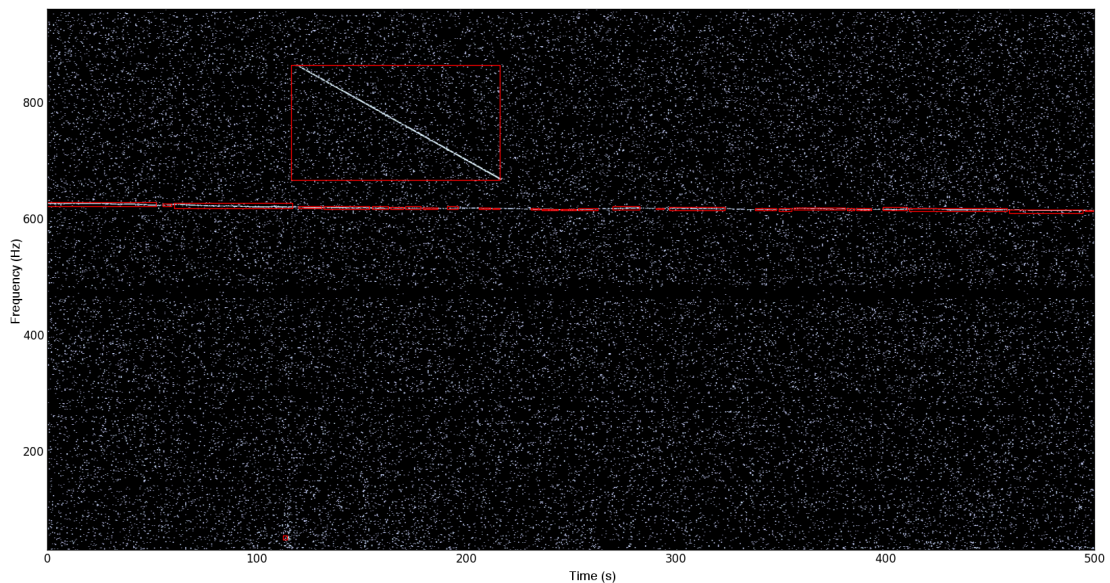


FIGURE 4.5: Thresholded tf-map of correlated HL data. Excess power from the wandering line is clustered and detected as events.

When the automated lineremoval process is applied the clusters from the line are identified as such and line removal is applied to the region where the line exists. It can be seen that with the line removal a lot more of the lower significance triggers are identified by X-Sphrad. There are some remaining regions of excess energy from the line which is picked up as events, however most of the lines power has been subtracted. The injection is also recovered similarly to before line removal and it's energy is not reduced by the line removal process.

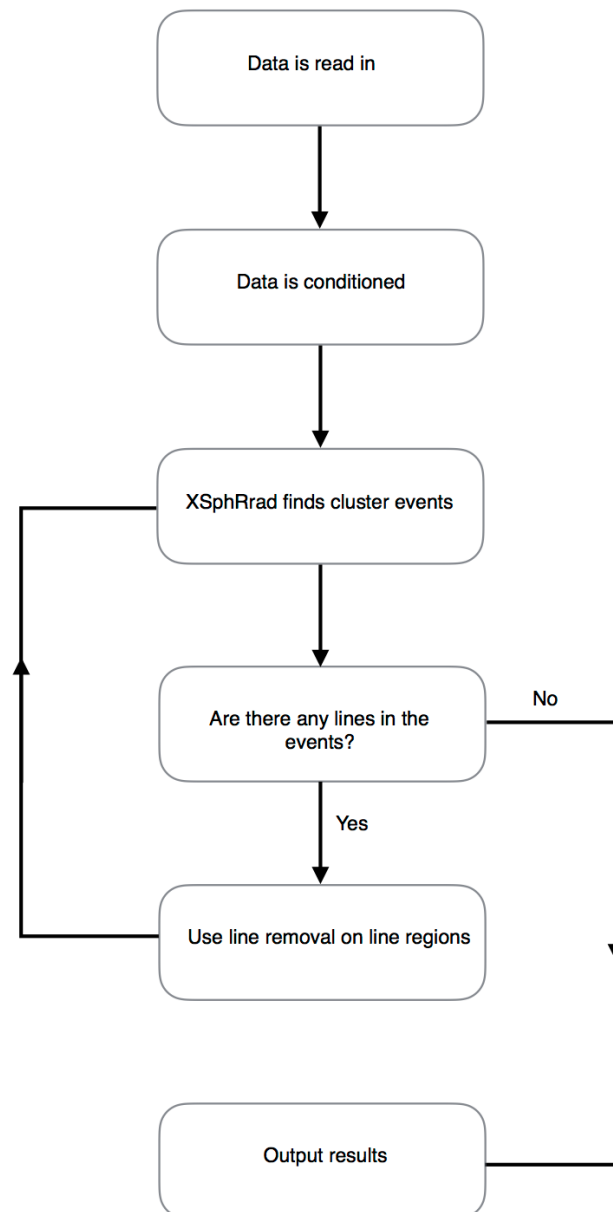


FIGURE 4.4: Flow chart for automated line removal process with X-SphRad.

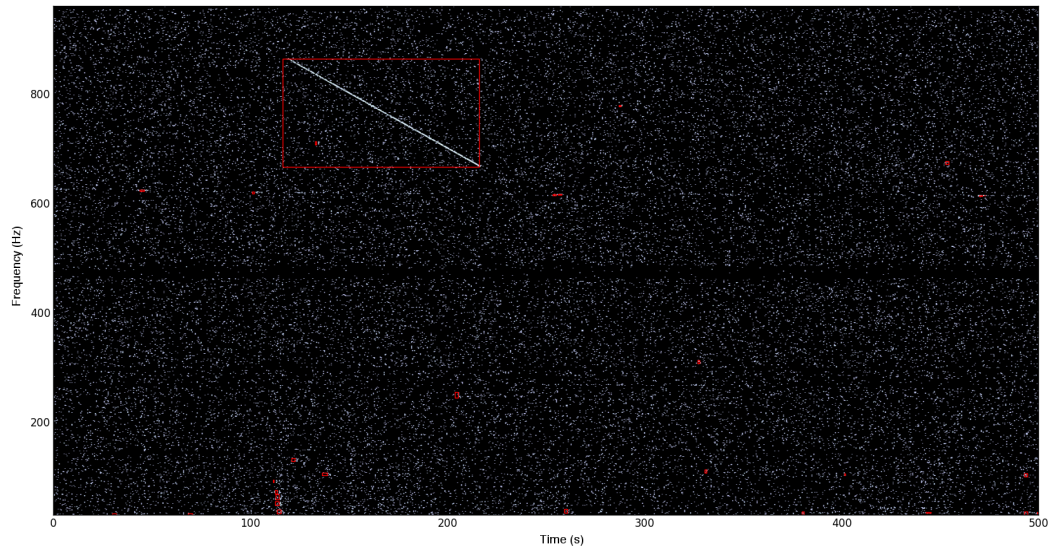


FIGURE 4.6: Thresholded tf-map of correlated HL data after line removal. Events at lower energies are now detected in the absence of the wandering particularly at lower frequencies.

This analysis with line removal was also completed without the bandpass filtering. It can be seen that when the frequency of the injection approaches the frequency of the line, it causes the line tracker to lose lock on the line. Towards the end of the segment of data it is able to remove some of the line energy however without bandpassing the line removal process is not successful at preventing the most of the line being identified as events.

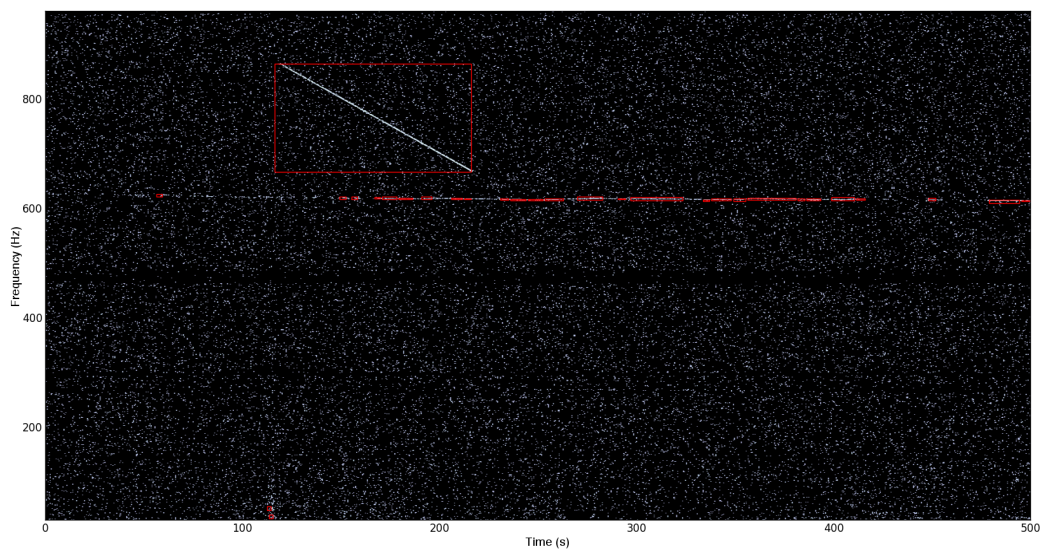


FIGURE 4.7: Thresholded tf-map of correlated HL data after line removal without bandpassing. Line tracker loses lock on the wandering line in the presence of the injection.

Several analysis were completed over the same segment of data adding varying injection scales both with and without the line removal process. From Figure 4.8 the output is dominated by events from the line with higher significance. When line removal is applied there is a larger variation in frequency for the surviving events which have significantly less energy than the events which came from the event. Compared to Figure 4.5 the injection is recovered as several events with smaller bounding boxes for these smaller injection scales. The amount of events coming from the injection for both processes is increased with increasing injection scale. More events from the injection are identified from the line removed data compared to the data with the line present.

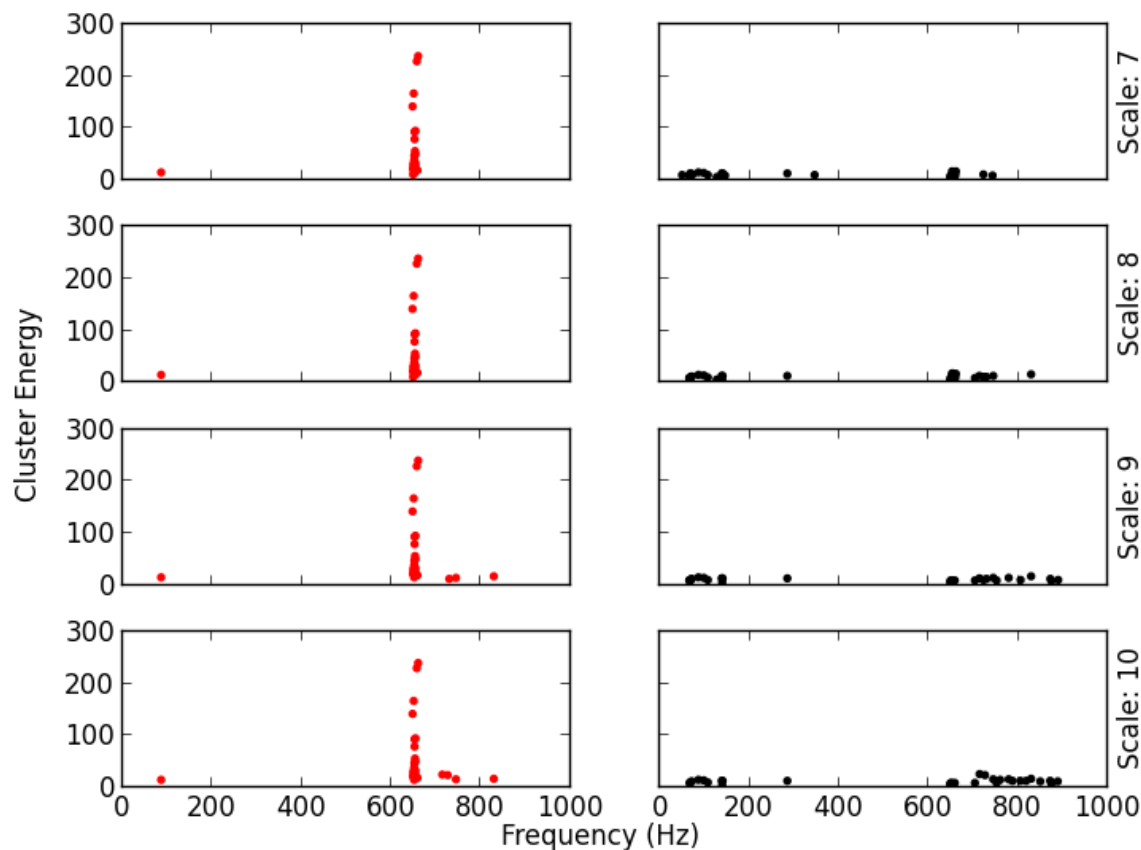


FIGURE 4.8: Energy of clustered events against central frequency. Red and black data points indicate events before and after line removal respectively. Injection scale is increased for each plot downwards. Increasing injection scale causes increasing events above wandering line frequency particularly after line removal.

4.3.3 O2 excited violin mode removal

While the automated version of the line removal would be preferable it is also computationally expensive and takes a long time to run. The main reason for this is how long the clustering process takes to run. Using this version means that the clustering algorithm needs to be run another two times at least for each frame of data. Another

version of line removal is where the frequency of the line is specified in the before the analysis starts. Line removal is then applied to every frame at this frequency before the clustering algorithm is applied. Although this may seem excessive, this will actually save time in comparison to the automated version.

The same analysis is completed with the normal whitening procedure and with the added line removal. The top ten surviving dummy on-source events from both analyses are shown in Tables 4.1 and 4.2. The time slide used to create these dummy on-source events is different for each analysis. Several of the loudest dummy on-source triggers from the normal analysis are sourced from the the excited 500 Hz violin mode. In comparison these events are not observed in the loudest triggers from the analysis with line removal. On first sight this may appear that the 500 Hz triggers have been removed, however this is not the case. When comparing the circenergy v.s. circinc plots, the background events from the line removed analysis have energy in the region of 10 order of magnitude higher than the regular analysis. This indicates that the line removal process has added some glitches into the data discussed in Chapter 2.

circenergy	incoherent circenergy	peak frequency (Hz)	duration (ms)	number of TF pixels
70.78	30.39	503.5	40500.0	221
21.42	5.9	503	34000.0	98
12.18	2.53	503.5	29500.0	91
11.21	2.44	503.5	28500.0	81
6.43	0.74	986	3000.0	12
6.13	0.87	907.5	3000.0	15
6.12	1.06	968	5000.0	14
5.96	0.5	916	2500.0	9
5.94	0.97	865.5	4000.0	12
5.78	0.72	743	3000.0	13

TABLE 4.1: Top 10 dummy on-source events without line removal. Top four events are long duration events from excited violin mode.

circenergy	incoherent circenergy	peak frequency (Hz)	duration (ms)	number of TF pixels
201.39	120.96	988	2500.0	15
55.27	28.76	792	3000.0	159
33.9	13.54	48	1000.0	3
32.38	9.07	783.5	2000.0	87
28.49	13.37	513	19500.0	144
17.81	7.35	976.5	2000.0	8
13.2	5.27	976	2500.0	46
13.2	4.77	980.5	1500.0	47
13.15	4.31	782.5	2000.0	41
12.43	3.71	998	4500.0	26

TABLE 4.2: Top 10 dummy on-source events with line removal. Fewer events seen with longer duration indicating line removal was successful.

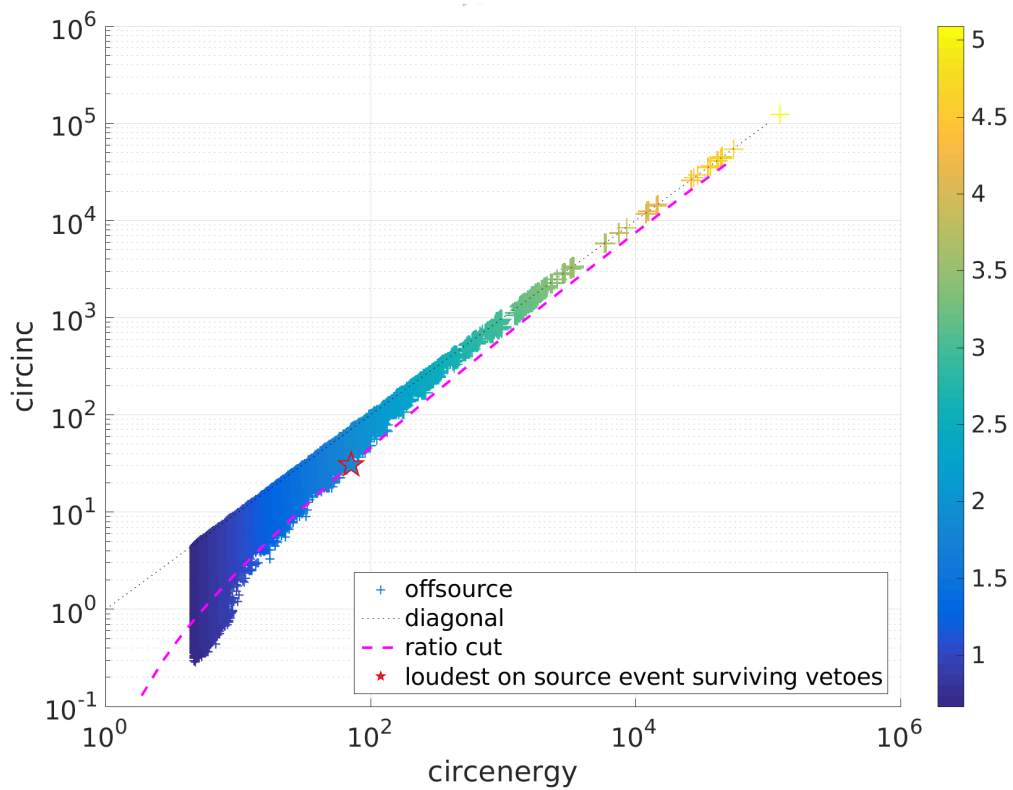


FIGURE 4.9: Incoherent v.s. coherent energies for offsource background without line removal. The colour axis is the base-10 logarithm of the cluster's coherent energy (circenergy).

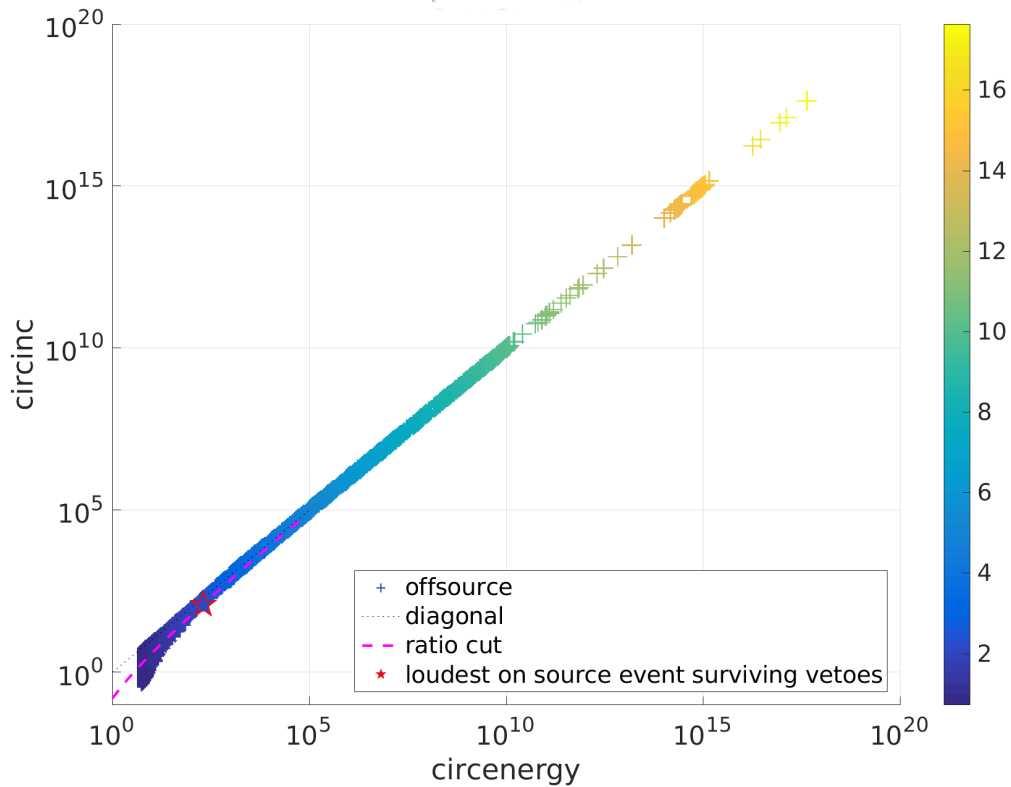


FIGURE 4.10: Incoherent v.s. coherent energies for off-source background with line removal. Events seen at much higher energies than without line removal indicating glitches have been introduced by the line removal process. The colour axis is the base-10 logarithm of the cluster's coherent energy (circenergy).

To investigate these glitches one segment of data for the simulations analysis which contained excess energy was analysed manually. This segment of data does not contain any of the 500Hz glitches from the violin modes so it was expected that the filter would not remove or add any excess energy to the data. From the tf-map in Figure 4.11 the glitch can clearly be seen after 150 seconds. This glitch is much louder than anything else in the data and only the injection is barely visible in the tf-map. Clearly if this glitch is in the data the thresholding that is applied to the data before clustering will cause most of the lower energy events to be lost.

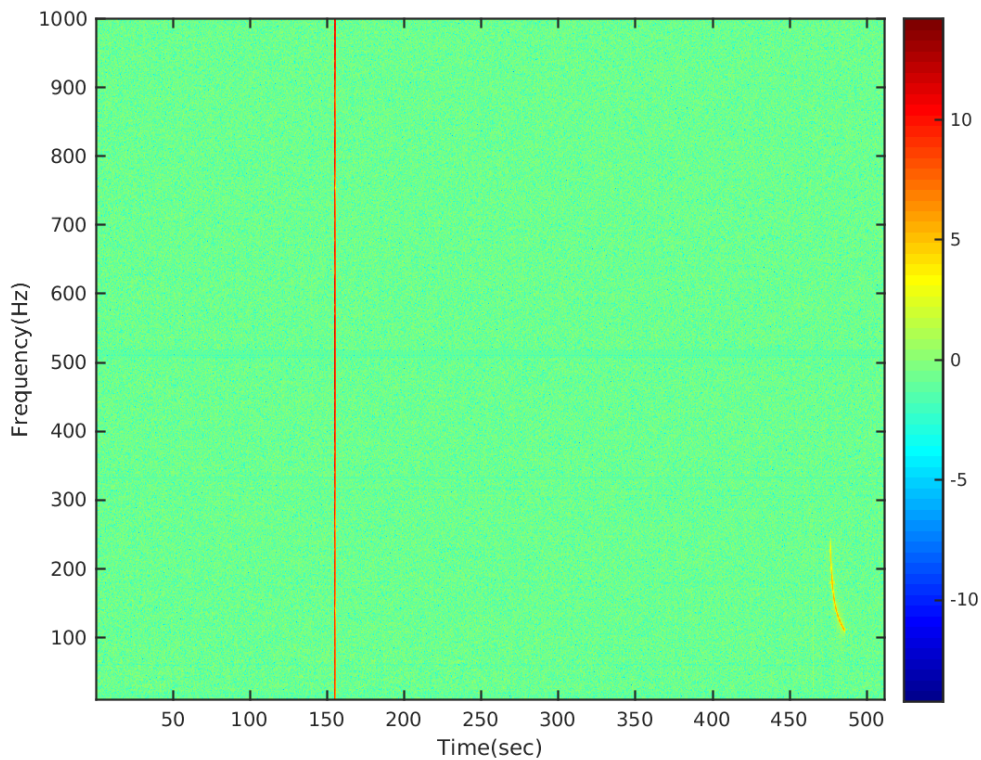


FIGURE 4.11: Followup tf-map of segment of injection analysis containing a glitch due to line removal after 150 seconds.

This glitch coincides with a drastic change in the tracking frequency which is 7 orders of magnitude above the Nyquist frequency for the data. This may be due to a short increase in background noise from the segment of data which the filter will detect as a change in phase. This version of the filter has no way of constraining its tracking frequency to within the Nyquist band of the data it is filtering. The same analysis was then completed without the band pass filtering before the linetracking. From Figure 4.13 it can be seen that the linetracking filter does vary in tracking frequency with the same glitch type behaviour. This does not have an impact on the filtered output and the largest excess energy that is observed is from the injection at the end of the segment.

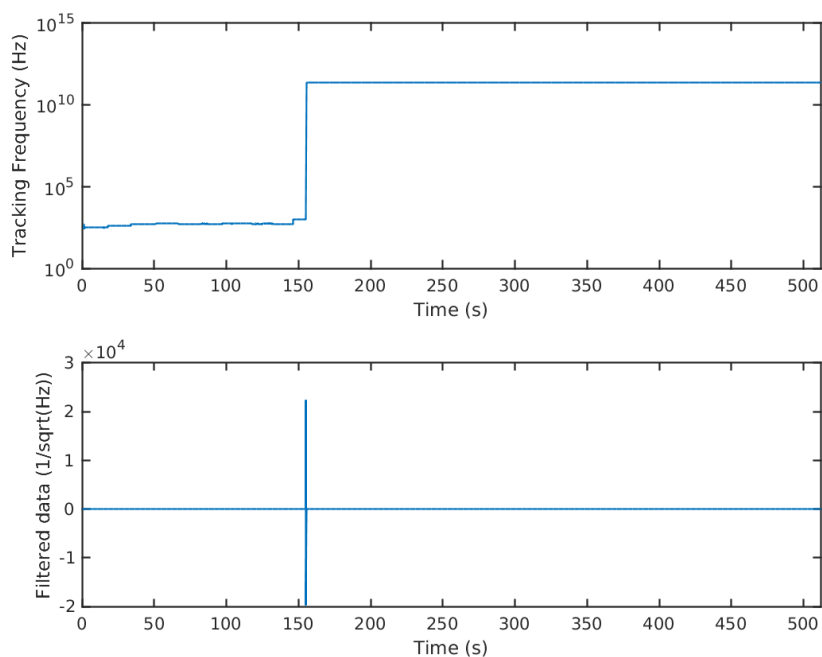


FIGURE 4.12: Time-series data from frequency tracking and filtered output with bandpassed line tracking process. Glitch appears at same time as large change in frequency

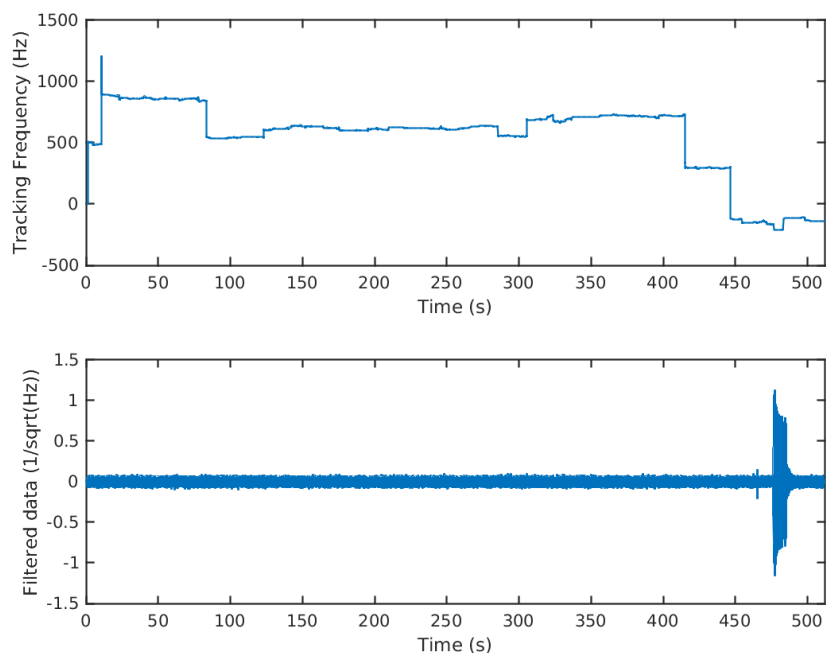


FIGURE 4.13: Time-series data from frequency tracking and filtered output from line tracking process without bandpassing. Glitch is no longer seen in time series data indicating the bandpassing was the cause of the glitch.

Chapter 5

Results from O2 analysis

In this chapter the results from the all-sky analysis using the X-SphRad pipeline with data from the O2 observation period are presented. Firstly the results from the 3 detector case (Hanford, Livingston and Virgo) are discussed followed by the results from the 2 detector case (Hanford and Livingston). Both of these sets of data are taken over the last month of O2 as this was the period where the Virgo detector was online. The total time for the analysis was 24 days however the pipeline requires periods of time with coincident data from each detector in the network. This means that for a segment to be used for analysis all detectors need to be in a locked state. The coincident time between detectors was 15.12 days for the 3 detector case and 16.95 days for the 2 detector case. The actual time used will be less than this since the pipeline also requires the input data to be quantised into 512 second segments. Both of these analyses search for clusters over the frequency range between 24 Hz and 1000 Hz. For the 3 detector analyses C01 frames are used whereas C02 frames are used for the 2 detector analysis.

The work in this chapter is based on the established pipeline X-Sphrad. I ran the 2 separate analyses using X-Sphrad mentioned previously and interpreted each set of results. The results from the 2-detector analysis simulations were plotted using scripts which I modified but were originally developed by Maxime Fayes [33].

5.1 3 detector analysis

During the O2 observation run one month of data existed where the two LIGO detectors and the Virgo detector were online and producing coincident data. This set of data presents the uncommon opportunity for all-sky analysis with three sets of data. One of the main benefits from this is that a null stream of data can be produced which is discussed in Section 4.2.6. The null stream can be used as a method to determine the legitimacy of signals detected from the coherent data stream.

For the closed box analysis of the O2 data from the three detectors, only events from the off-source background are considered. The time-slide which produces the highest significance event is used to construct a dummy on-source set of data. This data still contains events with non-physical time delay between detectors. The events considered for detection are the ones surviving the cuts applied to the data. Figure 5.1 displays the coherent v.s. incoherent energies for each of these events and the loudest event after cuts are applied. Background events are located around the diagonal line with $E_{SH} \approx I_{SH}$ and at lower values of E_{SH} . The event surviving cuts

is off from the diagonal with greater E_{SH} than I_{SH} which could be considered as a detection if this were the real on-source data.

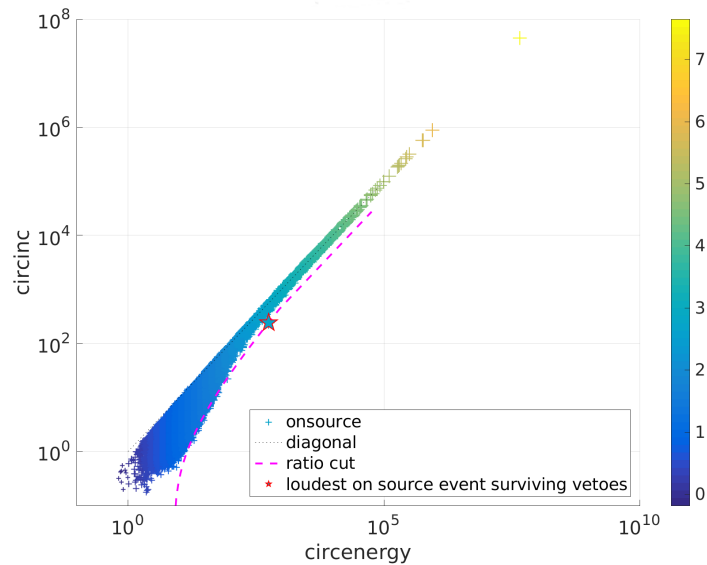


FIGURE 5.1: Incoherent v.s. coherent energy for 3 detector dummy on-source. Event can be seen passing the cut with $E_{SH} > I_{SH}$. The colour axis is the base-10 logarithm of the cluster's coherent energy (circenergy).

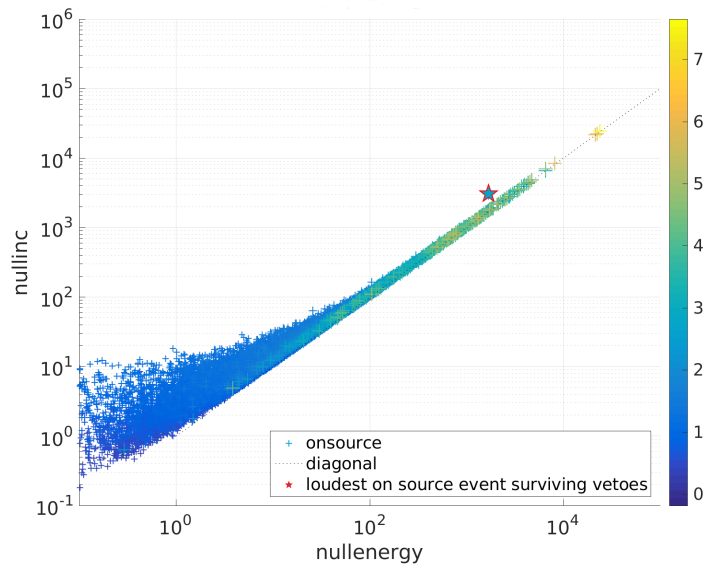


FIGURE 5.2: Incoherent v.s. coherent energy for 3 detector dummy on-source. Loudest event from previous figure observed here with $I_{null} > E_{null}$. The colour axis is the base-10 logarithm of the cluster's coherent energy (circenergy).

When looking at the same data in terms of the null stream the event also appears as a distinct point from the rest of the data. Again the background events can be seen on the diagonal line with $E_{null} \approx I_{null}$ but also at lower energies. The event seen in Figure 5.1 can be seen off the diagonal with higher I_{null} than E_{null} .

The event seen from Figures 5.1 and 5.2 was investigated by manually repeating the analysis of the data set. From the tf-map in Figure 5.3 the event can be seen around 250 seconds. As well as this several other glitches can be seen in the data with uniform distribution in frequency. This glitchy behaviour can be attributed to detector noise added by the Virgo detector. This is highlighted in Figure 5.4 which compares the relative spectra for each detector. The data from Virgo has a higher noise floor compared to the other detector as well numerous extra lines.

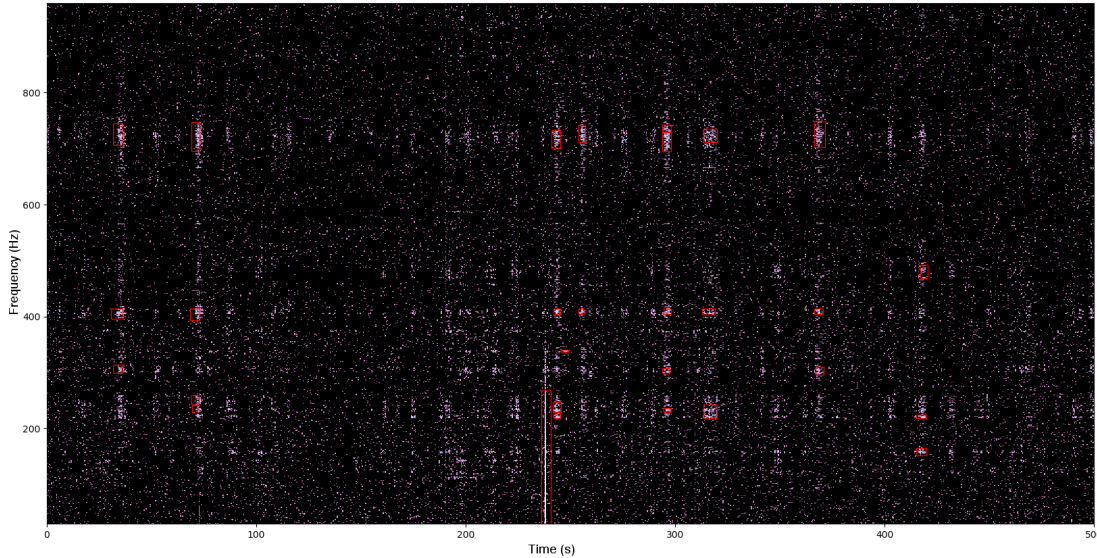


FIGURE 5.3: Thresholded tf-map from followup of highest significant event from the dummy on-source. Event can be seen as a glitch centred around 250 seconds. Other glitches can be seen with similar frequency distributions coming from Virgo detector noise.

The extra noise contribution from Virgo is reflected by the cuts generated after background tuning with injections. The alpha cut is set to 4 and the linear cut is at 2.1 which are much higher than the values for the 2 detector results discussed in Section 5.2.2. These high cut values can be attributed to the glitches from Virgo which produce high significance events due to their autocorrelation from Equation 4.11.

Figure 5.5 shows the event rate for this analysis for the off-source and dummy on-source results. This can be used to define the amount of events caused by the background noise in the detector or the FAR. The event significance before cuts for both background and foreground data range up to 6×10^7 before cuts and 6×10^2 after cuts. A large difference in event rate between the 'on-source' and off-source after cuts can be seen at higher significance. This can be attributed to the fact that the 'on-source' is the dummy on-source described previously which uses the time slide containing the highest significant event which passes cuts. The trend for the off-source event rate before cuts gives a good representation of the dummy on-source before cuts. This shows that the off-source contains an accurate estimation of the background.

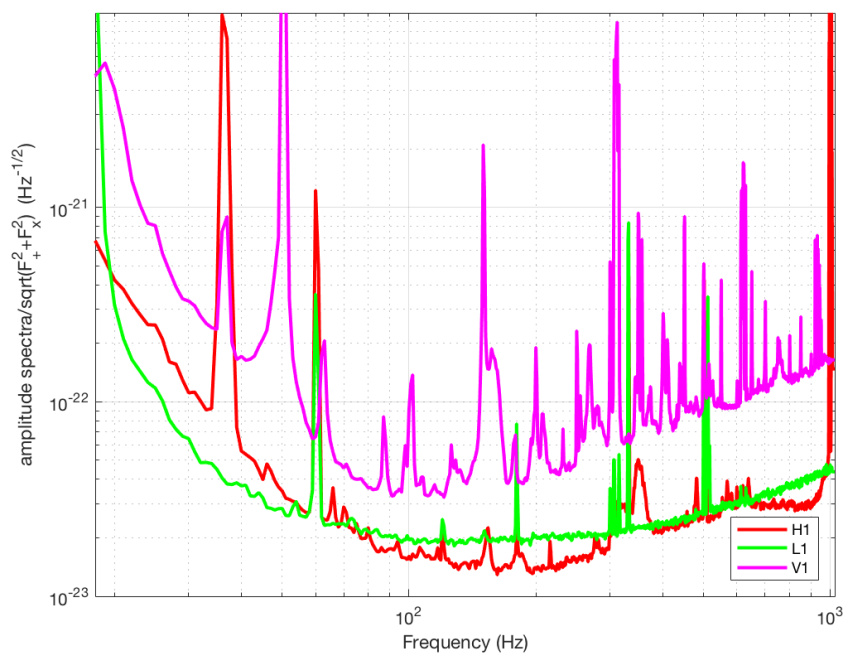


FIGURE 5.4: Average spectrum over analysis time for each detector. Higher noise floor and numerous lines can be seen for Virgo in comparison to the two LIGO detectors.

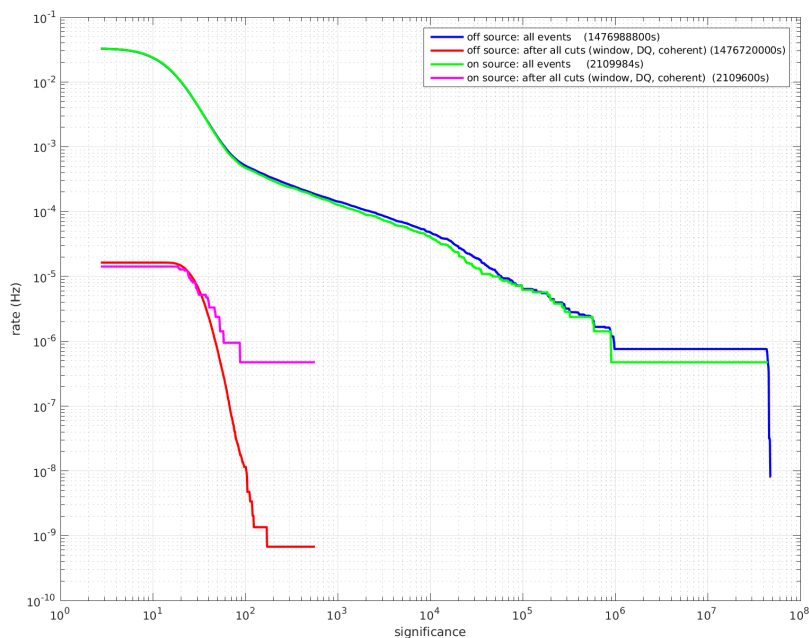


FIGURE 5.5: Event rates for off-source and dummy on-source before and after cuts for 3 detector analysis. Events at higher significance after cuts can be attributed to autocorrelated glitches from Virgo data.

5.2 2 detector analysis

5.2.1 Background and Foreground results

For the following results we firstly discuss the closed box followed by the open box results. Closed box indicates that the 'on-source' events are referring to the dummy on-source events. These events are generated from the time slide containing the most significant event after cuts from the off-source background. Open box indicates that the on-source events are real GW candidates and not from the off-source background.

Closed box

The event rates for the closed box 2 detector analysis are shown in Figure 5.6. The 'on-source' and off-source event rates for 2 detectors are significantly less than the 3 detector case due to the absence of the glitches from Virgo. The highest significance off-source event before cuts has a detection rate 2 orders of magnitude smaller than that from the 3 detector off-source from Figure 5.5. The off-source background gives a good representation of the 'on-source' for the most part although there are a few extra triggers at higher significance. The event rate for the highest significance event after cuts for both the on-source and off-source are 1 order of magnitude less than the equivalent for the 3 detector case. As well as this the highest significance event has significance an order of magnitude smaller than the equivalent for the 3 detector case.

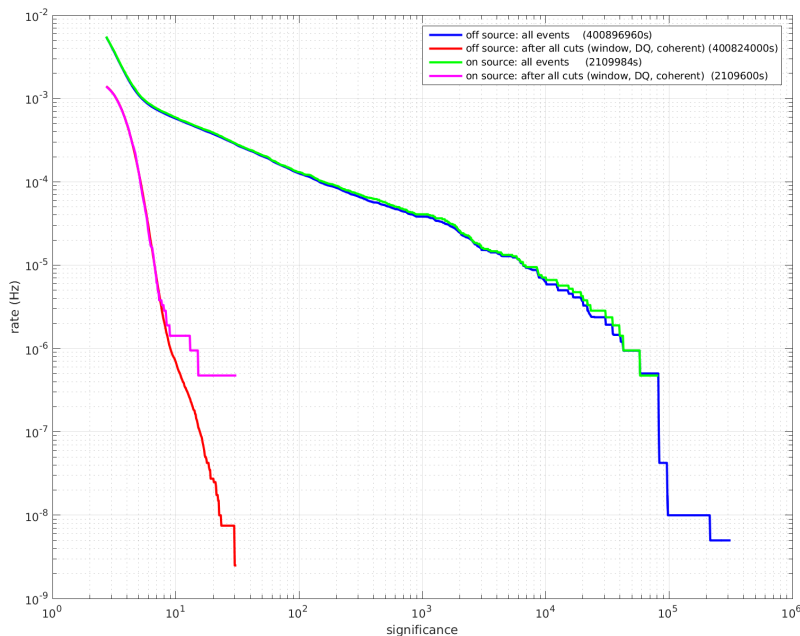


FIGURE 5.6: Event rates for off-source and dummy on-source before and after cuts for 2 detector analysis. Events before cuts will be dominated by glitches. Events after cuts show a sharper decrease in rate with increasing significance seen compared to the 3 detector closed box results in Figure 5.5

Open box

From Figure 5.7 the event rates for the real on-source events can be seen to decrease at a faster rate with increasing significance compared to the dummy on-source events seen in Figure 5.6. There are no distinct signals emerging from the background indicating that the remaining on-source events after cuts can be attributed to background triggers.

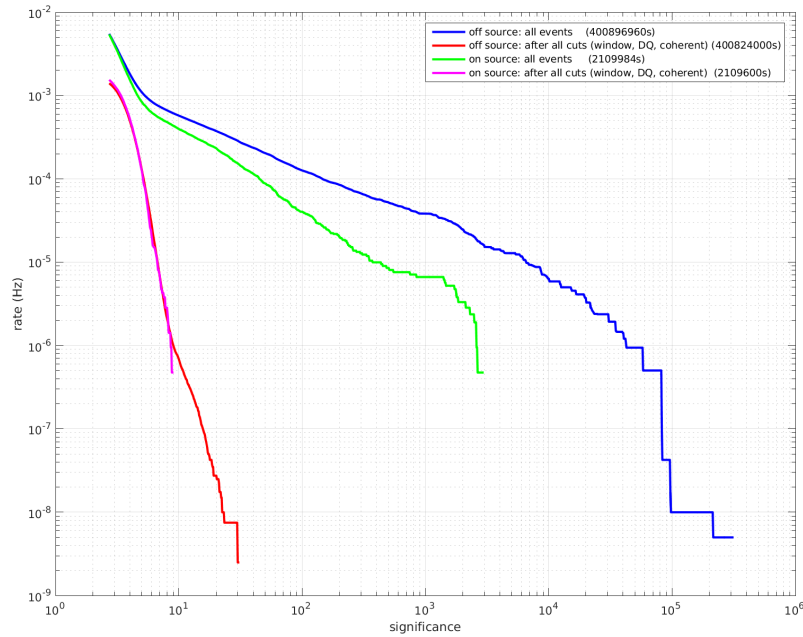


FIGURE 5.7: Event rates for off-source and on-source before and after cuts for 2 detector analysis. There are no on-source events after cuts emerging from the background at higher significance. This indicates that the on-source is comprised of only background events.

Figure 5.8 shows how the ratio between incoherent I_{SH} and coherent energy E_{SH} of events compares between the off-source background and on-source. For both sets of data there is a large population with equal E_{SH} and I_{SH} . The linear cut from Equation 4.12 is used to remove these events caused from background noise. These events on the diagonal have lower peak frequency than the events with $E_{SH} > I_{SH}$. The source of a large percentage of the population of events at lower energies can also be attributed to background events. The majority of the glitches from here are filtered out by the alpha cut from Equation 5.9.

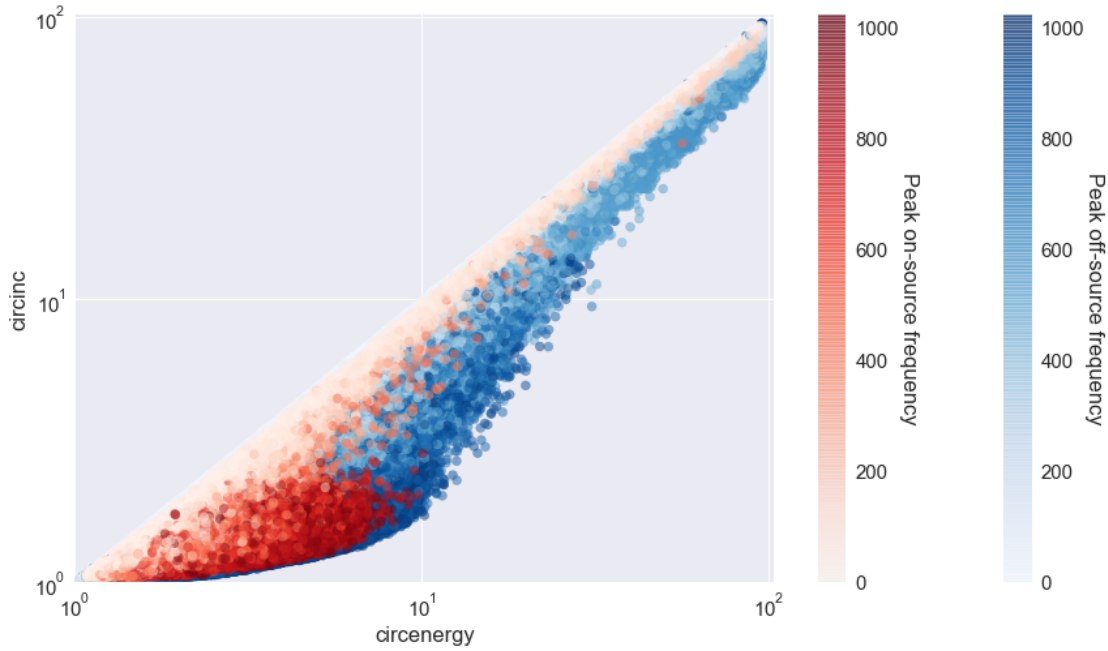


FIGURE 5.8: Coherent energies from on-source events (red) and off-source events (blue). Events with lower frequency tend to the diagonal of equal coherent and incoherent energies.

GPS time	Significance	Peak Freq (Hz)	Bandwidth (Hz)	Duration (s)
1187588010.5	9.07	893.5	14	3.5
1186414610.5	8.74	794.5	6	4.5
1185813342	8.51	807	13	3.5
1186551471	8.21	814.5	8	4
1187690882.5	8.14	887	11	2
1186605733	8.01	936	7	4.5
1186704297	7.7	957	7	44
1186984991	7.7	788.5	10	3
1186214085	7.48	879	13	2.5
1185965447.5	7.27	920	7	3

TABLE 5.1: Top 10 highest significance events from on-source surviving cuts. GPS time is with respect to the Hanford detector. From Figure 5.7 these can be attributed to background events.

5.2.2 Cuts

For the 2-detector analysis the alpha cut set at 3 meaning that the injections could be recovered at a lower hrss value. Figure 5.9 shows that the alpha cut values increase with frequency. This is partly due to the detector being more sensitive in these mid-range frequencies as seen in Figure 5.4. Also lower frequency events are more likely to be associated with glitches in the detector. This gives a bias in the amount of surviving triggers at higher frequencies compared to those at lower frequencies.

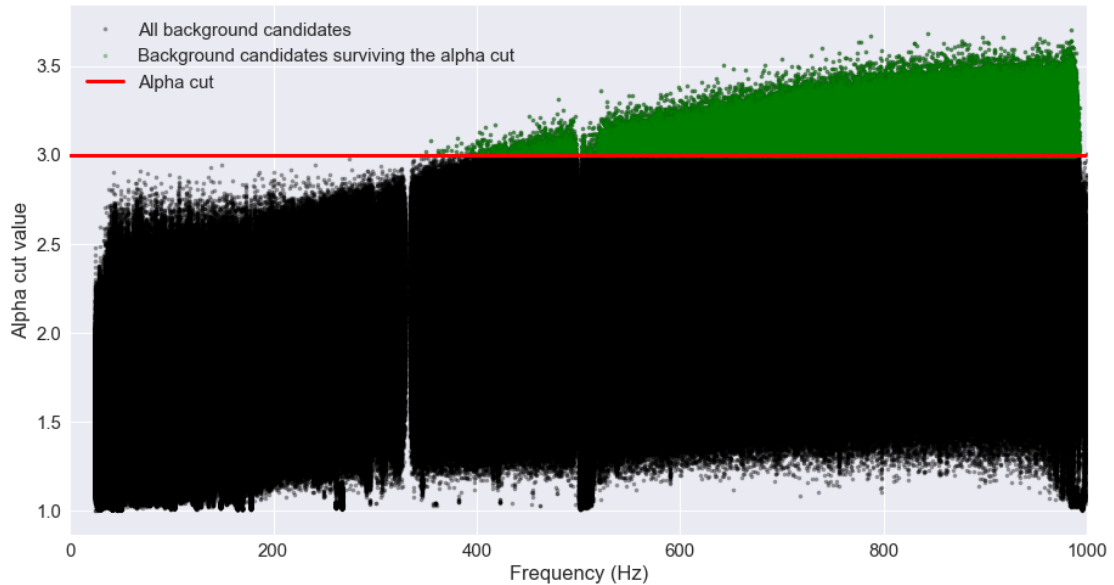


FIGURE 5.9: Distribution of alpha cut value with frequency. Events above red line indicate those which passed the cut. Higher frequency events more likely to survive the alpha cut.

In comparison to the alpha cut, the fixed ratio cut does not remove as many events making it almost redundant for this case. Figure 5.10 shows the initial event output and the surviving amount of events due to the alpha cut, fixed ratio cut and both combined. At lower frequencies the fixed ratio cut removes a small percentage of the events whereas the alpha cut has removed most of the events up to around 400 Hz. This bias means that only candidates above this frequency will be considered as events. There is also a reduction in events around 500 Hz due to the LPEF filtering. When filtering out the violin modes lines from this frequency band the LPEF filter reduces the energy contained within this region. For that reason there will be no surviving events from this region with the current method of whitening the data.

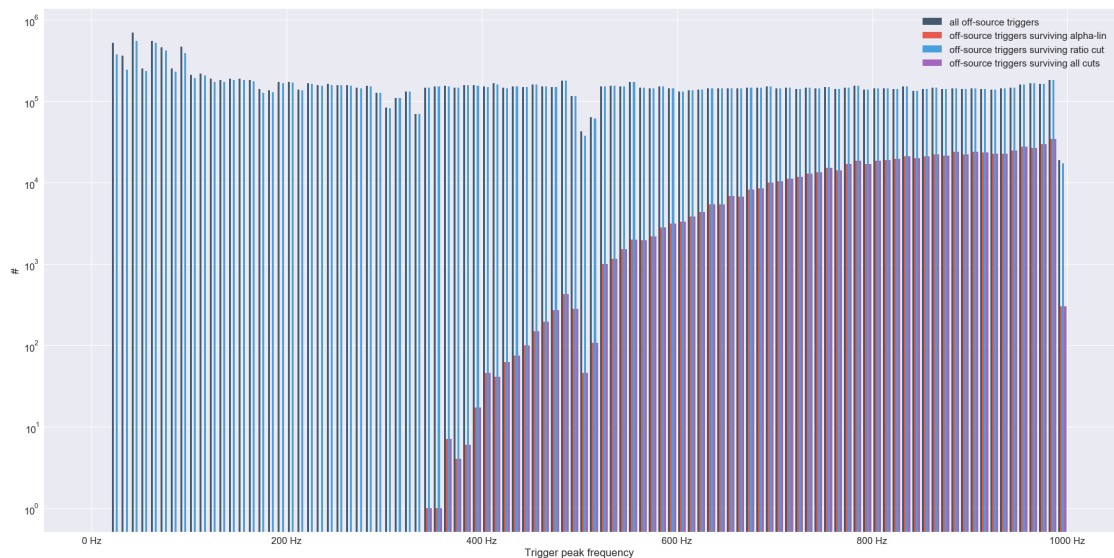


FIGURE 5.10: Histogram of events surviving different cuts over central frequency. Alpha cut reduces the amount of events significantly more than the linear cut.

5.2.3 Injection recovery

Simulated GW signals are injected into the correlated data in separate analyses in order to assess the sensitivity of the pipeline. By injecting signals at varying injection scales the pipeline’s sensitivity to GW signals from increasing source distance can be estimated. Injections are also used to tune the background cuts in post-processing, removing events caused by detector noise. The injections used here come from simulated astrophysical models and from ad-hoc models. Firstly we will discuss the results from the astrophysical models.

Astrophysical models

The first waveform family described here are modelled from Accretion Disk Instabilities (ADI). These models represent the GW emission from rapidly rotating black-hole–torus systems [62]. Two examples of this waveform family can be seen in Figures 5.11, 5.12 with varying duration and bandwidth. They are generally waveforms with starting frequency under 300 Hz with decreasing frequency in the time domain. Their duration also varies between 9 seconds for ADI-B and 236 seconds for ADI-C.

Waveform	Duration (s)	Min Freq. (Hz)	Max Freq. (Hz)
Adi-A	39	135	166
Adi-B	9	110	209
Adi-C	236	130	251
Adi-D	142	119	173
Adi-E	76	111	260
Magnetar-F	400	579	950
Magnetar-G	400	405	490

TABLE 5.2: Properties of injected astrophysical waveforms

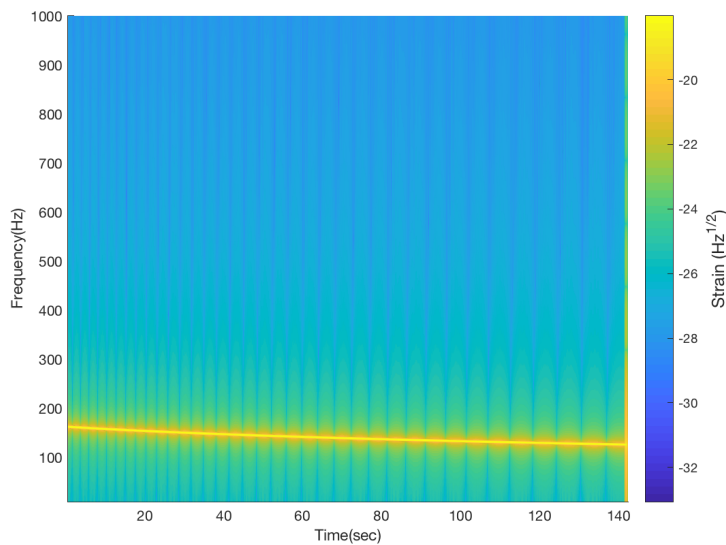


FIGURE 5.11: ADI-D injection waveform spectrogram. The profile of this waveform is an anti-chirp with a small bandwidth of 54 Hz and long duration of 142 seconds.

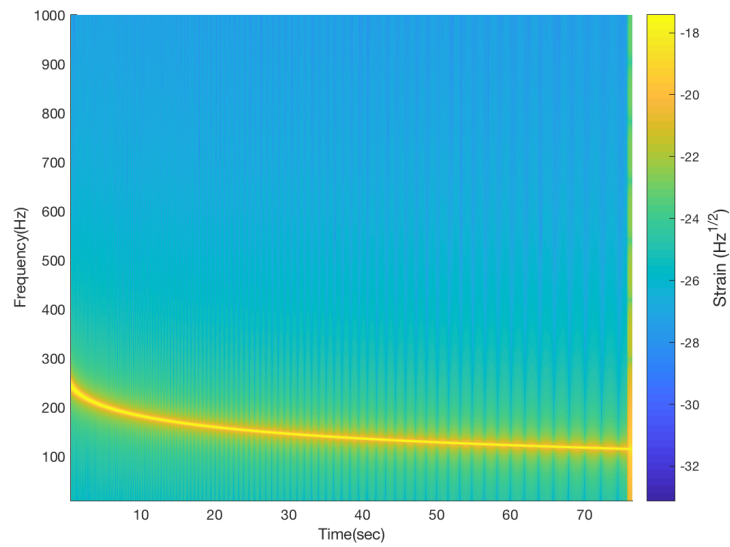


FIGURE 5.12: ADI-E injection waveform spectrogram. The profile of this waveform is an anti-chirp with a larger bandwidth of 149 Hz and a duration of 76 seconds.

For each waveform there is a relationship between the detected event duration and bandwidth. For waveforms with lower bandwidth the relationship is fairly linear with excess bandwidth occurring when injections are grouped with other background events. Increasing duration and bandwidth also relates to increasing injection scale. Injection scale here is inversely proportional to the distance between the source of the modelled signal and the detector. These injection scales are spaced logarithmically between 10 kpc and 1000 Mpc where larger injection scales relate to smaller distances and vice versa. The exact conversion factor between distance and injection scale varies for each waveform and is dependent on their modelled intrinsic amplitude.

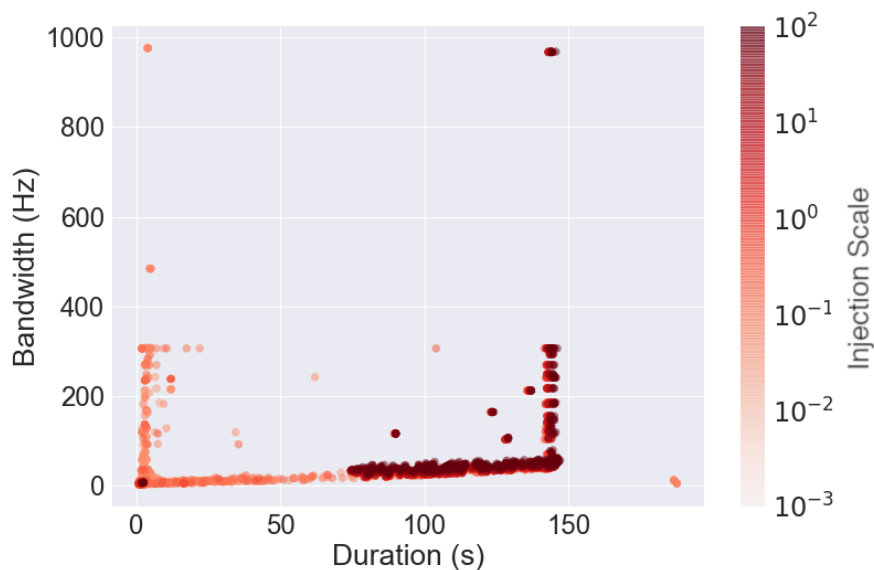


FIGURE 5.13: Duration v.s. bandwidth for all recovered ADI-D injections. Duration has a linear relationship with bandwidth for this waveform.

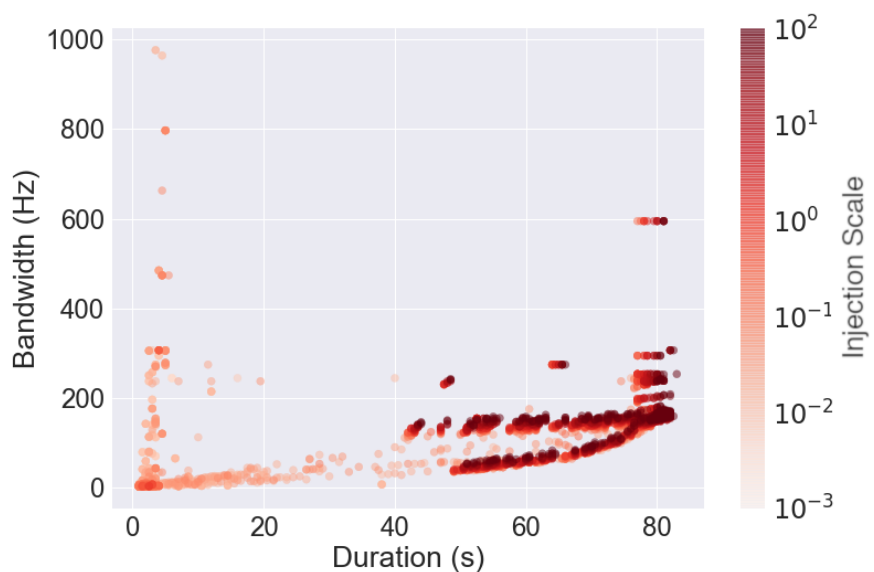


FIGURE 5.14: Duration v.s. bandwidth for all recovered ADI-E injections. The distribution of recovered waveforms is split into two trends due to larger injection bandwidth.

For waveforms with larger bandwidth, the recovered events split into two different trends. This is related to injections with more of a chirp or anti-chirp waveform. The energy distribution of these waveforms tend to be more focused in the lower frequency region. This can cause the only a only the lower frequency region to be clustered, resulting in lower bandwidth. Again at higher injection scales the events

duration and bandwidth also increases. Both of these trends converge at the bandwidth of the waveform at higher durations.

The distance to source for each injection is inversely proportional to the hrss value for the injection. Comparing Figures 5.15 and 5.16, the full duration of the ADI-B waveforms is recovered to a much larger distance than the ADI-C waveforms. The excess in duration at lower distance for the ADI-B waveforms is associated with Fourier leakage where the louder injections leak energy into surrounding pixels due to saturation. ADI-B waveform has energy compressed into shorter duration in comparison to the ADI-C waveforms. Due to this the duration for the ADI-C injections tends to be underestimated which also limits the distance at which they can be observed.

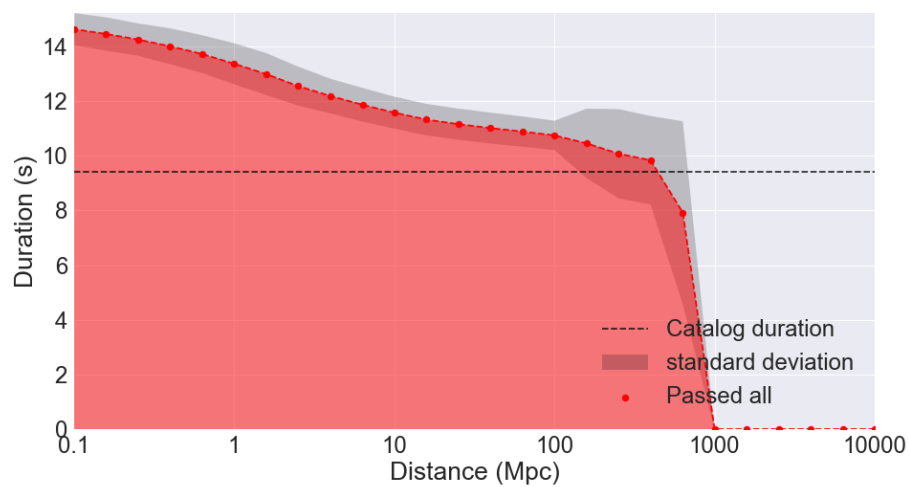


FIGURE 5.15: Recovered duration with increasing distance to source for ADI-B injections.

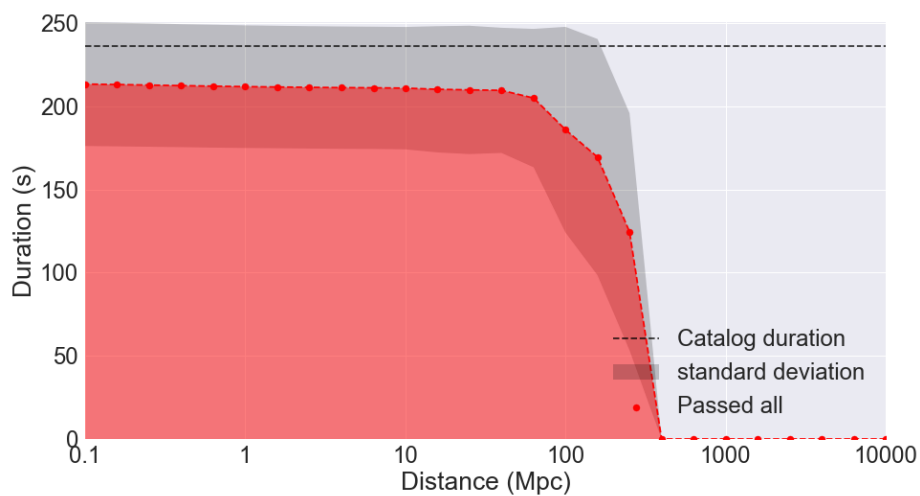


FIGURE 5.16: Recovered duration with increasing distance to source for ADI-C injections.

The magnetar family contains two very long duration waveforms (400 s) modelled from the GW emission from post merger neutron stars with toroidal magnetic fields [25]. The Magnetar-F waveform spans a large bandwidth of 371 Hz and a larger average df/dt than the Magnetar-G waveform. This results in a large splitting of the trend in bandwidth v.s duration seen in Figure 5.19.

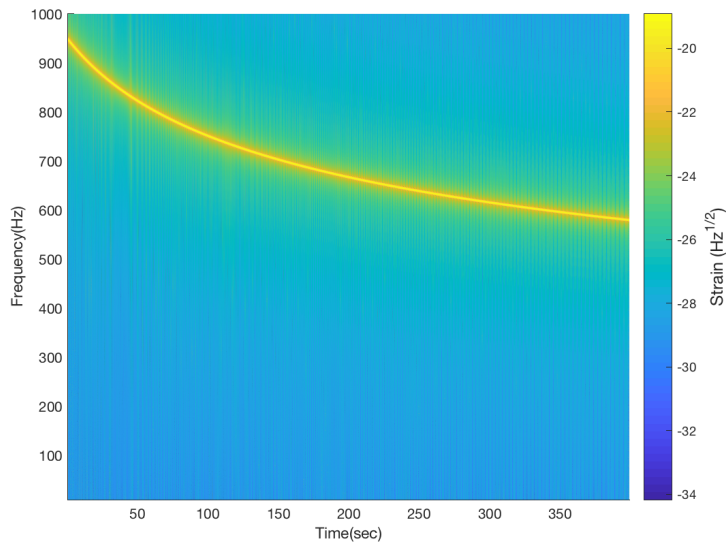


FIGURE 5.17: Magnetar-F injection waveform spectrogram

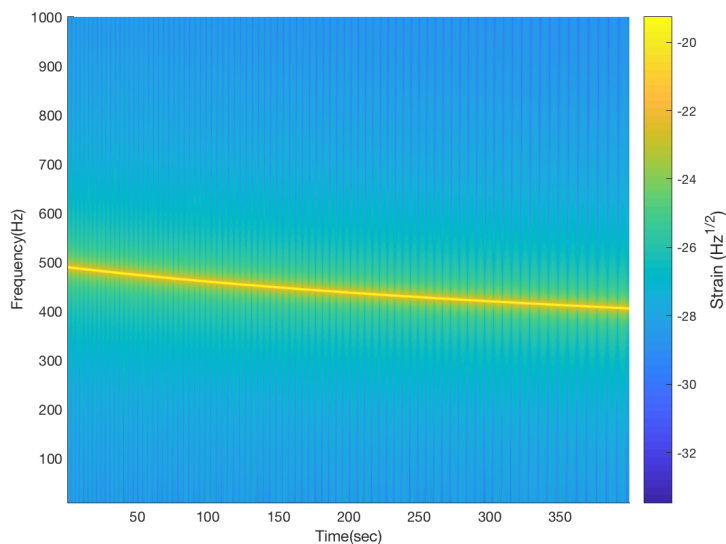


FIGURE 5.18: Magnetar-G injection waveform spectrogram

Again for these longer duration injections the full duration is not well recovered particularly at lower hrss values. Figure 5.20 shows that even over very short distances to the source the full duration is, on average, not recovered. This may be aided with the use of smart clustering however since the magnetar waveforms have a much lower intrinsic amplitudes compared to the ADI waveforms they will still not be as detectable over larger distances.

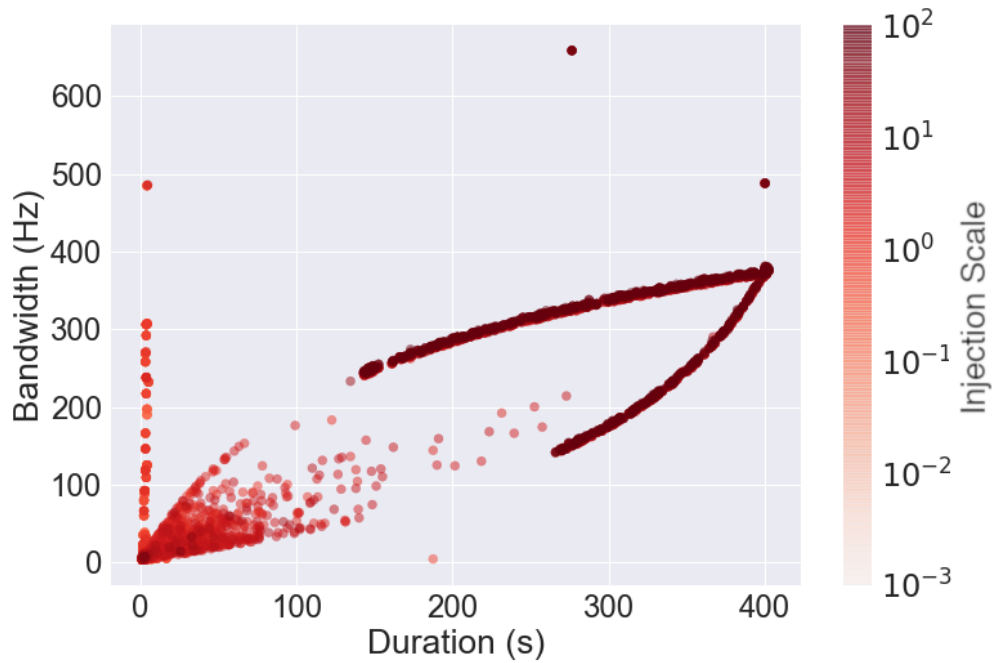


FIGURE 5.19: Duration v.s. bandwidth for all Magnetar-F injections. The distribution of recovered waveforms is split into two trends due to the large bandwidth of the MAgentar-F injections.

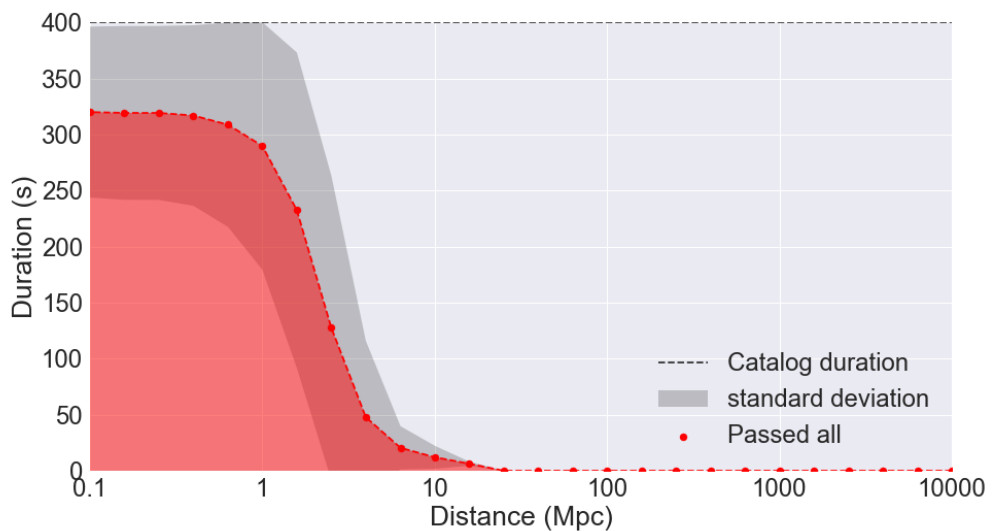


FIGURE 5.20: Averaged duration per distance from source for Magnetar-F injections.

Figure 5.21 shows the average distance to source at 50% and 90% detection efficiency for each of the astrophysical waveforms. Detection efficiency is defined as the percentage of events with significance above the loudest dummy on-source event which also survive the coherent ratio cuts. Again due to their lower amplitude compared to the ADI waveforms the magnetar waveforms have smaller average distance

by over an order of magnitude. Overall the ADI-B waveform with the shortest duration is recovered at the highest average distance to source.

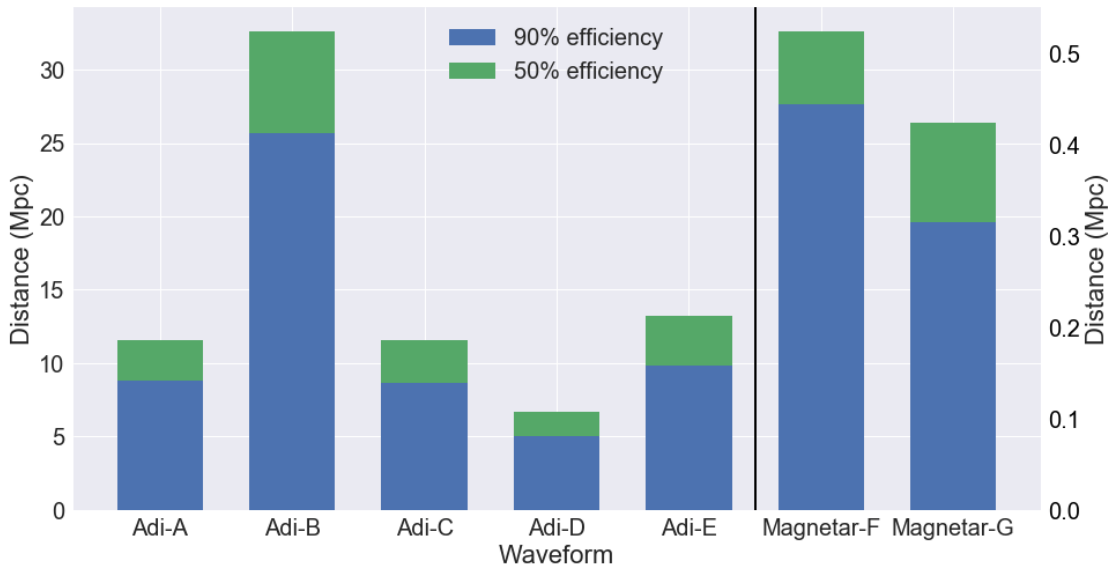


FIGURE 5.21: Sensitivity distances for recovery of astrophysical waveforms using X-SphRad. Larger bandwidth and duration of a waveform results in sensitivity at greater distances. Magnetar waveforms have lower intrinsic amplitudes than ADI waveforms meaning X-SphRad is only sensitive to them at shorter distances.

Ad-hoc models

The ad-hoc injection models are those which are not derived from a particular source. Instead they are used to test the pipelines sensitivity to waveforms with simple models. The waveforms also span a large range of parameter space which can show what duration and bandwidth the pipeline is most sensitive to for a particular set of data.

Waveform	Duration (s)	Min Freq. (Hz)	Max Freq. (Hz)
Mono-A	150	90	90
Mono-C	250	405	405
Line-A	250	50	200
Line-B	100	700	900
Quad-A	30	50	200
Quad-B	70	500	600
SG-A	150	90	90
SG-C	250	405	405
WNB-A	20	50	400
WNB-B	60	300	350
WNB-C	100	700	750

TABLE 5.3: Properties of injected ad-hoc waveforms

Firstly we consider the ad-hoc models which are based on sinusoidal waveforms. The first of these families are the monochromatic waveforms which have constant

frequency. In Figure 5.22 it can be seen that at lower distance to source the average bandwidth of the recovered Mono-A injection is significantly larger than the modelled bandwidth. This is due to the injection being clustered together with background glitches present in the data particularly at lower frequencies.

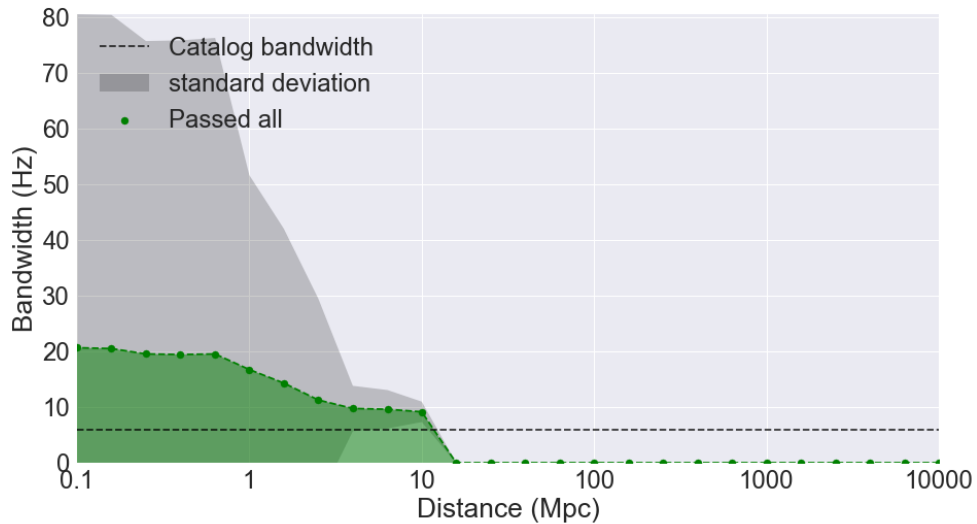


FIGURE 5.22: Bandwidth with increasing distance to source for Mono-A injections. Overestimate in bandwidth is associated with Fourier leakage.

These waveforms are often reduced in energy by the LPEF filtering used to whiten the data. Since they have constant frequencies they are filtered in the same way as any power line would be. From Figure 5.24 it can be seen that the shorter duration Mono-A injections can be detected at larger distance to source than the longer duration Mono-C injections. The longer duration events will result in a larger average power in that frequency band resulting in a larger reduction in power of this band when LPEF filtering is applied.

The linear injections are waveforms with frequency linearly dependent on time. Line-A and Line-B waveforms are sinusoids which linearly increase and decrease in frequency respectively. Figure 5.24 shows that X-SphRad is more sensitive to the Line-B waveforms. This may be due to the the frequency bias addressed previously which is more likely to cut events at lower frequencies. Line-B also has a larger bandwidth and shorter duration which results in higher detection efficiency similarly to the ADI-B injections.

The quadratic waveforms are sinusoids with frequency given by a quadratic function of time. Again because of frequency biasing, X-Sphrad is more sensitive to the Quad-B waveforms. These waveforms are susceptible to the effect of Fourier leakage where power from the injection is transferred to adjacent pixels. The result of this can be seen in Figure 5.23 where the amount of pixels for each injection increases with injection scale. If this effect were not present then the amount of pixels in the cluster should plateau to a constant amount at higher injection scales.

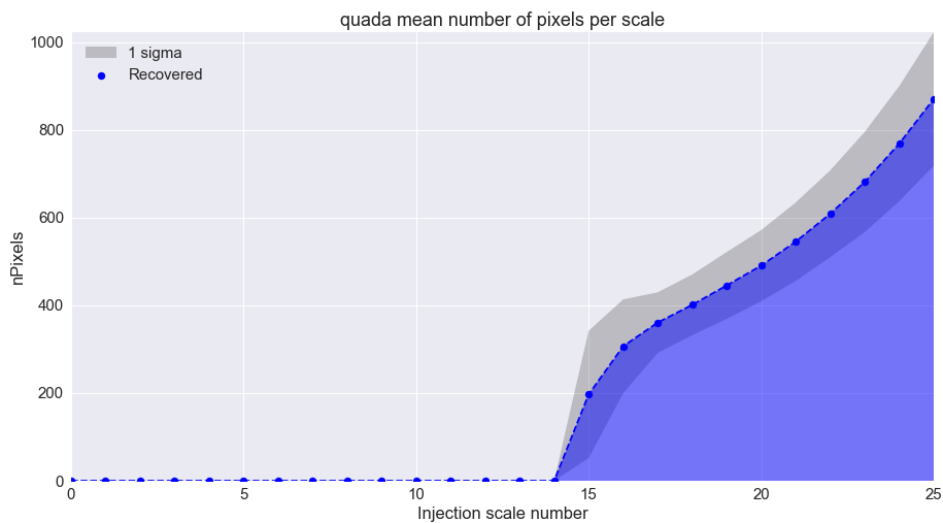


FIGURE 5.23: Number of pixels with increasing injection scale for Quad-A waveforms. Due to Fourier leakage, the recovered pixels continue to increase when they should reach a plateau.

The remaining ad-hoc waveforms are the Sine-Gaussian and White-Noise-Burst families. The Sine-Gaussian family use the same monochromatic waveforms mentioned previously and multiplies them with a Gaussian envelope. This should cause them to have the same problems with LPEF filtering however, from Figure 5.24, the pipeline has a greater sensitivity to them than the monochromatic waveforms. The effect of LPEF filtering might be reduced on these waveforms due to their wider bandwidth caused by the Gaussian envelope. From Figure 5.24 X-Sphrad is most sensitive to the Sine-Gaussian injection family in comparison to the other ad-hoc waveforms.

In contrast to the Sine-Gaussians, the White-Noise-Burst family have a much lower detection efficiency from X-SphRad. White-Noise-Bursts are band-passed white noise signals multiplied by a Gaussian envelope. These injections are similar to glitches caused by detector noise meaning the pipelines sensitivity to these injections relates to the sensitivity to glitches. From Figure 5.24 the intermediate duration WNB-B injections are recovered at the largest distance to source.

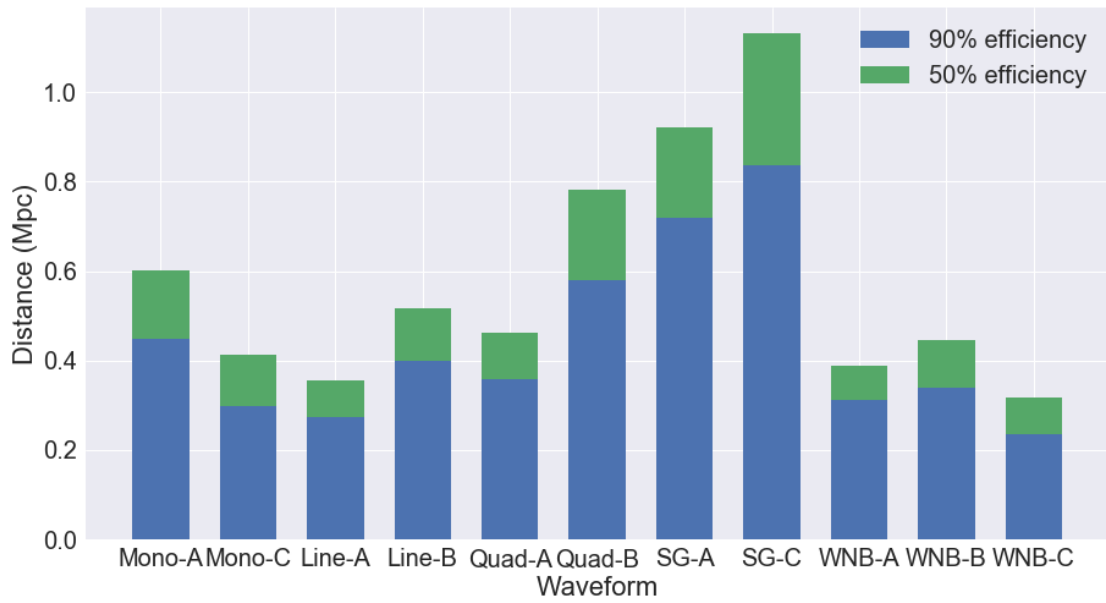


FIGURE 5.24: Sensitivity distance for ad-hoc waveforms at 50% and 90% detection efficiency. Although distance is not based on an astrophysical model, it still indicates how well waveforms are recovered in comparison with each other.

Chapter 6

Conclusion

Line-tracking with the iWave filter has several applications for signal processing GW data. We have shown that one of those applications is iterative line removal of all the lines that pollute the data. This is a less aggressive method for line removal in comparison to the LPEF filter which leaves gaps in sensitivity around the frequency bands where the lines were present. Line removal using iWave can also be used to filter out cases where LPEF filtering has failed. These cases exist when a sinusoidal signal is present in the data with non-static properties such as a wandering frequency. The iWave filter uses a PLL in it's design which allows it to track the wandering frequency of the sinusoid and correct the filters central frequency. We have also shown that tuning the gain and response time of the filter will alter how well it can track a given signal.

In order to develop iWave further I would look to make improvements on the speed at which the filter can subtract multiple lines from the spectrum. This has already begun development where the filter can now track multiple lines in a given frequency region simultaneously. By using this technique the speed at which iWave can iteratively filter out lines described in Chapter 2 can be significantly improved. As well as this a more genral use version of iWave should be developed which does not require tuning the gain and τ parameters before use. It can be difficult for inexperienced users to apply it to LIGO analysis projects due to this required tuning.

Parametric instabilities (PI) have been shown to limit the strain sensitivity of the LIGO interferometers. These occur due to opto-mechanical feedback caused by interaction between TEM modes of the laser with mechanical modes of the cavity test masses. In this thesis we have shown one method of mitigating these instabilities using the Electrostatic drivers ESD. A damping scheme was used to acquire mechanical mode signals from either the OMCPD or QPD. The mechanical mode signal is then used to drive the quadrants of the ESD to damp the mechanical mode. The iWave filter was also developed for real time tracking of the mechanical mode signal.

To develop this PI damping scheme further a solution to the iWave filter losing lock on low SNR modes should be investigated. A possible solution for this would be for iWave to indicate when it has lost lock when the error signal goes above a certain threshold. The filter should remain at the signal frequency of the previously tracked signal in an open-loop state until the signal rings up again within the frequency band. Further development to this scheme would use the on-site guardian system to control the filter states for ESD control of the mechanical modes. With more modes ringing up as the pwer increases it will soon become impossible to manually control each damping filter and will require an automated control system.

The X-SphRad pipeline is a method for performing all-sky searches for GW burst signals. The pipeline uses spherical harmonic decomposition when calculating the correlation between detectors. This allows for more efficient calculation of sky position dependent correlation. The use of spherical harmonics also provides a method rejecting background glitches from the output of an analysis. For strong GW signal candidates the coherent energy from higher order harmonic modes should be greater than the incoherent energy from lower order modes. We also investigated an example of a wandering line during O1 which reduces the pipelines ability to detect events comparatively lower in energy to the line. Using iWave to filter out this line was shown as an effective way to reduce the line energy and increase the amount of lower energy events detected. Automated line removal was also attempted over a period of O2 where an excited violin mode was causing similar problems. From this analysis, events at higher energy were observed and identified to be glitches from the filter output upon follow-up.

For iWave to be used in the future, the cause of the glitches seen in the excited violin mode analysis will need to be investigated. From the investigation described in this work they can be correlated with glitches in the frequency tracking using iWave's PLL. Other future work may go into investigating how iWave can improve the sensitivity of other pipelines in terms of pre-processing. Also the iterative line removal process described in Chapter 2 should be tested as an alternative to the LPEF whitening during X-Sphrad analysis. Again this would require an improvement in the speed at which iWave can filter out multiple lines in order for this to be possible.

The results from running the X-SphRad pipeline on data from the O2 observing run are presented. Two separate analyses were completed to compare the results from using the 2 detector (LH) and 3 detector (VLH) networks. The 3 detector results provide an opportunity to use null stream analysis which allows for further rejection of background events. The detector noise added by Virgo was seen to significantly increase the amount of background events compared to the 2 detector results. We have presented the on-source GW candidates measured from the 2-detector analysis which were consistent with the background. The results from injecting several waveforms are also discussed for the 2-detector analysis. In particular the relationship between bandwidth and duration for recovered waveforms was shown to have diverging trends higher bandwidth anti-chirp injections.

In terms of future work, the full O2 analysis will need to be completed using C02 calibrated data. As well as this better output plots from the pipeline should be developed in order to make more sense of the data. A lot of these are plotted in Chapter 5 but should be adapted into the pipelines webpage output.

Appendix A

Injection efficiency plots from 2 detector analysis

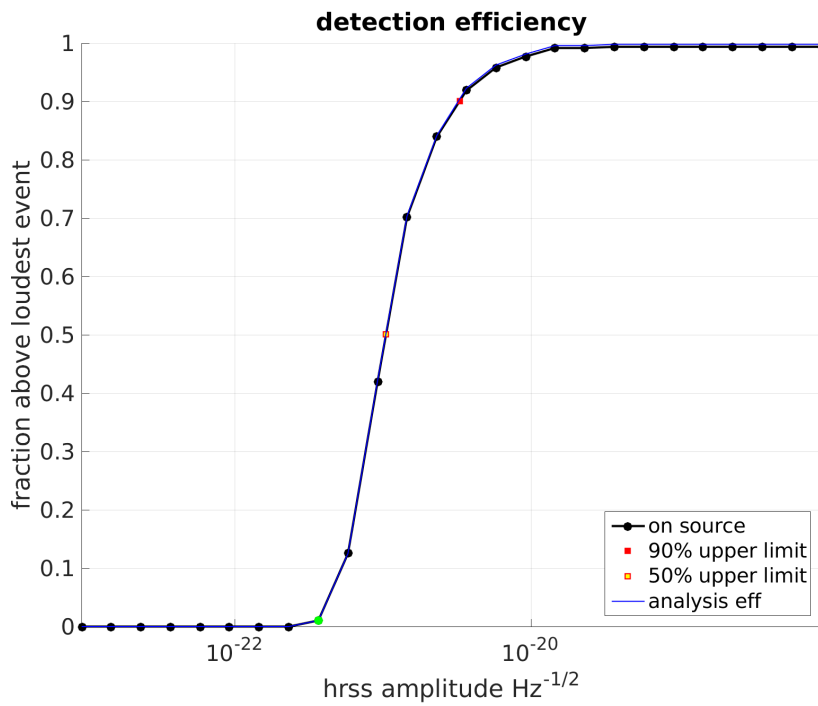


FIGURE A.1: **ADI-A**: Fraction of recovered injections with higher significance than the loudest dummy on-source event.

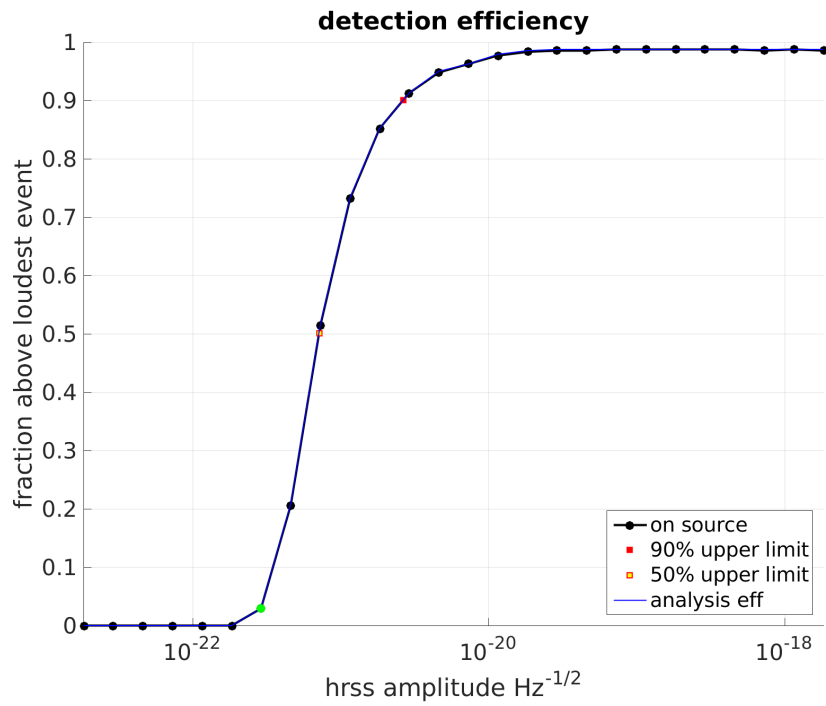


FIGURE A.2: **ADI-B**: Fraction of recovered injections with higher significance than the loudest dummy on-source event.

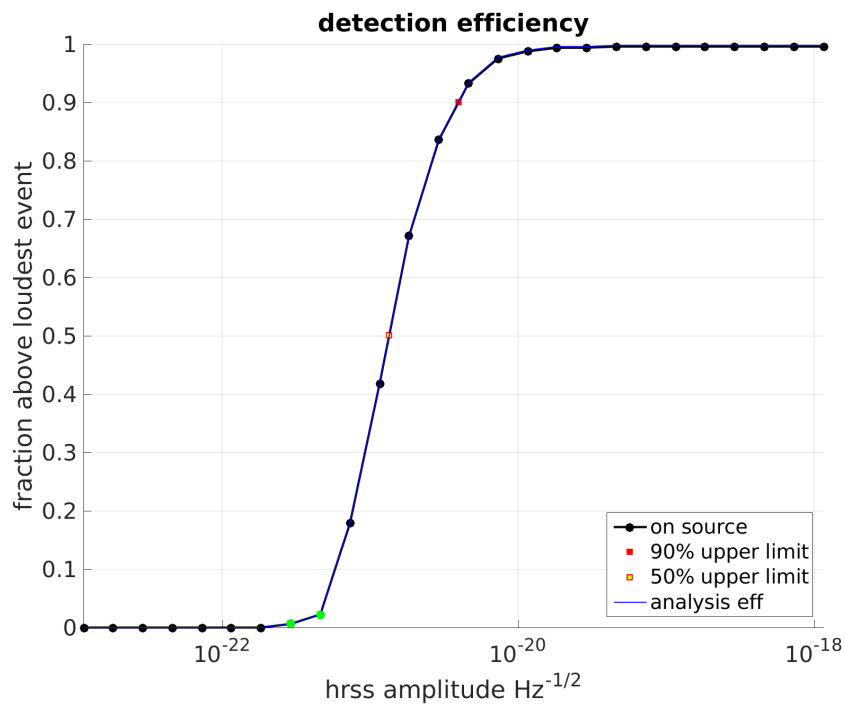


FIGURE A.3: **ADI-C**: Fraction of recovered injections with higher significance than the loudest dummy on-source event.

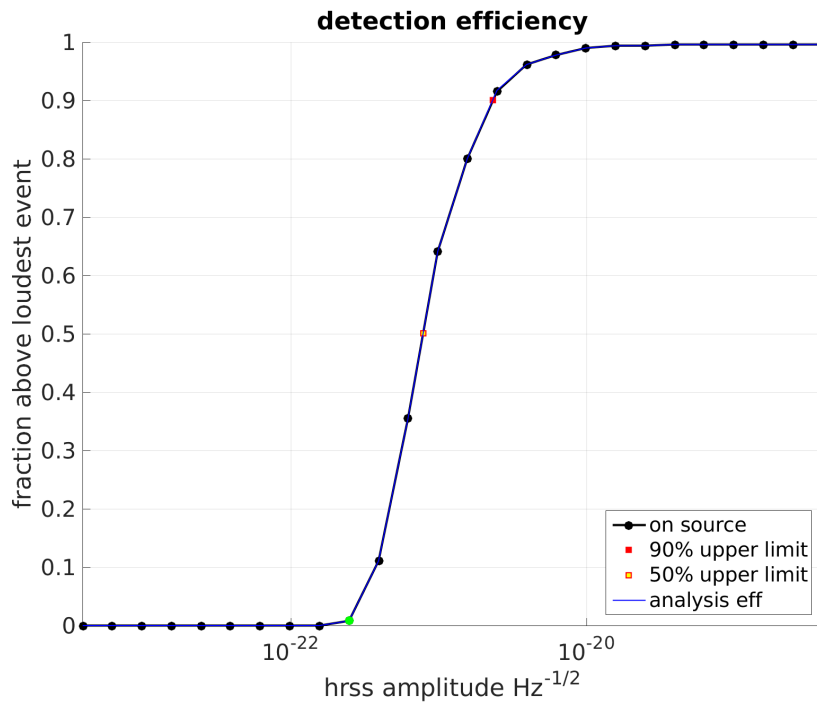


FIGURE A.4: **ADI-D**: Fraction of recovered injections with higher significance than the loudest dummy on-source event.

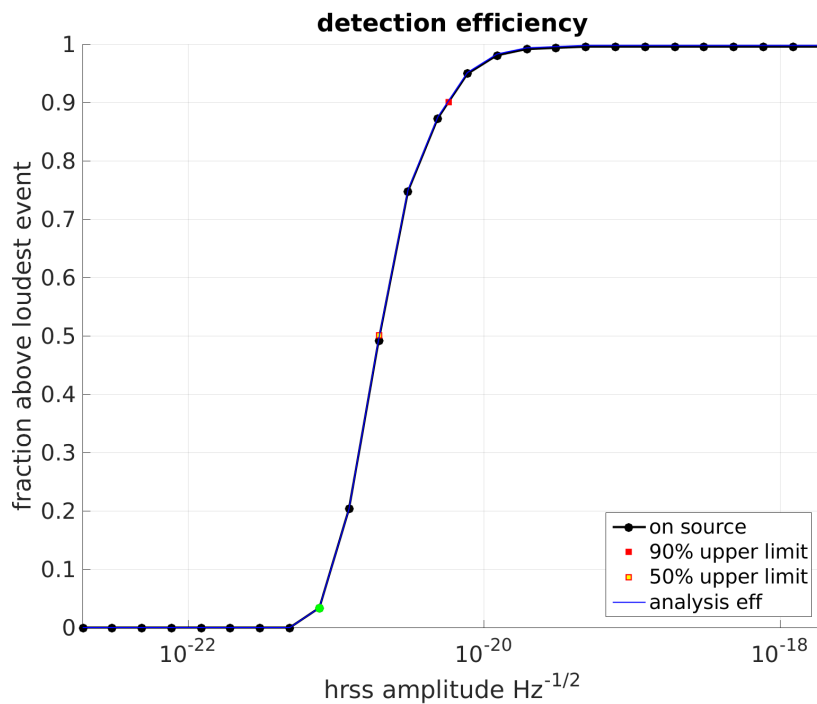


FIGURE A.5: **ADI-E**: Fraction of recovered injections with higher significance than the loudest dummy on-source event.

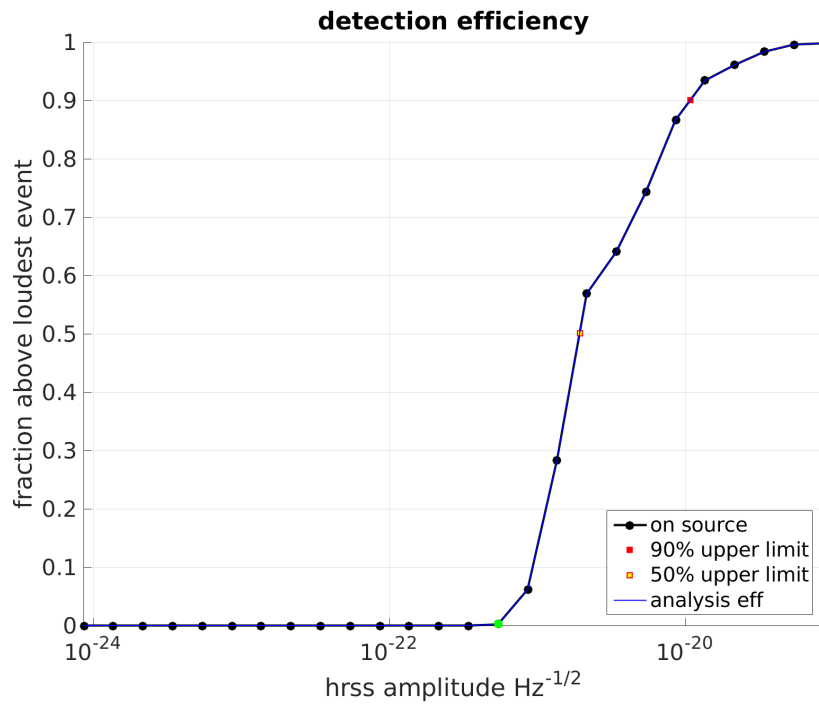


FIGURE A.6: **Magnetar F**: Fraction of recovered injections with higher significance than the loudest dummy on-source event.

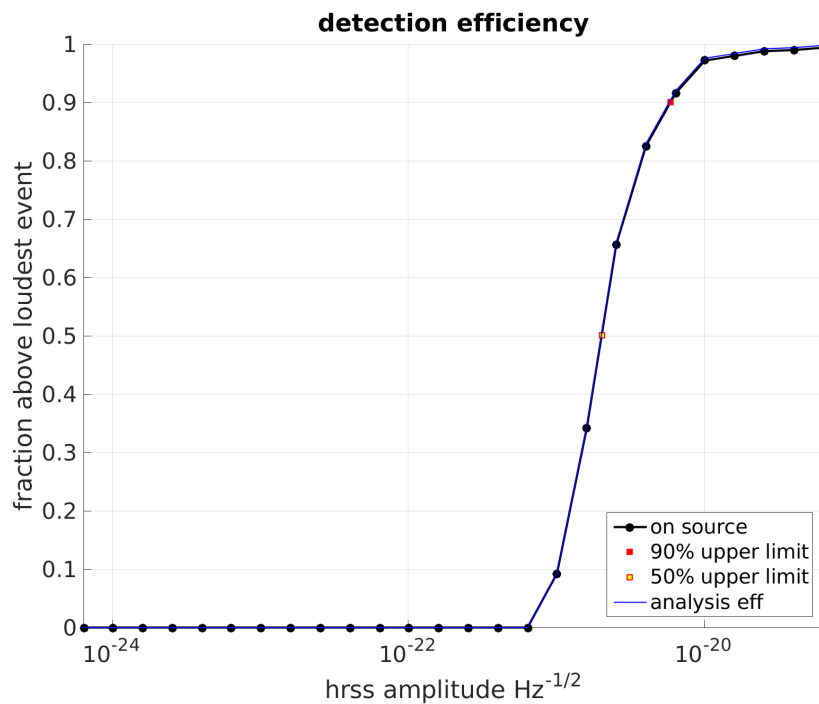


FIGURE A.7: **Magnetar G**: Fraction of recovered injections with higher significance than the loudest dummy on-source event.

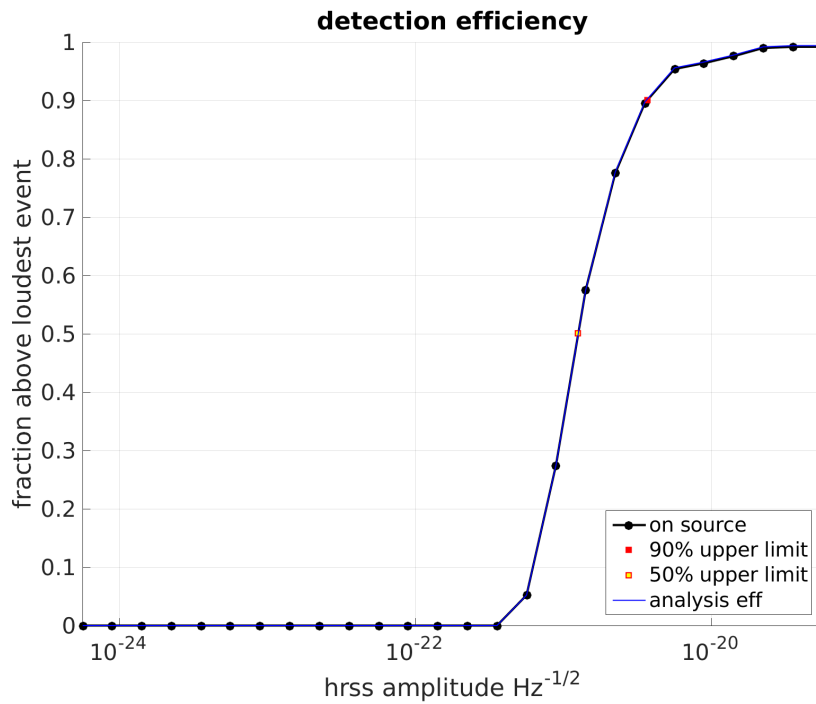


FIGURE A.8: **Mono A**: Fraction of recovered injections with higher significance than the loudest dummy on-source event.

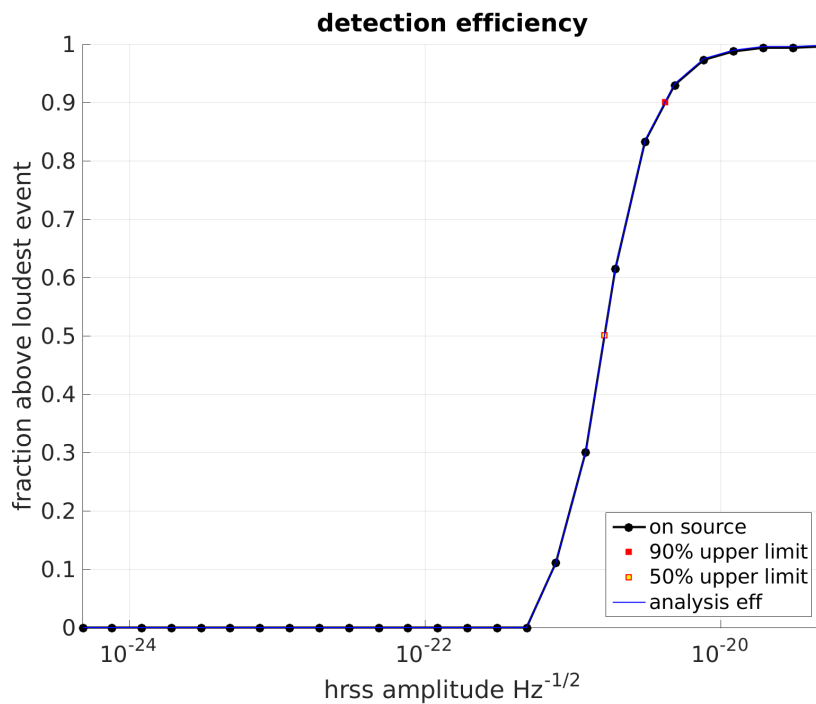


FIGURE A.9: **Mono C**: Fraction of recovered injections with higher significance than the loudest dummy on-source event.

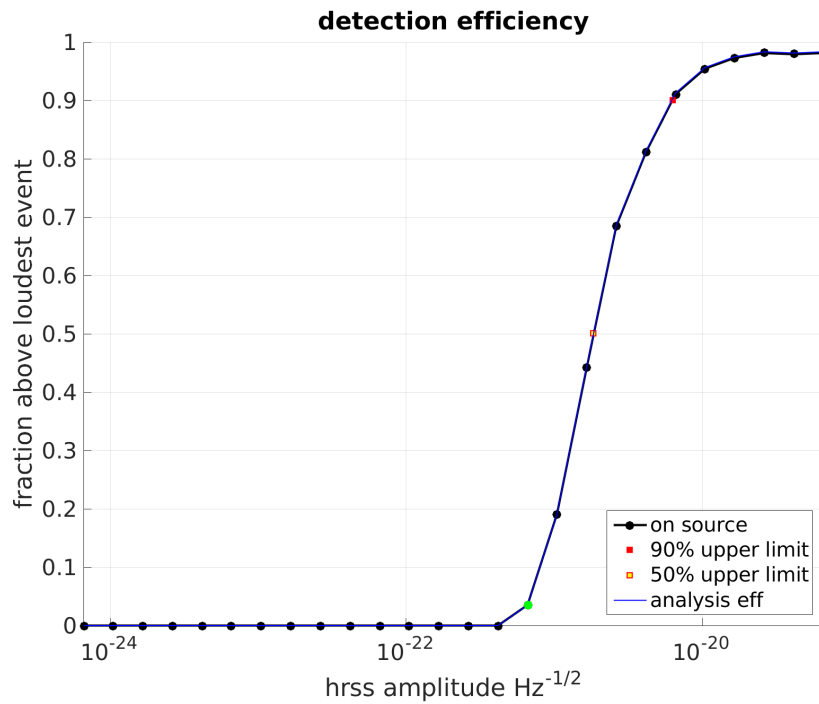


FIGURE A.10: **Quad A**: Fraction of recovered injections with higher significance than the loudest dummy on-source event.

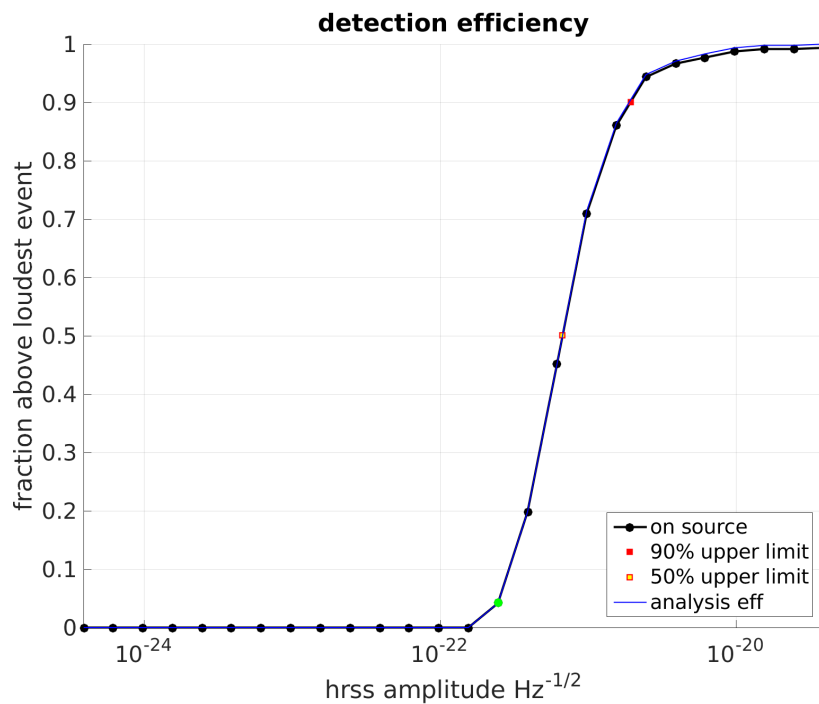


FIGURE A.11: **Quad B**: Fraction of recovered injections with higher significance than the loudest dummy on-source event.

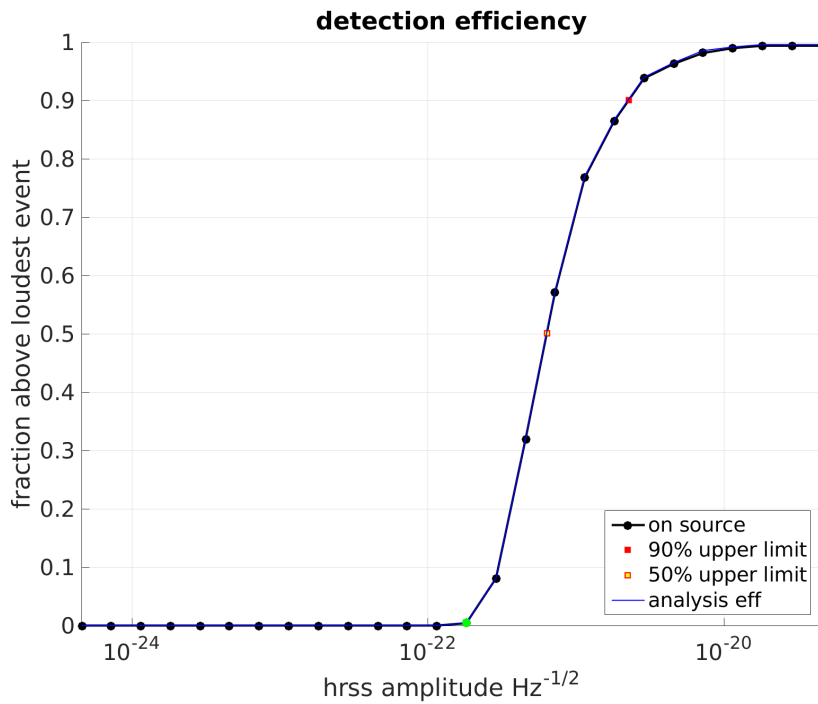


FIGURE A.12: **SGA**: Fraction of recovered injections with higher significance than the loudest dummy on-source event.

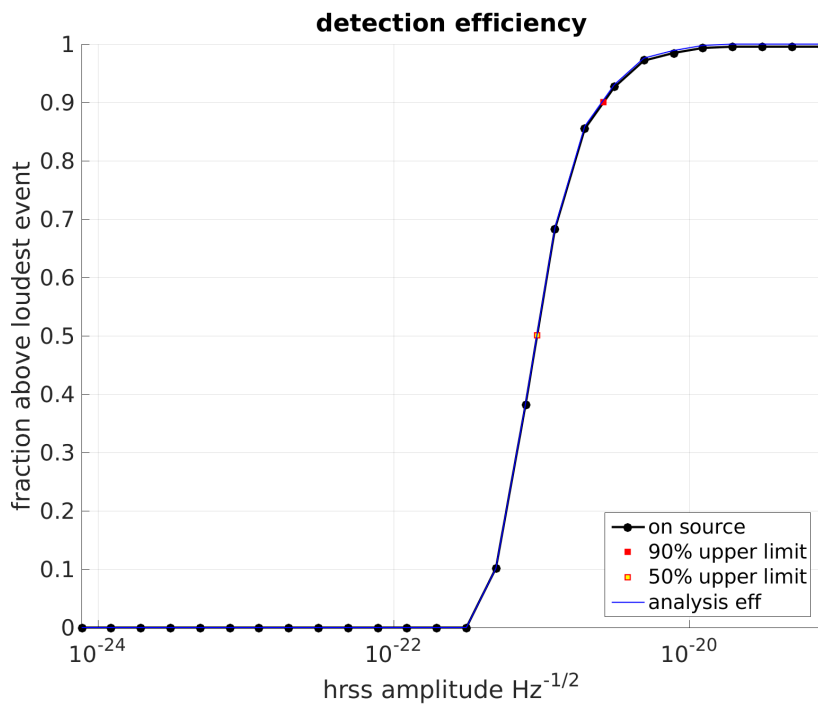


FIGURE A.13: **SGC**: Fraction of recovered injections with higher significance than the loudest dummy on-source event.

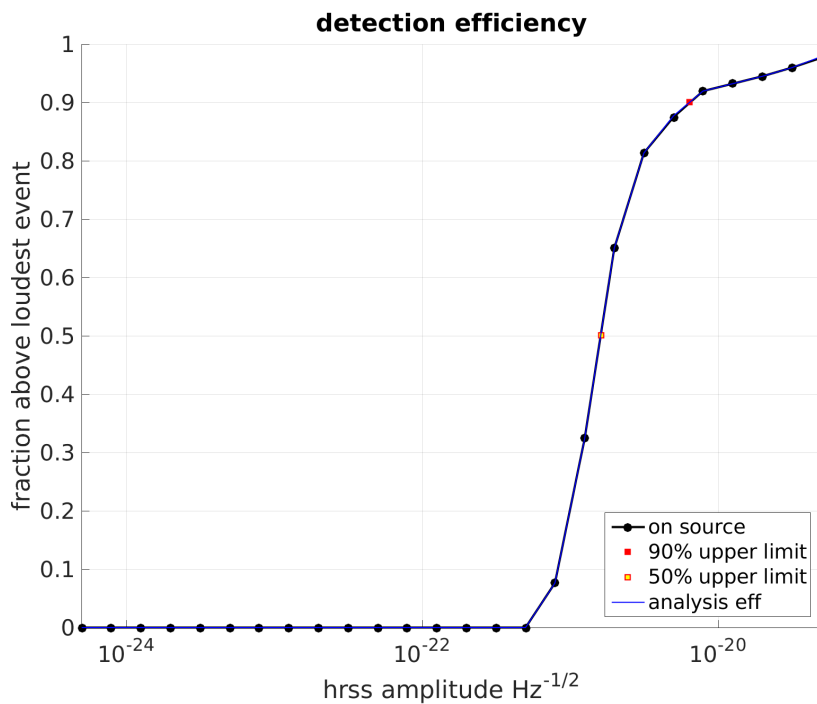


FIGURE A.14: **WNBA**: Fraction of recovered injections with higher significance than the loudest dummy on-source event.

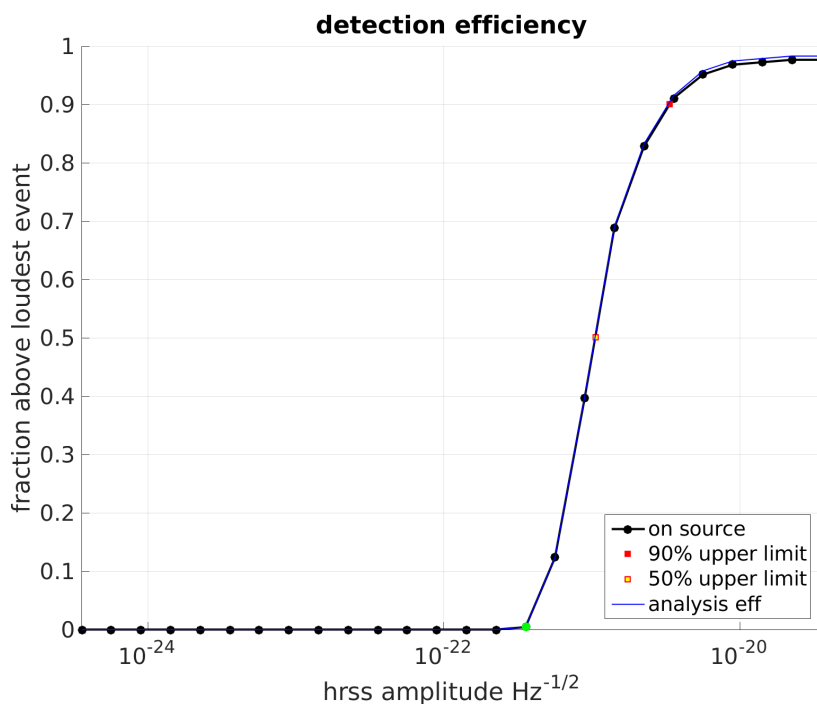


FIGURE A.15: **WNBB**: Fraction of recovered injections with higher significance than the loudest dummy on-source event.

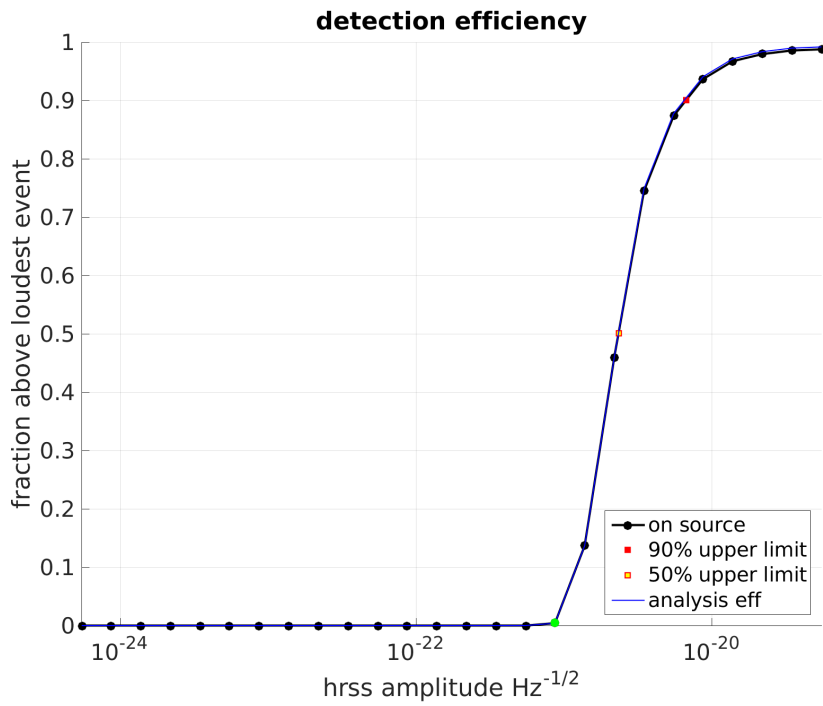


FIGURE A.16: **WNBC**: Fraction of recovered injections with higher significance than the loudest dummy on-source event.

Appendix B

Manual for X-SphRad analysis

Installing the pipeline

You can download the latest version of the pipeline from the svn using:

```
svn co https://svn.ligo.caltech.edu/svn/xpipeline/trunk.
```

This should create a directory called trunk which is the source file for the pipeline. This is then built using the following commands in the trunk directory.

```
./00boot
./configure --prefix=/home/<username>/<install dir> --with-matlab=/ldcg/matlab_r2015b --with-
xtarget=everything --with-frgetvectpath=/home/edaw/libframe/matlab
make
make install
```

Note that the directory after prefix is where the pipeline is installed to. I'd recommend keeping it close to the source directory but don't install it inside of the source directory as this can cause problems.

Setting up analysis

With the pipeline installed you can set up the environment for it i.e. setting the paths to everything in the pipeline so that your computer can find it. This is done by running the environment setup code in your :

```
source /home/<username>/xpipeline5483/Trunk/bin/envsetup.sh
```

source just means to run everything inside the .sh file line by line

Now that you have set up the environment we can run X on a set of data. You'll need four files to do this, grab.param, sphrad.ini, sphradparameters.txt and the veto definer file. These can be found in the template directory I've set up in /home/ross.kennedy/xtemplate_v2

grb.param

In this file you'll see the following

```
allsky.py -p sphrad.ini -n O1 -g 1127193342 -r 123.00 -d -45.00 -i H1 -i L1 -c /home/ross.kennedy/
waveforms/ --big-mem 2500 --long-inj
```

These are all inputs to set up a bunch of xpipeline jobs. The important input is -g 1127193342. This is you're starting gps time. This also points to our sphrad.ini file which is our parameter file for the analysis.

sphrad.ini

To set up our specific analysis we'll need to edit this file.

```
onSourceBeginOffset = 0
```

```
onSourceEndOffset = 30000
```

This is our start and end time for the analysis in seconds. If you want to start at the gps time from grb.param then leave this as zero.

```
channelList = DCS-CALIB_STRAIN_C02,DCS-CALIB_STRAIN_C02
```

```
frameTypeList = H1_HOFT_C02,L1_HOFT_C02
```

This is the channel data that we want to look at. Right now this is set for C02 strain data from both sites but you may need to change this depending on what data is available

veto-file = H1L1-HOFT_C02_O1_BURST.xml

This is the veto definer file i.e. what data shouldn't be used due to glitches. This needs to be in your folder you're running for the analysis.

[waveforms]

```
; ---- Sets of on-the-fly injections to be performed.
stamp_adi_a = stamp_adi_a_tapered!1~-1;1;linear
;stamp_adi_b = stamp_adi_b_tapered!1~-1;1;linear
;stamp_adi_c = stamp_adi_c_tapered!1~-1;1;linear
;stamp_adi_d = stamp_adi_d_tapered!1~-1;1;linear
;stamp_adi_e = stamp_adi_e_tapered!1~-1;1;linear
;stamp_pt_a_tapered = stamp_pt_a_tapered!1~-1;1;linear
;stamp_pt_b_tapered = stamp_pt_b_tapered!1~-1;1;linear
;stamp_maxgnetarf_tapered = stamp_maxgnetarf_tapered!1~-1;1;linear
;stamp_maxgnetarg_tapered = stamp_maxgnetarg_tapered!1~-1;1;linear
```

These are the injection waveforms we want to run analysis on. Each of these will run a separate analysis on top of the on and off source.

sphradparameters.txt

This is another parameter file that is needed to run the analysis. The one in the template directory should be fine for a simple analysis. You can edit things in here if you want to change things such as the amount of time shifts for the off source i.e. how many times we run on data that isn't coincident with each other in time.

Sending jobs to Condor

Once you have all these files set up we can now prepare the jobs to be sent to condor. To do this we run:

```
source grab.param
```

This should create a bunch of .dag files inside the analysis folder as well as the input, output and log folders. After this you can then submit each of these days using e.g.

```
condor_submit_dag grb_on_source.dag
```

This will submit the set of on source analysis jobs from the .dag file. I have written a script to submit all the jobs one after the other so you don't need to type them out each time. If you run

```
~ross.kennedy/tools/jobs_sub
```

in the folder with your .dag files it should do this for you.

You can also check on the progress of these jobs using

```
~ross.kennedy/tools/check.py
```

Running check.py in the folder with current running jobs should output something like this:

You can see the percentage of jobs that have been completed on the side of each analysis. The blue means the jobs finished successfully, black means the jobs are still running and red means that the jobs have failed. Underneath shows the errors associated with why jobs failed which can be useful for fixing them.


```

RETRY xdetection_off_source_seg438_b0cc68f710389b87b7ce80684099a213 2
VARS xdetection_off_source_seg438_b0cc68f710389b87b7ce80684099a213 macroargument0="./input/parameters_off_source_0.txt" macroargument1="438-438" macroargument2="./output/off_source" macroargument3="0"
JOB xdetection_off_source_seg439_ca6c84d16afa8aeb29ba233262ee16d0 xsearch.sub
RETRY xdetection_off_source_seg439_ca6c84d16afa8aeb29ba233262ee16d0 2
VARS xdetection_off_source_seg439_ca6c84d16afa8aeb29ba233262ee16d0 macroargument0="./input/parameters_off_source_0.txt" macroargument1="439-439" macroargument2="./output/off_source" macroargument3="0"
JOB xdetection_off_source_seg440_d9d9a95f2c4112db77ad8b6cd4334be5 xsearch.sub
RETRY xdetection_off_source_seg440_d9d9a95f2c4112db77ad8b6cd4334be5 2
VARS xdetection_off_source_seg440_d9d9a95f2c4112db77ad8b6cd4334be5 macroargument0="./input/parameters_off_source_0.txt" macroargument1="440-440" macroargument2="./output/off_source" macroargument3="0"
JOB xdetection_off_source_seg441_f6b7c170363c202dd3e759bbd899b7b4 xsearch.sub
RETRY xdetection_off_source_seg441_f6b7c170363c202dd3e759bbd899b7b4 2
VARS xdetection_off_source_seg441_f6b7c170363c202dd3e759bbd899b7b4 macroargument0="./input/parameters_off_source_0.txt" macroargument1="441-441" macroargument2="./output/off_source" macroargument3="0"
JOB xdetection_off_source_seg442_1923571555288d513a4a78ff590d3ef2 xsearch.sub
RETRY xdetection_off_source_seg442_1923571555288d513a4a78ff590d3ef2 2
VARS xdetection_off_source_seg442_1923571555288d513a4a78ff590d3ef2 macroargument0="./input/parameters_off_source_0.txt" macroargument1="442-442" macroargument2="./output/off_source" macroargument3="0"
JOB xdetection_off_source_seg443_5b1c3a6ed6df154736f44da39683426d xsearch.sub
RETRY xdetection_off_source_seg443_5b1c3a6ed6df154736f44da39683426d 2

```

From the search in the .dag file we can see these results. In JOB we see there is a .sub file which contains the executable we need to use. In VARS we see the arguments we need for the executable to run the job we want. Looking inside of search.sub we see the executable we need

```

universe = vanilla
executable = /home/ross.kennedy/pipelines/trunk_lineremoval_v2/Trunk/bin/xdetection

arguments = " $(macroargument0) $(macroargument1) $(macroargument2) $(macroargument3) "
environment = USER=$ENV(USER);HOME=$ENV(HOME);LD_LIBRARY_PATH=$ENV(LD_LIBRARY_PATH);XPIPE_INSTALL_BIN=$ENV(XPIPE_INSTALL_BIN);PATH=/usr/bin:/bin
priority = 0
request_memory = 2500
accounting_group_user = ross.kennedy
accounting_group = ligo.prod.o1.burst.allsky_ld.xoffline
log = /local/$ENV(USER)/allsky_jobs_simulations.logs_stamp_adi_e2b2c50f9-e953-4d62-a0a4-066b73694\9b1

error = logs/xsearch-$(cluster)-$(process).err
output = logs/xsearch-$(cluster)-$(process).out
notification = never
queue 1

```

Putting this together with the arguments gives us this command

```

/home/ross.kennedy/pipelines/trunk_lineremoval_v2/Trunk/bin/xdetection ./input/parameters_off_source_0.txt 441-441 ./output/off-source 0

```

This will manually run the job from your terminal allowing you to see why it broke. Sometimes running jobs manually may complete jobs that condor couldn't for some reason.

I have also written a python script which should run any failed job you want from the .rescue file. To call it just run

```
python ~/ross.kennedy/tools/retry_failed.py <rescue file name> <failed job>
```

In failed job here put 1 if you want to run the first job, 2 for the 2nd etc..

Creating webpage

Once all the jobs are finished we can now move on to getting some plots to look at. If you open the makepage.sh file in the analysis directory you should find this

```
DIR="/home/ross.kennedy/02/May_week1"
NAME="May_week1"
PUBLIC="/home/ross.kennedy/public_html/${NAME}/"
LOG="/usr1/ross.kennedy/${NAME}/"
TAG="May1_May7_r5482"

mkdir -p $PUBLIC
mkdir -p $LOG

xallskywebpage.py -g $NAME -d $DIR -a $DIR -w $PUBLIC -l $LOG -u $TAG -c alphaLinCutCirc -p 99.9\
-99.9 -s standardenergy -s circenergy --retry 5 --big-mem 30000 --priority 10
```

You will have to edit these strings to make sense for the analysis you have done. The NAME and TAG variables are the names of the directory and subdirectory they will be saved as in your public_html directory. After you've edited this you can run

```
source makepage.sh
```

This should make a folder called autoweb in the current directory. In auto web there should now be a file called grb_web.dag which you can submit in the same way as before

```
condor_submit_dag grb_web.dag
```

You can use check.py as well to see how far along it is. This job usually takes a while to do the last 1% so don't panic. Once it's finished you should have a new file in your folder ~/public_html. In this folder should be a .shtml file which is the webpage with all the plots. To access this page in a web browser go to <https://ldas-jobs.ligo.caltech.edu/>

Bibliography

- [1] URL: <https://alog.ligo-wa.caltech.edu/aLOG/index.php?callRep=21020>.
- [2] URL: <https://alog.ligo-wa.caltech.edu/aLOG/index.php?callRep=29408>.
- [3] URL: <https://alog.ligo-wa.caltech.edu/aLOG/index.php?callRep=17903>.
- [4] *A Brief History of LIGO* | Caltech. URL: <http://www.caltech.edu/content/brief-history-ligo>.
- [5] Abbott R. Abbott T. D. et al. Abbott B. P. “All-sky search for long-duration gravitational wave transients with initial LIGO.” In: *Physical Review D* (2016).
- [6] A.Einstein. “Approximative Integration of the Field Equations of Gravitation”. In: *The Collected Papers of Albert Einstein* 62 (May 1916). URL: <http://einsteinpapers.press.princeton.edu/vol6-trans/213>.
- [7] N.Rosen A.Einstein. “On Gravitational Waves”. In: *Journal of the Franklin Institute* 223.1 (Jan. 1937), pp. 43–54. URL: <http://www.sciencedirect.com/science/article/pii/S0016003237905830>.
- [8] B. P. Abbott et al. “Advanced LIGO”. In: *Classical and Quantum Gravity* 32.7 (2015), p. 074001. URL: <http://stacks.iop.org/0264-9381/32/i=7/a=074001>.
- [9] B. P. Abbott et al. “GW151226: Observation of Gravitational Waves from a 22-Solar-Mass Binary Black Hole Coalescence”. In: *Phys. Rev. Lett.* 116 (24 2016), p. 241103. DOI: 10.1103/PhysRevLett.116.241103. URL: <https://link.aps.org/doi/10.1103/PhysRevLett.116.241103>.
- [10] B. P. Abbott et al. “GW170817: Observation of Gravitational Waves from a Binary Neutron Star Inspiral”. In: *Phys. Rev. Lett.* 119 (16 2017), p. 161101. DOI: 10.1103/PhysRevLett.119.161101. URL: <https://link.aps.org/doi/10.1103/PhysRevLett.119.161101>.
- [11] B. P. Abbott et al. “LIGO: the Laser Interferometer Gravitational-Wave Observatory”. In: *Reports on Progress in Physics* 72.7 (2009), p. 076901. URL: <http://stacks.iop.org/0034-4885/72/i=7/a=076901>.
- [12] B. P. Abbott et al. “Observation of Gravitational Waves from a Binary Black Hole Merger”. In: *Physical Review Letters* 116.12 (Feb. 2016), pp. 4477–4479. URL: <https://journals.aps.org/prl/pdf/10.1103/PhysRevLett.116.061102>.
- [13] HU Enke et al. “A recent coincidence experiment of gravitational waves with long baseline”. In: *Chinese Physics Letters* 3.12, 529 (1986), p. 529. URL: http://cpl.iphy.ac.cn/EN/abstract/article_38908.shtml.
- [14] T T Fricke et al. “DC readout experiment in Enhanced LIGO”. In: *IOP Publishing Class. Quantum Grav.* ().
- [15] K Arai and the TAMA Collaboration. “Sensing and controls for power-recycling of TAMA300”. In: *IOP Publishing Class. Quantum Grav.* 19 (2002).

- [16] Carl Blair. “Parametric Instability in Gravitational Wave Detectors”. PhD thesis. University of Western Australia, 2017.
- [17] Carl Blair et al. “First Demonstration of Electrostatic Damping of Parametric Instability at Advanced LIGO”. In: *Phys. Rev. Lett.* 118 (15 2017), p. 151102. DOI: [10.1103/PhysRevLett.118.151102](https://doi.org/10.1103/PhysRevLett.118.151102). URL: <https://link.aps.org/doi/10.1103/PhysRevLett.118.151102>.
- [18] V.B. Braginsky, S.E. Strigin, and S.P. Vyatchanin. “Parametric oscillatory instability in Fabry–Perot interferometer”. In: *Physics Letters A* 287.5 (2001), pp. 331–338. ISSN: 0375-9601. DOI: [https://doi.org/10.1016/S0375-9601\(01\)00510-2](https://doi.org/10.1016/S0375-9601(01)00510-2). URL: <http://www.sciencedirect.com/science/article/pii/S0375960101005102>.
- [19] Aidan F. Brooks et al. “Overview of Advanced LIGO adaptive optics”. In: *Appl. Opt.* 55.29 (2016), pp. 8256–8265. DOI: [10.1364/AO.55.008256](https://doi.org/10.1364/AO.55.008256). URL: <http://ao.osa.org/abstract.cfm?URI=ao-55-29-8256>.
- [20] Kipp C. Cannon. “Efficient algorithm for computing the time-resolved full-sky cross power in an interferometer with omnidirectional elements”. In: *Phys. Rev. D* 75 (12 2007), p. 123003. DOI: [10.1103/PhysRevD.75.123003](https://doi.org/10.1103/PhysRevD.75.123003). URL: <https://link.aps.org/doi/10.1103/PhysRevD.75.123003>.
- [21] S Chatterji et al. “Multiresolution techniques for the detection of gravitational-wave bursts”. In: *Classical and Quantum Gravity* 21.20 (2004), S1809. URL: <http://stacks.iop.org/0264-9381/21/i=20/a=024>.
- [22] Chiang-Mei Chen, James M. Nester, and Wei-Tou Ni. “A brief history of gravitational wave research”. In: *Chinese Journal of Physics* 55.1 (2017), pp. 142–169. ISSN: 0577-9073. DOI: <https://doi.org/10.1016/j.cjph.2016.10.014>. URL: <http://www.sciencedirect.com/science/article/pii/S057790731630572X>.
- [23] The LIGO Scientific Collaboration & The Virgo Collaboration. “An upper limit on the stochastic gravitational-wave background of cosmological origin (article)”. In: *Nature* 460 (Aug. 2009), 990 EP –. URL: <http://dx.doi.org/10.1038/nature08278>.
- [24] K.S. Thorne C.W. Misner and J.A. Wheeler. *Gravitation*. 1973.
- [25] Simone Dall’Osso et al. “Gravitational Waves from Massive Magnetars Formed in Binary Neutron Star Mergers”. In: *The Astrophysical Journal* 798.1 (2015), p. 25. URL: <http://stacks.iop.org/0004-637X/798/i=1/a=25>.
- [26] Edward J. Daw. “A Bayesian Adaptive Filtering Approach to Dynamic Wave Tracking”. unpublished.
- [27] R. W. P. DREVER et al. “Search for Short Bursts of Gravitational Radiation”. In: *Nature* 246 (Dec. 1973), 340 EP –. URL: <http://dx.doi.org/10.1038/246340a0>.
- [28] Eddington Arthur Stanley Dyson Frank Watson and Charles R Davidson. “A Determination of the Deflection of Light by the Sun’s Gravitational Field, from Observations made at the Total Solar Eclipse of May 29, 1919.” In: *Philosophical Transactions of the Royal Society series A* 220 (1920), pp. 291–330.
- [29] M. Edwards. “On the search for intermediate duration gravitational waves using the spherical harmonic basis.” PhD thesis. Cardiff University, 2013. URL: <http://orca.cf.ac.uk/53498/>.
- [30] Mark Edwards and Patrick J Sutton. “A new glitch-rejection algorithm forged in the spherical harmonic basis”. In: *Journal of Physics: Conference Series* 363.1 (2012), p. 012025. URL: <http://stacks.iop.org/1742-6596/363/i=1/a=012025>.

- [31] Mark Edwards and Patrick J Sutton. “A new glitch-rejection algorithm forged in the spherical harmonic basis”. In: *Journal of Physics: Conference Series* 363.1 (2012), p. 012025. URL: <http://stacks.iop.org/1742-6596/363/i=1/a=012025>.
- [32] Matthew Evans et al. “Observation of Parametric Instability in Advanced LIGO”. In: *Phys. Rev. Lett.* 114 (16 2015), p. 161102. DOI: [10.1103/PhysRevLett.114.161102](https://doi.org/10.1103/PhysRevLett.114.161102). URL: <https://link.aps.org/doi/10.1103/PhysRevLett.114.161102>.
- [33] Maxime. Fays. “Exploring long duration gravitational-wave transients with second generation detectors”. PhD thesis. Cardiff University, 2017. URL: <http://orca.cf.ac.uk/110245/>.
- [34] Robert L. Forward. “Wideband laser-interferometer gravitational-radiation experiment”. In: *Phys. Rev. D* 17 (2 Jan. 1978), pp. 379–390. DOI: [10.1103/PhysRevD.17.379](https://doi.org/10.1103/PhysRevD.17.379). URL: <https://link.aps.org/doi/10.1103/PhysRevD.17.379>.
- [35] Robert L. Forward. “Wideband laser-interferometer gravitational-radiation experiment”. In: *Phys. Rev. D* 17 (2 1978), pp. 379–390. DOI: [10.1103/PhysRevD.17.379](https://doi.org/10.1103/PhysRevD.17.379). URL: <https://link.aps.org/doi/10.1103/PhysRevD.17.379>.
- [36] Andreas Freise and Kenneth Strain. “Interferometer Techniques for Gravitational-Wave Detection.” In: *Living Rev. Relativity* 13 (2010).
- [37] Tobin T Fricke et al. “DC readout experiment in Enhanced LIGO”. In: *Classical and Quantum Gravity* 29.6 (2012), p. 065005. URL: <http://stacks.iop.org/0264-9381/29/i=6/a=065005>.
- [38] Richard L. Garwin and James L. Levine. “Single Gravity-Wave Detector Results Contrasted with Previous Coincidence Detections”. In: *Phys. Rev. Lett.* 31 (3 July 1973), pp. 176–180. DOI: [10.1103/PhysRevLett.31.176](https://doi.org/10.1103/PhysRevLett.31.176). URL: <https://link.aps.org/doi/10.1103/PhysRevLett.31.176>.
- [39] *Gravitational Astrophysics. Martin Hendry and Graeme Woan.*
- [40] Yekta Gürsel and Massimo Tinto. “Near optimal solution to the inverse problem for gravitational-wave bursts”. In: *Phys. Rev. D* 40 (12 1989), pp. 3884–3938. DOI: [10.1103/PhysRevD.40.3884](https://doi.org/10.1103/PhysRevD.40.3884). URL: <https://link.aps.org/doi/10.1103/PhysRevD.40.3884>.
- [41] William P. Kells Hans S. Bantilan. “Investigating a Parametric Instability in the LIGO Test Masses”. In: (2006). URL: <https://dcc.ligo.org/T060207/public>.
- [42] Gregory M. Harry et al. “Thermal noise from optical coatings in gravitational wave detectors”. In: *Appl. Opt.* 45.7 (2006), pp. 1569–1574. DOI: [10.1364/AO.45.001569](https://doi.org/10.1364/AO.45.001569). URL: <http://ao.osa.org/abstract.cfm?URI=ao-45-7-1569>.
- [43] “Intuitive explanation of the phase anomaly of focused light beams.” In: *Journal of the Optical Society of America* 70 (1980), p. 877.
- [44] L Ju et al. “Strategies for the control of parametric instability in advanced gravitational wave detectors”. In: *Classical and Quantum Gravity* 26.1 (2009), p. 015002. URL: <http://stacks.iop.org/0264-9381/26/i=1/a=015002>.
- [45] I. Kimel and L. R. Elias. “Relations between Hermite and Laguerre Gaussian modes”. In: *IEEE Journal of Quantum Electronics* 29.9 (1993), pp. 2562–2567. ISSN: 0018-9197. DOI: [10.1109/3.247715](https://doi.org/10.1109/3.247715).

- [46] Wen L and Schutz B F. "Coherent network detection of gravitational waves: the redundancy veto". In: *Class. Quant. Grav* 22 (2005). URL: [arXiv:gr-qc/0508042](https://arxiv.org/abs/gr-qc/0508042).
- [47] B.T. Lantz. "Quantum Limited Optical Phase Detection in a High Power Suspended Interferometer." PhD thesis.
- [48] LIGO Scientific Collaboration. "First upper limits from LIGO on gravitational wave bursts". In: *Phys. Rev. D* 69 (10 2004), p. 102001. DOI: [10.1103/PhysRevD.69.102001](https://doi.org/10.1103/PhysRevD.69.102001). URL: <https://link.aps.org/doi/10.1103/PhysRevD.69.102001>.
- [49] LIGO Scientific Collaboration and Virgo Collaboration. "First targeted search for gravitational-wave bursts from core-collapse supernovae in data of first-generation laser interferometer detectors". In: *Phys. Rev. D* 94 (10 2016), p. 102001. DOI: [10.1103/PhysRevD.94.102001](https://doi.org/10.1103/PhysRevD.94.102001). URL: <https://link.aps.org/doi/10.1103/PhysRevD.94.102001>.
- [50] LIGO Scientific Collaboration, Virgo Collaboration, and IPN Collaboration. "Search for Gravitational Waves Associated with γ -ray Bursts Detected by the Interplanetary Network". In: *Phys. Rev. Lett.* 113 (1 2014), p. 011102. DOI: [10.1103/PhysRevLett.113.011102](https://doi.org/10.1103/PhysRevLett.113.011102). URL: <https://link.aps.org/doi/10.1103/PhysRevLett.113.011102>.
- [51] R. Loudon and P.L. Knight. "Squeezed Light". In: *Journal of Modern Optics* 34:6-7 (1987), pp. 709–759. DOI: [10.1080/09500348714550721](https://doi.org/10.1080/09500348714550721). URL: <https://doi.org/10.1080/09500348714550721>.
- [52] Ryan Lynch et al. "Effect of squeezing on parameter estimation of gravitational waves emitted by compact binary systems". In: *Phys. Rev. D* 91 (4 2015), p. 044032. DOI: [10.1103/PhysRevD.91.044032](https://doi.org/10.1103/PhysRevD.91.044032). URL: <https://link.aps.org/doi/10.1103/PhysRevD.91.044032>.
- [53] Brian J Meers. "Recycling in laser-interferometric gravitational-wave detectors". In: *Physical Review D* (1988).
- [54] John Miller. "On non-Gaussian beams and optomechanical parametric instabilities in interferometric gravitational wave detectors." PhD thesis. University of Glasgow, 2010.
- [55] John Miller et al. "Damping parametric instabilities in future gravitational wave detectors by means of electrostatic actuators". In: *Physics Letters A* 375:3 (2011), pp. 788–794. ISSN: 0375-9601. DOI: <https://doi.org/10.1016/j.physleta.2010.12.032>. URL: <http://www.sciencedirect.com/science/article/pii/S0375960110015719>.
- [56] Osamu Miyakawa et al. "Lock Acquisition Scheme For The Advanced LIGO Optical configuration". In: *Journal of Physics: Conference Series* 32:1 (2006), p. 265. URL: <http://stacks.iop.org/1742-6596/32/i=1/a=039>.
- [57] G. E. Moss, L. R. Miller, and R. L. Forward. "Photon-Noise-Limited Laser Transducer for Gravitational Antenna". In: *Appl. Opt.* 10:11 (Nov. 1971), pp. 2495–2498. DOI: [10.1364/AO.10.002495](https://doi.org/10.1364/AO.10.002495). URL: <http://ao.osa.org/abstract.cfm?URI=ao-10-11-2495>.
- [58] Chris Mueller. "The Advanced LIGO Input Mode Cleaner". In: ().
- [59] J. Palamos. *650Hz peak fixed, ALS COMM VCO TUNE OFS set to 2*. 2015. URL: <https://alog.ligo-wa.caltech.edu/aLOG/index.php?callRep=24092>.
- [60] "Predictions for the rates of compact binary coalescences observable by ground-based gravitational-wave detectors". In: *Classical and Quantum Gravity* 27:17 (2010), p. 173001. URL: <http://stacks.iop.org/0264-9381/27/i=17/a=173001>.

- [61] Maurice H. P. M. van Putten. "Gravitational Waveforms of Kerr Black Holes Interacting with High-Density Matter". In: *The Astrophysical Journal Letters* 684.2 (2008), p. L91. URL: <http://stacks.iop.org/1538-4357/684/i=2/a=L91>.
- [62] Maurice H. P. M. van Putten. "Proposed Source of Gravitational Radiation from a Torus around a Black Hole". In: *Phys. Rev. Lett.* 87 (9 2001), p. 091101. DOI: 10.1103/PhysRevLett.87.091101. URL: <https://link.aps.org/doi/10.1103/PhysRevLett.87.091101>.
- [63] B. S. Sathyaprakash and S. V. Dhurandhar. "Choice of filters for the detection of gravitational waves from coalescing binaries". In: *Phys. Rev. D* 44 (12 1991), pp. 3819–3834. DOI: 10.1103/PhysRevD.44.3819. URL: <https://link.aps.org/doi/10.1103/PhysRevD.44.3819>.
- [64] B. S. Sathyaprakash and Bernard F. Schutz. "Physics, Astrophysics and Cosmology with Gravitational Waves". In: *Living Reviews in Relativity* 12.1 (2009), p. 2. ISSN: 1433-8351. DOI: 10.12942/lrr-2009-2. URL: <https://doi.org/10.12942/lrr-2009-2>.
- [65] Bernard F. Schutz. *A First Course in General Relativity 2nd edition*. Cambridge University Press, 2009.
- [66] Irwin I. Shapiro. "Fourth Test of General Relativity". In: *Phys. Rev. Lett.* 13 (26 1964), pp. 789–791. DOI: 10.1103/PhysRevLett.13.789. URL: <https://link.aps.org/doi/10.1103/PhysRevLett.13.789>.
- [67] A. E. Siegman. *Lasers*. Mill Valley, Calif: University Science Books, 1986.
- [68] Patrick J Sutton et al. "X-Pipeline: an analysis package for autonomous gravitational-wave burst searches". In: *New Journal of Physics* 12.5 (2010), p. 053034. URL: <http://stacks.iop.org/1367-2630/12/i=5/a=053034>.
- [69] J. H. Taylor, L. A. Fowler, and P. M. McCulloch. "Measurements of general relativistic effects in the binary pulsar PSR1913 + 16". In: *Nature* 277 (1979). URL: <http://dx.doi.org/10.1038/277437a0>.
- [70] J. H. Taylor and P. M. McCulloch. "Evidence for the existence of gravitational radiation from measurements of the binar pulsar PSR 1913+16*". In: *Annals of the New York Academy of Sciences* 336.1 (1980), pp. 442–446. ISSN: 1749-6632. DOI: 10.1111/j.1749-6632.1980.tb15951.x. URL: <http://dx.doi.org/10.1111/j.1749-6632.1980.tb15951.x>.
- [71] The LIGO Scientific Collaboration, T. L. S, , Virgo Collaboration. "Search for Gravitational Waves Associated with Gamma-Ray Bursts during LIGO Science Run 6 and Virgo Science Runs 2 and 3". In: *The Astrophysical Journal* 760.1 (2012), p. 12. URL: <http://stacks.iop.org/0004-637X/760/i=1/a=12>.
- [72] The LIGO Scientific Collaboration, T. L. S. and The Virgo Collaboration. "The Advanced LIGO Detectors in the Era of First Discoveries." In: *Physical Review Letters* (2016). URL: <https://journals.aps.org/prl/pdf/10.1103/PhysRevLett.116.131103>.
- [73] "The LSC-Virgo White Paper on Gravitational Wave Searches and Astrophysics (2015-2016 edition)". In: (). URL: <https://dcc.ligo.org/LIGO-T1500055/public>.
- [74] J. A. Tyson. "Null Search for Bursts of Gravitational Radiation". In: *Phys. Rev. Lett.* 31 (5 July 1973), pp. 326–329. DOI: 10.1103/PhysRevLett.31.326. URL: <https://link.aps.org/doi/10.1103/PhysRevLett.31.326>.
- [75] J. Weber. "Anisotropy and polarization in the gravitational-radiation experiments". In: *Physical Review Letters* 25.24 (Mar. 1970).

-
- [76] J. Weber. "Observation of the thermal fluctuations of a gravitational-wave detector". In: *Physical Review Letters* 17.24 (Dec. 1966).
- [77] Joel M. Weisberg, David J. Nice, and Joseph H. Taylor. "Timing Measurements of the Relativistic Binary Pulsar PSR B1913+16". In: (2010). DOI: [10.1088/0004-637X/722/2/1030](https://doi.org/10.1088/0004-637X/722/2/1030). eprint: [arXiv:1011.0718](https://arxiv.org/abs/1011.0718).
- [78] R Weiss. "A Study of a Long Baseline Gravitational Wave Antenna System - Prepared for NSF Under NSF Grant PHY-8109581 to MIT". In: (1983).
- [79] R Weiss. "Electromagnetically coupled broadband gravitational antenna. Quarterly Progress Report 105, Research Laboratory of Electronics". In: (1972).